Dipl.-Ing. Martin Söllradl, BSc

Quantitative Gradient-Echo Imaging with Macroscopic B_0 Field Variations in the Brain

DOCTORAL THESIS

to achieve the university degree of
Doktor der technischen Wissenschaften

submitted to

Graz University of Technology

Supervisor

Univ.-Prof. Dipl.-Ing. Dr.techn. Rudolf Stollberger
Institute of Medical Engineering

Co-Supervisor

Assoz. Prof. Priv.-Doz. Dipl.-Ing. Dr.techn. Christian Langkammer
Department of Neurology
Medical University of Graz

Graz, Austria, November 2020

Abstract

Gradient-echo based magnetic resonance imaging (MRI) sequences are widely employed for T_1-weighted morphological and functional imaging. When acquiring multiple gradient-echo images with different echo times, the T_2^* decay allows insight into the tissue microstructure. Examples of different investigations include the T_2^* anisotropy in white matter nerve fibers, the determination of the water compartment in the myelin sheaths, or the visualization of abnormally high iron concentrations in deep gray matter.

Despite the improvement of *MRI* systems in the essential components, such as the main magnetic field, the shim and the gradient systems, macroscopic inhomogeneities of the magnetic field remain a major source of errors in the quantification of R_2^* ($=1/T_2^*$) relaxation rates. In 2D slice-selective measurement techniques, the signal dephasing is particularly pronounced in slice-direction because the slice thickness is usually much larger than the in-plane dimensions; consequently, the signal dephasing is strongly influenced by the excitation profile. All in all, this makes the exact quantification of tissue-specific parameters considerably more difficult.

To minimize the influence of these macroscopic field inhomogeneities, a signal model is presented, which allows for the description of macroscopic field inhomogeneities on the 2D multi-echo gradient-echo (mGRE) signal for arbitrary radiofrequency excitation pulses. The longer repetition time in 2D *mGRE* measurements with an interleaved slice acquisition than in 3D measurements is particularly suitable to reduce the influence of longitudinal relaxation. This is especially important in multi-compartmental analyses of the signal decay, such as the determination of the myelin water fraction (MWF). To benefit from an increased signal-to-noise ratio (SNR) at optimized flip angles, the model uses a numerical solver for the Bloch equations. Its advantage is that it is not limited to small flip angles compared with the analytical solution. It has been shown that applying the model leads to less influence of macroscopic field gradients on R_2^* and *MWF* values in comparison with signal models that do not account for macroscopic field variations.

In a second approach, an adaptive, slice-specific "z-shimming" method was developed, which uses slice-specific compensation moments between the gradient-echo acquisitions. The compensation moments remarkably reduce the influence of macroscopic field gradients compared with conventional *mGRE* sequences. Moreover, an improved *SNR* compared with a slice-independent "z-shimming" approach could be achieved.

The presented signal model, in combination with the new adaptive "z-shimming" approach, led to substantial improvements in the quality of R_2^* maps, assessed by the median and the interquartile range in different deep gray matter and white matter regions.

Keywords: field inhomogeneities, myelin water fraction, R_2^*, z-shimming, relaxometry

Kurzfassung

Gradientenecho-basierte Magnetresonanztomographie (MRT) Sequenzen werden für die Darstellung von T_1-gewichteten Bildern und in der funktionellen Bildgebung verwendet. Bei der Aufnahme von mehreren Gradientenechos mit unterschiedlichen Echozeiten erlaubt der T_2^*-Zerfall Rückschlüsse auf die Gewebsmikrostruktur. Beispiele dafür sind die T_2^*-Anisotropie in den Nervenfasern der weißen Substanz, die Bestimmung des wasseranteiligen Signals in den Myelinscheiden oder die Visualisierung von abnormal hohen Eisenkonzentrationen in bestimmten Gewebetypen.
Trotz der Verbesserung der MRT-Systeme in den wesentlichen Komponenten wie dem Hauptmagnetfeld, dem Shim- und dem Gradientensystem, bleiben makroskopische Inhomogenitäten des Magnetfeldes eine wesentliche Fehlerquelle bei der Nutzung der R_2^*-Relaxationsrate ($=1/T_2^*$). In schichtselektiven 2D-Messtechniken ist die Signaldephasierung in Schichtrichtung ganz besonders ausgeprägt, da die Schichtdicke normalweise viel größer ist als die orthogonalen Voxelbreiten innerhalb der Schicht. Dadurch beeinflusst das Anregungsschichtprofil die Signaldephasierung ganz erheblich. In Summe wird dadurch die genaue Quantifizierung von gewebespezifischen Parametern deutlich erschwert.
Um den Einfluss dieser makroskopischen Feldinhomogenitäten zu minimieren, wird in der vorliegenden Arbeit ein Signalmodell vorgestellt, das es ermöglicht, den Einfluss von makroskopischen Feldinhomogenitäten auf das 2D-multi-Echo-Gradientenecho (mGRE) Signal für beliebige Hochfrequenz-Anregungspulse zu beschreiben. Die bei 2D-Messungen mit verschachtelter Schichtaufnahme längere Repetitionszeit als bei 3D-Messungen eignet sich besonders dazu, den Längsrelaxationseinfluss zu reduzieren. Das ist insbesondere bei Multi-Kompartimentanalysen des Signalzerfalls wichtig, wie zum Beispiel bei der Bestimmung der „Myelin Water Fraction“ (MWF).
Um von einem erhöhten Signal-zu-Rauschverhältnis bei dafür optimierten Kippwinkeln zu profitieren, verwendet das Modell einen numerischen Löser für die Blochgleichungen und ist nicht wie die analytische Lösung auf kleine Kippwinkel beschränkt. Es konnte gezeigt werden, dass dieses Modell zu genaueren R_2^*- und MWF-Werten führt im Vergleich zu Signalmodellen, welche den Einfluss von makroskopischen Feldern nicht berücksichtigen.
In einem zweiten Ansatz wurde eine adaptive, schichtspezifische „z-Shimming“-Methode entwickelt, welche schichtspezifische Kompensationsmomente zwischen den Gradientenechoaufnahmen verwendet. Die Kompensationsmomente reduzieren, verglichen mit konventionellen mGRE-Sequenzen, deutlich den Einfluss von makroskopischen Feldgradienten. Des Weiteren konnte eine Verbesserung des Signal-Rausch-Verhältnisses im Vergleich zu einem schichtunabhängigen „z-Shimming“-Ansatz erzielt werden.
Das hier vorgestellte Signalmodell, in Kombination mit dem neuen adaptiven „z-Shimming“-Ansatz, führten in Summe zu einer substantiellen Verbesserung der Qualität von R_2^* in der Gradientenechobildgebung, welche mit dem Median und dem Interquartilsabstand in unterschiedlichen Hirnregionen der grauen Substanz und der weißen Substanz evaluiert wurde.

Schlüsselwörter: Feldinhomogenitäten, „Myelin Water Fraction“, R_2^*, „z-Shimming“, Relaxometrie

Affidavit

I declare that I have authored this thesis independently, have not used any other sources/resources than those listed, and have explicitly indicated all material which has been quoted either literally or by content from the sources used.

The text document uploaded to TUGRAZonline is identical to the present doctoral thesis.

Date	Signature

Acknowledgments

This thesis was written in cooperation with the Graz University of Technology and the Neuroimaging Research Unit at the Medical University of Graz. During the last four years, I had the opportunity to meet and to work with inspiring people who never shied away from helping or assisting me along the way.

Foremost, I would like to express my very great appreciation to my supervisor, Prof. Rudolf Stollberger, for triggering my interest in the exciting field of MRI and for his guidance through each stage of the process.

Moreover, I want to thank the examination committee and in particular my external reviewer and examiner, Assoc. Prof. Simon Robinson, for offering his time and providing me with valuable comments and suggestions in the final stages of the thesis.

I am deeply grateful to the people from the Neuroimaging Research Unit for their continuous support and the possibility to work in an excellent interdisciplinary team. Particularly, I want to thank Assoc. Prof. Christian Langkammer for his support and for introducing me to the field of R_2^* modeling. Further, I want to thank Assoc. Prof. Stefan Ropele for his insightful comments and suggestions during my PhD.

A special "Thank you" goes to all my colleagues and former colleagues from the Neuroimaging Research Unit and the Graz University of Technology. In particular, I want to thank Christoph Aigner, Christoph Birkl, Franz Hallwirth, Andreas Lesch, Oliver Maier, Lukas Pirpamer, Stefan Spann, Johannes Strasser, and Christian Tinauer for their generous support. They consistently offered their expertise when tricky questions or problems with the MRI came up, and on top of it, all were always a pleasure and fun to work with.

I want to express my gratitude to the revisors of the manuscript who read the full thesis or parts of it: Assoc. Prof. Christian Langkammer, Assoc. Prof. Stefan Ropele, Stefan Spann, and Bernd Buchmasser.

Last but not least, I want to thank my family, especially my parents Gertraud and Friedrich Söllradl, and my friends for their unwavering support and belief in me. I owe my deepest gratitude to my partner, Lena Franke, who supported me from the first day up to now. Although finalizing the thesis at the home office was often challenging in the extraordinary year of 2020, we were always a good team. Thank you!

Contents

1 Introduction

Contents

1.1 Introduction

Parallel to the invention of computed tomography (CT), another imaging methodology based on the nuclear magnetic resonance (NMR) was developed [180]. From the first *NMR* experiment in the 1930s, it took several years until Damadian performed the first successful *NMR* experiments in healthy and malignant tissue in 1971 [41]. He reported differences in the T_1 and T_2 relaxation times between healthy and malignant tissue, pushing the development of magnetic resonance imaging (MRI). Two years later, Lauterbur published the first 2D imaging experiment of two water probes [126], followed by the first in vivo image of a finger by using spatial encoding gradients [149]. Starting from the early experiments in the 1970s, *MRI* as an imaging method became popular because of its excellent soft tissue contrast without exposure to ionizing radiation.
Nowadays, *MRI* technology is indispensable with widespread applications in the medical field. A reason for the success of *MRI* is the continuous improvement of hardware and imaging techniques. One exciting field of ongoing *MRI* research is the development of quantitative magnetic resonance imaging (qMRI) methods that aim to improve limitations such as reproducibility and comparability of the clinically, more widely applied qualitative methods. In most clinical applications, T_1-, T_2-, or proton-density-weighted images are acquired based on the clinical question. Although these images provide excellent contrast for a particular question, the numeric values in a voxel provide only qualitative information. This hinders their meaningfulness for interpretation in longitudinal or cross-sectional studies. In contrast to that, *qMRI* addresses this issue by assigning a physically meaningful number to each voxel based on an underlying signal model. Quantitatively derived *MRI* parameters are ideally tissue-specific and independent of the sequence parameters or other external factors. However, there are still many challenges that need to be resolved

before *qMRI* can replace qualitative images. A major challenge is to build a reasonable signal model that accurately describes the observed signal with all accompanying factors influencing it.
The present thesis deals with the challenge of estimating quantitative parameters of the gradient-echo (GRE) signal decay with a focus on 2D acquisitions. In contrast to 3D acquisitions, a much larger repetition time (TR) can be chosen in 2D acquisitions with an interleaved slice acquisition. This brings that advantage that T_1 effects in multi-compartment relaxometry can be reduced [198]. Compared with spin-echo (SE) sequences, the missing refocusing pulse allows faster image acquisition and leads to low specific absorption rate (SAR), which makes *GRE* sequences especially preferable for ultra high field (UHF) *MRI* systems.
One of the biggest advantages and disadvantages of *GRE* imaging at the same time is the sensitivity to magnetic field variations. In the ideal case, the *GRE* signal changes are caused by magnetic field variations within a voxel and thus providing unique microstructural tissue information. A famous example is the blood oxygenation level dependent (BOLD) effect in functional magnetic resonance imaging (fMRI) based on magnetic susceptibility difference between oxygenated and deoxygenated blood [162]. The difference leads to magnetic field variations on the mesoscopic scale, which refers to a scale much bigger than the atomic scale but much smaller than the voxel size [246]. In *fMRI*, the difference can be measured as a signal change and provides important information of neuronal activity [163]. Similar, but on a scale much larger than the voxel size, for instance, susceptibility difference between air and tissue lead to an inhomogeneous magnetic field. These macroscopic field variations contain no tissue-relevant information, but they cause additional signal dephasing, which can mask tissue-associated changes, and additionally the field variations lead to distortions in the images. If the presence of macroscopic field variations are not accounted for in *GRE* approaches, the estimated quantitative values become inaccurate.
The methods described in the present PhD thesis improve quantitative values obtained with 2D radio frequency (RF)-spoiled *GRE* sequences such as R_2^* and myelin water fraction (MWF) in the presence of macroscopic field variations.

1.2 Outline of the Thesis

Chapter 2 describes the basics of the free induction decay (FID) with different relaxation mechanisms, followed by a brief introduction to *GRE* imaging. Further, it reviews the relation between quantitative parameters and the underlying tissue microstructure. To point out the motivation of this work, the last section shows the impact of macroscopic field variations on R_2^* estimation.
Chapter 3 provides a general overview of different methods that aim to reduce the effect of macroscopic field variations in *MRI*. The first section discusses basic and advanced shimming methods for improving magnetic field homogeneity during image acquisition.

The following section reviews various signal models that take into account field inhomogeneities in the modeling of the signal decay. The last sections discuss methods that modify the *GRE* sequence by using tailored *RF* pulses or z-shimming gradients.
Chapter 4 summarizes the practical *MRI* aspects such as *RF* excitation pulses and navigator echoes that were necessary to accomplish the objectives described in this thesis.
Chapter 5 introduces a signal model for 2D multi-echo gradient-echo (mGRE) sequences in the presence of macroscopic field variations, which was published in Magnetic Resonance in Medicine (MRM) [202]. The proposed signal model accounts for large flip angles to benefit from the signal-to-noise ratio (SNR) improvements in an interleaved 2D slice acquisition. The method was applied to R_2^* and *MWF* estimation.
Chapter 6 gives a comparison between 2D and 3D *mGRE* acquisition for R_2^* mapping. For the 2D data, the developed signal model was applied; for the 3D data, the voxel spread function (VSF) [250] was implemented.
To refine R_2^* mapping in the presence of macroscopic field variations, Chapter 7 presents a method that combines 2D z-shimming and signal modeling. The adaptive slice-specific approach was published in *MRM* [206].
Chapter 8 discusses the results and limitations of the methods presented in this thesis. It furthermore gives an outlook of promising future applications.

2

MRI Signal Relaxation and its Relationship to Tissue Microstructure

Contents

This chapter provides a general overview of quantitative *MRI* relaxation parameters with an emphasis on parameters obtained from *RF*-spoiled *mGRE* sequences. The first part reviews relaxation mechanisms, followed by the basic *MRI* sequences. The second part discusses the relationship between transverse relaxation parameters and the brain's microstructure in the context of potential clinical applications. The last part points out the challenges of estimating tissue-specific parameters with spoiled *mGRE* in the presence of macroscopic B_0 field variations.

2.1 Basic Principles of Signal Relaxation

2.1.1 FID and Relaxation Rates R_2, R_2', and R_2^*

A simple form of an *NMR* experiment is the measurement of the signal from a homogeneous sample containing, for example, hydrogen nuclei in a static magnetic field B_0. The hydrogen nuclei within the sample precise at the Larmor frequency ω_0, which is given by the product of B_0 and the gyromagnetic ratio γ. By applying an *RF* hard pulse at the Larmor frequency with amplitude $\hat{B}_1$ and duration T_{pulse}, the longitudinal magnetization rotates towards the transverse plane by the flip angle $\alpha = \hat{B}_1 T_{pulse}$. The free precision of the transverse magnetization induces a signal in the receiver coil and is called *FID* [76]. The signal $S(t)$ of the *FID* is commonly described in the literature by an exponential decay:

$$S(t) \propto \sin(\alpha) \exp(-R_2^* t), \tag{2.1}$$

where R_2^*, or $T_2^* = 1/R_2^*$, is the effective relaxation rate of the *FID*. R_2^* can be decomposed in a reversible relaxation rate R_2' ($T_2' = 1/R_2'$) and an irreversible relaxation rate R_2 ($T_2 = 1/R_2$):

$$R_2^* = R_2 + R_2'. \tag{2.2}$$

In R_2 relaxation the phase coherence between the spins is lost, caused by rapid random fluctuations in the magnetic field, leading to an irreversible reduction of the transverse magnetization [74]. In tissues, R_2 increases with field strengths. In the corpus callosum, for instance, from 4T to 11.7T an increase in R_2 from $17.3s^{-1}$ to $32.6s^{-1}$ was reported [44]. The T_2 value of solids is in the order of milliseconds and approaches the longitudinal relaxation time T_1 in liquids. At 3T, examples of R_2 values in human tissues are: $23.8s^{-1}$ in the liver, $10s^{-1}$ in gray matter (GM), $14.9s^{-1}$ in white matter (WM), and $2s^{-1}$ in cerebrospinal fluid (CSF) [173, 210].
In contrast to R_2, R_2' dephasing is reversible and the signal can be recovered with a *SE* by applying a 180° refocusing pulse [77]. Changes in R_2' are associated with magnetic field inhomogeneities that can occur at different scales with respect to the imaging voxel. For instance, paramagnetic particles, such as ferritin, cause field changes on the mesoscopic scale that affect R_2^*. Similarly, but much larger than the voxel size, macroscopic field variations caused by the subject's geometry and magnetic susceptibility influence R_2^*.
In the literature, a common assumption in Equation 2.1 is that the reversible relaxation of the *FID* can be described by an exponential decay with rate constant R_2'. However, this is only valid under certain circumstances [74] that will be discussed briefly.
Suppose that the spin density $\rho(x)$ along a direction x is Lorentzian distributed with:

$$\rho(x) = N_0 \frac{2b}{b^2 + 4\pi^2 x^2}, \tag{2.3}$$

where N_0 is the total number of spins, $b = 2\pi\Delta x$, and $2\Delta x$ is the full width half maximum (FWHM) of the distribution. Then, in the case of a constant field gradient with magnitude G_x', the reversible part of the signal at echo time (TE) is given by integration of the volume:

$$\tilde{\rho}(TE) = \int_{-\infty}^{\infty} \rho(x) \exp(-\gamma G_x' x TE) dx = N_0 \exp(-R_2' TE), \tag{2.4}$$

with $R_2' = \gamma \Delta x |G_x'|$. By introducing an averaged field inhomogeneity $\Delta B = |G_x'|\Delta x$, we can rewrite the equation for R_2^*:

$$R_2^* = R_2 + \gamma |\Delta B|. \tag{2.5}$$

Thus, this equation provides a simple relationship between R_2^* and the field inhomogeneity ΔB.
Another explanation, more realistic compared with the previous hypothetical case, is ar-

rived at by thinking of randomly distributed magnetic spheres in a medium. Each sphere has a susceptibility difference $\Delta\chi$ with respect to the medium, which causes a dipole field. Then, the sum of contributions of the magnetic dipoles to the signal decay is exponential in time in the static dephasing regime (Section 2.1.5) [24].

2.1.2 Magnetic Susceptibility

The magnetic susceptibility χ is a dimensionless quantity that describes the ability of a material to become magnetized. When placing a material in a magnetic field $\mathbf{H}$, the magnetic induction $\mathbf{B}$ inside the material in Tesla (T) is given by:

$$\mathbf{B} = \mu_0(\mathbf{H} + \mathbf{M}), \tag{2.6}$$

where μ_0 is the magnetic permeability of free space in Tm/A ($\mu_0 = 4\pi{\cdot}10^{-7}Tm/A$), and $\mathbf{M}$ the magnetization in A/m. in the case of non-ferromagnetic materials with isotropic magnetic properties, $\mathbf{M}$ relates to $\mathbf{H}$ by the constant χ:

$$\mathbf{M} = \chi\mathbf{H}. \tag{2.7}$$

and for $\mathbf{B}$ in Equation 2.6 as follows:

$$\mathbf{B} = \mu_0(1 + \chi)\mathbf{H}. \tag{2.8}$$

Based on the sign of χ, materials are differently classified. If $\chi > 0$, the material is paramagnetic and the magnetic field inside the material is strengthened. For $\chi < 0$, the material is diamagnetic and the field inside the material is weakened.
The human tissue susceptibility χ_{tissue} is largely diamagnetic because of its large water content ranging from $-11 \cdot 10^{-6}$ to $-7 \cdot 10^{-6}$ [194]. In MRI, instead of vacuum, often the susceptibility of water defines the reference for para- and diamagnetic tissues.

2.1.3 Longitudinal Relaxation Rate R_1

The longitudinal relaxation rate R_1, or relaxation time $T_1 = 1/R_1$, is a phenomenological quantity that describes the return of the longitudinal magnetization to thermal equilibrium. After applying a 90° RF pulse at the Larmor frequency, the spins exchange energy with their surrounding environment ("spin-lattice"), which can be described by [19, 74]:

$$M_z(t) = M_0(1 - e^{-R_1 t}), \tag{2.9}$$

where M_0 is the equilibrium magnetization and $M_z(t)$ the longitudinal magnetization at a certain time t. R_1 decreases with magnetic field strength. For instance, in the corpus callosum a decrease of R_1 from $0.91s^{-1}$ (4T) to $0.48s^{-1}$ (11.7T) has been reported [44]. The difference in R_1 between tissues can be explained by the rotational correlation time τ_c [20]. τ_c describes the time it takes a molecule to rotate about 1 radiant. Small molecules

have a short τ_c and large molecules follow a long τ_c. The highest probability for energy transfer is given when $\omega_0\tau_c = 1$, which leads to the highest R_1 [20]. Below ($\omega_0\tau_c \ll 1$) and above ($\omega_0\tau_c \gg 1$) less energy transfer occurs, leading to a decrease in R_1.
At 3T, typical R_1 values in tissues range from $1.2s^{-1}$ in the liver, $0.92s^{-1}$ in *WM*, $0.55s^{-1}$ in *GM*, to $0.26s^{-1}$ in *CSF* [173, 210].

2.1.4 Scale of Field Inhomogeneities

Section 2.1.1 discusses the reversible signal decay R_2' caused by magnetic field inhomogeneities, but so far, the scale of these field inhomogeneities has not been considered. Following the definition by Yablonskiy et al., field inhomogeneities can be divided into macroscopic, mesoscopic, and microscopic field inhomogeneities with respect to the voxel size [246].
The microscopic scale describes field inhomogeneities that appear on the atomic/molecular scale, and these field inhomogeneities are responsible for the irreversible R_2 relaxation. In contrast to that, the macroscopic scale refers to field variations much larger than the voxel size. These field disturbances originate from magnetic imperfections, poor shimming of the static magnetic field, or because of large susceptibility differences between air/tissue interfaces. Thus, signal changes caused by macroscopic fields provide no information and they mask tissue-specific information. The mesoscopic scale is between the macroscopic and microscopic scale and is much larger than the microscopic scale, but smaller than the voxel size. In contrast to the macroscopic scale, field variations on the mesoscopic scale contain tissue-specific information.
Figure 2.1 shows an example for the scale of macroscopic field variations. The field map (Figure 2.1A) indicates smooth macroscopic field variations associated with field distortions caused by the air tissue interfaces. Additionally, mesoscopic field variations can be detected, but their magnitude is much lower. For instance, a small difference between deep *GM* and *WM* tissue can be observed.

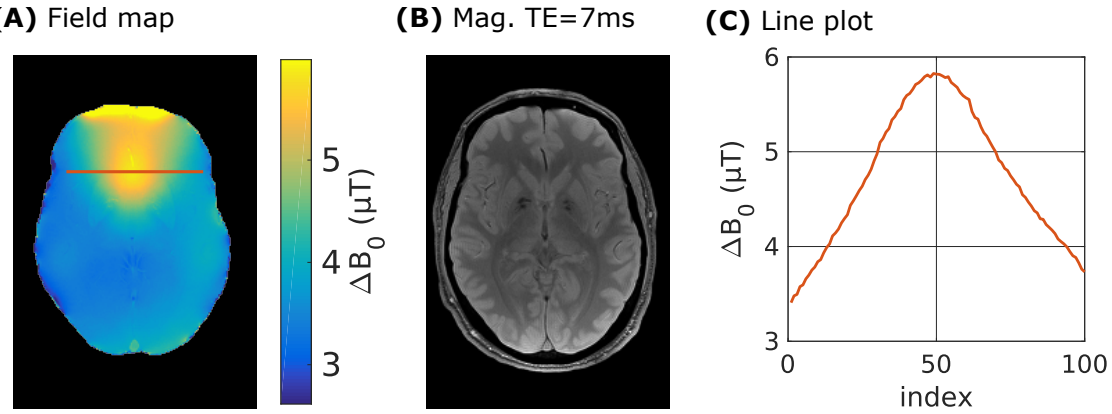

Figure 2.1: Example of field inhomogeneities in the brain. (A) illustrates a field map ΔB_0 estimated from *mGRE* data, (B) the magnitude image at $TE = 7ms$, and (C) the line plot of the red line in (A). The field map and line plot show macroscopic field variations much larger than the voxel size.

2.1.5 Motional Averaging and Static Dephasing Regime

To get insight into susceptibility-induced R_2^* changes on the mesoscopic/microscopic scale, different relaxation theories have been introduced [22, 66, 234, 247]. This section gives an overview following the notation of de Haan [46].

When placing magnetic particles into a medium the magnetic field inside the volume changes. The question is how this affects the effective relaxation rate R_2^*. For a single particle with radius R and magnetization M, the magnetic dipole field is given by:

$$B = \frac{\mu_0 M}{3}\frac{R^3}{r}\left(3\cos(\theta)^2 - 1\right), \tag{2.10}$$

where r is the distance from the center of the particle, μ_0 the permeability of free space, and θ the angle with respect to the dipole axes. In the medium, depending on the location, spins accumulate a different phase $\Delta\phi = \gamma B \Delta t$ in a time interval Δt.

Suppose that N particles, each with a volume v, are placed in a medium with volume V then the volume fraction f is given by $f = \frac{Nv}{V}$. To describe the effects of relaxation, a characteristic separation between particles can be defined [46]:

$$l = \left(\frac{\frac{4}{3}\pi}{f}\right)^{1/3} R. \tag{2.11}$$

If we now assume that water protons cannot move over time, each proton experiences the same magnetic field. In this case, an analytic solution for R_2^* is given by [24, 247]:

$$R_2^* = \frac{2\pi}{3\sqrt{3}} f \Delta\omega_0, \tag{2.12}$$

where $\Delta\omega_0$ describes the Larmor frequency shift caused by the magnetic field at the

equator of the magnetic particle. For a spherical particle, $\Delta\omega_0$ is given by [24, 247]:

$$\Delta\omega_0 = \frac{\gamma\mu_0 M}{3}. \tag{2.13}$$

This equation holds for protons that diffuse a minimal distance R_D, as long as R_D is much smaller than l. If $R_D/l \ll 1$, a single proton that travels from one place to another experiences virtually the same magnetic field and thus is independent of diffusion. This regime is referred to as static dephasing regime [247].
In contrast to that, in the motional averaging regime, diffusion cannot be neglected anymore because the traveled distance by the proton R_D is much larger than l ($R_D/l \gg 1$). In this regime, the protons diffuse a large distance where they experience different phase shifts which average out. In this regime R_2^* is calculated with [23]:

$$R_2^* = \frac{16}{45} f \Delta\omega_0^2 \tau_d, \tag{2.14}$$

where τ_d is the diffusion time calculated with the diffusion coefficient D and R:

$$\tau_d = \frac{R^2}{D}. \tag{2.15}$$

Here the two extreme cases of nearly static protons and protons which diffuse a large distance are discussed. For intermediate cases, the reader can refer to [22, 46].

2.2 Overview of Gradient- and Spin-Echo Sequences

2.2.1 Gradient-Echo Imaging

The following section reviews the fundamentals of *GRE* imaging. It starts with the basic principles of a *GRE* and summarizes the different *GRE* sequences with an emphasis on the *RF*-spoiled *GRE* sequence. The last section briefly introduces the *SE* and the asymmetric spin-echo (ASE) sequence.

2.2.1.1 The Gradient-Echo

Figure 2.2 illustrates the *GRE* formation. The plot in Figure 2.2A shows the *FID* oscillating at the Larmor frequency and its decay with T_2^*. The *GRE* is formed by two gradients, the prephasing gradient and the rephasing gradient (Figure 2.2B). Suppose that a gradient with arbitrary shape $G_x(t)$ is applied along the spatial direction x leading to a position-dependent phase change. At time T, the accumulative phase $\phi(x,t)$ is given by integration:

$$\phi(x,t) = \gamma \int_0^T G_x(t) x t \; dt \tag{2.16}$$

The prephasing gradient leads to phase dispersion, resulting in an accelerated decay. Assuming a duration T_p and a magnitude G_p of the prephaser, the phase $\phi_p(x)$ is given by $\phi_p(x) = -G_p T_p x$. In the next step, a rephasing gradient is applied with opposite polarity, which successively reverses the accumulated phase $\phi_p(x)$. As soon as the areas between the prephasing and rephasing gradient are equal, the accumulative phase $\phi(x, t = TE)$ becomes zero, and the *GRE* is formed at *TE*. After *TE*, the signal again decays faster caused by induced phase dispersion of the rephasing gradient.

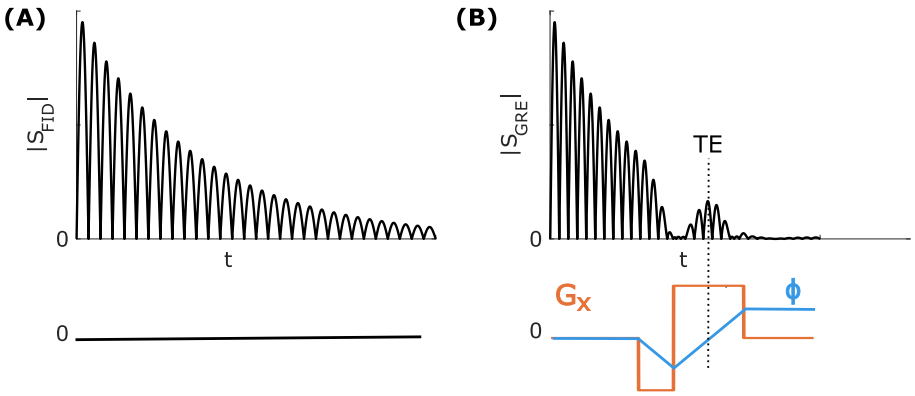

Figure 2.2: Illustrative example of the *GRE* formation. (A) shows the *FID* signal $|S_{FID}|$ and (B) the formation of a *GRE*. The negative part of the gradient G_x (prephasing gradient) dephases the signal and the positive rephases it again. The *GRE* is formed when the accumulative phase ϕ is zero (blue line).

2.2.1.2 Gradient-Echo Sequences

The above section discusses the *GRE* formation from a single *RF* pulse. However, standard *MRI* sequences typically apply a repetitive pattern of pulses with a *TR*. In 1958 Carr described the steady-state free precession (SSFP) in an *NMR* experiment where phase-coherent pulses with a spacing of *TR* are applied [26]. From this basic experiment, different types of fast *GRE* based imaging sequences were developed.
Suppose that $TR \ll T_2 \leq T_1$, then between two successive pulses the magnetization does not have sufficient time to reach equilibrium. After a certain number of pulses, the magnetization reaches a steady-state, leading to an identical signal for each repetition. The different *GRE* sequences are distinguished by different steady-state signals that are obtained by manipulating gradients or the *RF* phase between the pulses. Figure 2.3 shows a generic *GRE* sequence from which the different subtypes can be derived. In general, all these rapid *GRE* sequences can be summarized as *SSFP* sequences [193].
Figure 2.4A illustrates the balanced steady-state free precession (bSSFP) sequence in which the net moment is zero in all gradient directions between two *RF* pulses [168]. The contrast of *bSSFP* sequences is given by T_2/T_1 [193]. One main limitation of *bSSFP* is the periodic variation of the signal profile as a function of the off-resonance frequency

[63]. The profile is relatively constant for a wide range of phase values, but at an accumulated phase of $\pm\pi$ within one *TR* the signal abruptly drops to zero. This results in zero magnitude images along the off-resonance frequency, which is known as banding artifacts. To minimize banding artifacts, *TR* should be between $3 - 6ms$ [193]. Another option, but this comes with a prolonged scan time, is the constructive interference in steady-state (CISS) sequence [193]. In *CISS* two sets of *bSSFP* images are acquired with different pairs of α. In the first run images are acquired using $\pm\alpha$, and in the second run with constant α. This leads to a spatial shift of the banding artifacts and an image without banding artifacts can be reconstructed by performing a maximum intensity projection (MIP), for instance.
One application of *bSSFP* is cardiac imaging where the fast acquisition and the T_2/T_1 ratio offers a better contrast between muscle and blood than T_1-weighted images [193]. Moreover, the *bSSFP* leads to higher *SNR*. Another application is angiography where the ratio T_2/T_1 of the blood and of the surrounding tissue provides an excellent contrast [193].
In contrast to *bSSFP*, non-*bSSFP* have a residual moment before the next *RF* pulse is applied. In the gradient-spoiled sequence (Figure 2.4B), a spoiler gradient is applied after the readout gradient, which results also in T_2/T_1 contrast. Another non-balanced *bSSFP* is the reversed gradient-spoiled echo (Figure 2.4C). Here, the spoiler gradients are applied before k-space acquisition. The contrast is again T_2/T_1-weighted, but because the spoiler destroys the *FID*, the sequence is stronger T_2-weighted.
With none of these sequences a pure T_1 contrast can be achieved. A T_1 contrast is desired, for example, in contrast-enhanced imaging. Paramagnetic contrast agents such as a gadolinium-based agents reduce T_1 and T_2, but the ratio T_2/T_1 is similar. To get a T_1 weighting, *RF*-spoiled gradient-echo sequences are used, which are discussed in the next section.

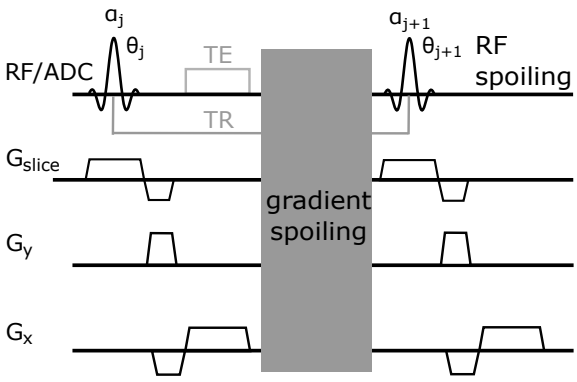

Figure 2.3: A generic *GRE* sequence that allows to build the basic *SSFP* sequences. Depending on the gradient spoilers and the phase cylce θ_j of the jth *RF* pulse, different contrasts are obtained.

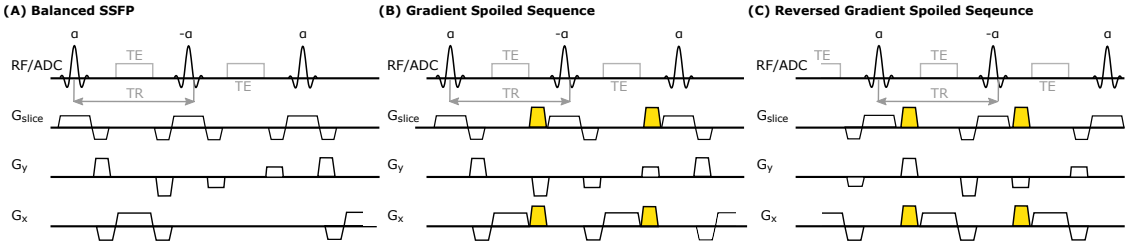

Figure 2.4: Overview of *SSFP* sequences. (A) shows a *bSSFP* in which the moment is balanced between the pulses. The gradient-spoiled sequence (B) applies a spoiler after the readout, and in the reversed gradient-spoiled sequence (C) the spoiler is applied before the readout.

2.2.1.3 RF-Spoiled Gradient-Echo Imaging

To obtain a T_1 contrast, TR must be smaller than T_1 ($TR < T_1$) and the transverse magnetization prior to every pulse has to be completely spoiled. Zur et al. [260] showed that this condition cannot be achieved if the same spoiling gradient is applied at between each RF pulse. Also, varying the amplitude between the repetitions does not allow perfect spoiling because spins at different positions experience different phase values. Therefore, the spoiling efficiency varies across the image [36]. To vary the phase of the transverse magnetization, the phase of the RF pulse [36] or the frequency of the RF synthesizer can be changed for a fixed period of time before the next excitation [259].
Applying a certain scheme of phase shifts to the B_1 field of the jth pulse is referred to as RF-spoiling. In numerical simulations, Zur et al. determined a phase increment of $\theta_0 = 117°$ for the phase shift θ_j as the optimal spoiling condition [259]:

$$\theta_j = \theta_{j-1} + j\theta_0, \qquad j = 1, 2, 3... \tag{2.17}$$

By applying this phase cycling to the RF pulses, it is possible to achieve a purely T_1-weighted image.
The contrast of the RF-spoiled GRE can be explained by the steady-state equation. Assuming ideal spoiling of the transverse magnetization prior to the next RF pulse and that a steady-state is reached, the signal $S_{spoil}(TE)$ is given by [58]:

$$S_{spoil} = M_0 \sin(\alpha) \frac{1 - e^{-TR/T_1}}{1 - \cos(\alpha) e^{-TR/T_1}} e^{-TE/T_2^*} \tag{2.18}$$

where M_0 is the equilibrium magnetization. The choice of the sequence parameters TR, TE, and α defines the weighting of the image. Generally, all images are proton-density (M_0)-weighted and the susceptibility contrast (T_2^*) increases with TE. The T_1 weighting increases by shortening TR or increasing α.

2.2.2 The Spin-Echo

This section briefly reviews the *SE* as one of the basic *MRI* sequences. Further, it introduces the *ASE* as a hybrid version of *SE* and *GRE*, which is especially interesting for studying the relations between R_2, R_2^*, and R_2'.
Figure 2.5A shows a basic 2D *SE* sequence. After the 90° excitation pulse, the *FID* decays with T_2^* and after $TE_{SE}/2$ a 180° slice-selective refocusing pulse is applied. The refocusing pulse rotates the spin assemble by 180°, causing the spins to rephase and to form a *SE* at TE_{SE} [77]. In contrast to the *GRE*, the *SE* sequences recover the reversible part of the *FID*. Before and after the refocusing pulse, a pair of crusher gradients is usually applied. The crusher on the right side of the refocusing pulse has the purpose to spoil a potential *FID* arising from an imperfect refocusing pulse. This might occur because of B_1^+ field variation or a flip angle variation along the excited profile. The left crusher balances the phase accumulation caused by the right crusher.
In a conventional *SE* the timing of the readout gradient is chosen so that $\phi(x,t) = 0$ when the *SE* is formed. However, it is also possible to shift the readout with a certain time Δ relative to the center of the spin-echo (Figure 2.5B). This is known as *ASE* and allows additionally to measure the reversible signal component as a function of Δ [52, 242].

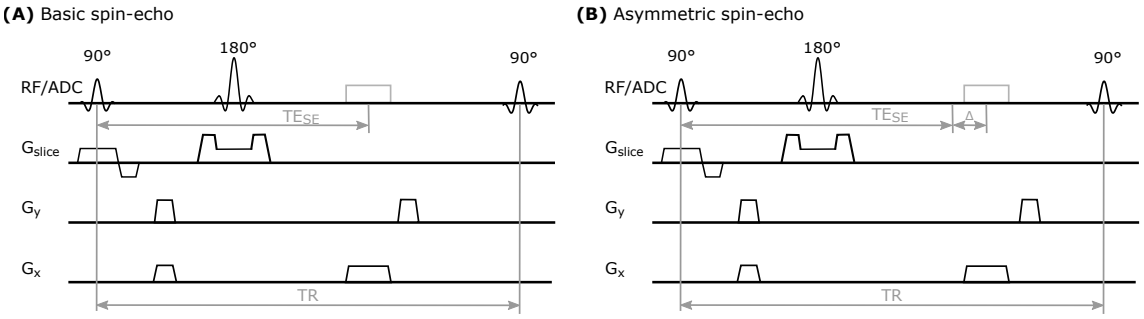

Figure 2.5: A basic 2D multi-slice *SE* sequence (A) and an *ASE* sequence (B). In the *ASE* sequence, the readout is shifted by a certain time Δ to acquire a *GRE* at $TE_{SE} + \Delta$.

2.3 Relating Transverse Signal Relaxation to Tissue Microstructure

With the advent of *UHF MRI* systems *GRE* sequences have been extensively used to link the observed signal decay to cellular structures in recent years. The following section gives an overview of quantitative *GRE* imaging with a focus on transverse relaxation parameters. It discusses applications ranging from iron quantification in deep *GM* with R_2^*, over R_2^* anisotropy in *WM* to quantification of myelin with myelin water imaging (MWI).

2.3.1 Cell Types in the Nervous System

The brain is part of the central nervous system (CNS) and is divided into the hindbrain (the medulla, pons, and cerebellum), midbrain, and forebrain (diencephalon, and cerebral hemispheres). The two major cell types in the *CNS* are the nerve cells (neurons), which are responsible for information propagation, and the glial cells (glia) involved in various vital supporting functions [109]. Compared with neurons, glia cells occur about 10 to 50 times more frequently in the *CNS* [209].
The three major types of glia cells are the oligodendrocytes, Schwann cells, and astrocytes. The oligodendrocyte and Schwann cells elaborate the myelin sheath around the axons in different parts of the nervous system. In the *CNS* a single oligodendrocyte envelops an average of 15 axonal internodes, whereas Schwann cells occur in the peripheral nervous system enveloping only one internode of one axon. Among glia cells, the largest number are the irregular star-shaped astrocytes making up about 20% to 50% of brain volume. They are involved in a variety of functions, such as nutrition supply or forming the blood-brain barrier [109].
Neurons are excitable cells and the signal units of the nervous system. Each neuron has a cell body (soma), which contains the metabolic center with a nucleus and the endoplasmic reticulum. From the cell body, a single long axon extends to a variable number of short dendrites responsible for signal receiving. The action potential is conducted along the axon to other cells [109]. The propagation speed, which is important for rapid communication, is determined by the diameter of the axon and the myelin sheath. In bare axons, the speed is proportional to the square root of the diameter. Therefore, a substantial increase in speed would require a large diameter occupying a substantial amount of space. In vertebrates, this limitation could be resolved through evolution of the fatty insulating myelin sheath, which is wrapped around the axon. This allows to increase the propagation speed of the nerve impulse by about 10 to 100 times [209]. Along the axon, the myelin sheath is interrupted by the nodes of Ranvier where the action potential is regenerated. The end of the axon is divided into fine branches where the signal is transmitted via synapse to other neurons [109].

2.3.2 Iron Quantification

2.3.2.1 Iron and its Association with Neurodegenerative Diseases

The trace element iron is involved in many biological processes such as oxygen transport, mitochondrial respiration, myelin synthesis, and neurotransmitter synthesis and metabolism [37]. In the case that iron homeostasis is disrupted and iron level exceeds the capacity of storage proteins or other molecules, it might lead to oxidative damage and cell death [117]. In the healthy brain, iron accumulates rapidly in the f irst two decades of life, followed by a slower increase [79]. Besides the iron accumulation with age, iron ac-

cumulation is further associated with different neurodegenerative diseases. In Parkinson's disease, the total iron concentration in specific regions of the substantia nigra increases with disease severity [50, 96, 184]. For the neurodegenerative and inflammatory disease multiple sclerosis (MS), iron decreases in normal-appearing *WM* [80], while in deep *GM* regions iron increases with the disease's duration and severity [78, 189]. In Alzheimer's disease, the characteristic amyloid plaques and neurofibrillary tangles have elevated concentrations of zinc, copper, and iron [34, 142, 185], leading to oxidative stress [192].

2.3.2.2 Iron-Sensitive MRI Methods

The non-invasive assessment of iron with *MRI* is of great interest because of the close relationship between various diseases and iron. About 70% of the iron in the human body is found in hemoglobin and the rest in non-heme compounds. In the human brain, most of the non-heme iron is stored in the proteins ferritin and hemosiderin. These are the only two proteins considered having enough iron concentration to affect *MRI* signal [195]. Ferritin is built up with 24 proteins arranged symmetrically to form a hollow shell with a $8nm$ diameter cavity, which allows to store up to 4500 Fe(III) iron atoms making up to 30% of its molecular mass [60, 88]. In contrast to highly-structured ferritin, hemosiderin is heterogeneous with considerable variations in size; the stored iron is thought to originate from degraded ferritin [243].
In the literature, a sensitivity of all relaxation parameters (e.g., R_1, R_2, R_2', and R_2^*) for iron has been reported. This section summarizes different iron-sensitive *MRI* methods. It focuses on relaxation parameters, but methods targeting the phase of the signal such as quantitative susceptibility mapping (QSM) [137] and susceptibility-weighted imaging (SWI) [75, 182] are also employed. For more information on phase-related methods, the reader can refer to [73, 121, 164].
R_2: The effect of iron on T_2-weighted images has been reported first in animal models in the liver in 1983 [211]. In this study, Stark et al. investigated differences between hepatitis, fatty liver, and hepatic iron overload.
The relationship between iron-associated T_2 shortening has been studied in vitro experiments with ferritin. In these experiments a linear dependency of R_2 on loading factor and the applied field strength has been reported [226, 228]. The loading factor describes the number of iron atoms stored within ferritin. Consequently, R_2 depends only on the number of iron atoms independently of the number of ferritin proteins and loading factor. Interestingly, the linear field dependency of the relaxation is contrary to the quadratic dependency predicted by the outer sphere theory (OST) [66]. The *OST* describes the relaxation of solvent water protons caused by the magnetic nanoparticle. In this theory, water protons diffuse through the magnetic field gradients leading to an irreversible relaxation. To resolve the quadratic relation between R_2 and field strength, Gossuin proposed a model based on proton exchange between bulk water and exchangeable protons located at the surface of proteins [70]. The adapted model leads

to a linear dependency of R_2 on field strength [70]. Further, it is closely related to the static dephasing regime [247], which also predicts a linear relationship. However, interpreting these results for in vivo application is still challenging mainly because of the inhomogeneous distribution in tissue [69].
In vivo, the relation between R_2 and iron has been investigated by comparing estimated R_2 values in brain regions [65, 89, 95, 225, 227] with the iron concentrations estimated by Halgren et al. [79] or by plotting R_2 as a function of age [196]. All these results show a good correlation between iron and R_2 in subcortical *GM* over the entire physiological range. However, these results provide only a qualitative description, as the actual iron content cannot be assessed in vivo. To bridge this gap, studies have been performed with *MRI* on post-mortem tissue followed by chemical analyses of the tissue for quantifying the iron concentration [120, 230]. These studies confirmed a linear relation between iron and R_2 in subcortical *GM*.
FDRI: The field-dependent R_2 increase (FDRI) approach investigates the change of R_2 by acquiring R_2 maps at two different field strengths [7]. The method has been used to study the effects of iron in Alzheimer's and Huntington's disease and in normal aging [8–10, 10]. While this approach offers the possibility of using the field dependency for the relaxometry, *FDRI* has the disadvantage that it requires a second *MRI* system. Compared with *SWI* and *QSM*, a greater specificity for detecting non-heme iron-rich regions was found for the *FDRI* [15, 172].
$\mathbf{R_2'}$: Ordidge et al. proposed to estimate R_2' with an *ASE* sequence that acquires a train of *GRE* after the *SE* [169]. By performing an additional measurement with a different *TE* of the *SE*, but with the same echo timings of the readout gradients, R_2' and R_2 can be calculated. Additionally, the approach applies z-shimming gradients to compensate for macroscopic field gradients [169]. With this method, higher R_2' and R_2^* were reported in the substantia nigra for Parkinson's disease compared with controls, whereas for R_2 no significant differences were found [68].
To accelerate the approach, in the partially-refocused interleaved multiple echo (PRIME) sequence, a second refocusing pulse is included [153]. The sequence allows to estimate R_2' in a single acquisition. Similar to previous results, differences of R_2' and R_2^* were reported in the substantia nigra for Parkinson's diseases [71].
The gradient-echo sampling of FID and echo (GESFIDE) sequence acquires *GREs* before and after the refocusing pulse, which allows to estimate R_2' and R_2 from a single measurement [147]. In several *GM* regions and from frontal cortical *WM*, a higher iron specificity for R_2' was reported [65] compared with the results from Halgren et al. [79].
It is argued that R_2' is more specific for paramagnetic particles compared with R_2. As mentioned above, R_2 is related to diffusion whereas R_2' contributions are reversible, independent of the diffusion coefficient of the water protons [169]. Hikita et al. compared *GESFIDE* with a multiple spin-echo (MSE) sequence in 13 healthy subjects. They concluded that R_2 seems better suited because macroscopic field variations contribute to a large extend to R_2' [95].

R_2^*: From an *MRI* perspective, measuring R_2^* by a *mGRE* has some clear advantages compared to *MSE* sequences. For instance, *GRE* sequences lead to a lower *SAR* and a shorter echo spacing is possible. In *MSE* sequences, one of the major challenges are stimulated echoes. If not properly compensated for, stimulated echoes lead to an undesired T_1 dependency of the estimate R_2 [175]. Although advanced modeling approaches for the signal pathways are promising (e.g. [12]), applications in *UHF MRI* systems are limited because of *SAR* issues.
Besides the technical advantages of *mGRE* sequences, a higher correlation for R_2^* in *GM* and *WM* than for R_2 was found in an in situ study [120]. In this study, the iron concentration was chemically determined in different regions after *MRI*. This finding was also confirmed in another study with deceased MS patients [230].

In summary, various *MRI* approaches based on the characterization of the relaxation rates have been investigated for iron estimation in the brain. All these methods show a good correlation, but choosing the most sensitive based on the current literature is difficult.

2.3.3 R_2^* and Phase Anisotropy

The anisotropy of certain *MRI* parameters with respect to the main magnetic field B_0 has been reported in various tissues [93]. A prominent example for the signal dependency with respect to B_0 in *SE* sequences is the magic angle effect. These signal variations are caused by dipolar interactions of collagen-bound water in collagen-rich tissues such as tendons, ligaments, nerves, and menisci [27, 64, 156]. Another well known example is diffusion tensor imaging (DTI) to study the orientation of whiter matter fibers [157]. In principle, water mobility in the direction of the fiber is higher than perpendicular to it, which allows reconstructing the main orientation by acquiring diffusion-weighted images in different directions [54].
In recent years, the anisotropy of R_2^* and the phase signal in *WM* fiber has been extensively studied. This chapter summarizes these findings and reviews different signal models that try to explain the anisotropy.

2.3.3.1 R_2^* and Fiber Orientation

The feasibility of studying anatomical details on a much finer scale increased with *UHF MRI* sytems. In one of the first high-resolution experiments ($0.2x0.2x0.5mm^3$), Li et al. reported a large heterogeneity between *WM* fibers in 2006 [138]. At 3T, a combined analysis of R_2^* and *DTI* showed that fibers running along the anterior posterior direction have larger R_2^* than fibers in superior-inferior direction [30]. The authors attributed the difference between the directions to structural differences between the fibers or to the fiber orientation with respect to B_0. In a similar investigation by Denk et al., variations of the phase and R_2^* could be confirmed [47]. Additionally, measurements with different head orientations showed that tissue orientation rather than tissue composition is responsible

for the observed phase and R_2^* changes. By performing experiments with two different head orientations, Wiggins et al. demonstrated in a macaque model (7T) that fiber orientation unambiguously is a major contribution of *WM* heterogeneity [238]. This was later confirmed by Bender and Klose by performing in vivo measurements with normal and tilted head position [13]. Further, their results indicate an orientation dependency of R_2^* on the angle θ towards B_0 with $\sin(\theta)^2$. This is in accordance with the predicted solution of Yablonskiy et al. in the static dephasing regime for a parallel set of cylinders [247].
Aforementioned works are inherently restricted by the range of possible head orientations within the scanner. To get better insight into the angular dependency of R_2^* in *WM* fibers, Lee et al. performed measurements with a formalin-fixed post-mortem sample at different orientations [134]. They evaluated the variation of R_2^* as a function of the angle with two models. The first model assumes that sources of microscopic susceptibility such as iron and myelin are highly aligned with the axon leading to orientation-dependent decay. Based on the solution of Yablonskiy et al. for parallel cylinders [247] and sufficiently long *TEs*, Lee et al. modeled R_2^* with:

$$R_2^* = c_0 + c_1 \chi \sin\theta^2 \tag{2.19}$$

Their results indicate a clear dependency of R_2^* on θ, but Equation 2.19 could only partly explain the observed signal variation. In the model in Equation 2.19, an isotropic susceptibility difference between cylinders and surrounding medium is assumed. However, fiber bundles show anisotropic behavior with respect to the B_0 orientation. In 2010, Liu observed an anisotropic susceptibility in the *CNS* of an ex vivo mouse brain with a 7T small-bore scanner [141]. By performing measurements with different orientations of the brain, Liu reconstructed an apparent susceptibility tensor (AST). Around the same time, in a post-mortem experiment Lee et al. [132] suggested an anisotropic susceptibility for fiber bundles. In these experiments a section of the corpus callosum, which reflects highly aligned fiber bundles, was cut into five sections. By rotating every second section by 90°, the authors could study the effect of the microstructure while minimally affecting the macroscopic structure. They explained the difference in resonance frequencies between aligned and 90°-rotated fiber bundles by an anisotropic susceptibility.
To account for anisotropic susceptibility, Lee et al. extended Equation 2.19 by introducing an isotropic χ_{iso} and an anisotropic component χ_{aniso} that depends on the angle θ [134]:

$$\begin{aligned} \chi &= (\chi_{iso} + \chi_{aniso}) \sin\theta^2 \\ &= \left(\chi_{iso} + \chi_\perp + (\chi_\perp + \chi_\parallel) \sin(\theta + \epsilon)^2\right) \sin\theta^2 \end{aligned} \tag{2.20}$$

where $\chi_\perp$ and $\chi_\parallel$ are the relative volume susceptibilities when the cylinders are perpendicular or parallel to B_0. ϵ accounts for potential phase offset by the distribution of perturbers and the susceptibility anisotropy that results from the perturbers' molecular structure [134]. By applying Equation 2.20 to the measured R_2^* variations, Lee et al. could achieve a better representation. These results further suggest that susceptibility

anisotropy contributes to the observed *WM* heterogeneity. Further, with the observed angular dependency of R_2^* they could reconstruct *WM* fiber orientation maps that were closely related to *DTI* derived orientations [134].

2.3.3.2 Biophysical Signal Models

To explain the observed heterogeneity in *WM*, various biophysical signal models have been proposed. The generalized Lorentzian approach (GLA) by He and Yablonksiy takes tissue architecture and its orientation to B_0 into account [91]. In this work, the concept of the Lorentzian sphere for calculating the magnetic field created by structures within the sphere was translated to a more general case: the Lorentzian cylinder. By applying this approach to highly anisotropic structures, such as an axon, a $\sin\theta^2$ dependency on the frequency shift can be predicted. Luo et al. validated the theory in an isolated optical nerve, which closely resembles the circular geometry, by measuring the phase variation as a function of θ [144]. Their results show that the *GLA* is better suited than the Lorentzian sphere approximation. However, the theoretical concept has been a matter of debate [57, 248].
The hollow cylinder model of Wharton and Bowtell [236] represents a volume of fibers with an infinite long hollow cylinder where the inner of the hollow cylinder models the myelin sheath. To describe the orientation dependency of fibers, they modeled the myelin sheath with an anisotropic susceptibility tensor. Furthermore, the authors considered the fast signal decay of the myelin water within the myelin sheath [148] and additionally they accounted for a chemical exchange of protons between the water and macromolecules [199, 258]. Simulations and experiments indicate that with the hollow cylinder model observed magnitude and phase variations in fibers can be accurately described [236].
The relationship between observed complex signal decay and its relation to fiber orientation has been further investigated by Sati et al. [191]. In the experiments, they performed measurements with human and marmoset brain tissue parallel and perpendicular to B_0 at 7T. The measured signal decay was fitted to a complex signal model $S(t)$ with three compartments:

$$S(t) = \sum_{i=1}^{3} A_i \exp(-R_{2,i}^* t) \exp(-2\pi i \Delta f_i) \tag{2.21}$$

where A_i is the signal amplitude at $t = 0$ for the ith compartment, $R_{2,i}^*$ the relaxation rate, and Δf_i the frequency shift with respect to the local mean resonance frequency. The three compartments are associated with intracelluar, extracelluar, and the myelin water trapped in the lipid bilayers. Their results are in accordance with Hwang et al. [101], who reported three distinct compartments and different frequency offsets depending on fiber orientation. Additionally, Sati et al. performed simulations on the microscopic scale where they modeled fibers with small infinite long hollow cylinders with varying radii and constant g-ratio (ratio between the inner radius of the cylinder over the outer radius).

Further, they carried out simulations with different fractions of interstitial water, axonal water, and myelin water, and they described the field shift by an anisotropic susceptibility tensor. In contrast to the hollow cylinder model, no exchange between protons has been considered, but diffusion effects were included. Interestingly, Sati et al. found that the best description of the observed signal decay is given when diffusion is accounted for [191]. Following the idea of Sati et al. [191] of microstructural based signal modeling, Chen et al. performed forward simulation with a geometrical model built up on literature values for the g-ratio, axon packing, diameter, and susceptibility [29]. Again, three compartments representing interstitial water, axonal water, and myelin water were incorporated, and the susceptibility differences of the axonal and myelin water with respect to interstitial water have been considered. They calculated the frequency shifts associated with these compartments with the analytic solution for an infinite cylinder [74]. In terms of phase evolution with respect to B_0 orientation, the authors found that the geometrical model can resemble the observed phase compared with the predicted $\sin\theta^2$ dependency by the *GLA* [91] and susceptibility anisotropy [132]. For R_2^*, Chen et al. measured a sinusoidal-shaped increase with θ for the experimental data that could be quite well explained by the model. When comparing fits of the experimental data with $\sin\theta^2$ and the $\sin\theta^4$, which is attributed to myelin magnetic anisotropy [134], a $\sin\theta^2$ relation leads to statistically better results. The results suggest that isotropic modeling of the susceptibility is sufficient. However, Chen et al. conducted the measurements at 3T, which might be less sensitive compared with the 7T measurements of Lee et al. [134]. Another interesting finding is that compared with the simulation of Sati et al. [191] diffusion effects on signal evolution were negligibly small.
Based on the findings of anisotropic susceptibility, Yablonskiy and Sukstanskii proposed the generalized Lorentzian tensor approach (GLTA) as an extension of the *GLA* [249]. In this phenomenological model, a relation between the phase as well as the structural and magnetic anisotropy of the underlying microstructure including multi-compartment tissue structure was derived by applying Maxwell's equations and a statistical approach.

2.3.4 Myelin Water Imaging

2.3.4.1 Introduction

In the previous section, it was already mentioned that the measured signal from *WM* results from several compartments. Relatively early, compared to the first in vivo reports of myelin water images, Vasilescu et al. did identified three distinct compartments in the signal decay from the sciatic nerve of a frog in *NMR* experiments [222]. They speculated that the fastest component with a T_2 of $17ms$ was related to proteins and phospholipids, the intermediate component with $70ms$ to axoplasmic water, and the slow component with $310ms$ to extracellular water. The T_2 time of the fast component reveals that one of the main challenges in *MWI* with *MRI* is to capture the short component.
In 1994, MacKay et al. [148] acquired the first in vivo myelin water images using a

single-slice *MSE* sequence with hard refocusing pulses. With this setup, the *TE* and the influence of stimulated echo could be reduced for measuring the short component. They have associated the short component to water molecules trapped within the lip bilayers of the myelin sheath. As a measure of the myelin content, the authors introduced the term *MWF*.

To estimate the *MWF*, the measured data with *MSE* sequence can be fitted to a sum of M exponential functions with a non-negative least squares (NNLS) algorithm (Equation 2.22). Figure 2.6 shows an example of a multi-compartment fit in a fixed post-mortem sample. The plotted T_2 spectrum reveals three different compartments (Figure 2.6C). To estimate the *MWF*, MacKay et al. defined a T_2 cut-off. The signals from all s_j below the cut-off are attribute to myelin water and the *MWF* is estimated by the sum of the myelin components over to whole signal.

$$S_{tissue} = \sum_{j=1}^{M} s_j \exp\left(-\frac{TE}{T_{2,j}}\right) \tag{2.22}$$

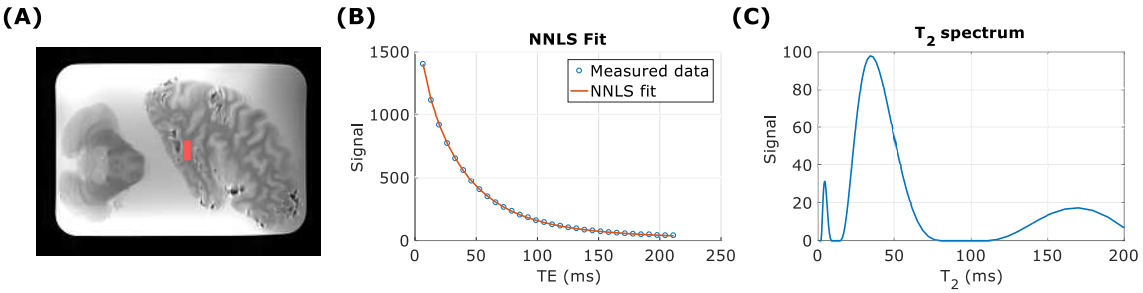

Figure 2.6: Example of the *MWF* estimation in formalin-fixed brain tissue. (A) shows the brain tissue with a rectangular region of interest (ROI) in red, and the plot (B) shows the measured signal from the *ROI* with the *NNLS* multi-compartment fit. The fitted T_2 spectrum (C) reveals three different compartments. The data was measured with a *MSE* sequence with hard refocusing pulse and Poon spoiling [175]

2.3.4.2 Validation

The relation between myelin water and microstructure has been validated in several studies. Webb et al. analyzed T_2 spectra of an injured and normal peripheral nerve over the time course after injury in an animal model [232].Additionally, the authors compared results histomorphometrics. The results indicate that the short myelin component is a good measure of total myelin content. Further validation studies of formalin-fixed *MS* brains show that the *MWF* correlates well with myelin sensitive staining [122, 124]. These findings suggest that the *MWF* can be used to monitor demyelination and remyelination. Also in the spinal cord, a good correlation between staining and the *MWF* in *GM* and *WM* was found [116]. However, an important assumption in the multi-compartment model is

the slow inter-compartmental water exchange. In a study of formalin-fixed spinal cords of rats, Dula et al. found differences in *MWF* values of different healthy fiber tracts, but with approximately the same myelin content. Their results point out that inter-compartmental water exchange is an important factor [56]. In a followup study with anesthetized rats, these results could be confirmed and explained by including water exchange in numerical simulations [86].

2.3.4.3 Clinical Applications

MWI has been applied for studying mainly demyelinating diseases such as *MS*. One characteristic of *MS* is the formation of demyelinated regions in the *CNS*, mostly referred to as lesions or plaques. Visual assessment of lesions with *MRI* is standard for clinical diagnosis, but its quantification with *MRI* is still challenging. *MWI* is a potential *MRI* method for indirectly measuring the myelin content. In a study with *MS* patients, Laule et al. reported a decrease in *MWF* and an increased water content compared with normal appearing white matter (NAWM) of controls [123]. They attributed the changes to the loss of myelin. Similar results were obtained by estimating the *MWF* from *mGRE* data at 7T. In a study by Li et al., they found a significant decrease of the *MWF* in enhancing and non-enhancing lesions, but not between the lesion types [139]. With the multi-comparment driven-equilibrium single-pulse (mcDESPOT) sequence, Kittzler et al. observed also drop of *MWF* in lesions [111]. Additionally, the authors found a correlation between the extended disability status scale (EDSS) in *MS* patients with the deficient *MWF* volume fraction [111]. The deficient *MWF* volume is a voxel-based marker derived from *MWF* and image segmentation. Besides lesions, in diffusive-appearing white matter (DAWM) a reduction of *MWF* was reported [125, 154]. The *DAWM* is a transient region between lesions and *NAWM* with intermediate signal intensity.
For more insights into clinical applications of *MWI*, the reader can refer to the recent review of Lee et al. [131].

2.3.4.4 Sequence and Signal Modeling

As already mentioned, the reference method by MacKay et al. [148] applies hard pulse for refocusing in the *MSE*. Hence, the method is restricted to single-slice acquisition and requires long *TR* to allow sufficient T_1 recovery. Since then, various modifications of the original sequence and new sequences were developed to allow a more efficient acquisition. In this thesis the focus of *MWI* is on spoiled *GRE*, but additionally a brief overview of other sequence types is given. For in-depth comparison between different *MWI* methods, the reader can refer to the technical review of Alonso-Ortiz et al. [3].
Compared with a standard *MSE* the gradient and spin-echo (GRASE) sequence enables a faster acquisition of the k-space [170]. To accelerate imaging, the *GRASE* sequence acquires additional *GREs* before and after the *SE*. Prasloski et al. proposed a 3D version for whole brain *MWI* in 15 minutes [177]. Another type of sequences for *MWI* are T_2

preparation methods [165, 166]. Apart from these T_2 methods, the *mcDESPOT* approach [49] is based on driven-equilibrium single-pulse observation of T1 (DESPOT1) and driven-equilibrium single-pulse observation of T2 (DESPOT2) [32, 48].
A promising alternative to the reference *MSE* approach are spoiled *mGRE* sequences. Because of the missing non-selective refocusing pulses, an interleaved multi-slice acquisition is possible, increasing the covered volume by measuring multiple slices within a TR. This also leads to much less *SAR* compared with the *MSE*, which makes it especially favorable for *UHF*. Further, a shorter echo spacing is possible because of the missing refocusing pulses and crushers, and consequently the first echo of the echo train TE_1 can be decreased. For example, in an *MSE* sequence designed for *MWI* the minimal achievable TE_1 is approximately $10ms$, while for *mGRE* values of $2ms$ are possible.
In 2007, Du et al. reported the first *MWF* maps obtained with a spoiled *mGRE* in formalin-fixed brains of a deceased patient with *MS* and non-*MS* [55]. The *MWF* maps were estimated from a fit of the magnitude data to a three-compartment model. Later, Hwang et al. demonstrated the feasibility for in vivo *MWF* mapping with a 2D *mGRE* sequence [101]. In this study, they acquired eight slices with a slice thickness of $4mm$ and $1.1x1.1mm^2$ in-plane resolution in $8.5min$ [101]. With a 3D mGRE sequence, Lenz et al. demonstrated whole brain coverage in less than $10min$ [135]. Compared with previous works, Lenz et al. applied a *NNLS* approach for fitting the data instead of assuming a fixed number of three compartments [135]. The fitted spectrum of the T_2^* decay indicated two distinct compartments, one myelin water and one intracellular/extracellular compartment [135].
Van Gelderen et al. further investigated the multi-exponential decay at 3T and 7T [221]. To increase *SNR*, they measured a single slice with 50 repetitions and 19 echoes. Moreover, the authors evaluated the dependency of the signal decay on fiber orientations by averaging the signal in three different *ROIs*. In the *ROIs*, fibers were oriented perpendicular, parallel, and mixed with respect to B_0. For evaluation of the magnitude data of the *ROIs*, van Gelderen et al. assumed a three-compartment model:

$$|S(t)| = \sum_{k=1}^{3} A_k \exp(-R_{2,k}^* t) \exp(-2\pi i f_k). \tag{2.23}$$

Each compartment k has an amplitude A_k, effective relaxation rate $R_{2,k}^*$, and a frequency component f_k. In this model, the second component f_2 is set to zero because it is assumed that it is on resonance. In this work, van Gelderen et al. confirmed the appearance of a short component [221]. Their results indicate that a model with frequency components explains the observed variations of amplitude and frequency of the short component with respect to B_0 better than using only the magnitude et al. [101, 221]. In addition, based on the R^2 of the fit, they concluded that a two-pool model in equation 2.23 is better suited for 3T [221].
Given these findings, Nam et al. [161] proposed a complex three-compartment model

for *MWF* estimation from the complex data rather than using only the magnitude data (equation 2.23):

$$|S(t)| = (A_{my}\exp(-R^*_{2,my}t)\exp(-2\pi i\Delta f_{my+mac}) + A_{ex}\exp(-R^*_{2,ex}t)\exp(-2\pi i\Delta f_{ex+mac}) + A_{ax}\exp(-R^*_{2,ax}t)\exp(-2\pi i\Delta f_{ax+mac}))\exp(\varphi_0), \tag{2.24}$$

with my denoting the myelin component, ax the axonal water compartment, ex the extracellular water compartment, and φ_0 an initial phase term. Each of the compartments has an additional phase term that describes the frequency shift of the macroscopic field f_{mac} and the compartment-specific shift (e.g. $\Delta f_{my+bg} = f_{my} + f_{mac}$). The authors compared their model approach at 3T with a magnitude only method of Hwang et al. [101] and the magnitude and frequency model of van Gelderen et al. [221]. They found that their model fits the data better. By comparing different numbers of fitted echoes ranging from 16 to 32, Hwang et al. suggested that 16 echoes are sufficient to fit the model parameters.

Apart from the advantages, many challenges are associated with *mGRE* sequences, which need to be considered for a reliable quantification. The first one are macroscopic field variations that lead to a faster signal decay and thus to a mis-quantification [101]. Different approaches for dealing with this problem have been proposed based on postprocessing of *mGRE*, or the usage of z-shimmin gradients in combination with postprocessing [2, 128, 130, 198]. A detailed overview of these approaches is given in Chapter 3. Another issue are phase errors arising from physiological noise and the system itself. For example, the respiratory cycle can induce slight variations in B_0 leading to phase encoding errors [220]. The acquisition of a navigator echo allows to measure the relative phase fluctuations [100], which is essential for accurate *MWF* estimation [130, 160, 198]. More information on implementation of a navigator echo and the phase correction is given in Chapter 4. Another source of phase errors is related to the *MRI* system itself. If a bipolar readout gradient is used, timing errors and eddy currents can lead to phase shifts between even and odd echoes. Recently, Shin et al. proposed gradient pairing to overcome these effects by acquisition of two images. After the first acquisition, the polarity of the readout gradient, phase encoding, and the slice encoding is switched for the acquisition of the second image. [198]. Further, flow compensation with saturation pulses or compensation gradients has been shown to be beneficial [130, 160, 198].

2.4 Challenge: Macroscopic Field Variations

Figure 2.7 shows an example of the impact of macroscopic field variations on R_2^* quantification. In areas of the frontal lobe and the corpus callosum, the field map (Figure 2.7B) shows macroscopic field variations caused by the air/tissue interfaces of the frontal and nasal cavities. By estimating the gradient of the field map in the slice-direction, the field gradients g_z reveal values from $-100\mu T/m$ to $150\mu T/m$.
The field gradients affect the signal decay (Figure 2.7 A) and they lead to a bias in the estimated R_2^* values (Figure 2.7D) if not accounted for. To reduce the influence of g_z, Chapter 5 introduces a numerical signal model, and Chapter 7 proposes an adaptive z-shimming approach that compensates g_z by applying compensation gradients.

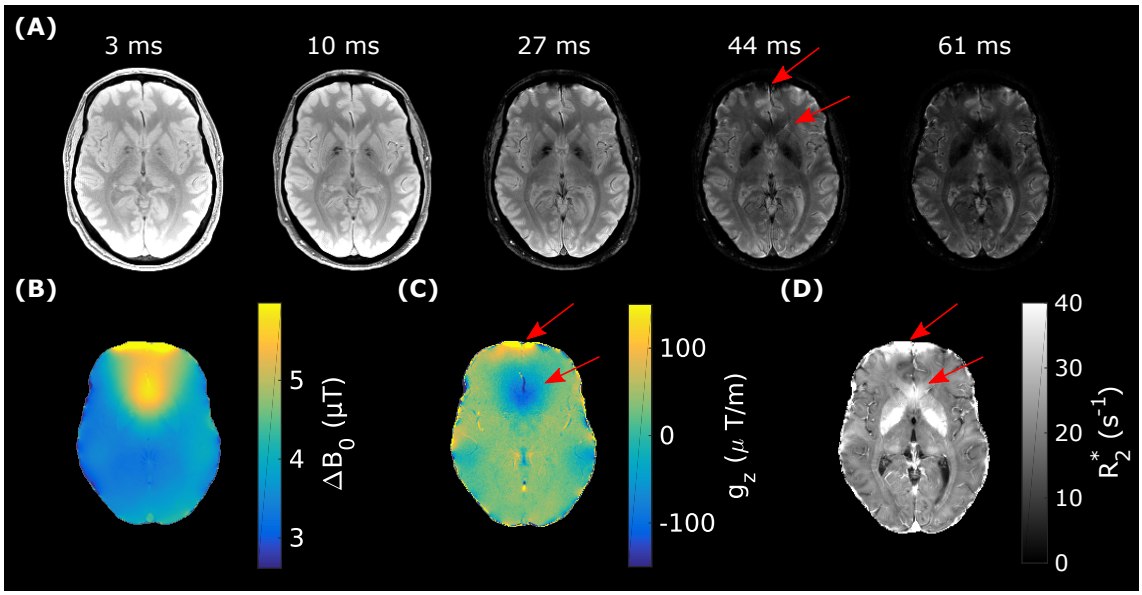

Figure 2.7: Example of macroscopic field variations on R_2^* estimation with a monoexponential signal model. (A) shows the magnitude images at five different *TEs*, (B) the field map ΔB_0, (C) the field gradient map in the slice-direction, and (D) the estimated R_2^* map. The red errors indicate areas with large macroscopic field variations. In these areas the signal dephases faster, leading to a bias in R_2^* if they are not accounted in the signal model.

3

Methods for Reducing and Modeling of Macroscopic Field Variations

Contents

This chapter reviews approaches for reducing the effects of macroscopic B_0 field variations in *MRI*. In general, one of the overall goals in *MRI* is to achieve a homogeneous magnetic field within the imaged volume to ensure that spins precise at the same Larmor frequency. If that is not achieved, an inhomogeneous field, depending on the strength, will lead to geometric distortion in the slice-selection and readout directions in *SE* and *GRE* sequences [143], and additionally to a signal loss in *GRE* sequences caused by intravoxel dephasing [5, 176, 183].

3.1 Shimming

Shimming refers to the process of achieving a homogeneous field within the *MRI* scanner by applying additional magnetic fields that compensate unwanted field variations.
The shimming methods can be distinguished between active and passive shimming. In active shimming, a current running through a coil generates the magnetic field and in passive shimming, the field originates from magnetic particles placed along the scanner.

3.1.1 Passive Shimming

Field inhomogeneities of the main magnetic B_0 field arise because of a non-perfect manufacturing process of the coils, steel rods in concrete walls, or with the magnetic shielding from the scan room [105, 229]. Therefore, before commissioning a new *MRI* system on a facility, vendors perform passive shimming to achieve the promised field homogeneity. In this context, an important quantity to assess the field quality is the peak-to-peak variation

of the magnetic field at the diameter of spherical volume (DSV) in the iso-center. For example, a vendor guarantees within $45cm$ DSV a variation of 5 parts per million (ppm) for 3T system, so the greatest variation on the sphere is $0.6\mu T$ $(3T/(5\cdot 10^6))$. The requirement in terms of field uniformity is about 10 ppm on a DSV with $50cm$ [146]. However, before the passive shimming up to hundreds ppm can occur [25].
In passive shimming, the vendors measure the field variations on the DSV by collecting the FID with a coil. Based on the theory that the magnetic field can be described with spherical harmonics [188], it is possible to homogenize the field by inserting steel bars around the bore of the magnet [99].

3.1.2 Active Shimming

Active shim coils can be divided into superconductive coils in the cyrostat and resistive coils. Besides the passive shim, some vendors use superconductive coils to shim the magnet to the demanded specifications [229]. However, the main application of active shim coils is to compensate for magnetic field variations caused by the subject itself. If a subject is moved into the bore of the MRI system, the magnetic field gets distorted depending on the subject's geometry and the susceptibility differences between air and the various tissue types. Active shimming reduces or should ideally compensate subject induced field variations.
The resistive shimming coils are located around the bore of the scanner and they are designed to generate spherical harmonic field patterns. In MRI, the shim order refers to the order of spherical harmonics that can be provided by the coils. Depending on the field strength, MRI systems are equipped with a different shim order. A first order shim is provided for field strengths smaller 3T, for $\geq 3T$ second order shim coils are included, and for 7T third order shim coils are additionally available [229]. Development of higher order shim coils has been restricted to limited space within the bore. However, higher order shim coils would be necessary to correct higher-order field inhomogeneities, for instance, near the nasal cavities [112, 114]. An alternative to overcome this is issue is dynamic shim updating (DSU). DSU uses the relation that the required spherical harmonic order decreases with the image volume [43]. Thus, a slice in a 2D acquisitions requires a lower shim order acquisitions than the same volume in 3D acquisitions. The first DSU approaches applied linear slice-specific shim gradients [18, 158], which later have been extended to higher orders [45, 108, 113]. Nonetheless, the DSU relies on spherical harmonics and is therefore limited by the shim coil order of the MRI system [112].

3.1.3 Local Passive Shimming

To overcome the limited number of spherical harmonics in active shimming, different approaches with locally placed magnetic shim pieces have been proposed. Wilson et al. created a local passive shim to compensate field inhomogeneity in the inferior frontal

cortex [240]. By placing a block of pyrolotic graphite, which is highly diamagnetic with an anisotropic susceptibility, they could show that the field inhomogeneity noticeably diminished. The method was further refined by using different mouth shims [241], and it was evaluated in a different study [38]. A limitation of this approach is that the optimal shim device dependents on the subject and evaluated brain region [241]. Similar, Yang et al. proposed a passive shimming method in which the shim material Niobium was mounted adjustable at the head coil [253]. They calculated the position of the four Niobium probe with an optimization algorithm that used the acquired field map to find the optimal position.

3.1.4 Local Active Shimming

In the last two decades, promising approaches beyond the large active shim coils based on spherical harmonics have been developed. Addressing the limited order of spherical harmonics terms, Juchem et al. proposed to place electrical shim coils arranged on the head coil to compensate field inhomogeneities in the prefrontal cortex [108]. They extended the multi-coil (MC) concept to an array with 48 coils showing remarkable improvements compared with a static spherical harmonic shim [107, 108]. When comparing dynamic *MC* approach with *DSU*, an improved field homogeneity in areas such as the prefrontal cortex can be achieved because the dynamic *MC* is not restricted by *MRI* system's shim order [108]. Additionally, eddy currents are negligibly small [108].
A drawback of the original proposed dynamic *MC* shimming is the additional space required by the shim coils next to *RF* coils. To reduce the overall space of *RF* and shim coils, recent efforts have focused on integrating the *RF* and shim coils in a single unit [82, 213, 219].
Harris et al. proposed a different concept for local active shimming [87]. Rather than using coils with a fixed shape, Harris et al. suggested controlling the magnetic field by adjusting distinct current pathways on a mesh by solid-state switches [87].

3.2 Signal Modeling

The approaches discussed in the previous section aim to achieve a more homogeneous magnetic field. Apart from promising methods such as integrated *RF* and shim coils [82, 213, 219], current state-of-the-art *MRI* systems use active shimming with spherical harmonics. Even in the case of good shim, some field inhomogeneities remain, particularly in regions with severe field inhomogeneities such as in the prefrontal cortex or the temporal lobe. These field inhomogeneities influence the signal decay leading to quantification errors. By incorporating theses macroscopic field variations in a signal model, their influence on quantitative *MRI* can be noticeably reduced.
This section starts with a general model for signal encoding in the presence of macroscopic field variations and reviews approaches for 2D and 3D acquisition.

3.2.1 General Signal Equation

Based the notation of Yablonskiy et al. [250], the signal encoding $\tilde{S}(\mathbf{k}, TE)$ of a spoiled *GRE* can be described as:

$$\tilde{S}(\mathbf{k}, TE) = \int \rho(\mathbf{r}, TE) \exp(-2\pi i \mathbf{k}\mathbf{r} + i\Delta\omega(\mathbf{r}, TE + t) + i\varphi_0(\mathbf{r}))d\mathbf{r}, \tag{3.1}$$

where $\rho(\mathbf{r}, TE)$ is the ideal signal as function of the TE at position $\mathbf{r} = [x, y, z]$ that depends on the tissue properties and *MRI* system parameters.

For example, in tissues the signal depends on the proton density and the relaxation properties, which might be a monoexponential decay with R_2^* or a multi-exponential decay as proposed for *WM* [55, 148]. System related changes of $\rho(\mathbf{r}, TE)$, to name a few, can be caused by the *RF* excitation pulse, 2D or 3D acquisitions, the type of sequence (spoiled *GRE* versus balanced *GRE*) and the sequence settings, or the coil sensitivities.
In Equation 3.1, the first exponential describes the ideal signal encoding. The two additional phase terms account for the frequency $\Delta\omega(\mathbf{r}, TE + t)$ of the macroscopic field variations and a phase offset $\varphi_0(\mathbf{r})$ caused by, for instance, by the phase of B_1^+ field. The time t during *GRE* acquisition is zero at the center of the readout. The k-space encoding is defined by:

$$\begin{aligned} 2\pi k_x &= \gamma G_x t_x \\ 2\pi k_y &= \gamma G_y t_y \\ 2\pi k_z &= \gamma G_{slice} t, \end{aligned} \tag{3.2}$$

where G_x and G_y are the phase encoding gradients with duration t_x and t_y, and G_{slice} is the readout gradient in z-direction. Starting from this forward model, the influence of $\omega(\mathbf{r}, TE + t)$ on the signal dephasing can be described. For the following considerations for 2D and 3D acquisitions, it is assumed that the readout gradient is much bigger than macroscopic field gradients [250]. Therefore, potential geometric distortions caused by the phase accumulation during t are considered to be negligible small.

3.2.2 Modeling Approaches for 2D mGRE

2D acquisitions require only one phase encoding direction because of the slice-selective excitation. Consequently, in Equation 3.2 $k_z = 0$, and in the case of Cartesian sampling, the readout is performed in either x or y direction. A common assumption in 2D acquisitions is that intravoxel dephasing predominantly occurs in slice-selective direction and in-plane dephasing is often neglected. This is justified by the usually larger slice-thickness Δz than the in-plane resolution. Therefore, intravoxel dephasing predominantly occurs in slice-selective direction.
With these assumptions, the signal $S(TE)$ of a 2D spoiled *GRE* in a voxel can be expressed as:

$$\begin{aligned} S(TE) &= \int \rho(z, TE) \exp(i\omega(z)TE)dz \\ S(TE) &= \int S_{tissue}(TE)\underline{M}_{xy}(z, TE = 0) \exp(i\omega(z)TE)dz, \end{aligned} \tag{3.3}$$

where $S_{tissue}(TE)$ describes the ideal signal from the tissue assuming a homogeneous voxel, $\underline{M}_{xy}(z, TE = 0)$ the complex transverse magnetization at $TE = 0$, and $\exp(i\omega(z)TE)$ accounts for the phase dispersion caused by the macroscopic field $\omega(z)$.
Starting from this equation, various approaches for modeling the signal decay in the presence of $\omega(z)$ were developed. In one of the first approaches, Fernandez-Seara and Wehrli describe the signal $S(TE)$ in the presence of a macroscopic field gradient g_z by a sinc-funtion [59]. To derive the signal model, two additional assumptions are necessary. First, the macroscopic field is slow varying in space compared with Δz. Hence, $\omega(z)$ can be approximated by a linear function along the slice [246]:

$$\omega(z) \approx \omega_0 + \gamma g_z z \tag{3.4}$$

where ω_0 is the magnetic field offset in the slice and g_z a constant macroscopic field gradient. Second, the shape of the slice profile is an ideal rectangular function. With these assumptions, we can rewrite Equation 3.3:

$$\begin{aligned} S(TE) &= \int S_{tissue}(TE)\underline{M}_{xy}(z, TE = 0) \exp(i\omega_0(z)) \exp(i\gamma g_z)dz \\ &= \int S_{tissue}(TE)\text{rect}\left(\frac{z}{z_0}\right) \exp(i\omega_0(z)) \exp(i\gamma g_z)dz \\ &= S_{tissue}(TE)\text{sinc}\left(\frac{\gamma}{2} g_z TE z_0\right), \end{aligned} \tag{3.5}$$

where $\text{rect}(\frac{z}{z_0})$ is a rectangular function defined in Equation B.1. Equation 3.5 reveals the important relationship between TE, z_0, and g_z. For example, given a constant g_z, the signal attenuation can be strongly reduced by decreasing z_0, or TE. Using Equation 3.5, Fernandez-Seara and Wehrli estimated R_2^* and g_z iteratively from the measured data assuming a monoexponential signal decay ($S_{tissue}(TE) = S_0 \exp(-R_2^* TE)$) [59]. A drawback of this approach is that fitting is challenging because Equation 3.5 has several local minima and maxima [59]. To improve the fitting procedure, Dahnke and Schaeffter estimated an initial value $G_{z,init}$ from the field map gained in an additional scan [39]. Rather than assuming a linear varying field in slice-direction, Yang et al. extended the model to a quadratic varying field [254]. However, deviations from the ideal slice profile lead to a deviation from the sinc-shaped signal decay, resulting in a bias of the estimated parameters.
Addressing the variations of the slice profile, Preibisch et al. proposed an analytic solution for arbitrary RF excitation pulses [178]. They assume that steady-state effects can be neglected ($TR \gg T_1$) and that a small flip angle is used. By applying the small tip angle

approximation, $M_{xy}(z)$ can be estimated with the inverse Fourier transform of the *RF* excitation pulse envelope $B_1(t)$ [98]. Then, the integral along z in Equation 3.3 represents another Fourier transform. Thus, the signal dephasing of g_z has the same shape as $B_1(t)$. By substituting t with $\frac{g_z}{G_{slice}}TE$, for $S(TE)$ follows [178]:

$$S(TE) = B_1\left(\frac{g_z}{G_{slice}}TE\right) S_{tissue}(TE), \tag{3.6}$$

with G_{slice} being the amplitude of the slice-selection gradient.

Figure 3.1A illustrates an example for two sinc-Hanning-windowed pulses with different pulse duration T_{pulse} and time bandwidth product (TBP) (Figure 3.1A). The short pulse ($T_{pulse} = 1ms$) results in a broad slice profile, while the long pulse ($T_{pulse} = 4ms$) leads to a narrower profile (Figure 3.1B). In the presence of g_z the signal dephases with the shape of the excitation pulse (Figure 3.1C) as described by Equation 3.6 for small flip angles. The analytic solution is an elegant way to correct for the effect of g_z for an arbitrary *RF* excitation pulse. However, a downside of the method is that it might not allow the full *SNR* benefit in 2D acquisitions with long *TR* because of the restriction to small flip angles. Therefore, in this thesis a numerical solution for arbitrary pulses and flip angles was developed [202]. The proposed approach is covered in Chapter 5.

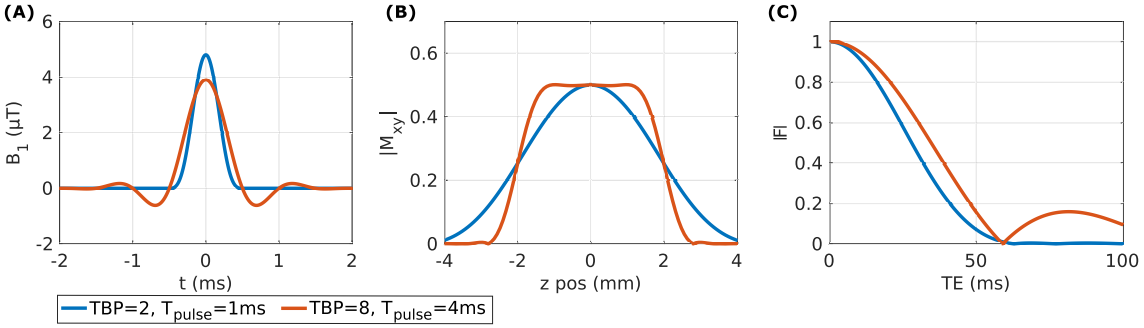

Figure 3.1: Examples of signal dephasing in the presence of a field gradient $g_z = 100\mu T/m$ for two different slice-selective *RF* excitation pulses. (A) shows the *RF* pulse envelopes for the sinc-Hanning-windowed pulses with $TBP = [2, 8]$ and pulse duration $T_{pulse} = [1ms, 4ms]$ to achieve a flip angle $\alpha = 30°$ in the center of the slice. (B) plots the magnitude of the transverse magnetization $|M_{xy}|$ and (C) illustrates the signal dephasing $|F|$ caused by g_z as a function of TE.

3.2.3 Modeling Approaches for 3D mGRE

To describe the influence of macroscopic field variations on signal dephasing in 3D acquisitions, Yablonskiy proposed the *VSF* [250]. To solve the general signal Equation 3.1, a few assumptions are necessary. First, the phase $\varphi_0(\mathbf{r})$ and the macroscopic field $b(\mathbf{r})$ at position $\mathbf{r} = (x, y, z)$ can be described by a linear function in the nth voxel:

$$\begin{aligned}\varphi_{0,n}(\mathbf{r}) &= \varphi_{0,n} + \varphi_{nx}(x - x_n) + \varphi_{ny}(y - y_n) + \varphi_{nz}(z - z_n)\\ b_n(\mathbf{r}) &= b_n + g_{nx}(x - x_n) + g_{ny}(y - y_n) + g_{nz}(z - z_n),\end{aligned} \tag{3.7}$$

where $\boldsymbol{\varphi_n}$ and $\boldsymbol{g_n}$ describe the gradients of the phase and the macroscopic field in all three spatial directions x, y, and z. Second, the continuous signal $\rho(\mathbf{r}, TE)$ can be substituted with the averaged signal $\rho_n(TE)$ within the nth voxel.
With these assumptions, we can rewrite the measured k-space signal from Equation 3.1. This involves several steps and for the sake of simplicity, all steps are elaborated for the 1D case (x-direction). In addition, Figure 3.2 illustrates the different steps in an example. In the first step, $\rho(\mathbf{r}, TE)$ is split up in a sum of N_x integrals, in which each voxel with size a_x is integrated separately:

$$\begin{aligned}\tilde{S}(k_x, TE) &= \int \rho(x) \exp(-2\pi i k_x x + i\gamma b(x) TE + i\varphi_0) dx\\ &= \sum_{n=1}^{N_x} \int \mathrm{rect}((x - x_n)/a_x) \rho(x) \exp(-2\pi i k_x x + i\gamma b(x) TE + i\varphi_0(x)) dx,\end{aligned} \tag{3.8}$$

where $\mathrm{rect}((\mathrm{x} - \mathrm{x_n})/\mathrm{a_x})$ is a rectangular function that restricts the integration to the size of a voxel from $x_n - a_x/2$ to $x_n + a_x/2$ (Equation B.1). Then, by substituting $\rho(x)$ with ρ_n, and $b(x)$ and $\varphi_0(x)$ with the linear approximations (Figure 3.2A-D), the measured signal in the k_x-space becomes[1]:

$$\tilde{S}(k_x, TE) = \sum_{n=1}^{N_x} \rho_n \exp(\gamma b_n + \varphi_0 n) \exp(-2\pi i k_x x_n) a_x \ \mathrm{sinc}(a_x(k_x - k_n)). \tag{3.9}$$

Extending Equation 3.9 to all three spatial dimensions gives:

$$\begin{aligned}\tilde{S}(\mathbf{k}, TE) = \sum_n \sigma_n(TE) \exp(i\gamma b_n TE + i\varphi_{0,n}) \exp(-2\pi i \mathbf{k}\mathbf{r_n})\\ \mathrm{sinc}[(k_x - k_{nx})a_x]\mathrm{sinc}[(k_y - k_{ny})a_y]\mathrm{sinc}[(k_z - k_{nz})a_z],\end{aligned} \tag{3.10}$$

where $\sigma_n = V\rho_n = a_x a_y a_z \rho_n$ is the signal from the nth voxel and V denotes the voxel volume. The shift in k-space k_{nj} caused by the field and phase gradients is given by:

$$2\pi k_{nj} = \gamma g_{nj} TE + \varphi_{nj}, \qquad j = x, y, z. \tag{3.11}$$

The sinc functions in Equation 3.10 describe the effects of the discrete sampling and the shift because of the macroscopic field, approximated with g_{nj} and φ_{nj} in each voxel.

[1] A complete derivation of Equation 3.9 can be found in the Appendix B.2.

The overall goal defined in Equation 3.10 is to reconstruct an image $\sigma_n(TE)$ without contributions of the sinc functions. However, in a standard image reconstruction of Cartesian sampled data an inverse fast Fourier transform (IFFT) is performed to estimate $S_n(TE)$. By applying an *IFFT* in a single direction, the signal $S_n(k_x, TE)$ in the image domain is given by:

$$S_n(TE) = \frac{1}{N_x} \sum_{k_x} \tilde{S}(k_x, TE) \exp(-2\pi k_x x_n). \tag{3.12}$$

Substituting in Equation 3.10 yields:

$$S_n(TE) = \frac{1}{N} \sum_{m} \sigma_m(TE) \exp(i\gamma b_m TE + i\varphi_{0,m}) \sum_{q} \operatorname{sinc}(q - q_m) \exp(2\pi i q(n-m)), \tag{3.13}$$

with $q = k_x a_x$ and q_m is the 1D phase dispersion:

$$2\pi q_m = (\gamma g_{mx} TE + \varphi_{mx}) a_x. \tag{3.14}$$

Equation 3.13 explains the relation between σ_m and the reconstructed signal $S_n(TE)$. It shows that the original σ_m is convoluted with sinc functions that describe the phase dispersion and the finite sampling. The example in Figure 3.2F illustrates the estimated signal $S_n(TE)$ from the k_x-space data (Figure 3.2E) with an *IFFT*. Compared with σ_m (Figure 3.2B), the signal $S_n(TE)$ dephases with TE and additional Gibb's ringing occurs, especially near sharp transitions.
With the forward model proposed by Yablonskiy et al. in Equation 3.13, it is possible to account for these effects [250].
By introducing the *VSF* ψ_{nm}, Equation 3.13 can be simplified to:

$$S_n(TE) = \sum_{m} \psi_{nm}(TE) \sigma_m(TE). \tag{3.15}$$

where ψ_{nm} is:

$$\psi_{nm}(TE) = \eta(n, m, q_m(TE)) \exp(i\varphi_{0,m} + i\gamma b_m TE), \tag{3.16}$$

with

$$\eta(n, m, q_m(TE)) = \sum_{q} \operatorname{sinc}(q - q_m(TE)) \exp(2\pi i q(n-m)). \tag{3.17}$$

Thus, ψ_{nm} describes the spreading of an ideal voxel $\sigma_m(TE)$ caused by the macroscopic field and the sampling. To estimate $\psi_{nm}(TE)$ in the 2D or 3D case, the variables m, n, and q are substituted with vectors for the spatial directions (e.g. for 3D $m = (m_x, m_y, m_z)$, $n = (n_x, n_y, n_z)$, and $q = (q_x, q_y, q_z)$).

To solve Equation 3.16, the unknown parameters of g_{nj}, φ_{nj}, $\varphi_{0,m}$, and b_m have to be estimated. This can be achieved with the measured signal $S_n(TE)$, which can be described by:

$$\begin{aligned} S_n(TE) &= |S_n(TE)| \exp(i\varphi_n(TE)) \\ &= |S_n(TE)| \exp(i(\varphi_{0,n} + \gamma b_n TE)). \end{aligned} \tag{3.18}$$

Consequently, $\varphi_{0,n}$ and b_n can be obtained by fitting a linear equation to the phase signal of the echoes. Then, a numerical gradient of the $\varphi_{0,n}$ and b_n maps in all three spatial directions can be calculated to estimate φ_{nj} and g_{nj}.
To reduce the computational complexity of Equation 3.15, Yablonskiy et al. proposed a similarity approximation that exploits the property that signals from neighboring voxels are similar [250]:

$$\sigma_m(TE) = \sigma_n(TE) \frac{|S_m(TE=0)|}{|S_n(TE=0)|}. \tag{3.19}$$

Thus, Equation 3.15 can be reduced to:

$$\begin{aligned} S_n(TE=0) &= \sigma_n(TE) F_n(TE) \\ &= \frac{1}{|S_n(TE=0)|} \sum_m \psi_{nm}(TE) |S_m(TE=0)|, \end{aligned} \tag{3.20}$$

where $F_n(TE)$ summarizes the influence of the macroscopic field variations. In Equation 3.20, the sum is estimated for each voxel n over all neighboring voxels m. However, a smaller number of neighboring voxels N_{neigh} might be sufficient for the estimation of $F_n(TE)$ [250].
Figure 3.3 shows an example of the estimated $F_n(TE)$ with a different number of neighbors N_{neigh} of the example signal ρ in Figure 3.2. Further, the reconstructed signal $S_n(TE)$ was corrected for the macroscopic field variations with the different $F_n(TE)$ functions (Figure 3.3 (parts B and D)). Both functions reduce the influence by correcting $S_n(TE)$, but with $N_{neigh} = 32$ it captures also the Gibb's ringing. A drawback is that increasing N_{neigh} is computational intense. To speed up computation, Yablonskiy et al. proposed to filter the measured data with a Hanning filter to reduce Gibb's ringing and the number of N_{neigh} [250]. To adapt the signal model, the Hanning filter is incorporated in Equation 3.17. A detailed evaluation between filtering and non-filtering of the data can be found in Chapter 6.

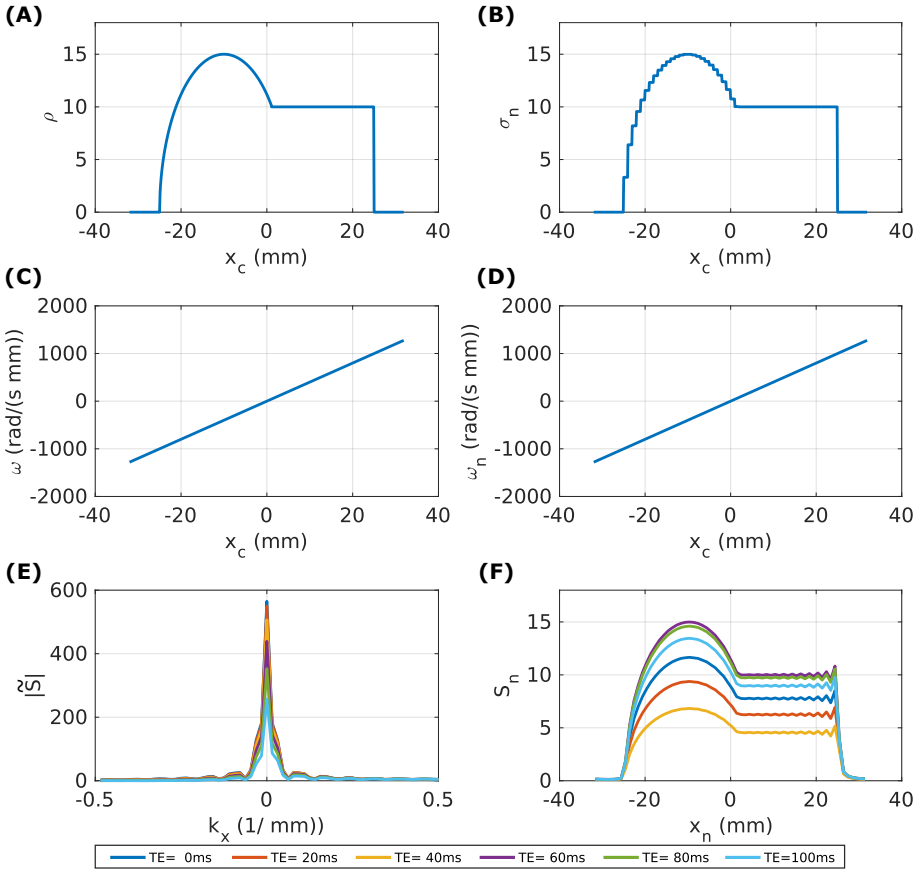

Figure 3.2: Steps involved for describing the signal of a 3D *GRE* signal in the presence of macroscopic field variations with the *VSF* [250]. The continuous signal $\rho(x)$ (A) along the x direction is averaged in each voxel denoted with σ_n (B) and the macroscopic field $\omega(x)$ (C) is approximated by a linear function in each voxel $\omega(x) = \gamma b(x)$ (D). Using Equation 3.10, the k-space signal (E) is estimated for different *TEs*. Then, the signal $S_n(TE)$ (F) is reconstructed performing an *IFFT*, which reveals increasing signal decay with *TE* and additional Gibb's ringing.

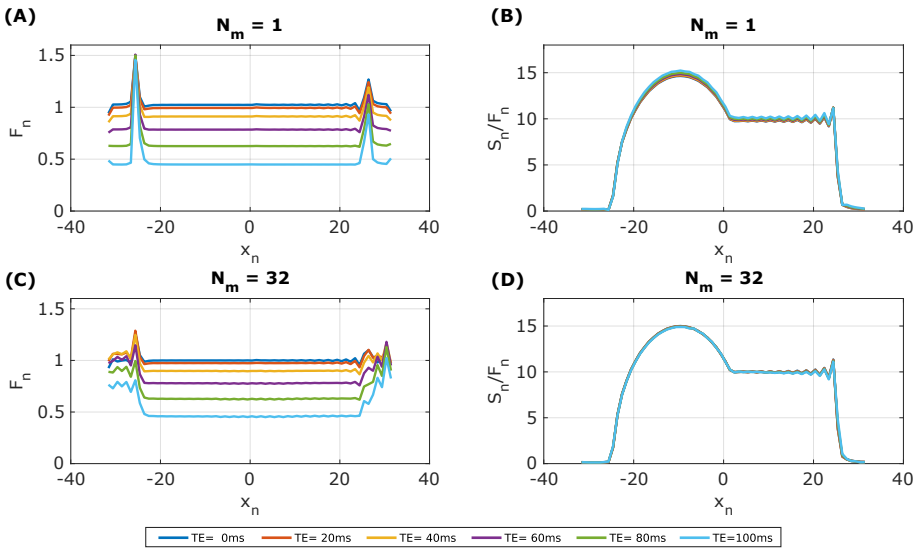

Figure 3.3: Estimated F_n as function of TE for the example in Figure 3.2 for different number of neighbors $N_{neigh} = 1$ and $N_{neigh} = 32$ (A,C) and the corrected signal $S_n(TE)/F_n(TE)$ (B,D).

3.3 Tailored RF Pulses

Another approach for reducing with macroscopic field variations in *GRE* imaging focuses on the design of tailored *RF* pulses. Conventional *RF* pulses are usually designed to achieve a constant phase variation through the slice. In tailored *RF* pulses, the phase varies along the slice to compensate intravoxel dephasing. In one of the first publications on this topic, Cho and Ro optimized the *RF* pulse to achieve a quadratic phase variation through the slice [31]. Because of the quadratic variation of the phase, the signal dephasing reduces for a constant g_z. The pulse design was further refined by measuring phase evolution in a specific *ROI*, which allows to design the phase of the *RF* pulse such that the signal rephases at a certain *TE* [28]. However, a drawback of these approaches is that in the case of a homogenous field ($g_z \approx 0$) the measured signal is much smaller than the signal obtained with a conventional pulse. Therefore, more recent pulse design approaches aim to compensate phase dispersion locally with 3D tailored *RF* pulses [85, 212, 256].

3.4 Z-Shimming with Compensation Gradients

To compensate intravoxel signal dephasing caused by macroscopic field gradients, z-shimming approaches apply compensation moments before image acquisition.
Figure 3.4 illustrates the basic concept introduced by Frahm et al. [62]. By changing the area of the slice-selection refocusing gradient, the additional moment compensates a certain g_z. From these first z-shimming experiments various approaches were proposed, which can be roughly divided into 2D and 3D approaches with multi- or single-scan acquisition. The focus in the following section is on *GRE* sequences, but compensation moments can also be applied in echo planar imaging (EPI) acquisition [35, 92, 140, 151, 208].

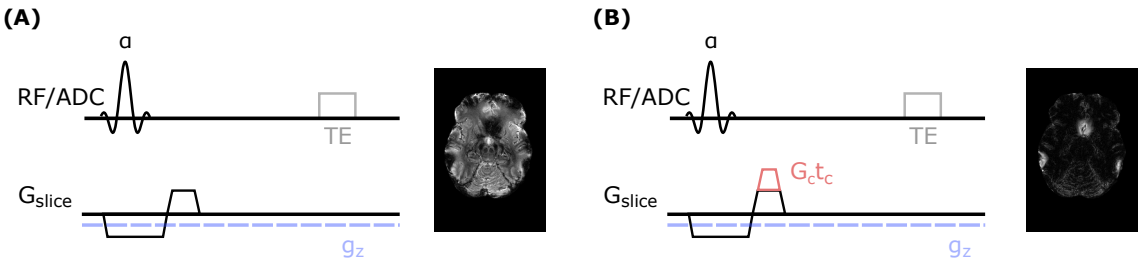

Figure 3.4: Basic principle of z-shimming demonstrated by Frahm et al. [62]. (A) shows a standard *GRE* sequence where the field gradient g_z is superimposed with the slice-selection gradient G_{slice}. The measured image at *TE* shows faster signal decay close to the nasal cavities and tympanic cavity. By changing the amplitude of the slice-selection rephasing gradient, the effect of g_z is reversed (B), and the signal recovers in areas with a field gradient value of g_z. In other areas, divergent from g_z, the signal is dephased because of the additional gradient.

3.4.1 2D z-Shimming

Yang et al. extended the original work of Frahm et al. [62] and proposed the 2D multi gradient-echo with magnetic susceptibility inhomogeneity compensation method (MGESIC) sequence [251]. Figure 3.5A illustrates the *MGESIC* sequence diagram. Rather than varying the area of G_{slice}, the method applies three identical compensation moments between the readout gradients. Therefore, the first echo image is a standard *GRE* without compensation, followed by three echoes with increasing accumulative compensation moments. The final image is reconstructed by summing up the individual images. To avoid a potential T_2^* bias, the echo spacing should be as short as possible in the *MGESIC* approach [251].
Another way for describing the effect of g_z is to interpret it as a shift in the frequency domain k_z from the center [252]:

$$I_{vox}^{2D}(k_z) = F\{\underline{M}_{xy}(z, TE = 0)\exp(-i\gamma g_z TEz/2\pi)\} = \underline{M}_{xy}(k_z - k_{z,0}), \tag{3.21}$$

where $k_{z,0} = \gamma g_z TE/2\pi$ describes the k-space shift.
The gradient-echo slice excitation profile imaging (GESEPI) method acquires N images with different slice refocusing gradient offsets (Figure 3.5B) [252]. The offsets are chosen such that N increments of ΔG_c within an interval of a maximum compensation gradient $\pm G_c^{max}$ are compensated. By measuring the N images, each image has a different k_z value, and thus the images represent the solution of Equation 3.21. Then, in each voxel of the N images, the signal in each voxel varies depending on g_z, and the maximum signal is given for an ideal compensation when $k_z = k_{z,0}$. By performing an inverse Fourier transform (FT) in k_z direction, an image series with the excitation profile is obtained [252]:

$$I_{vox}^{3D}(z) = F^{-1}\{I_{vox}^{2D}(k_z)\} = M(z)\exp(-i\gamma g_z TEz/2\pi). \tag{3.22}$$

Equations 3.22 shows that g_z only has an influence on the phase and not on the magnitude $|M(z)|$. Extending the approach to multi gradient-echo slice excitation profile imaging (mGESEPI), the effect of g_z on R_2^* mapping minimizes (Figure 3.5C) [255]. However, a disadvantage is that it requires a large number of images (16 in the original publication for in vivo imaging [252]). To increase efficiency, Truong et al. proposed the blipped multi gradient-echo slice excitation profile imaging (bmGESEPI), which applies additional compensation moments between the acquisition of M echoes (Figure 3.5D) [218]. This reduces the scan time by a factor of M compared with the *mGESEPI* approach.

Figure 3.6 shows the first single scan R_2^* mapping method based on z-shimming proposed by Wild et al. [239]. In a *mGRE* sequence, they inserted a repetitive block of three compensation gradients with identical duration between successive echoes. The first compensation gradient has a magnitude ηG_c, the second $-2\eta G_c$, and the last ηG_c, with

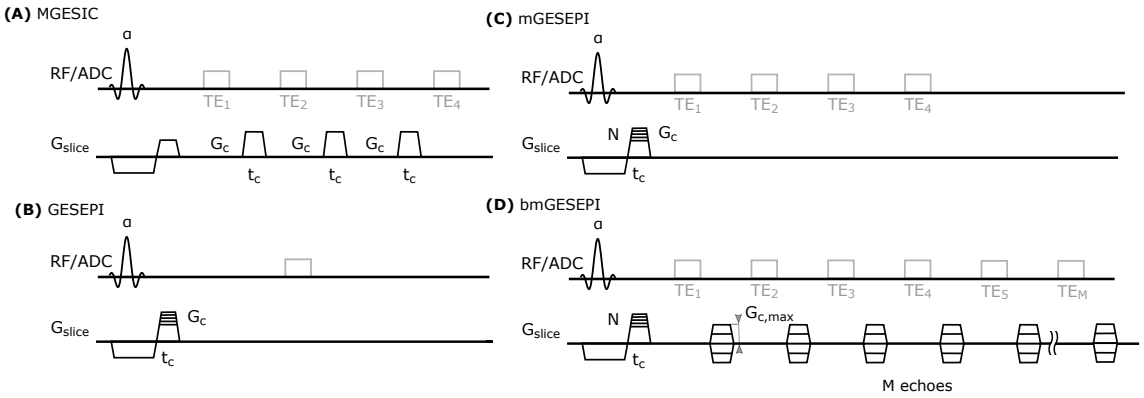

Figure 3.5: Schematic sequence overview of different z-shimming approaches. The *MGESIC* method (A) applies compensation moments in-between echo acquisition [251]. The *GESEPI* method acquires multiple images with different compensation moments by varying the slice-selection rephasing gradient [252], and the *mGESEPI* (C) acquires several echo images [255]. The *bmGESEPI* approach (D) adds additional compensation moments in-between echo acquisition to reduce the required number of images [218].

η being a scaling factor. Hence, the sequence acquires in each block an image without a compensation moment, one compensation moment for negative g_z, and one for positive g_z. By assuming an ideal slice profile, a combined image is calculated by taking the root mean square of the individual images of one block. Then, Wild et al. estimated R_2^* from the combined images using the first TE of each block for the calculations. A drawback of the method is that the echo spacing should be as short as possible because it neglects T_2^* decay for image combination. Furthermore, it assumes an ideal slice profile, which might lead to an additional bias depending on the type of excitation pulse.

Figure 3.6B shows another single scan method proposed by Meng and Lei for R_2^* mapping [152]. In this approach, they estimated R_2^* from the first echo without compensation gradient and from a combined image of the successive echoes. For the combined image, a strong compensation gradient is applied with $G_{c,max}$ and duration Δ. This strong gradient is stepwise compensated by applying small gradients with amplitude G_s and duration δ in-between the echoes. The gradients are designed such that the moment of the largest gradients is compensated at the image number $P/2$ where P is the total number of acquired echo images. As in the *GESEPI* approach, Meng et al. combined the individual gradients with the Fourier transform (Equation 3.22).

Previous methods for R_2^* mapping have in common that they assume an ideal slice profile, and that the echo images of a certain interval can be combined neglecting T_2^* decay. However, as discussed in Section 3.2, Preibisch et al. proposed a solution to calculate the signal decay in the presence of g_z with the RF excitation pulse envelope for small tip angles [178]. Given this relation, Nam et al. proposed to use the solution to describe the effect of z-shim gradients on the signal decay [159]. For each TE, the signal is calculated with the solution in Equation 3.6 [178], but instead of the moment of g_z the sum of the

g_z moment and the accumulated compensation moment of the z-shim gradients is used. Further, Nam et al. proposed a method that compensates linear increasing positive and negative g_z. They applied the compensation gradients alternatingly with linear increasing amplitude (Figure 3.6C) [159]. After compensation of a single positive or negative g_z, the moment is balanced by applying the same gradient moment with opposite polarity. Hence, the sequence acquires additional standard $mGRE$ images with zero z-shim moment.
Later, Lee et al. proposed a similar approach for MWF mapping, which also takes into account the slice profile for minimizing the effects of g_z on MWF [128]. It differs from the z-shim pattern proposed by Nam et al. in two aspects. First, Lee et al. do not apply z-shim gradients in the first echoes to avoid signal crushing in homogeneous regions. Second, the method only compensates a positive g_z because they argue that in most brain regions g_z is positive.

3.4.2 3D z-Shimming

Similar to the 2D multi-scan approach [252], Glover proposed a 3D z-shim method that acquires additional images with different increments of the slice refocusing lobe [67]. In 3D acquisitions additional phase encoding steps Δk_z are acquired:

$$\Delta k_z = \frac{1}{N_{slice}\Delta z}, \tag{3.23}$$

where N_{slice} is the number of slices and Δz the slice thickness. The maximum k-space encoding is given by $k_{max,3} = 1/(2\Delta z)$. In the case of a field gradient g_z, the phase offset $\Delta k_{off} = \gamma g_z TE/(2\pi)$ might be shifted outside the sample space depending on the magnitude of g_z and TE ($k_{max,3} < \Delta k_{off}$) leading to a signal loss. By varying the slice refocusing lobe, it is possible to shift the window of the acquired k-space samples. To sample the phase offset Δk_{off}, the maximum phase encoding has to be moved towards $k_{max,3'}$ assuming that most regions have the same polarity of g_z, and that the window is shifted towards one direction of k_z:

$$k_{max,3'} = k_{max,3} + |\Delta k_{off}| \tag{3.24}$$

Given that $k_z < k_{max,3'}$, the required number of encoding steps $N_{k,3}$ is:

$$N_{k,3} = N_{slice} + |\Delta k_{off}|/\Delta k_z = N_{slice}(1 + \frac{|k_{off}|\Delta z}{2\pi}) \tag{3.25}$$

Consequently, it requires $N_{k,3}/N_{slice}$ additional acquisitions compared without z-shimming and $N_{z,3} = N_{k,3} - N_{slice} + 1$ images can be reconstructed. To get a single image from the $N_{z,3}$ z-shim images, a maximum intensity projection or sum of squares combination can be used. In conjunction with a field map ΔB_0 map another possibility is to calculate Δk_{off} and choose for each voxel the corresponding z-shim image that fits Δk_{off}.

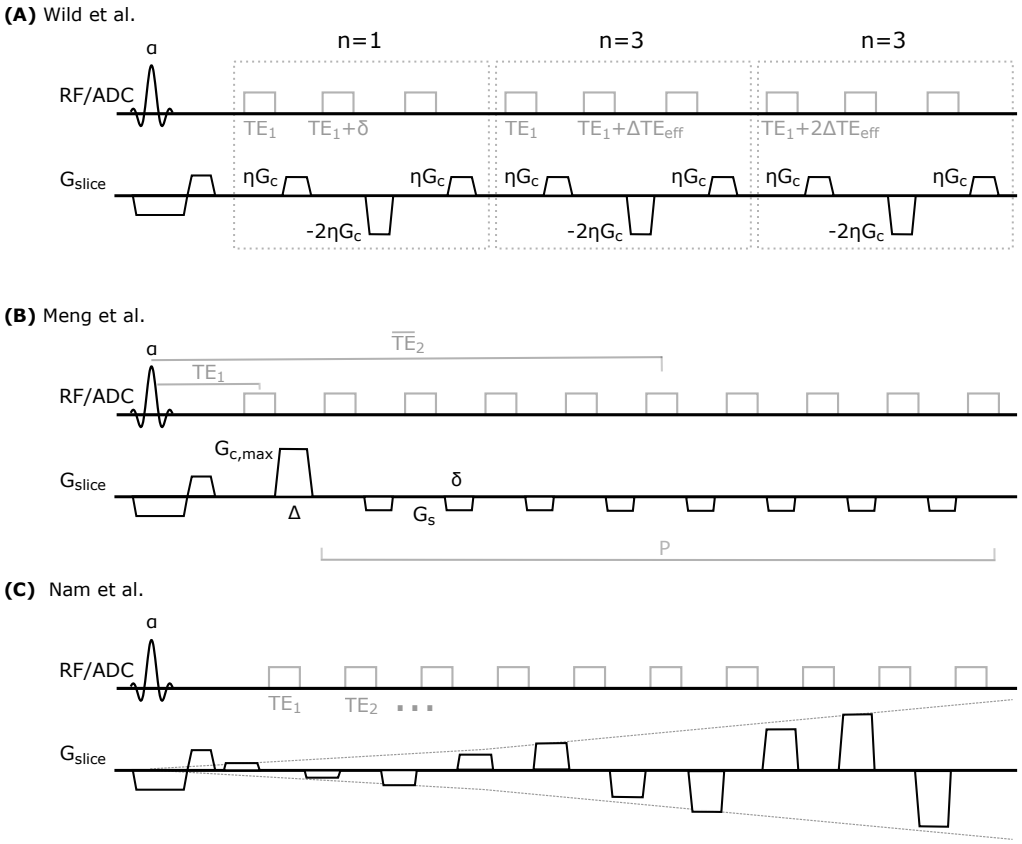

Figure 3.6: Schematic single-scan z-shimming sequences for R_2^* mapping. The method by Wild et al. (A) applies a repetitive pattern of z-shim gradients (dashed gray boxes) [239]. Composite images are calculated for all blocks, which are then used for R_2^* estimation. The approach by Meng et al. (B) applies a strong compensation gradient after the first echo followed by small compensation moments with opposed polarity between each echo [152]. The P images are used to obtain a composite image at $\overline{TE}_2$. From the first echo image and the composite image, R_2^* is estimated. In (D), Nam et al. apply linear increasing compensation moments to compensate a positive and negative g_z. R_2^* is obtained by fitting a signal model accounting for the slice profile to the measured signal, g_z, and the compensation moments [159].

Han et al. [81] proposed a method to improve R_2^* mapping for 3D acquisition in a single-scan z-shim approach. The approach applies an alternating pattern of compensation moments between the echo acquisition. Therefore, echo images with an even echo number are standard *mGRE* images and odd images are compensated images. To estimate R_2^*, Han et al. added the z-shim moments in the modeling of the *VSF* [250]. The adapted *VSF* model allows describing the signal for each *TE* and to fit R_2^* from the measured signal. An essential step for the *VSF* is an accurate estimation of g_z in each voxel, which is especially challenging in areas with large g_z. For that reason, the authors additional used an algorithm to estimate the field map including the z-shim images [83]. Apart from R_2^* mapping, Oh et al. proposed a sequence for improved susceptibility

weighted imaging [167]. Instead of two images, they acquire an additional image with a compensation gradient. By using information of all three images, Oh et al. achieved improved image quality in the vessels in the frontal lobe compared with standard acquisition.

4 Practical MRI Aspects

Contents

A large part of the present thesis focuses on the development of a signal model for describing the 2D *mGRE* signal in the presence of a macroscopic field gradient g_z. The following chapter summarizes the various adaptations from the vendor's standard *mGRE* sequence that have been implemented on the 3T *MRI* system (Magnetom Prisma, Siemens, Erlangen, Germany). The first part describes the implementation of the different 2D *RF* excitation pulses and the measurement of the slice profile. The second part deals with the measurement of physiologically induced B_0 variations with navigator echoes. This has been found to be an essential prerequisite to allow accurate signal modeling. Further, it explains the phase correction and coil combination of the raw data to reconstruct the image from the raw data.

4.1 RF Excitation Pulse

In the case of a nonadiabtic excitation pulse, the variation of the flip angle $\alpha(\omega)$ can be approximated by the modulus of the inverse Fourier transform of the *RF* excitation pulse envelope $B_1(t)$ in center of the slice [14, 98]:

$$\sin(\alpha(\omega)) \approx \alpha(\omega) \approx \pm\gamma \left| \int_0^t B_1(t') \exp(i\omega t') dt' \right|. \tag{4.1}$$

Consequently, a short hard pulse results in a broad sinc-shaped spectrum, whereas a long sinc pulse leads to a narrow rectangular shaped spectrum. To control the width of the excited slice, a slice-selection gradient is turned on with an amplitude G_{slice}, which frequency encodes the slice direction z by the frequency $\omega(z) = \gamma G_{slice} z$. Given that the *RF* pulse has a bandwidth of $\Delta\omega$, then for the slice thickness Δz follows:

$$\Delta z = \frac{\Delta\omega}{\gamma G_{slice}} \tag{4.2}$$

Hence, Δz is controlled either by varying G_{slice} or by changing the RF pulse to achieve a different $\Delta\omega$. To allow a reasonable comparison between different pulses, it is desirable that all pulses have similar Δz at a certain α. Then, the shape of the slice profile dominates the signal dephasing and not variations in Δz. In one of the first experiments, we used the vendor's standard pulses and amplitudes of G_{slice}, but these pulses lead to different Δz caused by G_{slice}. Figure 4.1 shows the results of the measured slice thickness Δz_{meas} compared with the nominal slice thickness Δz for two RF pulses. It shows that Δz_{meas} is larger than Δz and different for the two pulses. For a better comparison, four different RF pulses with a similar Δz for all pulses at a certain α were designed. To achieve this, the amplitude of G_{slice} was estimated with a numerical Bloch solver [1] such that Δz matches the simulations for $\alpha = 30°$ for each pulse. The first three pulses were sinc-Hanning-windowed pulses, each with a different pulse duration T_{pulse} and TBP, and a Gaussian pulse. The pules shapes of the sinc-Hanning-windowed pulses were calculated with Equation 4.3 and for the Gauss pulse with Equation 4.4.

$$B_{1,sinc-Hanning}(t) = \frac{1}{2}\text{sinc}\left(\frac{TBP\ t}{T_{pulse}}\right)(1+\cos(2\pi t/T_{pulse})) \tag{4.3}$$

$$B_{1,Gauss}(t) = e^{\frac{-t^2}{2T_{pulse}\sigma^2}} \tag{4.4}$$

Figure 4.2 shows the measured slice profile for the three sinc-Hanning-windowed pulses and the Gaussian pulse acquired at three different flip angles α. The slice profiles were obtained by switching the frequency encoding to the slice-selection direction. Table 4.1 lists the estimated Δz_{meas} from the measured data. In contrast to the vendor's pulses, Δz_{meas} corresponds now to the nominal Δz for $\alpha = 30°$. When comparing the four pulses, the sinc-Hanning-windowed pulses with $T_{pulse} = 1ms$ and $T_{pulse} = 2ms$ and the Gaussian pulse lead to a similar slice profiles. The increase of z_{meas} with α is explained by the solution of the Bloch equations. While the Fourier approximation results in a constant Δz independent of α, the solution with the Bloch equations allows describing the slice profile accurately for all α.

4.2 Navigator for Physiological Noise Compensation

4.2.1 Physiological Noise and Navigator Echoes

A prerequisite for an accurate description of the GRE signal in the presence of g_z is that contributions from physiologically induced field fluctuations are minimized. During k-space acquisition, it is usually assumed that the resonance frequency is constant over the acquisition period. However, apart from the system's B_0 drift and bulk motion, field variations can be caused by physiologically induced fluctuations due to the cardiac or

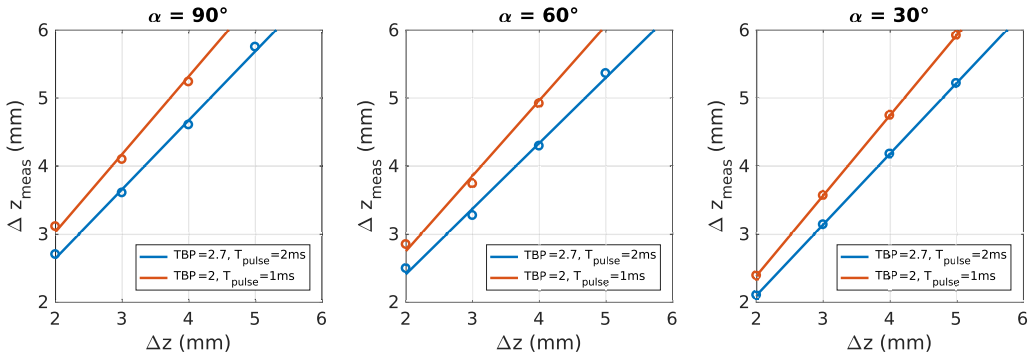

Figure 4.1: Comparison between the measured slice thickness Δz_{meas} versus the nominal slice thickness Δz for three different flip angles. Each plot shows results for two standard sinc-Hanning-windowed *RF* excitation pulses of the vendor's *GRE* sequence. For both pulses, Δz_{meas} is larger than Δz and different between the pulses.

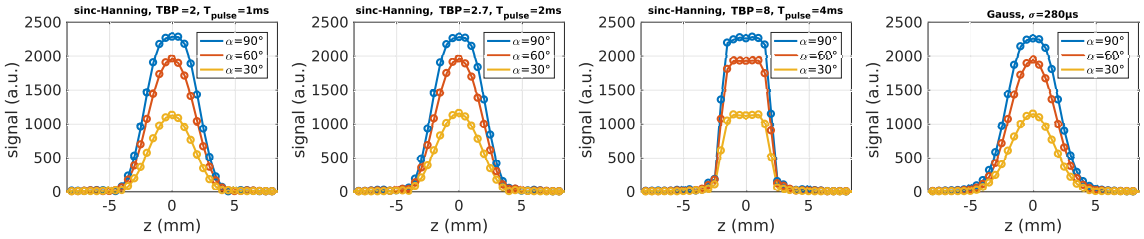

Figure 4.2: Measured signal along the slice for the four *RF* pulses each acquired with three flip angles. The first three plots show results for sinc-Hanning-windowed pulses with increasing *TBP* and T_{pulse} (from left to right) and the last plot illustrates the results using a Gaussian pulse. Table 4.1 summarizes the corresponding measured slice thickness Δz_{meas}.

Table 4.1: Measured slice thickness Δz_{meas} of the implemented *RF* pulses using three different flip angles α. By setting G_{slice} to the value estimated with the Bloch solver, comparable Δz_{meas} are obtained.

Pulse	Δz_{meas}(mm)		
	$\alpha = 90°$	$\alpha = 60°$	$\alpha = 30°$
sinc-Hanning, $TBP = 2$, $T_{pulse} = 1ms$	4.61	4.20	3.96
sinc-Hanning, $TBP = 2.7$, $T_{pulse} = 2ms$	4.51	4.15	4.01
sinc-Hanning, $TBP = 8$, $T_{pulse} = 4ms$	4.09	4.02	3.97
Gauss $\sigma = 200\mu s$	4.58	4.17	4.02

respiratory cycle [174, 245]. These field variations lead to phase error in the k-space encoding. For respiratory fluctuations, a strong correlation between phase fluctuation and a respiratory belt was observed. The amount of phase fluctuations highly depends on the subject [220]. Versluis et al. reported that the contributions from physiologically induced B_0 fluctuations are four times larger than movement artifacts in Alzheimer's patients [223]. An explanation for these variations is given by the movement of the

chest, causing magnetic field variations that range up to the brain. To describe these variations, Raj et al. proposed a simplified model, which is illustrated in Figure 4.3 [181]. The model mimics the head and upper torso by a cylinder containing water. The cylinder contains a spherical cavity with a radius R and susceptibility difference $\Delta\chi$ with respect to the water. The spherical cavity produces a dipole field $\Delta B(x, y, z)$ given by Equation 4.5 [194]. Depending on R and $\Delta\chi$, field variations in the imaging plane can be modeled. Raj et al. validated the model by changing $\Delta\chi$ with the oxygen concentration in the cavity. Although variations in $\Delta\chi$ can induce field variations, they concluded that changes in R via the lung volume are more likely responsible variations in $\Delta B(x, y, z)$ [181].

$$\Delta B(x, y, z) = \frac{\frac{1}{3}\Delta\chi B_0 R^3 (2z^2 - x^2 - y^2)}{(x^2 + y^2 + z^2)^{5/2}} \tag{4.5}$$

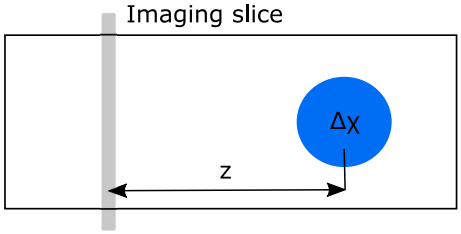

Figure 4.3: Simple model for describing the physiologically induced B_0 changes in an imaging slice proposed by Raj et al. [181]. They model the head and upper torso with a water containing cylinder and a cavity with susceptibility difference $\Delta\chi$ and radius R for the lungs. The magnetic field variations caused by the cavity are described by the dipole field in Equation 4.5.

To measure these phase variations, Hu et al. proposed to use navigator echoes [100]. For each phase encoding step, a navigator echo acquires an additional echo, but without phase encoding ($k_y = 0$). Figure 4.4 shows two different options for the acquisition. In the original work they acquired the navigator echo before k-space acquisition (Figure 4.4A) [100], but it is also possible to measure it after phase encoding by rewinding the phase encoding gradient before echo acquisition (Figure 4.4B) [235].
Figure 4.5 illustrates an example of the estimated phase fluctuations during repetitive measurements in a single slice. The left plot shows a periodic variation of the phase signal with some smaller higher frequency variations. By performing a fast Fourier transform (FFT), a frequency of about 13 cycles/minutes can be assigned to the prominent slow variations. Based on the literature [100, 220, 223], this frequency corresponds to respiratory induced fluctuations. The higher frequency content in the signal might be addressed to pulsation [127], but no distinct peak is observable in the frequency spectrum.

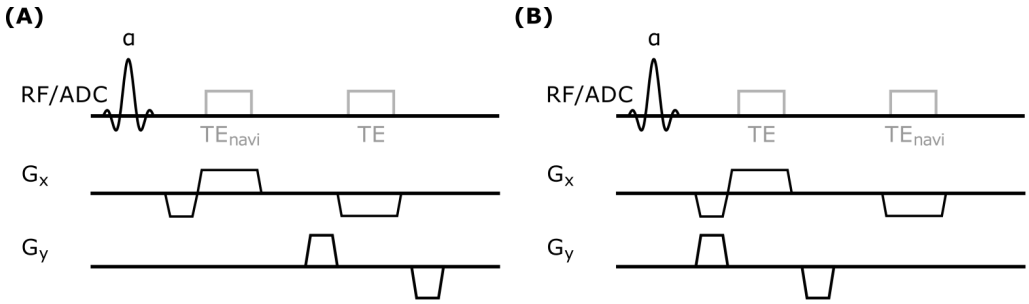

Figure 4.4: Two different approaches for acquiring a navigator echo to estimate physiologically induced B_0 variations at the echo time TE_{navi}. In (A), the navigator echo is acquired before image acquisition and in (B) after image acquisition and rewinding of the phase encoding.

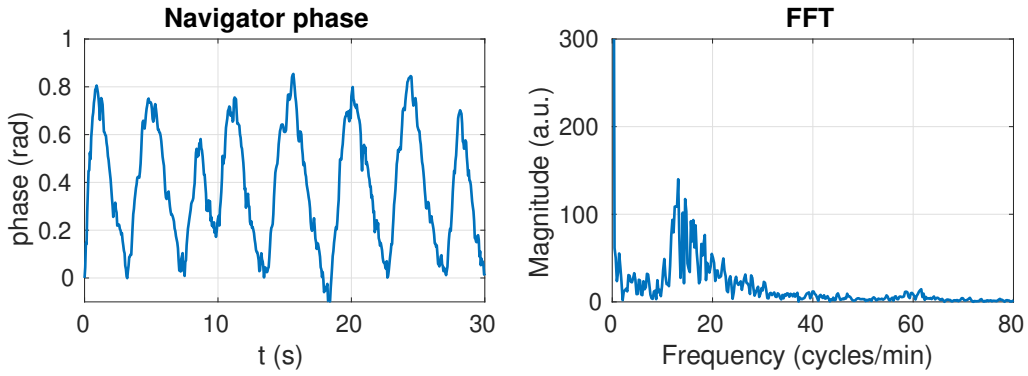

Figure 4.5: Example of the estimated phase fluctuations from the navigator echo in a single slice from a continuous measurement (25 measurements, $TE_{navi} = 47ms$, $TR = 50ms$ with 208 phase encoding lines). The left image shows the phase in a time frame of $30s$, and on the right the FFT from the entire acquisition is plotted. The plots show a clear respiratory induced fluctuation with a frequency around 13 cycles/minute.

4.2.2 Estimation of Phase Fluctuations from Navigator Echoes

Figure 4.6 shows the processing steps for estimating the phase fluctuations $\phi_{corr}[n_{phase,m}]$ from the navigator signal from nth phase encoding line $n_{phase,m}$. The steps are the same for both approaches in Figure 4.4. For each coil channel m, from the complex raw data (Figure 4.6A) an $IFFT$ in read-out direction is performed to estimate the projection for each $n_{phase,m}$ (Figure 4.6B). The resulting phase signal $\angle S_{navi,B}$ can be decomposed in a signal that is equal for all lines $n_{phase,m}$, such as a channel specific phase offset or object related phase variations, and in phase fluctuations that vary from line to line. To remove the line independent phase, a reference line is chosen, which is subtracted from all lines. The subtraction is achieved by multiplying all $n_{phase,m}$ lines with the complex conjugate of the reference line (Figure 4.6C). By taking the mean of the resulting signal $S_{navi,C}$ for each $n_{phase,m}$ line, $\phi_{corr}[n_{phase,m}]$ is obtained (Figure 4.6C). This step is repeated for all coils (Figure 4.6D). By comparing Figure 4.6C and Figure 4.6D similar noise like fluctuations are measured in all coils.

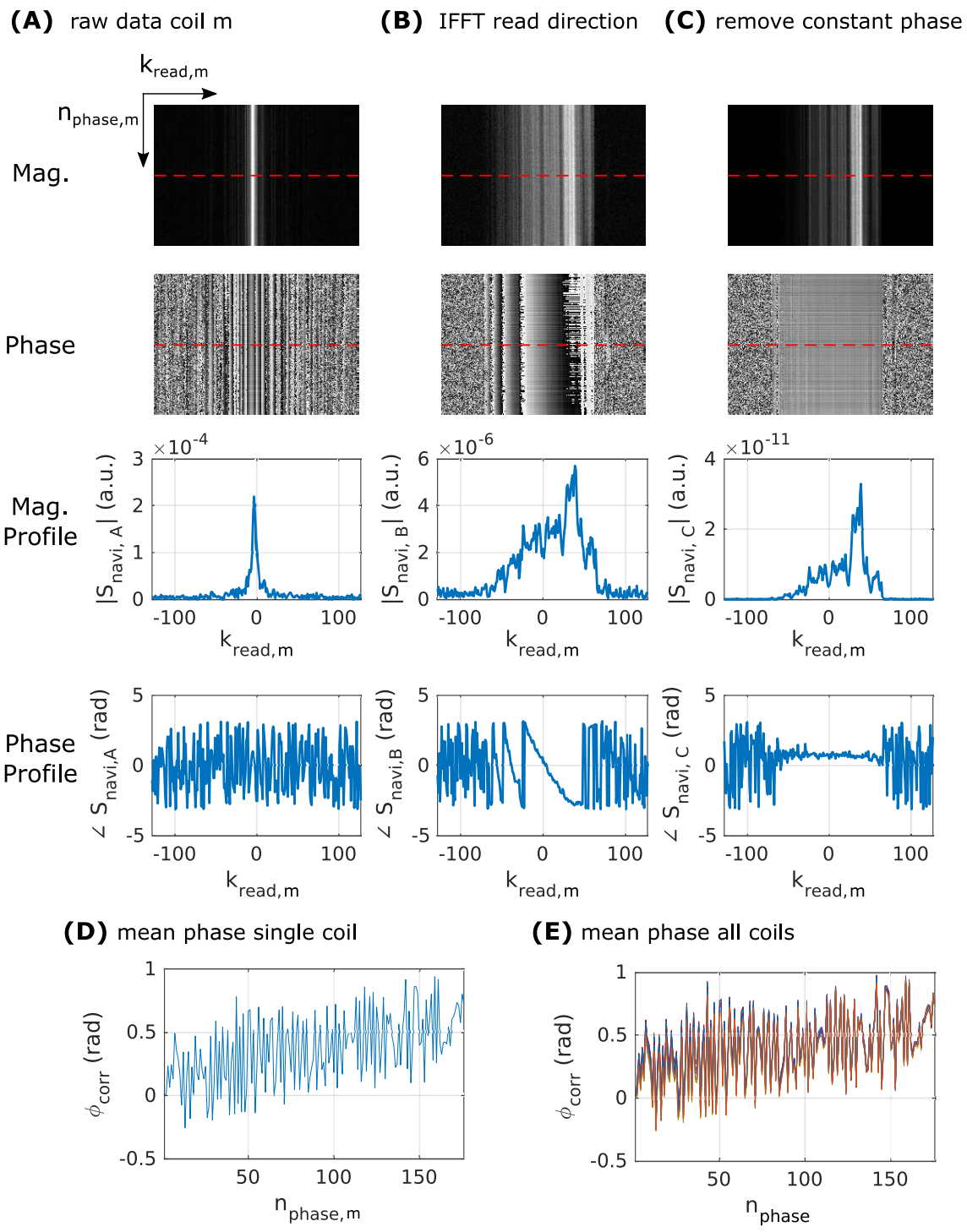

Figure 4.6: Processing steps of the navigator echo S_{navi} for correction of physiologically induced B_0 fluctuations. First, for each navigator echo $n_{phase,m}$ (A) an *IFFT* is performed for each coil m (B). Next, the constant phase of the object itself is removed by multiplying all $n_{phase,m}$ lines by the complex conjugate of a reference line (e.g., first acquired line $n_{phase,m} = 1$) (C). To estimate the phase correction $\phi_{corr}[n_{phase,m}]$ (D), the mean is calculated from the complex signal (C).

4.2.3 Coil Combination and Image Reconstruction

After the estimation of $\phi_{corr}[n_{phase,m}]$, the raw data has to be corrected with $\phi_{corr}[n_{phase,m}]$ for each echo. Figure 4.7 illustrates the different steps exemplary shown for the fourth echo image $S_m(TE_4)$. Assuming that $\phi_{corr}[n_{phase,m}]$ from the time of excitation until the echo time TE_{navi} increases linearly, the corrected raw data is obtained for each channel m [235]:

$$S_m^{corr}(k_{read,m}, TE) = S_m(k_{read,m}, TE) \exp\left(-i\frac{\phi_{corr}[n_{phase,m}]}{TE_{navi}}TE\right), \tag{4.6}$$

where the ratio $\frac{TE}{TE_{navi}}$ describes the linear scaling of the navigator phase. In the next step the M coil images have to be combined to a single image, which is referred to as coil combination. An overview of various coil combination methods can be found in [186]. In phased array coils, the signal of the phase at a position $\mathbf{r}$ for the mth coil can be decomposed in [186]:

$$\phi_m(\mathbf{r}, TE) = \phi_{0,m}(\mathbf{r}) + \Delta\omega(\mathbf{r})TE, \tag{4.7}$$

where $\phi_{0,m}(\mathbf{r})$ is a channel dependent phase offset and $\Delta\omega(\mathbf{r})TE$ describes the channel independent phase accumulation caused by the magnetic field. To avoid destructive interference in the combined images caused by different $\phi_{0,m}(\mathbf{r})$ by simple complex summation of the individual images, the coil dependent phase term has to be removed. Compared with single echo acquisition, multi-echo acquisition offers the advantage that $\phi_{0,m}(\mathbf{r})$ can be estimated or eliminated before coil combination. Luo et al. proposed a method that combines the images $S_{comb}(TE_i)$ of the ith echo as follows [145]:

$$S_{comb}(TE_i) = \frac{1}{M}\sum_{m=1}^{M} \lambda_m \bar{S}_m^{corr}(TE_1) S_m^{corr}(TE_i) \tag{4.8}$$

by multiplying all images of the same coil m with the complex conjugate $\bar{S}_m^{corr}(TE_1)$ of the first echo TE_1 before summation, it eliminates the coil dependent $\phi_{0,m}(\mathbf{r})$. To account for different noise levels in the coil images, the data is weighted with the factor λ_m [145]:

$$\lambda_m = \frac{\frac{1}{M}\sum_{l=1}^{M}\sigma_l^2}{\sigma_m^2}, \tag{4.9}$$

where σ_m is the noise amplitude in a channel m estimated in a noisy ROI in the magnitude image.

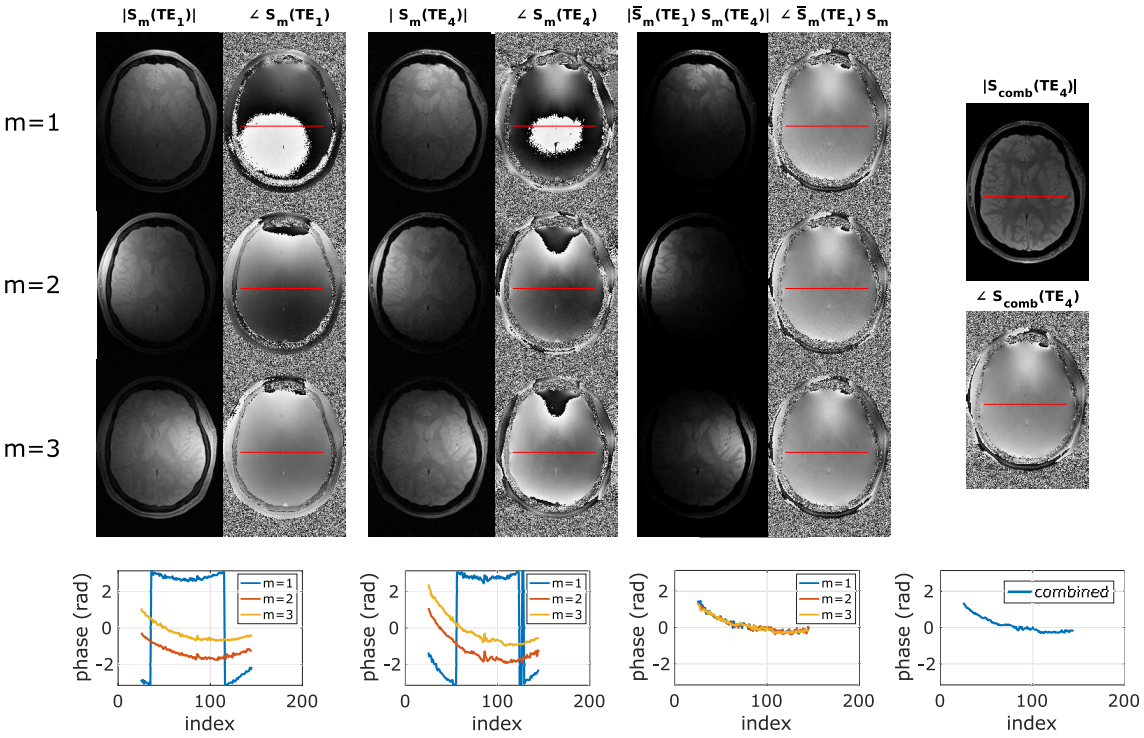

Figure 4.7: Example of the coil combination proposed by Luo et al. for multi-echo data [145]. The first two blocks of images show the magnitude and phase of the first echo with TE_1 and the fourth echo with TE_4 for coils $m = [1, 2, 3]$ out of $M = 16$ coils. The results of the multiplication of the fourth echo $S_m(TE_4)$ with the complex conjugate of the first echo $\bar{S}_m(TE_4)$ are illustrated in the third block. The images on the right side show the combined image $S_{comb}(TE_4)$, obtained by the weighted summation with σ_m of the third block. The phase variation along the red line in the phase images is plotted on bottom.

4.2.4 Example Phase Correction

Figure 4.8 shows an example of the signal decay with and without phase correction. In Figure 4.8A, echo images were reconstructed including the phase of the navigator echo while in Figure 4.8B this variation was not considered. The difference between the echoes (Figure 4.8C) reveals spatial and temporal artifacts. Additionally, the signal decay in two *ROIs* is plotted indicating the temporal variations deviating from a monoexponential signal decay.

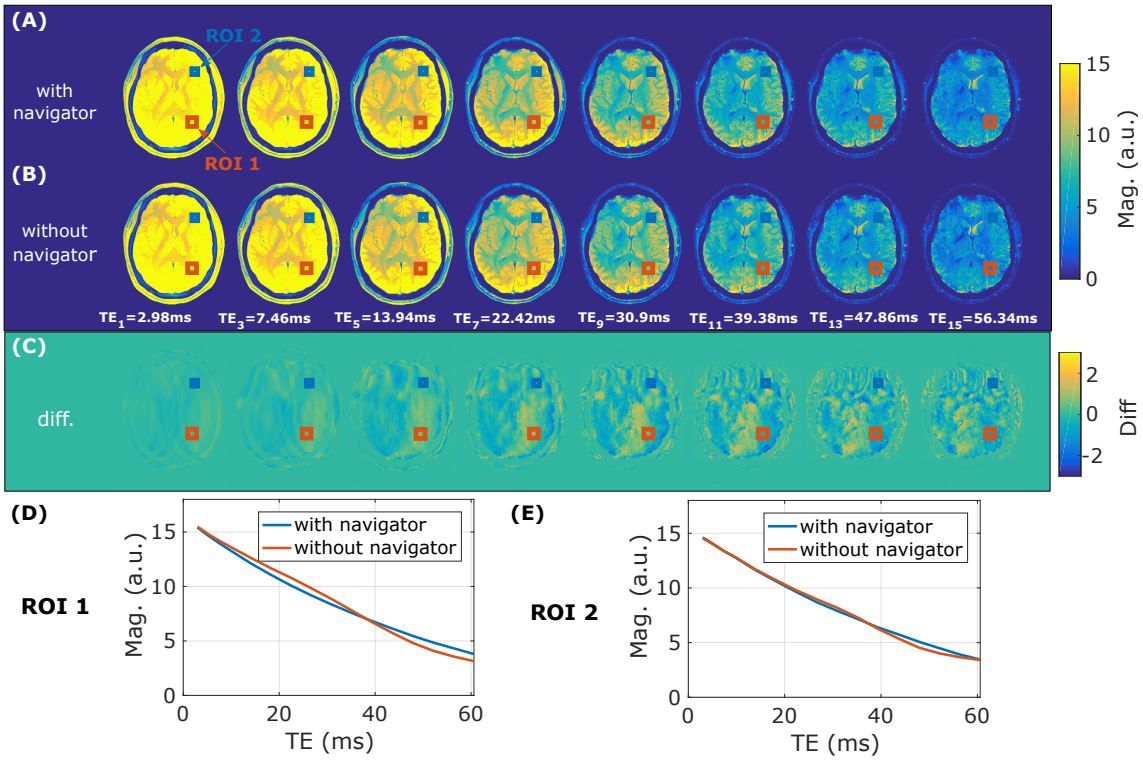

Figure 4.8: Example of a signal decay reconstructed from a 2D *mGRE* acquisition with (A) and without considering the phase of the navigator (B). Every second echo starting from $TE_1 = 2.98ms$ to $TE_{15} = 56.43ms$ is shown. The difference between the images of row (A) and (B) is illustrated in (C).

5

R_2^* and MWF Estimation Using Larger Flip Angles

This chapter is based on the publication:

M. Soellradl, A. Lesch, J. Strasser, L. Pirpamer, R. Stollberger, S. Ropele, and C. Langkammer. Assessment and correction of macroscopic field variations in 2D spoiled gradient-echo sequences. *Magnetic Resonance in Medicine*, 84(2):620–633, 2020, doi: 10.1002/mrm.28139

and on the ISMRM abstract:

M. Soellradl, S. Ropele, and C. Langkammer. Gradient echo modelling with macroscopic field variations and large flip angles. In *Proceedings of the 27th Annual Meeting of ISMRM*, Montreal, Canada, 2019

Contents

5.1 Introduction

Section 3.2 reviews different signal modeling approaches for the *RF*-spoiled *GRE* sequence. For 2D acquisitions, the signal in the presence of a macroscopic field gradient g_z is given by the analytic solution of Preibisch et al. [178]. Based on the small tip angle approximation, the signal dephasing is described by the shape of the *RF* excitation pulse $B_1(t)$ [178]. In an interleaved slice acquisition, the *TR* is usually rather large to allow multi-slice acquisition ($TR > 1s$), leading to an Ernst angle that might be beyond the limit for the small tip angle approximation. Therefore, the potential increase in *SNR* for larger flip angles is limited by the maximum possible angle which fulfills the small tip angle approximation.

To overcome this limitation, we propose a numerical model for solving the signal dephasing in the presence of g_z for an arbitrary RF excitation pulse and flip angle. Extending the model from Hernando et al. [94], we also investigate variations of the transmit RF field B_1^+ and the effect of scaling of the slice profile caused by the superposition of g_z and the slice-selection gradient G_{slice}. We further demonstrate with phantom and in vivo measurements that, depending on the RF pulse shape, the polarity of G_{slice} has to be considered for larger flip angles to account for through-slice phase variations. The proposed model substantially improves the quality of R_2^* maps and MWF maps acquired with arbitrary excitation pulses and flip angles.

5.2 Methods

5.2.1 Theory

In the presence of macroscopic field variations $\Delta\omega(z)$ the signal $S(t)$ of a 2D RF-spoiled GRE is proportional to the integral over the complex transverse magnetization $\underline{M}_{xy}(z) = |M_{xy}|e^{i\varphi_{xy}(z)}$ weighted with $\Delta\omega(z)$ along the slice-selective direction z. Thus, depending on $\underline{M}_{xy}(z)$ and $\Delta\omega(z)$, additional signal dephasing is observed in contrast to the theoretical monoexponential signal decay with R_2^*. If $\Delta\omega(z)$ is smooth and slowly varying in space, $\Delta\omega(z)$ can be approximated with a linear function $\Delta\omega(z) = \Delta\omega_0 + \gamma g_z z$ in each slice [246]. By assuming the origin of z being in the center of the slice, the equation for $S(t)$ reads as:

$$\begin{aligned} S(t) &= e^{-R_2^* t} \int_{-\infty}^{\infty} \underline{M}_{xy}(z, \alpha\xi, \lambda, E_1) e^{i\Delta\omega(z)t} dz \\ &\approx e^{-R_2^* t} \int_{-\infty}^{\infty} \underline{M}_{xy}(z, \alpha\xi, \lambda, E_1) e^{i\Delta\omega_0 t} e^{i\gamma g_z z t} dz, \end{aligned} \tag{5.1}$$

where g_z denotes the field gradient and $\Delta\omega_0$ the field offset. $\underline{M}_{xy}(z)$ depends on several factors (including ξ, λ, and E_1) discussed in detail subsequently. Depending on the ratio of TR to the longitudinal relaxation time T_1, which is included in the exponential term $E_1 = e^{-TR/T_1}$, and the effective flip angle $\alpha_{eff}(z)$ through the slice, the solution for $|M_{xy}(z)|$ changes according to the steady-state equation for GRE sequences [58]:

$$|M_{xy}(z, \alpha\xi, \lambda, E_1)| = S_0 \sin\left(\alpha_{eff}(z, \alpha\xi, \lambda)\right) \frac{1 - E_1}{1 - \cos\left(\alpha_{eff}(z, \alpha\xi, \lambda)\right) E_1}. \tag{5.2}$$

When TR is much larger than T_1, Equation 5.2 simplifies and $|M_{xy}(z)|$ is obtained by the sine of α_{eff} times the equilibrium magnetization S_0.

$$|M_{xy}(z, \alpha\xi, \lambda, E_1 = 0)| = S_0 \sin\left(\alpha_{eff}(z, \alpha\xi, \lambda)\right). \tag{5.3}$$

Here, $\alpha_{eff}(z)$ is obtained for a certain slice-selection gradient G_{slice} and the applied excitation pulse with a certain shape and amplitude. For small flip angles, the slice profile $\alpha_{eff}(z)$ can be estimated for an RF pulse envelope $B_1(t)$ with the small flip angle

approximation [98]. However, larger flip angles require solving the Bloch equations for $|M_{xy}(z)|$ and $\varphi_{xy}(z)$.
Extending previous studies, the factors ξ and λ were added to describe two effects that affect $\alpha_{eff}(z)$ and thus signal dephasing. First, variations of the active transmit field B_1^+ cause a deviation from the nominal flip angle α, which can change the effective flip angle profile $\alpha_{eff}(z)$ and therefore requires α to be scaled with ξ, obtained from the normalized B_1 map. Second, g_z is superimposed with G_{slice} leading to either broadening or narrowing of the slice profile described by the factor λ [183] as follows:

$$\lambda = \frac{G_{slice}}{G_{slice} + g_z}. \tag{5.4}$$

To investigate the impact of the described parameters on signal dephasing in the presence of g_z, four different models have been studied. Summarizing Equation 5.1 in a tissue-specific signal component $S_{tissue}(t)$ (e.g., $S_{tissue}(t) = S_0 e^{-R_2^* t}$) and a component $F_i(t)$ describing the signal dephasing due to $\Delta\omega(z)$, the model $S_i(t)$ can be written as $S_i(t) = S_{tissue}(t)F_i(t)$. The four models are defined as follows:

$$S_1(t) = S_{tissue}(t)F_1(t) = S_{tissue}(t) \tag{5.5}$$

$$\begin{aligned} S_2(t) &= S_{tissue}(t)F_2(t) \\ &= S_{tissue}(t)\int_{-\infty}^{\infty} |M_{xy}|(z, \alpha, \lambda = 1, E_1 = 0)e^{i\gamma g_z z t}dz \end{aligned} \tag{5.6}$$

$$\begin{aligned} S_3(t) &= S_{tissue}(t)F_3(t) \\ &= S_{tissue}(t)\int_{-\infty}^{\infty} |M_{xy}|(z, \alpha, \lambda = 1, E_1 = 0)e^{\varphi_{xy}(z,\alpha,\lambda=1,E_1=0)}e^{i\gamma g_z z t}dz \end{aligned} \tag{5.7}$$

$$\begin{aligned} S_4(t) &= S_{tissue}(t)F_4(t) \\ &= S_{tissue}(t)\int_{-\infty}^{\infty} |M_{xy}|(z, \alpha\xi, \lambda, E_1 = 0)e^{\varphi_{xy}(z,\alpha\xi,\lambda,E_1=0)}e^{i\gamma g_z z t}dz. \end{aligned} \tag{5.8}$$

The model $S_1(t)$ serves as an uncorrected reference without modeling $\underline{M}_{xy}(z)$ and $\Delta\omega(z)$. Then, for $S_2(t)$, only the magnitude along the slice $|\underline{M}_{xy}(z)|$ was considered neglecting $\varphi_{xy}(z)$. In $S_3(t)$, $\varphi_{xy}(z)$ was included, and in $S_4(t)$ the model was extended by additionally incorporating B_1^+ and λ variations.

5.2.2 Numerical Implementation

Signal dephasing caused by g_z was estimated numerically for F_2 to F_4 assuming $E_1 = 0$. In the first step, $\underline{M}_{xy}$ was estimated for a certain RF excitation pulse and G_{slice} with a freely available numerical Bloch solver using MATLAB (MathWorks, Natick, MA) [1]. Simulations were carried out with temporal resolution of $2\mu s$ and spatial resolution of $80\mu m$ with 2501 spatial points. The normalized envelope $B_1(t)$ was scaled to achieve

$\alpha_{eff}(z = 0) = \alpha\xi$ in the center of the slice. Rather than estimating $\underline{M}_{xy}$ for each voxel with ξ and λ, calculations were accelerated by estimating $\underline{M}_{xy}$ in steps of $\Delta\xi = 0.05$ followed by linear interpolation to $\Delta\xi_{intp} = 0.005$. Variations of λ were incorporated by multiplying the sampling points along z with λ, to scale the thickness of the slice. In the last step, the integral along z for given g_z was solved by numerical integration.

5.2.3 Simulations

To investigate the influence of the G_{slice} polarity and flip angle α on F_3, simulations for $\alpha = 30°$ and $\alpha = 90°$ with negative and positive polarity of G_{slice} were performed. Based on the vendor's standard *GRE* pulse, a sinc-Hanning-windowed excitation pulse with a pulse duration T_{pulse} of $2ms$ and a *TBP* product of 2.7 was chosen for the experiments. A G_{slice} of $8.29mT/m$ was determined with the Bloch solver to achieve a slice thickness Δz of $4mm$, as defined by *FWHM* of $|M_{xy}|$, for $\alpha = 30°$. Based on the observed field gradients in phantom measurements, g_z was set to $100\mu T/m$ for all simulations. In the in vivo measurements of the brain, field gradients up to $300\mu T/m$ have been reported in areas such as orbitofrontal cortex or inferior temporal lobe [233].
Exploiting the relevance of individual parameters for modeling F_4, a sensitivity analysis was performed for φ_{xy}, B_1^+, and λ with the same sinc-Hanning-windowed excitation pulse. To estimate the relevance of φ_{xy}, simulations with $g_z = 100\mu T/m$ were carried out for F_4 with varying α from 10° to 90°, each with positive and negative G_{slice} polarity. Results were compared with simulations for model F_2 considering only the magnitude $|M_{xy}|$ of the slice profile ($\varphi_{xy} = 0$). For evaluation, root mean squared error (RMSE) over time for each α between F_4 and F_2 was calculated.
The sensitivity to B_1^+ was simulated by scaling B_1^+ for each flip angle ($\alpha = 30°$ and $\alpha = 90°$) with a factor ξ (ranging from 0.6 to 1.4) for $g_z = 100\mu T/m$. The results for F_4 obtained for different ξ were compared with those for $\xi = 1$ by plotting the *RMSE*. The same steps as for B_1^+ were carried out for λ by changing the value from 0.8 to 1.2.
A crucial assumption of the proposed models is that for a given α, *TR* is long enough to avoid changes of $|M_{xy}|$ due to incomplete T_1 relaxation ($E_1 = e^{-TR/T_1} \neq 0$). Hence, the steady-state solution in Equation 5.2 was included to estimate signal dephasing F_{T1} in the presence of $g_z = 100\mu T/m$ for different E_1:

$$F_{T_1} = \int_{-\infty}^{\infty} \underline{M}_{xy}(z, \alpha\xi, \lambda, E_1) e^{\varphi(z,\alpha\xi,\lambda,E_1)} e^{i\gamma g_z z t} dz. \tag{5.9}$$

For each TR/T_1 (ranging from 1 to 5) the Ernst angle α_{Ernst} was calculated and simulations with the sinc-Hanning-windowed *RF* pulse ($T_{pulse} = 2ms$ and $TBP = 2.7$) were carried out by setting $\alpha = \alpha_{Ernst}$, $\alpha = 0.8\alpha_{Ernst}$ and $\alpha = 0.6\alpha_{Ernst}$. Obtained results were compared by calculating the *RMSE* over time between F_{T1} and F_3.

5.2.4 Phantom Experiments

To validate the results from the simulations of dephasing effects for different α and G_{slice} polarity, phantom measurements have been performed. For the phantom, a plastic cylinder ($\varnothing = 12cm$ and length $= 20cm$) was filled with agarose gel ($5g/L$), which was doped with $110\mu mol/L$ Magnevist® to shorten T_1.
The phantom was scanned on a 3T *MRI* system (Magnetom Prisma, Siemens, Erlangen, Germany) twice by a *mGRE* sequence with $\alpha = 30°$ and $\alpha = 90°$ each with alternating polarity of G_{slice}. The same sinc-Hanning-windowed excitation pulse ($T_{pulse} = 2ms$ and $TBP = 2.7$) as for the simulations and $|G_{slice}| = 8.29mT/m$ was used to achieve $\Delta z = 4mm$ for $\alpha = 30°$. Other sequence parameters were: field of view (FOV)$= 128x128mm^2$, in-plane resolution $= 1x1mm^2$, 32 monopolar echoes with bandwidth (BW)$= 500Hz/px$, $TE_1 = 4ms$, $\Delta TE = 5ms$, $TR = 3s$, 25 slices with 0% interslice gap. For B_1 mapping, a Bloch-Siegert sequence with the same resolution was used [190].
The g_z map was obtained by using the central difference from the field map ΔB_0 to estimate the gradient in the ith slice:

$$g_z(x, y, z_i) = 0.5\frac{\Delta B_0(x, y, z_{i+1}) - \Delta B_0(x, y, z_{i-1})}{\Delta z}. \tag{5.10}$$

Single side difference was used for the first ($i = 1$) and last slice ($i = N$). ΔB_0 was estimated from a linear fit of the first six echoes of the unwrapped phase (PRELUDE unwrapping [103]). From the measured data, R_2^* maps were estimated in MATLAB with the *lsqnonlin()* function with models S_1 to S_4.
As indicated in Figure 5.1, when varying G_{slice} amplitude slightly within the model, it was found that results could be further improved when using $G_{slice} = 8.5mT/m$ for all analyses.

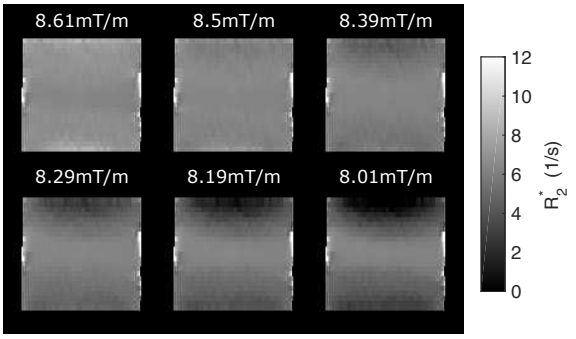

Figure 5.1: Coronal R_2^* maps from the phantom measurements ($\alpha = 90°$) estimated for a varying slice-selection gradient G_{slice} within the model. The most homogeneous map was obtained with $G_{slice} = 8.50\mu T/m$.

5.2.5 Influence of TR/T_1

Phantom measurements with different $TR = [125ms, 250ms, 500ms, 1s, 1.5s, 2s, 3s, 5s]$ and $\alpha = [30°, 60°, 90°]$ were carried out with the *mGRE* sequence to investigate steady-state effects for modeling. A Bloch-Siegert sequence was used for B_1 mapping [190]. In addition, T_1 was measured with $0.5x0.5mm^2$ in-plane resolution by changing the readout direction to the slice direction. Results were evaluated by estimating R_2^* with model S_4 for each TR and α.

5.2.6 In Vivo R_2^* and MWF experiments

To evaluate the proposed modeling for in vivo application, R_2^* and *MWF* mapping experiments were performed on the same 3T *MRI* system with 10 subjects (age range = 26-50 years). The study was approved by the local ethics committee and all subjects gave written informed consent. In addition, subjects were scanned with an anatomical magnetization-prepared rapid gradient-echo (MPRAGE) sequence with $1mm^3$ isotropic resolution for regional evaluation of R_2^* and *MWF* maps.
For R_2^* mapping, subjects were scanned twice with a *mGRE* sequence with alternating G_{slice} polarity using a sinc-Hanning-windowed excitation pulse ($T_{pulse} = 2ms$ and $TBP = 2.7$) with $\alpha = 85°$ (Ernst angle assuming $T_1 = 1s$). Other sequence parameters were: $FOV = 256x208mm^2$, in-plane resolution$= 1x1mm^2$, $|G_{slice}| = 11.05mT/m$ to achieve $\Delta z = 3mm$, 17 monopolar echoes with $BW = 500Hz/px$, $TE_1 = 2.87ms$, $\Delta TE = 3.59ms$, $TR = 2.5s$, 30 slices with 0 % interslice gap. The last echo was a navigator echo at $TE_{navi} = 65.4ms$ to correct for physiologically induced field variations [100]. Then, for each channel, the nth phase encoding line $S_n(k_x, TE)$ was corrected as described by Wen et al. [235] and the coil images were combined with the method proposed by Luo et al. [145]. A detailed description about the navigator echo and the coil combination can be found in Chapter 4.
For B_1 mapping, a highly accelerated method based on the Bloch-Siegert shift was used [136]. The field map for calculating g_z was obtained from the difference of the unwrapped phase of the first and third echo divided by TE difference. From the data, R_2^* maps were obtained using the models S_1, S_3, and S_4. The difference between the models was regionally assessed by calculating the mean and standard deviation of R_2^* in all subjects in *GM* and global *WM* masks. *GM* masks were segmented from the *MPRAGE* images with FMRIB software library (FSL) FIRST [171] and the global white matter masks with SIENAX [201], part of *FSL* [200]. All masks were affinely registered to *mGRE*-space with *FSL* FMRIB's linear image registration tool (FLIRT) [102, 104].
For *MWF* mapping, all subjects were scanned with a slightly adapted *mGRE* sequence to account for the fast decaying myelin water component. Short echo spacing ($\Delta TE = 2.2ms$) was achieved with a bipolar readout gradient, which was inverted in a second acquisition to compensate for phase errors between even and odd echoes. Other sequence parameters were: sinc-Hanning-windowed excitation pulse with $T_{pulse} = 1ms$ and $TBP = 2$,

$\alpha = 85°$, $G_{slice} = 14.15mT/m$, $FOV = 255x105mm^2$, in-plane resolution = $1.14x1.14mm^2$, $\Delta z = 4mm$, 27 bipolar echoes $BW = 500Hz/Px$, $TE_1 = 2.37ms$, $\Delta TE = 2.2ms$, $TR = 2s$, $TE_{navi} = 63.8ms$, 25 interleaved slices with 0% interslice gap, total scan time 12 minutes. Again, a highly accelerated B_1 map was acquired [136].
After correction of the data with the navigator echoes, the two *mGRE* images were registered using *FSL FLIRT* [104] before averaging. *MWF* estimation was based on a multi-exponential T_2^* relaxation times model [237] with M = 200 water components:

$$S_{tissue} = \sum_{j=1}^{M} s_j \exp\left(-\frac{TE}{T_{2,j}^*}\right). \tag{5.11}$$

Evaluation of data was performed by estimating *MWF* maps using models S_1, S_3 and S_4 with the *NNLS* algorithm of the MERA toolbox [53] and a cut-off for myelin water $T_{2,my}^* < 25ms$ [135]. For S_3 and S_4, the measured signal S was corrected with F_3 and F_4, respectively, before parameter estimation.
Regional evaluation of *MWF* maps was performed in *WM* tracts with the JHU *WM* atlas [155]. The atlas was nonlinearly registered with *FSL* FNIRT to the *MPRAGE* images and transformed to the *mGRE* space using *FSL FLIRT* [102, 104]. Before evaluation, masks were manually checked and adjusted with ITK-SNAP [257].
In a single scan session, eight *mGRE* data sets were acquired from one subject (male, age = 29) using four different excitation pulses with $\alpha = 30°$ and $\alpha = 85°$ for each pulse. The first pulse was a $2ms$-long Gaussian-pulse with $\sigma = 280\mu s$ ($B_1(t) = e^{-\frac{t}{2\sigma}}$) and the other three were sinc-Hanning-windowed pulses with different $TBP = [2, 2.7, 8]$ and $T_{pulse} = [1ms, 2ms, 4ms]$. $G_{slice} = [10.56, 18.87, 11.05, 15.65]mT/m$ was estimated with the Bloch solver for $\Delta z = 3mm$ and $\alpha = 30°$. Other sequence parameters, as well as B_1 mapping, were as described for in vivo R_2^* mapping. The differences between the pulses were assessed by estimating R_2^* maps with S_4.

5.3 Results

5.3.1 Simulations

Figure 5.2 shows simulation results for sinc-Hanning-windowed excitation pulse with positive and negative G_{slice} polarity for $\alpha = 30°$, and $\alpha = 90°$. It reveals that the polarity has no influence on $|M_{xy}(z)|$ of the slice profile (Figure 5.2A-B), whereas $\varphi_{xy}(z)$ is inverted when flipping polarity (Figure 5.2C-D). Consequently, F_3 depends on the polarity of G_{slice} (Figure 5.2E-F), an effect which is stronger pronounced for $\alpha = 90°$.
The sensitivities of the model parameters $\varphi_{xy}(z)$, B_1^+, λ and TR/T_1 are illustrated in Figure 5.3. When neglecting $\varphi_{xy}(z)$ in Figure 5.3A, the *RMSE* substantially increases for $\alpha > 40°$ with larger *RMSE* for negative G_{slice}. For $\alpha = 90°$, the *RMSE* is 5.5% for negative polarity and 4.5% for positive polarity, respectively.
The sensitivity to B_1^+ variations in Figure 5.3B strongly depends on the nominal flip angle

α. For $\alpha = 30°$, the *RMSE* was below 0.5% for all simulated values of ξ ($\alpha_{effective} = \alpha\xi$) with a moderate increase for $\alpha = 60°$ to 1% for $\xi = 1.3$. With 2.9% the *RMSE* was three times higher for $\alpha = 90°$. The influence of λ on the signal is relatively small compared with B_1^+ and $\varphi_{xy}(z)$ with an *RMSE* of 0.8% for a strong g_z with 500 $\mu T/m$ and minimal dependency on α (Figure 5.3C).

The simulated error due to neglecting T_1 for different TR/T_1 in Figure 5.3D shows an exponential decrease of the *RMSE* with increasing TR/T_1 for all simulated flip angles. For all TR/T_1 ratios, the highest *RMSE* was estimated when using the Ernst angle α_{Ernst} and declines non-linearly for $0.8\alpha_{Ernst}$ and $0.6\alpha_{Ernst}$. For example, for $TR/T_1 = 1$ the *RMSE* decreases from 2.8% to 1.8% to 1.2% for all simulated flip angles while for $TR/T_1 = 2$ the *RMSE* reduces from 1.2% to 0.8% to 0.5%.

When comparing the simulated errors by neglecting φ_{xy} in Figure 5.3A with T_1 effects in Figure 5.3D, the *RMSE* of φ_{xy} becomes dominant with increasing TR/T_1 ratio. Given that $TR/T_1 > 2$, which results in $\alpha_{Ernst} > 82°$, then the *RMSE* is smaller than 1.2%, whereas the *RMSE* due to neglecting φ_{xy} is at least higher than 3.3% depending on G_{slice} polarity.

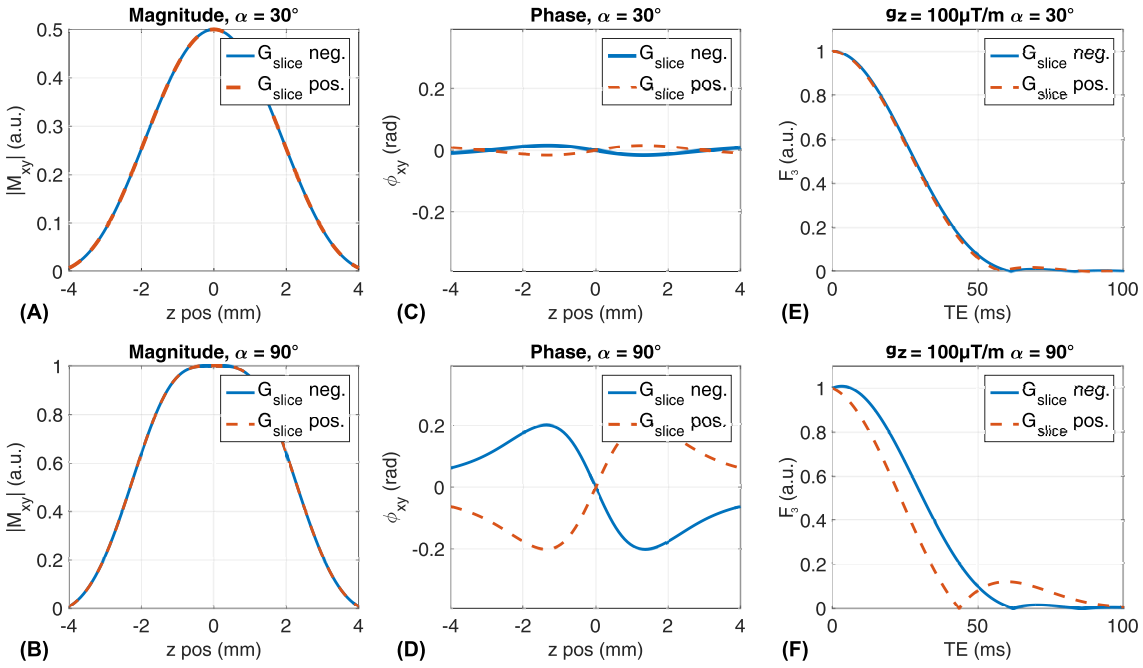

Figure 5.2: Simulation results for magnitude $|M_{xy}|$ (A-B) and phase φ_{xy} (C-D) of the slice profile, and the resulting dephasing F_3 (E-F) with a macroscopic field gradient $g_z = 100\mu T/m$ for a sinc-Hanning-windowed excitation pulse (pulse duration $T_{pulse} = 2ms$, $TBP = 2.7$). For each α (top $\alpha = 30°$, bottom $\alpha = 90°$), simulations were performed with positive (red dotted line) and negative (solid blue line) G_{slice} polarity. There is no difference in the magnitude (A-B) but the mirrored phase for $\alpha = 90°$ (D) causes different F_3 (F).

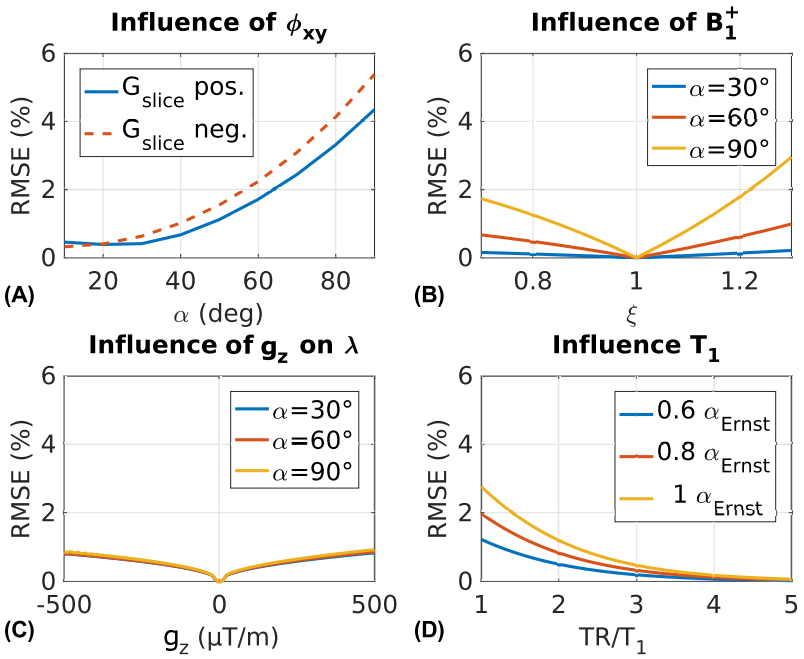

Figure 5.3: Sensitivity analysis of the numerical model parameters. (A) compares the effect of including phase in F_4 versus the magnitude model F_2 for positive and negative G_{slice} polarity and $g_z = 100\mu T/m$. Effects of B_1^+ variations on F_4 are shown in (B) with a macroscopic field gradient $g_z = 100\mu T/m$ and the influence of g_z on the slice encoding described with λ are illustrated in (C). In (D), the *RMSE* for neglecting T_1 for different TR/T_1 ratios is plotted assuming $g_z = 100\mu T/m$. For each TR/T_1, the *RMSE* was estimated between the F_4 and F_{T_1} for α_{Ernst}, $0.8\alpha_{Ernst}$ and $0.6\alpha_{Ernst}$.

5.3.2 Phantom Experiments

R_2^* values estimated with the monoexponential model S_1 are plotted as a function of g_z for $\alpha = 30°$ and $\alpha = 90°$ with positive and negative G_{slice} polarity in Figure 5.4. R_2^* increases proportional with g_z for $\alpha = 30°$ (Figure 5.4A) with up to eight times higher R_2^* values for $g_z = 150\mu T/m$ than for $g_z = 0\mu T/m$. For $\alpha = 30°$, negligibly small differences between the polarity of G_{slice} and the sign of g_z were found, whereas for $\alpha = 90°$ (Figure 5.4B) positive and negative g_z yielded different R_2^* values and a dependency on the polarity of G_{slice}. Moreover, Figure 5.4 shows the normalized averaged signal decay for $|g_z| = 100\mu T/m$ plotted with positive and negative g_z, explaining the difference in estimated R_2^* values. For $\alpha = 90°$ with positive G_{slice} and $g_z > 0$ (blue line), the signal decays faster than for $g_z < 0$ (red) and vice versa when switching G_{slice} polarity.
Figure 5.5 compares R_2^* maps obtained from fits using models S_2, S_3, and S_4 for $\alpha = 30°$ (Figure 5.5A) and $\alpha = 90°$ (Figure 5.5B), each with positive and negative G_{slice} polarity. In addition, the g_z-map and B_1 map are illustrated in Figure 5.5C. While results for $\alpha = 30°$ are comparable for all models, considerable differences for $\alpha = 90°$ between the models and G_{slice} polarity were found. When using only the magnitude $|M_{xy}|$ in model S_2

to estimate R_2^* for $\alpha = 90°$, it was not possible to recover R_2^* without the influence of g_z. R_2^* values for $g_z > 0$ were overestimated for positive G_{slice} and underestimated for $g_z < 0$, and switching to negative G_{slice} polarity inverted the results. Extending the model S_2 by adding φ_{xy} in S_3 yielded better maps, which are less influenced by the G_{slice} polarity. Additionally, including B_1^+ and λ in S_4 substantially improved R_2^* maps, with minimal differences between G_{slice} polarities. Further, estimated R_2^* maps using S_4 with $\alpha = 90°$ are comparable with maps estimated from $\alpha = 30°$ for both G_{slice} polarities.
Figure 5.6 illustrates the effects of neglecting T_1 for signal modeling. Estimated R_2^* maps with S_4 (Figure 5.6A) indicate an overestimation of R_2^*, depending on TR and α in the presence of g_z (Figure 5.6B). For $\alpha = 30°$, increased R_2^* values are observable only up to a TR of 500 ms while for $\alpha = 90°$ these effects extend up to a TR of $1.5s$. These TR values correspond to a TR/T_1 ratio of 0.67 and 2.01 for the estimated $T_1 = 740ms$. The origin for the R_2^* overestimation is shown in (Figure 5.6C), where the averaged measured signal along the slice profile is plotted. Depending on α and TR, the steady-state solution changes causing a modeling error in the presence of g_z. Between different TRs for $\alpha = 30°$, the profiles show less variations compared with $\alpha = 90°$, leading to different signal dephasing for the same g_z. Besides T_1 effects, for $TR > 2s$, SNR benefits can be observed for maps acquired with $\alpha = 90°$ compared with $\alpha = 30°$.

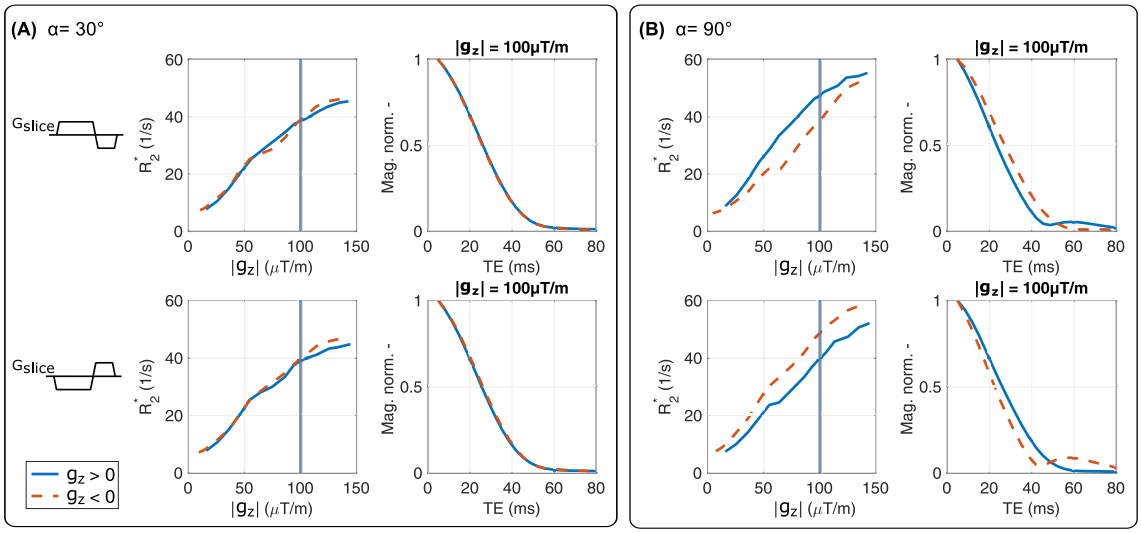

Figure 5.4: Comparison of R_2^* values estimated from the phantom experiments with the mono-exponential model S_1 are plotted as function of g_z for $\alpha = 30°$ (A) and $\alpha = 90°$ (B) with positive and negative slice-selection gradient G_{slice}. Additionally, the averaged normalized signal decay is plotted for $|g_z| = 100\mu T/m$. The dotted red line represents a positive g_z and the solid blue line a negative g_z. For $\alpha = 30°$, no relevant differences between the polarity of G_{slice} and g_z are observed, whereas for $\alpha = 90°$, a flipped G_{slice} polarity substantially affects R_2^*.

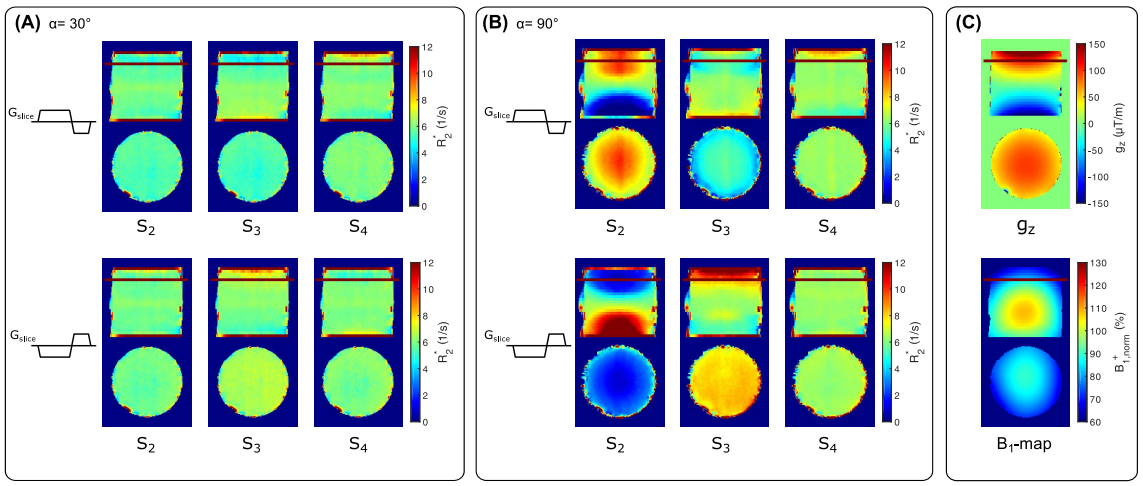

Figure 5.5: Coronal and axial slices of estimated R_2^* maps from the phantom measurements for different signal models (S_2-S_4). Although all correction models yield relatively comparable R_2^* values for $\alpha = 30°$ (A), the high flip angle results for $\alpha = 90°$ (B) highlight the effect of B_1^+ and λ correction. Full modeling with S_4 also eliminates the influence of the polarity of the slice-selection gradient G_{slice} at $\alpha = 90°$. The corresponding g_z maps and B_1 maps are shown in (C).

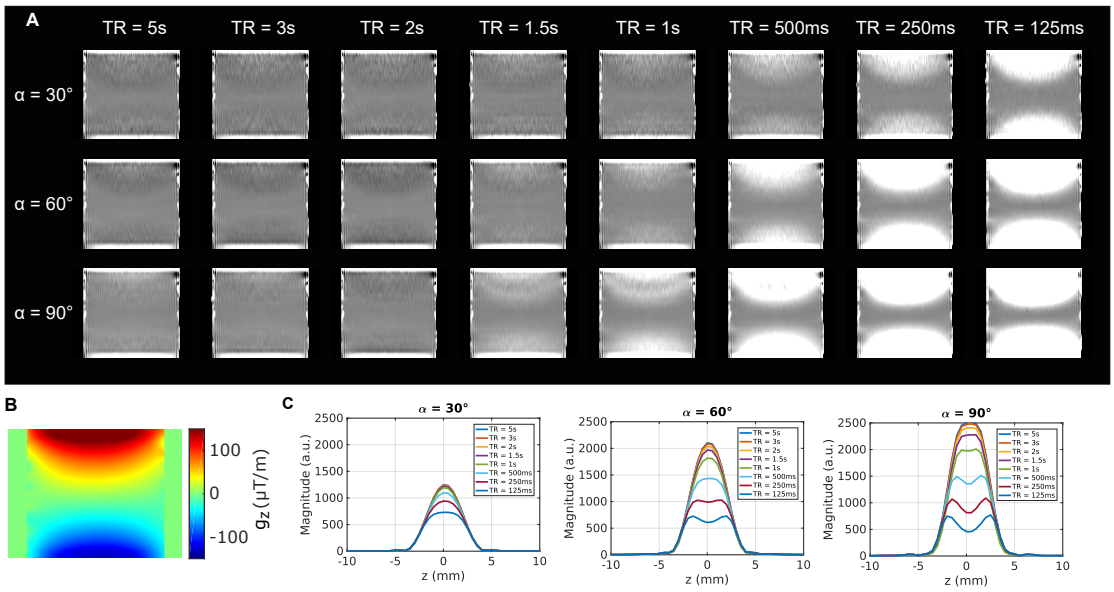

Figure 5.6: Experimental evaluation of TR/T_1 dependency for R_2^* modeling in phantom measurements. Coronal R_2^* maps were estimated using S_4 for different TR and α (A). The minimum TR required for avoiding T_1 effects increases with the magnitude of g_z (B) and α. $T_1 = 740 \pm 86ms$ was estimated with an inversion recovery sequence. In addition, the measured signal along the slice for each α and TR is plotted (C) showing the different steady-state solutions.

5.3.3 In Vivo Experiments

In-vivo results of R_2^* maps obtained with model S_1 and S_4 are illustrated in Figure 5.7 for both G_{slice} polarities. When comparing S_1 (Figure 5.7A-B) with S_4 (Figure 5.7D-E), much higher R_2^* values are observed in maps using S_1 compared with S_4. In addition, the difference map between positive and negative G_{slice} polarity for each model reveals strong variations of R_2^* values with up to $10s^{-1}$ for S_1 in areas with strong g_z (Figure 5.7C). In contrast, maps estimated with S_4 substantially suppressed the impact of G_{slice} polarity with difference values below 1 s^{-1} (Figure 5.7F).
In Table 5.1 the regional evaluation of R_2^* values with the corresponding mean $|g_z|$ across all subjects is presented. Compared with the other models, highest R_2^* values were obtained with S_1 in all anatomical regions. In addition, the difference between G_{slice} polarities increased with the mean $|g_z|$ value in each region for S_1. For example, in the caudate nucleus, where the smallest $|g_z|$ was observed with $20\mu T/m$, the difference between polarities was below $0.1s^{-1}$, whereas in the brainstem it was $7.46s^{-1}$ at a mean $|g_z|$ of $89\mu T/m$. R_2^* values generally decreased when using S_2, but the difference between polarities was slightly increasing compared with S_1. Applying models S_3 and S_4 reduced the discrepancy between G_{slice} polarities to a maximum of $2.01s^{-1}$ and $1.25s^{-1}$ in the brainstem. In all other regions, the difference was much smaller with values below $0.8s^{-1}$. Between models S_3 and S_4, rather small changes could be observed generally.
The difference between R_2^* estimation with S_3 and S_4 is shown in Figure 5.8, pointing out the effect of modeling B_1^+ and λ in S_4. When visually comparing the difference maps in Figure 5.8A and Figure 5.8B, a strong correspondence between the magnitude of g_z (Figure 5.8C) and B_1^+ (Figure 5.8D) can be observed for both G_{slice} polarities.
The R_2^* maps from data acquired with four different excitation pulses and two different flip angles are shown in Figure 5.9. Visually, only minor differences between all maps are observable. Higher SNR can be observed in maps with $\alpha = 85°$ compared with $\alpha = 30°$. Mean regional R_2^* values were in good agreement after applying models S_3 and S_4 (Table 5.1). For example, in global WM, the largest standard deviation of R_2^* between the acquisitions was found for S_1 with $1.59s^{-1}$, due to the different pulses and flip angles. By using S_2, it decreased to $0.82s^{-1}$ and for S_3 and S_4, the estimated values were $0.19s^{-1}$ and $0.2s^{-1}$, respectively.
Figure 5.10 shows representative slices of MWF maps from five subjects obtained with models S_1, S_3, and S_4. It shows that with S_1, in areas with strong g_z, such as in the frontal and temporal lobe, the MWF estimation was not feasible because of the fast signal decay, whereas the proposed approaches allowed a reconstruction in these areas. Between maps with models S_3 and S_4, no considerable differences were found indicating that B_1^+ and λ had a negligible small influence.
As shown in Figure 5.10, the MWF in the genu of the corpus callosum is underestimated with S_1 because of g_z. Using S_3 and S_4 enabled us to recover MWF values in these areas with a median of 12.09 % and 12.66%, respectively. Our MWF results are within the

range of reported values: For the genu of the corpus callosum, Lee et al. [133] reported approximately 12% for their postprocessing approach, and Alonso-Ortiz et al. [2] around 16%. Furthermore, in the body of the corpus callosum the proposed models yielded to an increase of MWF from 3.7% with S_1 to 6.65% and 6.67% for S_3 and S_4, respectively. Interestingly, this analysis demonstrated that rather small $|g_z|$ with around $10\mu T/m$ in the body of the corpus callosum severely effects MWF estimation when using the simple model S_1. Table 5.3 summarizes the median MWF values in all 10 subjects in different WM regions for models S_1, S_3, and S_4.

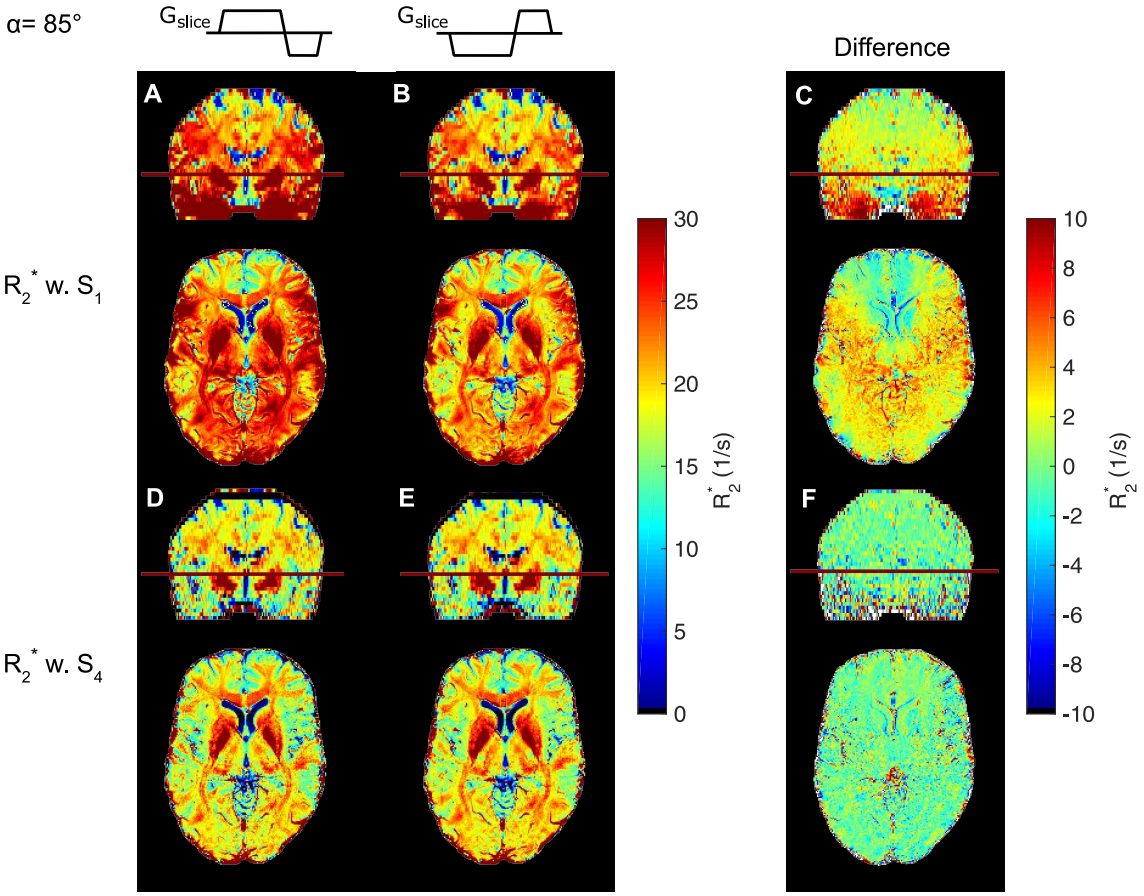

Figure 5.7: Comparison of coronal and axial R_2^* maps obtained from monoexponential model S_1 (A-B) with maps from the proposed numerical model S_4 (D-E) for positive and negative slice-selection gradient G_{slice}. The difference map between G_{slice} polarities for each model is illustrated in (C) and (F). The S_1 model shows R_2^* overestimation and substantial impact of the G_{slice} polarity (C), which were mitigated using S_4 (F).

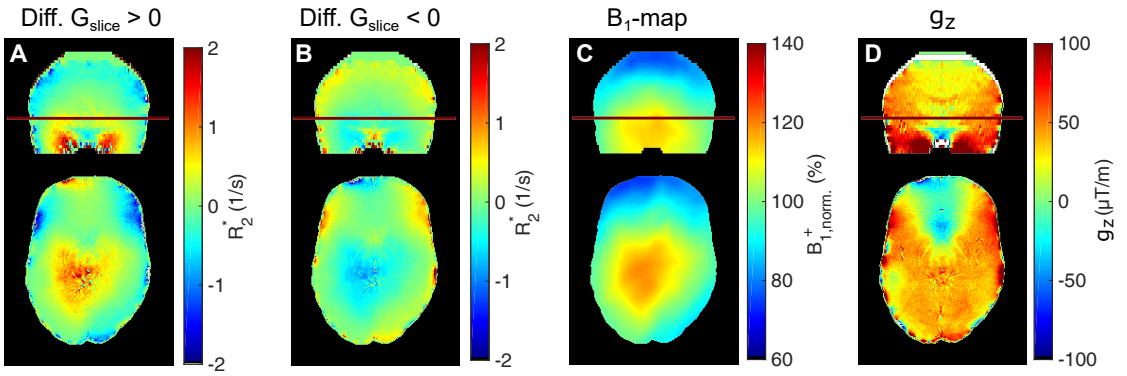

Figure 5.8: Difference between R_2^* maps estimated with S_4 (which includes B_1^+ and λ variations) and S_3 for positive (A) and negative slice-selection gradient G_{slice} (B). Coronal (upper row) and axial (lower row) views are shown. Additionally, the B_1 map (C) and g_z map (D) are illustrated. Depending on G_{slice} polarity, R_2^* varies in areas with higher B_1^+ and g_z variations.

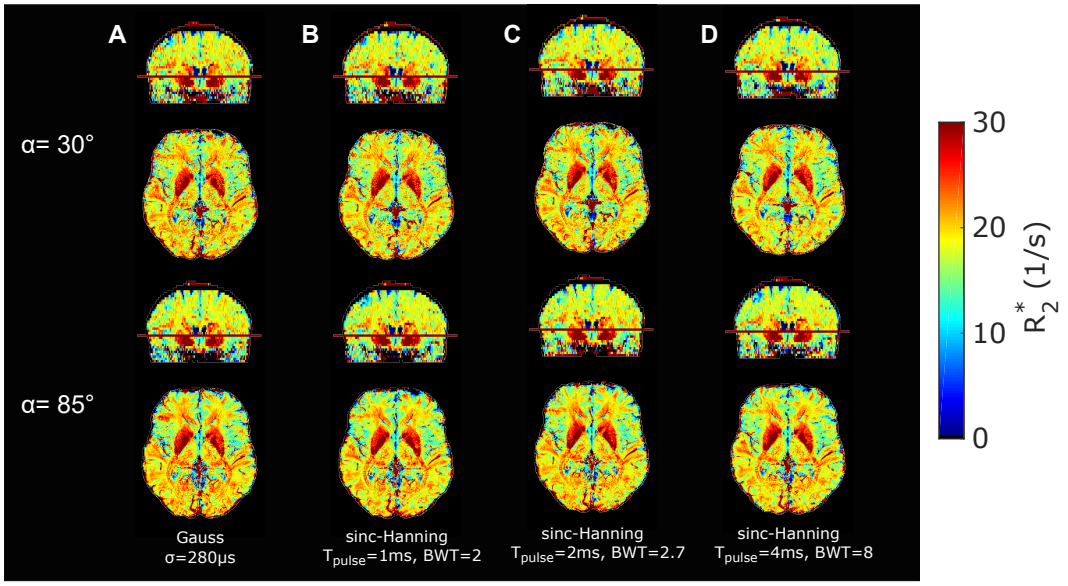

Figure 5.9: R_2^* maps estimated with model S_4 from *mGRE* data acquired with four different excitation pulses (A-D) for $\alpha = 30°$ (top row) and $\alpha = 85°$ (bottom row). Regional evaluation of R_2^* can be found in Table 5.1.

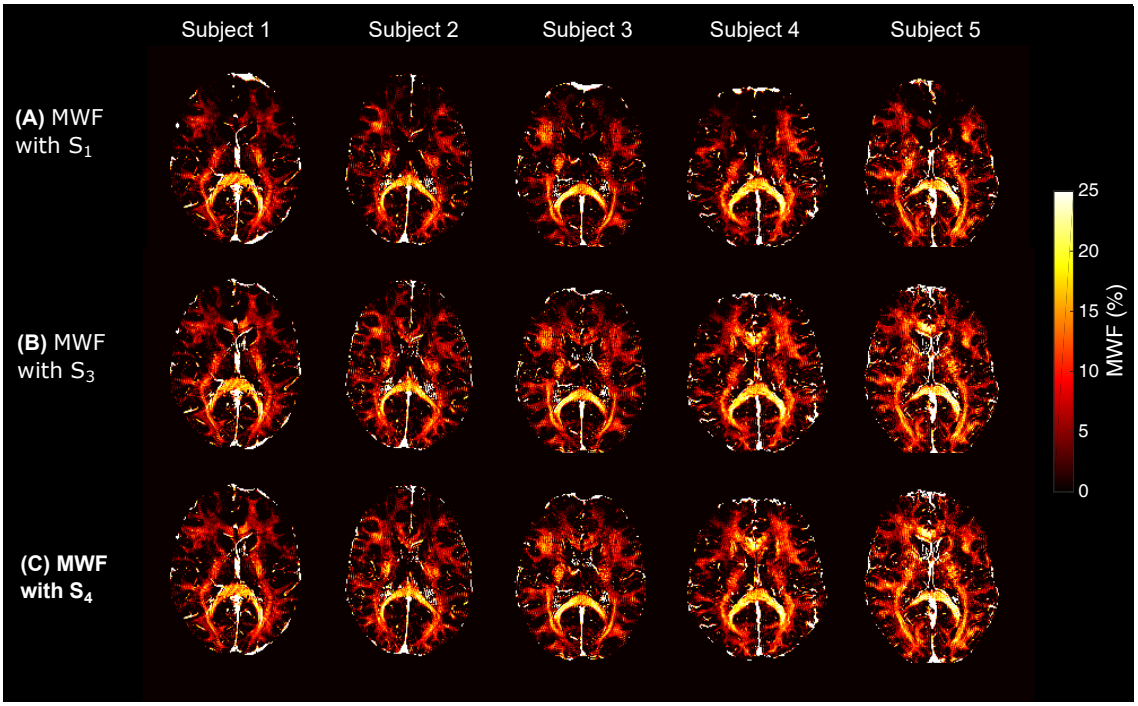

Figure 5.10: Representative MWF maps from five subjects obtained by using models S_1 (A), S_3 (B), and S_4 (C). The proposed models S_3 and S_4 allow to recover MWF values in areas strongly affected by the field gradient g_z (e.g., in frontal areas).

Table 5.1: R_2^* values (s^{-1}) from models S_1 to S_4 in different brain regions for 10 subjects with the corresponding $|g_z|$ values for positive and negative G_{slice}. R_2^* and $|g_z|$ values are shown as mean (standard deviation).

Region	G_{slice}	S_1		S_2		S_3		S_4		$\lvert g_z\rvert(\mu T/m)$	
Global WM	pos.	26.34	(1.16)	21.11	(0.61)	20.10	(0.58)	19.63	(0.62)	43.06	(8.81)
	neg.	23.72	(0.97)	18.17	(0.58)	19.89	(0.54)	20.17	(0.50)	43.68	(8.40)
Caudate Nucleus	pos.	23.36	(1.53)	21.46	(1.47)	21.81	(1.40)	21.82	(1.40)	20.47	(3.57)
	neg.	23.41	(1.61)	21.58	(1.32)	21.58	(1.28)	21.52	(1.27)	20.42	(3.22)
Pallidum	pos.	39.83	(2.78)	36.56	(2.58)	35.60	(2.65)	34.85	(2.71)	34.38	(8.75)
	neg.	36.86	(2.75)	33.50	(3.08)	35.07	(2.85)	35.61	(2.81)	34.03	(8.73)
Putamen	pos.	29.11	(2.14)	25.78	(1.70)	25.02	(1.76)	24.49	(1.80)	32.69	(5.84)
	neg.	26.97	(2.06)	23.52	(2.05)	24.91	(1.90)	25.28	(1.87)	32.90	(5.87)
Thalamus	pos.	25.84	(1.80)	22.34	(0.64)	21.33	(0.62)	20.34	(0.84)	33.65	(8.75)
	neg.	22.61	(0.97)	18.80	(1.24)	20.50	(0.87)	21.22	(0.74)	34.41	(8.83)
Brainstem	pos.	35.15	(7.97)	20.34	(2.07)	17.58	(1.77)	15.10	(1.60)	88.61	(35.73)
	neg.	27.70	(6.99)	11.21	(1.96)	15.08	(1.53)	16.45	(1.55)	89.90	(34.79)

Table 5.2: Influence of pulse shape and flip angle for modeling R_2^*. R_2^* values (s^{-1}) were estimated with models S_1 to S_4 from $mGRE$ data acquired with four different pulses and $\alpha = 30°$ and $\alpha = 85°$. It shows a flip angle and pulse shape dependency for S_1 in all regions. By applying S_2, differences decrease, but R_2^* values remain larger for $\alpha = 85°$ than for $\alpha = 30°$. With S_3 and S_4 the flip angle dependency can be improved, leading to minimal differences of R_2^* between the pulses. In S_4, B_1^+ and λ have a small additional effect on R_2^* estimation, compared with S_3.

		Global WM							
Pulse	α	S_1		S_2		S_3		S_4	
Gauss	30°	26.62	(9.00)	19.94	(4.26)	19.85	(4.29)	19.85	(4.28)
	85°	28.41	(10.07)	21.46	(4.44)	19.80	(4.03)	19.27	(4.26)
sinc-Hanning BWT=2	30°	25.46	(8.25)	19.50	(4.07)	19.71	(4.07)	19.69	(4.07)
	85°	27.33	(9.46)	21.12	(4.64)	20.07	(4.18)	19.59	(4.28)
sinc-hanning BWT=2.7	30°	25.28	(8.55)	19.47	(4.03)	19.61	(4.03)	19.61	(4.03)
	85°	26.94	(8.74)	20.84	(4.19)	19.71	(3.90)	19.26	(4.03)
sinc-Hanning BWT=8	30°	23.40	(6.64)	19.46	(3.84)	19.43	(3.85)	19.41	(3.84)
	85°	24.89	(7.06)	20.83	(4.02)	19.81	(3.76)	19.49	(3.83)
Mean (standrad dev.)		26.04	(1.59)	20.33	(0.82)	19.75	(0.19)	19.52	(0.20)
		Caudate Nucelus							
Pulse	α	S_1		S_2		S_3		S_4	
Gauss	30°	25.32	(3.76)	23.13	(3.38)	23.15	(3.36)	23.14	(3.37)
	85°	25.70	(3.95)	23.42	(3.58)	23.49	(3.18)	23.41	(3.15)
sinc-Hanning TBP=2	30°	24.87	(3.32)	22.95	(3.18)	23.07	(3.14)	23.07	(3.14)
	85°	25.24	(3.90)	23.18	(3.67)	23.42	(3.30)	23.36	(3.27)
sinc-hanning TBP=2.7	30°	24.75	(3.41)	22.89	(3.32)	23.00	(3.28)	23.00	(3.28)
	85°	25.30	(3.72)	23.37	(3.53)	23.53	(3.17)	23.46	(3.15)
sinc-Hanning TBP=8	30°	24.14	(2.94)	22.98	(2.89)	23.00	(2.88)	22.99	(2.88)
	85°	24.38	(3.31)	23.12	(3.42)	23.30	(3.04)	23.28	(3.03)
Mean (standrad dev.)		24.96	(0.52)	23.13	(0.19)	23.24	(0.22)	23.21	(0.19)
		Thalamus							
Pulse	α	S_1		S_2		S_3		S_4	
Gauss	30°	26.95	(3.85)	19.70	(4.37)	19.58	(4.40)	19.50	(4.41)
	85°	29.35	(4.47)	22.31	(4.15)	20.22	(4.33)	18.63	(4.60)
sinc-Hanning TBP=2	30°	25.64	(3.61)	19.03	(4.19)	19.29	(4.18)	19.19	(4.19)
	85°	28.06	(4.16)	21.42	(4.05)	20.00	(4.19)	18.57	(4.42)
sinc-hanning TBP=2.7	30°	25.50	(3.63)	19.08	(4.20)	19.24	(4.20)	19.17	(4.20)
	85°	28.03	(4.19)	21.54	(4.16)	20.02	(4.31)	18.62	(4.53)
sinc-Hanning TBP=8	30°	23.17	(3.43)	18.89	(3.96)	18.83	(3.96)	18.75	(3.96)
	85°	25.51	(3.90)	21.35	(4.13)	19.94	(4.23)	18.91	(4.36)
Mean (standrad dev.)		26.53	(1.96)	20.41	(1.38)	19.64	(0.49)	18.92	(0.34)
		Putamen							
Pulse	α	S_1		S_2		S_3		S_4	
Gauss	30°	30.90	(4.84)	25.27	(4.22)	25.19	(4.22)	25.16	(4.22)
	85°	32.49	(5.51)	26.98	(4.24)	25.44	(3.97)	24.74	(3.91)
sinc-Hanning TBP=2	30°	29.98	(4.56)	24.82	(4.08)	25.05	(4.07)	25.01	(4.07)
	85°	31.85	(5.01)	26.62	(4.06)	25.59	(4.03)	24.94	(4.03)
sinc-hanning TBP=2.7	30°	29.71	(4.39)	24.69	(4.04)	24.84	(4.03)	24.81	(4.02)
	85°	31.39	(5.10)	26.34	(4.10)	25.23	(3.89)	24.61	(3.82)
sinc-Hanning TBP=8	30°	27.91	(4.02)	24.55	(3.88)	24.50	(3.87)	24.46	(3.87)
	85°	29.49	(4.56)	26.21	(4.12)	25.14	(3.90)	24.66	(3.84)
Mean (standrad dev.)		30.46	(1.48)	25.69	(0.96)	25.12	(0.34)	24.80	(0.23)

Table 5.3: *MWF* values (%) with models S_1, S_3, and S_4 in different *WM* regions for 10 subjects. *MWF* values are shown as median (IQR). In addition, corresponding $|g_z|$ values are listed as mean (standard deviation).

Region	S1	S3	S4	$g_z(\mu T/m)$
Genu corpus callosum	4.37 (3.93)	12.09 (5.91)	12.66 (5.98)	54.53 (10.84)
Body corpus callosum	3.70 (3.15)	6.65 (1.90)	6.67 (2.00)	9.81 (3.41)
Splenium corpus callosum	14.10 (2.32)	14.23 (2.24)	14.03 (2.06)	4.93 (1.41)
Superior corona radiata	7.06 (2.04)	8.20 (1.72)	8.22 (1.69)	5.28 (1.96)
Posterior corona radiata	7.14 (1.41)	7.34 (1.55)	7.34 (1.53)	3.28 (1.25)
Superior longitudinal fasciculus	8.71 (1.19)	8.94 (0.91)	8.93 (0.92)	4.58 (1.10)

5.3.3.1 Navigator Echo

Figure 5.11 shows two examples *MWF* maps reconstructed with and without the phase of navigator. The phase has substantial influence on the quality of the estimated *MWF* maps.

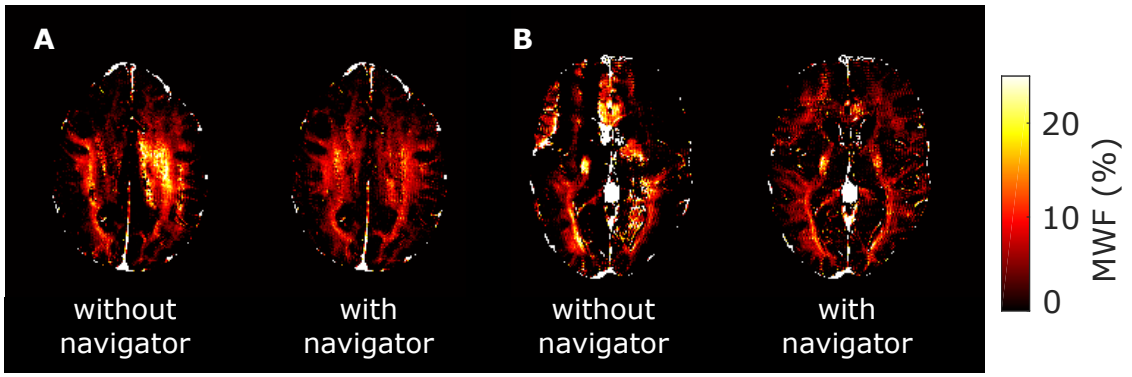

Figure 5.11: Two examples, (A) and (B), of obtained *MWF* maps without and with the phase of the navigator echo.

5.4 Discussion

In this work we have introduced a numerical model for the signal dephasing of 2D *mGRE* sequences for arbitrary excitation pulses in the presence of a macroscopic field gradient g_z. In contrast to existing analytical solutions, our model is based on solving the Bloch equations numerically, which allows to estimate signal dephasing for any given flip angle α. We have shown that it is indispensable to consider the phase along the slice profile φ_{xy} and the polarity of the slice-selection gradient G_{slice} for describing the signal dephasing for higher α. In our experiments, the threshold was approximately 60°, but this may also vary with the *RF* pulse shape.

Compared to existing models [2, 11, 39, 59, 97, 129, 178], which include the slice profile and assume linear varying macroscopic field variations, with the proposed model it is possible to explain different signal decays for different signs of g_z observed when using larger flip angles. As illustrated in Figure 5.2, this mismatch is explained by the phase variation φ_{xy} along the slice profile causing either a faster dephasing or a short period of rephasing followed by dephasing. Consequently, depending on the pulse shape and effective flip angle, the polarity of the gradient G_{slice} must be included for modeling, as switching polarity inverts φ_{xy} and thus signal dephasing.

In addition to the polarity dependency of G_{slice}, the effects of B_1^+ variations and scaling of the slice profile with λ have been investigated in model S_4. However, changes of R_2^* due to B_1^+ and λ were relatively small compared with S_3 (Table 5.1). Evaluation has been performed under assumption that with an ideal model the estimated R_2^* map should be

independent of G_{slice} polarity. For the models S_1 and S_2, strong differences between G_{slice} polarities were found, primarily due to φ_{xy} and by using S_3 it was substantially reduced. However, the main challenge for validation of the models was that, in vivo, no ground truth was available.

Another important aspect is the assumption that TR for a given α is sufficiently long to avoid T_1 influence in the presence of g_z. The experimental results in Figure 5.6A are in accordance with simulation results in Figure 5.3D, where the error decreases with TR/T_1 and the minimum TR/T_1 required enlarges with α. To gain SNR, it is desirable to use α_{Ernst}, but care should be taken on potential errors due to T_1 and B_1^+. By increasing TR/T_1, both α_{Ernst} and the overall SNR increase; however, the errors due to B_1^+ magnified. For example, as illustrated in Figure 5.3, when $TR/T_1 = 2$ the error when neglecting T_1 is about 1.2% for $\alpha = \alpha_{Ernst} = 77°$. By comparing errors caused by B_1^+ variation, a deviation of $\xi = 1.15$ leads to errors in a similar range. Thus, without knowing T_1 it is not possible to separate these effects, but it can be adjusted by the RF pulse shape. For instance, to estimate R_2^* more accurately, longer RF pulses can be used to obtain a slice profile closer to the ideal, rectangular shape. This would have the advantage that signal dephasing is influenced less by B_1^+ and TR/T_1, but it would lead to stronger φ_{xy} variations and zero crossings because of the sinc-shaped signal decay in the presence of g_z. However, for MWF estimation very short pulses are needed, which will be more sensitive to these factors. Optimization of the RF pulses for specific applications was beyond of the scope of this work, but different pulses and their effects can be included and studied with the provided framework.

When comparing different modeling approaches, we can distinguish between models that fit parameters of $F(t)$ from the signal decay [59, 254] and models that use information from the pulse and field map to calculate $F(t)$ [11, 97, 178]. Approaches fitting $F(t)$ are more flexible in terms of model deviations from the ideal slice profile. For example, the sinc function used in the model approach by Fernandez-Seara and Wehrli [59] is well suited to model a variety of signal decays observed with different excitation pulses. Similarly, when modeling the macroscopic field as a quadratic function, the effects of non-ideal slice profile are inherently compensated for [254]. However, in these models, the parameter estimation is often challenging because of the multiplication of $F(t)$ with $S_{tissue}(t)$, thereby requiring the acquisition of many echoes. In contrast, with the analytical solution or our proposed numerical approach for $F(t)$, only the parameters of the tissue model S_{tissue} need to be estimated. Thus, if the properties of the RF pulse are available, a detailed description of $F(t)$ is possible, favoring a closed or numerical solution. To select an appropriate model for a certain RF pulse and flip angle, the provided framework can be used to evaluate the expected error of different modeling approaches. If φ_{xy} might be neglected for a specific RF pulse and flip angle, then an analytic solution yields a faster solution of $F(t)$.

This work has similar limitations as other related postprocessing approaches [2, 11, 39, 59, 94, 97, 97, 178]. The assumption of a linear varying magnetic field in slice direction might not hold in some areas with large susceptibility changes, which is especially pro-

nounced at higher field strengths. However, as we have solved the dephasing along the slice direction by numerical integration, the model can be easily adapted to describe the dephasing also for a quadratic varying magnetic field. Furthermore, in-plane dephasing effects are neglected. In 2D acquisitions the slice thickness is usually much larger than the in-plane resolution, but this might reduce accuracy in areas where the macroscopic in-plane field variations are high. A possible solution to account for in-plane dephasing could be to calculate the *VSF* in-plane as proposed by Yablonskiy et al. [250] and multiply the result with F_3 or F_4, respectively. Given that g_z is rather strong and that the signal dephasing is mainly driven by g_z, a reliable parameter estimation is difficult to achieve due to the fast signal decay. To overcome this issue, for *MWF* and R_2^* it has been shown that z-shim gradients between echoes can improve maps by rephasing the signal with appropriated compensation gradients [81, 128]. Therefore, future work will focus on extending our model by including the moment of the z-shim gradients in the modeling to describe the signal dephasing accordingly for every echo.
In addition to variations of the macroscopic field, variation of the phase offset φ_0 at $TE = 0$ could potentially influence signal dephasing. Contributions to φ_0 in phased array coils can be divided into receive coil-dependent (B_1^-) and receive coil-independent (e.g., B_1^+ phase) [186]. To reconstruct the navigator corrected raw data, a multi-echo approach was used to combine the individual coil data [145]. In this approach, for each coil, images from all echoes are multiplied with the complex conjugate of the first echo, which removes inherently all components of φ_0 of the coil combined data. The development of the proposed models pointed out that the use of navigator echoes is highly recommended to compensate for phase errors from physiologically induced B_0 fluctuations. As illustrated in Figure 5.11, depending on the subject's reconstruction of parameter maps, not having the navigator echoes caused similar artifacts, as reported by Nam et al. [161]. If variations of φ_0 should be included for example a ROEMER [187] or SENSE [179] reconstruction could be applied.
The scan time of the here proposed applications is about 6 minutes for R_2^* maps and 12 minutes for *MWF* maps. This is clinical acceptable for whole brain investigations, but further investigations will also focus on combination with accelerated imaging methods such as 2D controlled aliasing in volumetric parallel imaging (CAIPIRINHA) [21].

5.5 Conclusion

Proper modeling of the signal dephasing in the presence of g_z for larger flip angles requires the consideration of $|M_{xy}|$ and φ_{xy} with correct G_{slice} polarity. Furthermore, B_1^+ and λ variations can potentially lead to a bias in the estimated model parameters, depending on the excitation pulse. Consequently, the proposed model allows to minimize effects of g_z, which is highly relevant for accurate R_2^* and *MWF* mapping of the entire brain based on 2D *mGRE*.

6 2D versus 3D Gradient-Echo Sequences

Contents

6.1 Introduction

The main sequence differences between 2D and 3D acquisitions in *MRI* are the *RF* pulse, which excites a volume instead of slice, and the second phase encoding gradient for encoding the volume. There are two basic types of pulses, the non-selective *RF* excitation and the slab-selective *RF* excitation. The slab-selective excitation restricts the excited volume by applying an *RF* pulse with a small slice-selection gradient G_{slice}. The name slab refers to the excited volume. Slab-selective excitation brings the advantage that the excited volume is reduced and consequently wrap-around artifacts outside the *FOV* are minimized. In contrast to that, non-selective excitation *RF* pulses excite the whole volume by applying a short hard-pulse.
In terms of slice thickness, 3D acquisitions allow acquiring much thinner slices compared with 2D acquisitions. In 2D, the slice-thickness results from the bandwidth of the *RF* excitation pulse Δf and the amplitude of the slice selection gradient G_{slice} (Equation 4.2). Hence, increasing G_{slice} gives thinner slices, but this is limited by the gradient system. Another option is to use longer *RF* pulses to decrease Δf. In contrast to 2D, the slice thickness in 3D acquisitions is given by:

$$\Delta z_{3D} = \frac{1}{N_{phase,2}\Delta k_z} \tag{6.1}$$

Therefore, Δz_{3D} decreases by increasing the number of phase encoding steps $N_{phase,2}$, or by decreasing the k-space step size Δk_z.
The acquisition time TA results for 2D acquisitions from the number of phase encoding

steps $N_{phase,1}$ times the number of slices N_{slices} and the TR ($TA_{2D} = N_{phase,1}N_{slices}TR$). In 3D acquisitions, N_{slices} is replaced by the $N_{phase,2}$ ($TA_{3D} = N_{phase,1}N_{phase,2}TR$).
In terms of SNR efficiency, 3D acquisitions are superior to 2D by the factor of $\sqrt{N}_{phase,2}$ if we assume that the same voxel volume and TR is used [14].
However, in 2D measurements, we can increase TR and this allows to acquire a single k-space line of several slices within TR. If TR is chosen long enough, a k-space can be be measured for each slice. This acquisition scheme is referred to as multi-slice or interleaved slice acquisition. Compared with 3D acquisitions with short TR, the longer TR enables using larger α to increase the signal.
In general, the SNR for 2D and 3D acquisitions is proportional to [14]:

$$\begin{aligned} SNR_{2D} &\propto S_{0,2D}(TR_{2D}/T_1, \alpha_{2D})\Delta x\Delta y\Delta z\sqrt{N_{phase,1}NexT_{acq}}, \\ SNR_{3D} &\propto S_{0,3D}(TR_{3D}/T_1, \alpha_{3D})\Delta x\Delta y\Delta z\sqrt{N_{phase,1}N_{phase,2}NexT_{acq}}, \end{aligned} \tag{6.2}$$

where Δx, Δy, and Δz are the voxel dimensions in all three spatial directions, $N_{phase,1}$ and $N_{phase,2}$ the number of phase encoding steps, T_{acq} the acquisition time, and Nex the number of averages. T_{acq} is the time during the readout. $S_{0,2D}$ and $S_{0,3D}$ describe the steady-state signal for the spoiled GRE sequences, which depend on the ratio TR/T_1 and α. Using the steady-state equation for the 3D and 2D acquisition and assuming equal voxel size, N_{phase_1}, Nex, and T_{acq}, the SNR ratio is given by [14]:

$$\begin{aligned} \frac{SNR_{3D}}{SNR_{2D}} &= \frac{S_{0,3D}}{S_{0,2D}}\sqrt{N_{phase,2}} \\ &= \frac{(1-\exp(-TR_{3D}/T_1))\sin\alpha_{3D})(1-\exp(-TR_{2D}/T_1))\cos_{2D})}{(1-\exp(-TR_{2D}/T_1))\sin\alpha_{2D})(1-\exp(-TR_{3D}/T_1))\cos\alpha_{3D})}\sqrt{N_{phase,2}}. \end{aligned} \tag{6.3}$$

Therefore, the SNR ratio between 3D over 2D acquisitions is given by $\sqrt{N_{phase}}$ times the ratio $S_{0,3D}$ to $S_{0,2D}$. As TR_{2D} and α_{2D} are usually much larger in an interleaved slice acquisition, the ratio between the signals is < 1. Thus, the smaller ratio counteracts $\sqrt{N_{phase}}$.
Using the Ernst angle, Johnson et al. showed that often a similar or equal SNR efficiency can be achieved between 2D and 3D acquisitions [106].
Apart from the basic properties of 2D and 3D spoiled gradient-echo sequences [14, 25], relatively little attention has been given to the comparison between different signal decays in the presence of macroscopic field variations. In the case of 2D acquisitions, the signal decay results from the shape of the slice profile and the variations of the macroscopic field along the slice [39, 59, 94, 178, 202, 254]. For 3D acquisitions, the signal decay depends on the macroscopic field variations, the k-space trajectory, potential k-space filters, and the number of k-space samples. To describe these effects on signal dephasing, Yablonskiy et al. proposed the VSF [250].
In the following chapter we describe a comparison between 2D and 3D spoiled GRE acquisitions, focusing on signal dephasing and modeling of the signal decay in the presence

of macroscopic field variations. For signal modeling of the 3D data, we applied the *VSF* [250] and for the 2D data we used the signal model developed in this thesis [202]. The methods were evaluated with phantom and in vivo measurements in terms of R_2^* mapping. In addition to the advanced signal models, the R_2^* maps were estimated with a monoexponential signal model without incorporating macroscopic field variations.
This study shows that within the same acquisition time similar results can be achieved with 2D and 3D approaches if an adequate signal model is used.

6.2 Methods

To asses the differences in signal dephasing in the presence of macroscopic field variations for 2D and 3D acquisitions, phantom and in vivo measurements have been performed. Except for TR and α, acquisition parameters between 2D and 3D acquisitions were the same. In the 2D acquisitions, a larger α and longer TR was used because of the interleaved slice acquisition. Thus, both acquisitions had the same voxel size and acquisition time, allowing a reasonable comparison between 2D and 3D. To study the impact of macroscopic field variations on signal dephasing, a monoexponential signal decay model for R_2^* was used. To account for macroscopic field variations, in the 3D acquisitions the *VSF* [250] model and for 2D acquisitions, the signal model of Soellrald et al. was applied [202].

6.2.1 Phantom Measurements

For the phantom measurements, a homogeneous agar phantom was built. This phantom should ideally have a constant R_2^* in the absence of macroscopic field variations. It was made of $5g/L$ agar and, to reduce T_1, the liquid agar was doped with $110\mu mol/L$ Magnevist®before solidification. Imaging was preformed with 3T MR imaging system (Magnetom Prisma, Siemens, Erlangen, Germany) using an 8-channel knee coil. For the 3D acquisitions, the sequence parameters of the $mGRE$ were: $FOV = 128x128x144mm^3$, matrix size $128x128x48$, slab-selctive excitation with flip angle $\alpha = 21°$, $TR = 51ms$, $BW = 500Hz/pixel$, 20 echoes acquired using bipolar acquisition with an echo spacing $\Delta TE = 2.18ms$ starting from the first echo time $TE_1 = 3.5ms$ and a navigator echo at $TE_{Navi} = 48.38ms$. For the 2D acquisitions, a slice-selective sinc-Hanning-windowed RF excitation pulse with a pulse duration $T_{pulse} = 2ms$ and $TBP = 2.7$ was used with $\alpha = 60°$. In total, 48 slices with a slice thickness $\Delta z = 3mm$ were acquired in an interleaved slice acquisition with a TR of $2430ms$. All other parameters were the same as for the 3D acquisitions.

6.2.2 In Vivo Measurements

The head of a male subject (30 years) was scanned with a 2D and 3D $mGRE$ sequence. The sequence parameters for the 3D acquisitions were: $FOV = 224x128x144mm^3$, matrix size $224x128x48$, slab-selective excitation with flip angle $\alpha = 21°$, $TR = 51ms$, $BW = 500Hz/pixel$, 20 echoes acquired with bipolar acquisition with an echo spacing $\Delta TE = 2.22ms$, $TE_1 = 2.87ms$, and a navigator echo at $TE_{Navi} = 48.72ms$. For the 2D acquisitions, the same slice-selective excitation pulse as for the phantom with $\alpha = 60°$ was used. 48 slices with $\Delta z = 3mm$ were acquired with an interleaved slice acquisition using a TR of $2430ms$. The acquisition time for both sequences was $7min$ and $28s$. Besides the $mGRE$ sequences, an anatomical $MPRAGE$ scan with a voxel size of $1mm^3$ was performed.

6.2.3 Data Processing and Evaluation

Physiologically induced phase fluctuations were first corrected in the raw data using the navigator echos. Then the individual coil images were combined. Both steps are described in Section 4.2. Before coil combination, the 3D data was reconstructed in two different ways. First, the raw data was reconstructed without filtering and second, as proposed by Yablonskiy et al. [250], a 3D Hanning filter was applied to reduce Gibb's ringing. In addition, the in vivo data was reconstructed without the navigator echoes to study the impact of physiologically induced fluctuations between 2D and 3D acquisitions. Afterwards, for all acquisitions, the field gradient maps g_x, g_y, and g_z were estimated by calculating the gradient of field map ΔB_0 in all three spatial. To calculate the gradient, the *gradient()* function in MATLAB was used, which is based on finite differences. After the phase unwrapping using PRELUDE [103], the field map was obtained by fitting a linear equation to the first 4 echoes of the unwrapped phase.
Then, for the non-filtered and filtered 3D data, the signal dephasing $F_{3D}(TE, N_{neigh})$ and $F_{3D,filt}(TE, N_{neigh})$ was estimated for a different number of neighbors N_{neigh} with the VSF. For the 2D data, the signal dephasing in the slice-direction F_{2D} was estimated as described for the signal model F_3 in Soellradl et al. [202]. For all three cases, R_2^* maps were estimated by non-linear fitting the following equations to the the reconstructed signal:

$$S_{3D}(TE) = S_0 \exp(-R_2^*\, TE) F_{3D}(TE, N_{neigh}), \tag{6.4}$$

$$S_{3D,filt}(TE) = S_0 \exp(-R_2^*\, TE) F_{3D,filt}(TE, N_{neigh}), \tag{6.5}$$

$$S_{2D}(TE) = S_0 \exp(-R_2^*\, TE) F_{2D}(TE), \tag{6.6}$$

where S_0 describes the signal at $TE = 0$. For each acquisition, the estimated R_2^* values from the different acquisitions were evaluated within global WM and GM masks. The

subcortical *GM* masks were obtained from the *MPRAGE* images using *FSL* FIRST [171] and global *WM* masks were derived from the *MPRAGE* images with SIENAX [201] which is part of *FSL* [200]. Afterwards, the masks were affinely registered to the *mGRE* images using *FSL* FIRST [171].

6.3 Results

6.3.1 Phantom Measurements

Figure 6.1 compares the measured normalized signal decay with the estimated signal dephasing (Figure 6.1A). For the 3D, the 3D filtered, and the 2D data the signal was averaged in two *ROIs* with different field gradient values (Figure 6.1B). The signal decay shows variations depending on the acquisition and magnitude of the field gradients.
The 2D and the filtered 3D data show both a smooth decay, but the filtered data decays much faster than the 2D data. The signal of the non-filtered 3D data decays relatively slow and, depending on the field gradient, the signal decays faster after a certain TE. Further, the signal of the non-filtered 3D shows a signal overshoot at approximately $TE = 20ms$ caused by Gibb's ringing. By applying a Hanning window, the overshoot vanishes, and the signal is smoothed. The filtering further results in a faster signal decay. When comparing the 2D signal with the non-filtered 3D signal, the signal decays smoother but it reaches roughly the same signal amplitude at the last echo (*ROI* 1). The filtered 3D signal decays faster than the non-filtered 3D and the 2D data approximately for $TE > 10ms$.
Besides the signal decay, Figure 6.1A illustrates the averaged estimated dephasing function for the non-filtered 3D (F_{3D}), filtered 3D ($F_{3D,filt}$), and the 2D data (F_{2D}). For the 3D data, the plots show additionally the influence of N_{neigh}. The largest difference in the curves is given for the non-filtered data, whereas for the filtered data no visual difference can be observed.
Figure 6.2 shows obtained R_2^* maps with S_{mono} for the three investigated cases. Similar to the different signal decays in Figure 6.1, different R_2^* maps are observable. For the non-filtered 3D data (Figure 6.2A), local variations are present because of Gibb's ringing. The filter removes these variations in the filtered R_2^* maps, but the R_2^* values are much more affected by the field gradients. For example, in slice 16 the 3D filtered data shows R_2^* values about a factor five larger than for the non-filtered case. When comparing the 3D non-filtered data with the 2D data, a similar overestimation in R_2^* is observed. The reference R_2^* value of the phantom was $6.4s^{-1}$, which was estimated in a *ROI* in the center of the phantom (field gradients are approximately 0).
Figure 6.3 illustrates the estimated R_2^* when including the macroscopic field variations in the signal models. In contrast to a conventional monoexponential signal model, the overestimation of R_2^* (Figure 6.2) can be reduced for all analyzed cases. However, depending on the acquisition type, with and without filtering, and N_{neigh} different R_2^* maps are obtained. To better characterize these differences, Figure 6.4 plots the median of R_2^*

against the field gradient g_z in averaged intervals of $20\mu T/m$. For the non-filtered 3D, R_2^* depends on N_{neigh} with the most homogeneous map obtained with $N_{neigh} = [5, 5, 5]$. Apart from errors caused by the field gradients, in all maps Gibb's ringing related artifacts can be observed. In contrast to that, in the filtered 3D R_2^* maps the ringing is removed. Additionally, the results of the filtered 3D data indicate only a minor dependency on the number of N_{neigh}. From $N_{neigh} = [1, 1, 1]$ to $N_{neigh} = [2, 2, 2]$, an improvement was found in the R_2^* maps (e.g. 6.3B slice 36) whereas from $N_{neigh} = [2, 2, 2]$ to $N_{neigh} = [5, 5, 5]$ no visual difference can be observed. Thus, $N_{neigh} = [2, 2, 2]$ seems to be sufficient to describe the signal dephasing of the filtered data. The visual assessment of R_2^* maps and R_2^* as a function of g_z further reveals that in a large range of field gradient values ($g_z \approx \pm 100\mu T/m$) the original R_2^* value can be recovered (6.4^{-1}). When comparing 2D with the 3D R_2^* maps, a good performance for negative values up $-200\mu T/m$ was found, but an underestimation of R_2 for increasing positive g_z is visible (Figure 6.4).

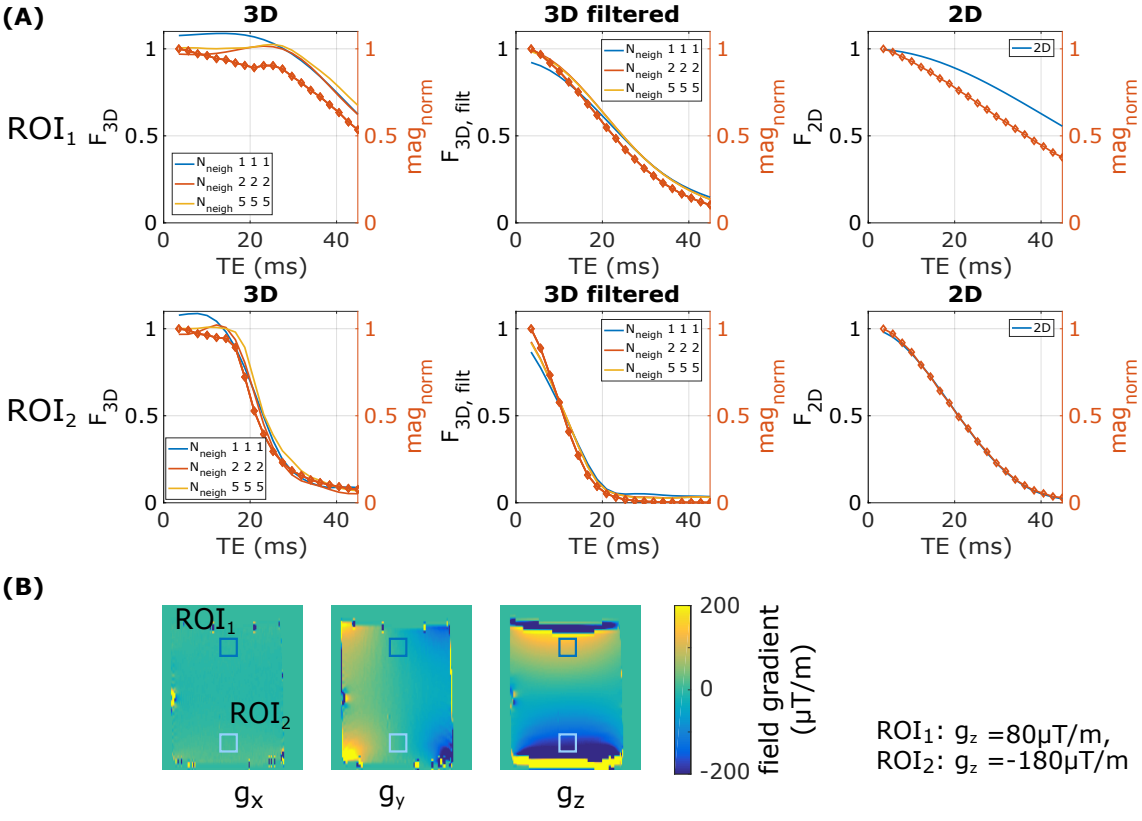

Figure 6.1: Comparison of the measured normalized signal decay mag_{norm} (red line with squares) with the estimated signal dephasing for non-filtered 3D F_{3D}, filtered 3D $F_{3D,filt}$, and 2D data F_{2D}. (A) shows the averaged normalized signal decay and the estimated signal dephasing function from two *ROIs*. For F_{3D} and $F_{3D,filt}$, the dephasing functions were estimated for a different number of neighbors N_{neigh}. (B) shows a coronal slice of the field gradient maps g_x, g_y, and g_z and the two *ROIs* for the evaluation.

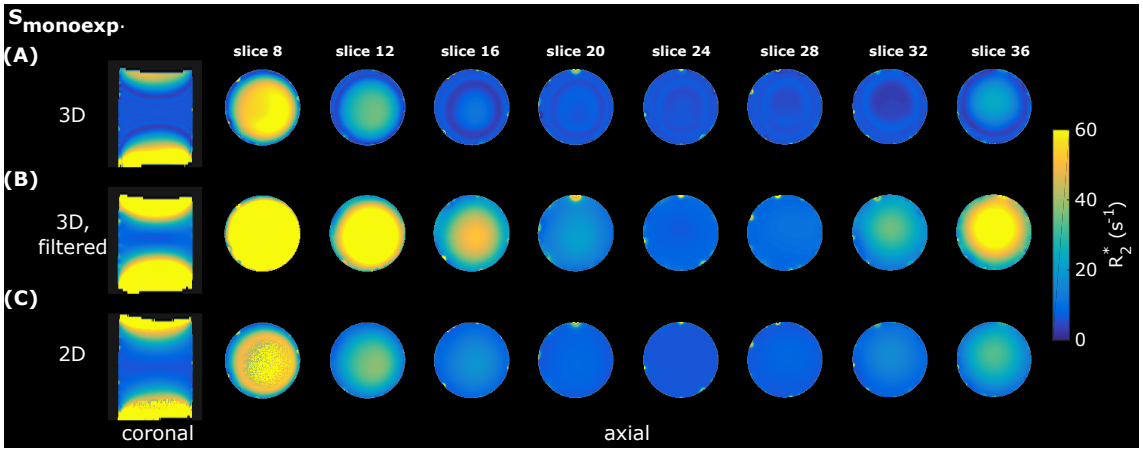

Figure 6.2: R_2^* maps estimated from the non-filtered 3D, filtered 3D, and 2D data using the monoexponential signal model S_{mono} in the homogeneous phantom. Depending on the acquisition, R_2^* is differently overestimated.

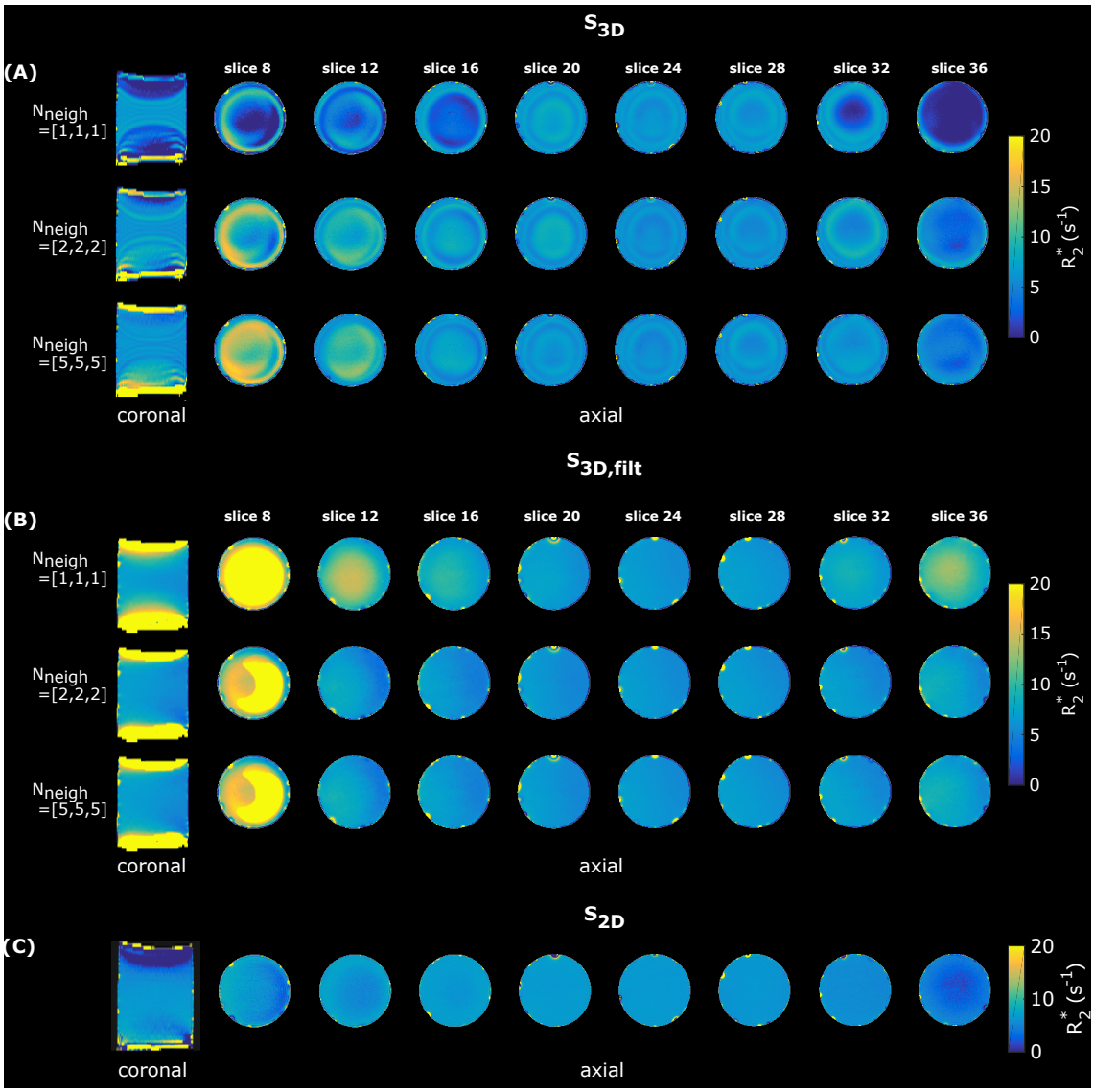

Figure 6.3: Estimated R_2^* maps from the phantom measurements with the signal models that account for macroscopic field gradients in the non-filtered 3D (A), filtered 3D (B), and 2D data (C). For the both 3D data sets, additional results are shown with different numbers of neighbors N_{neigh} for estimating the *VSF*.

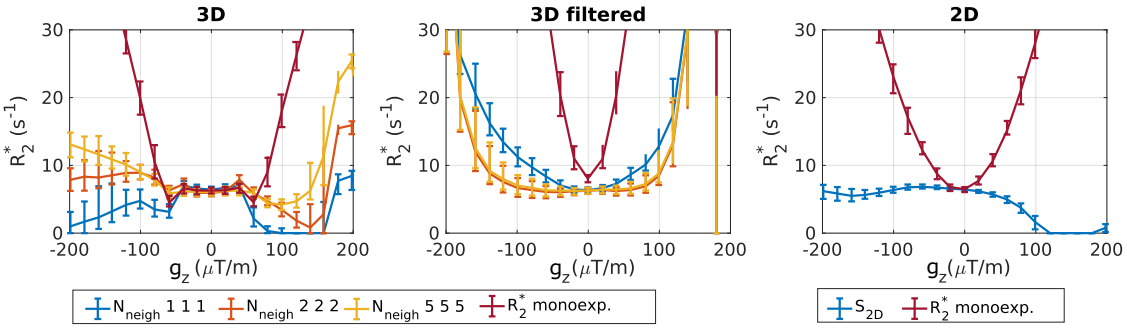

Figure 6.4: R_2^* as a function of the field gradient g_z from the non-filtered 3D, filtered 3D, and 2D data in the phantom. For the 3D data, different numbers of neighbors N_{neigh} were used for calculation of the VSF. Values were averaged in an interval of $20\mu T/m$ from the slice number 5 to 43.

6.3.2 In Vivo Measurements

Figure 6.5 shows R_2^* maps obtained by fitting the non-filtered 3D (Figure 6.5A), the filtered 3D (Figure 6.5B), and the 2D data (Figure 6.5A) to the monoexponential signal model S_{mono}. Additionally, Figure 6.6 illustrates the field gradient map g_z in z-direction. Depending on the data and field gradients strength, R_2^* is differently overestimated. The weakest influence of the field gradients on R_2^* shows the non-filtered 3D data, followed by the 2D data with a slightly larger sensitivity. Compared with the non-filtered 3D and the 2D data, by far the strongest impact of the field gradients on R_2^* is given for the filtered 3D data. Even in relatively homogeneous slices with small field gradients, such as slice 37, the filtering leads to a much larger R_2^*.
The results with the *VSF* model for the 3D data are illustrated in Figure 6.7 for the non-filtered and in Figure 6.8 for the filtered data. In both Figures, the R_2^* maps in (A) were obtained with S_{mono} and these are compared in (B-D) with the R_2^* maps estimated with different numbers of neighbors N_{neigh}. The Figures show that applying the *VSF* yields improved R_2^* maps. In contrast to the filtered data, a dependency on N_{neigh} can be seen for the non-filtered data as indicated by the red arrows in Figure 6.7. A visual comparison of the maps shows sharper edges and more details in the non-filtered maps.
Figure 6.9 compares R_2^* maps estimated from the non-filtered 3D data (Figure 6.9A) with the filtered (Figure 6.9B) and the 2D data (Figure 6.9C). As indicated by the red arrows Figure 6.9, the filtered R_2^* tends to overestimate R_2^* more than the non-filtered data and the non-filtered data underestimates R_2^* in areas with strong field gradients. The 2D R_2^* maps are similar to the non-filtered 3D R_2^* maps, but with a tendency to an R_2^* underestimation.
Table 6.1 lists quantitative R_2^* values of the different approaches. The results are in accordance with the visual observations. When comparing the R_2^* values estimated with S_{mono} and the results from *VSF* of the non-filtered 3D, only minor difference in R_2^* can be observed for different N_{neigh}. By applying the 3D Hanning filter, the R_2^* values obtained with S_{mono} are are nearly doubled. For instance, in the brainstem R_2^* is $18.68s^{-1}$ for the non-filtered 3D and $39.81s^{-1}$ for the filtered 3D data. For the 2D data R_2^* (with S_{mono}) are slightly higher than the non-filtered 3D data, but much smaller than the filtered 3D data. When applying the *VSF* to the filtered data, the overestimation of R_2^* caused by the filtering and the field gradients decreases. Nonetheless, the values in all evaluated regions are elevated compared to the non-filtered 3D data. When comparing the effect of N_{neigh}, it shows that for the non-filtered data $N_{neigh} > [2, 2, 2]$ has an impact on R_2^*, whereas for the non-filtered data only minor changes are observable. Generally, the 2D median values estimated with S_{2D} are in a similar range to the values from the 3D filtered data with $N_{neigh} = [5, 5, 5]$. Interestingly, the interquartile range (IQR) is smaller in all evaluated regions with S_{2D} than for the non-filtered 3D data, suggesting lower R_2^* variations in 2D data set.

Table 6.1: Regional R_2^* (s^{-1}) evaluation (represented as median (IQR)) of non-filtered 3D, the filtered 3D, and the 2D data in one subject.

	data	Global WM	Global GM	Cudate Nucelus	Pallidum	Putamen	Thalamus	Hippocampus	Brainstem
3D	S_{mono}	19,89 (3,47)	17,91 (5,86)	20,59 (3,60)	33,73 (8,76)	23,66 (4,45)	20,17 (4,38)	19,12 (9,80)	18,68 (4,19)
	$N_{neigh} = [1,1,1]$	19,48 (3,39)	16,16 (5,77)	20,33 (4,07)	32,16 (9,31)	23,17 (4,43)	19,71 (4,54)	11,24 (8,35)	16,49 (5,51)
	$N_{neigh} = [2,2,2]$	19,99 (3,46)	17,08 (5,42)	20,07 (3,91)	32,85 (8,43)	23,92 (4,65)	20,73 (4,22)	15,34 (6,57)	19,04 (5,28)
	$N_{neigh} = [5,5,5]$	19,40 (3,30)	16,44 (5,17)	19,88 (3,86)	32,10 (8,34)	23,11 (4,61)	19,85 (4,19)	14,69 (5,85)	17,73 (4,94)
3D filtered	S_{mono}	30,42 (11,71)	31,31 (17,19)	24,49 (5,46)	48,36 (7,84)	35,51 (9,71)	33,74 (6,20)	53,52 (23,05)	39,81 (8,78)
	$N_{neigh} = [1,1,1]$	21,40 (3,13)	19,28 (4,96)	21,39 (3,02)	34,45 (6,83)	24,97 (3,81)	22,20 (3,78)	17,35 (4,89)	20,98 (4,36)
	$N_{neigh} = [2,2,2]$	20,62 (2,85)	18,41 (4,88)	21,14 (2,91)	33,36 (7,15)	24,08 (3,52)	21,19 (3,81)	14,80 (5,83)	19,24 (4,26)
	$N_{neigh} = [5,5,5]$	20,77 (2,88)	18,56 (4,87)	21,19 (2,92)	33,56 (7,17)	24,27 (3,54)	21,39 (3,80)	15,15 (5,81)	19,53 (4,26)
2D	S_{mono}	22,87 (4,78)	21,33 (7,49)	21,66 (3,02)	37,39 (5,37)	27,00 (5,13)	24,36 (3,78)	28,86 (11,91)	24,85 (5,42)
	S_{2D}	19,27 (3,24)	16,74 (4,52)	20,36 (2,70)	32,78 (6,19)	23,03 (3,85)	19,92 (3,52)	14,97 (4,87)	17,81 (15,57)

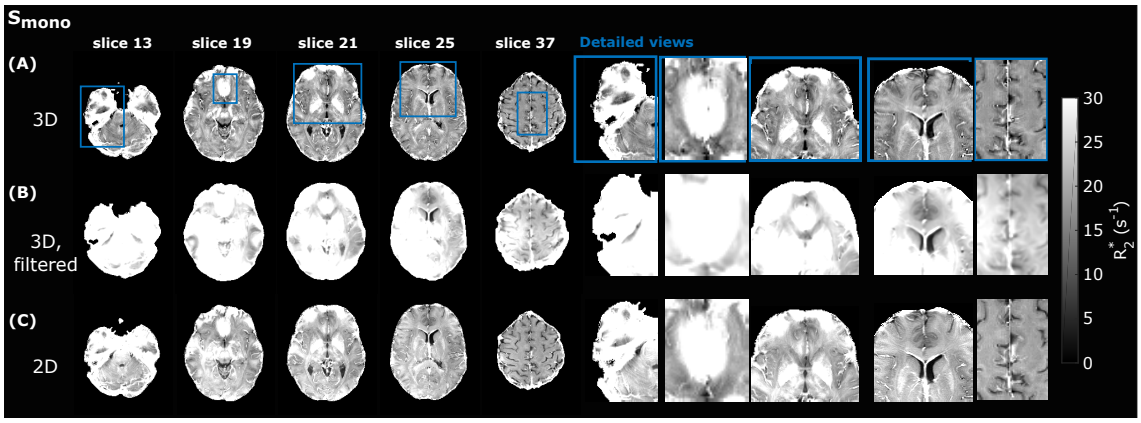

Figure 6.5: R_2 maps estimated with a monoexponential signal model S_{mono} from the non-filtered 3D (A), the filtered 3D (B), and the 2D data (C). All maps show R_2^* overestimation in areas with macroscopic field variations. Compared with the non-filtered 3D and 2D data, the 3D filtered shows the strongest overestimation.

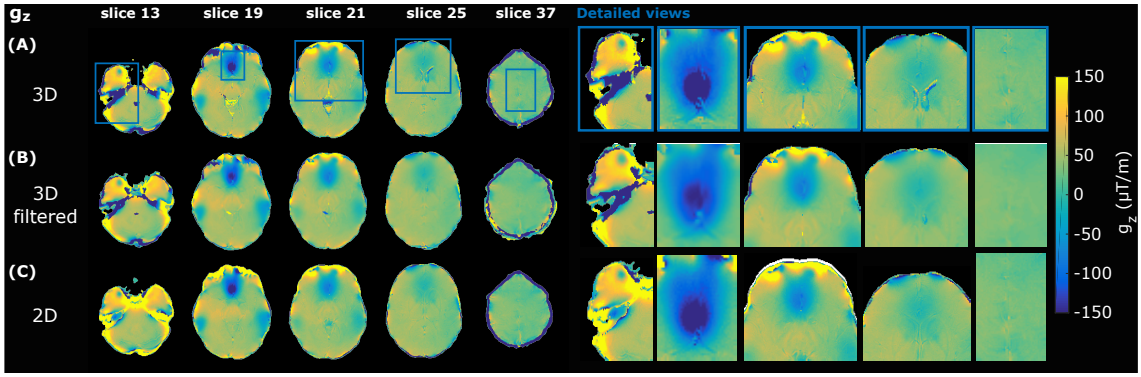

Figure 6.6: Estimated field gradient maps g_z in z-direction from the phase data of the 3D non-filtered, 3D filtered, and 2D data.

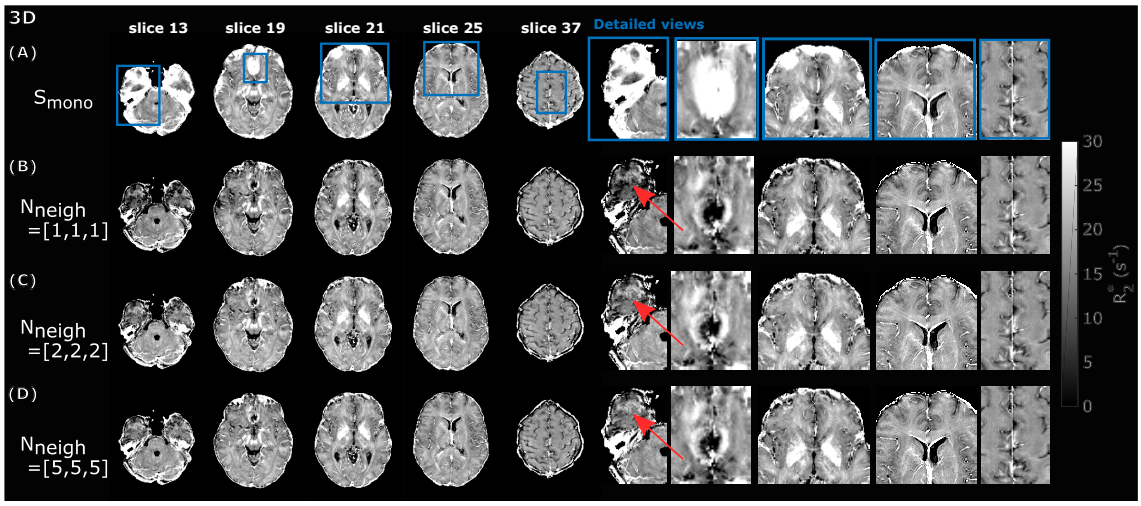

Figure 6.7: Comparison of R_2^* maps estimated with a monoexponential signal model (A) and by applying the *VSF* approach with different numbers of neighbors N_{neigh} for the non-filtered 3D data (B-D). The red arrows indicate differences in R_2^* for different N_{neigh}.

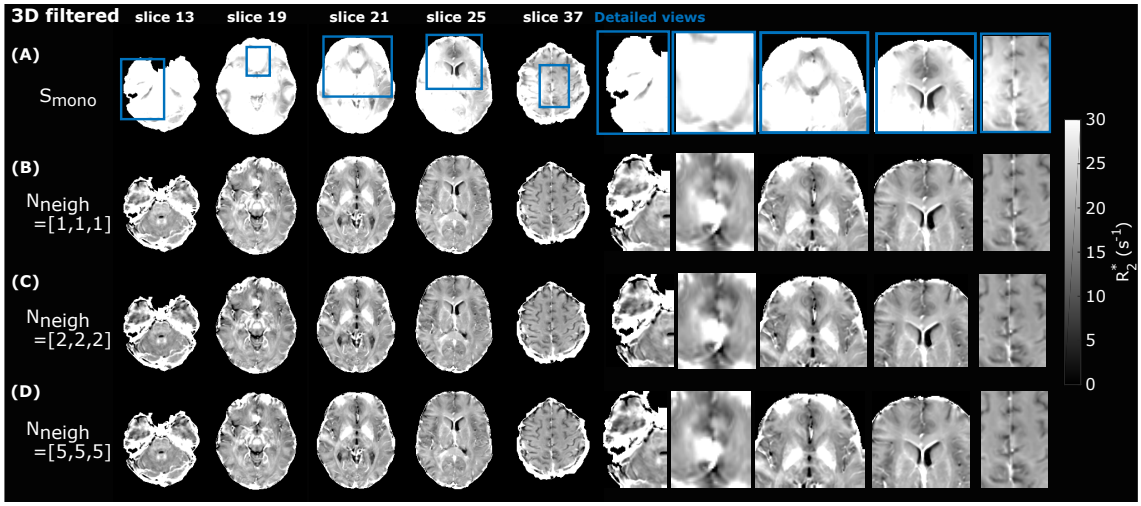

Figure 6.8: Comparison of R_2^* maps estimated with a monoexponential signal model (A) and by applying the *VSF* approach with different numbers of neighbors N_{neigh} for the filtered 3D data (B-D). Compared with the non-filtered data in Figure 6.7, visually no dependency on N_{neigh} can be observed.

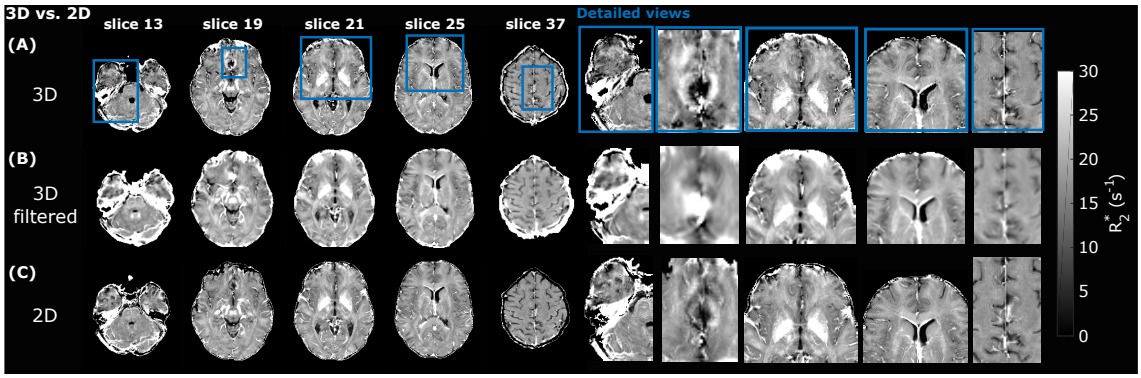

Figure 6.9: Comparison of R_2^* maps obtained from the non-filtered 3D ($N_{neigh} = [5, 5, 5]$) (A), the filtered 3D ($N_{neigh} = [2, 2, 2]$) (B), and the 2D data (C).

6.3.2.1 Influence of Navigator Echo

Figure 6.10 demonstrates the effect of the acquired navigator phase on the resulting R_2^* maps for the non-filtered 3D (Figure 6.10A), the filtered 3D (Figure 6.10B), and the 2D data (Figure 6.10C). Independent of the acquisition, in all three R_2^* maps similar R_2^* variations are observable if the phase of the navigator is not incorporated into the model (left). When including the phase in the image reconstruction, the resulting R_2^* maps (middle) clearly improve. The difference images (right) on the right show R_2^* variations of about $\pm 5 s^{-1}$.

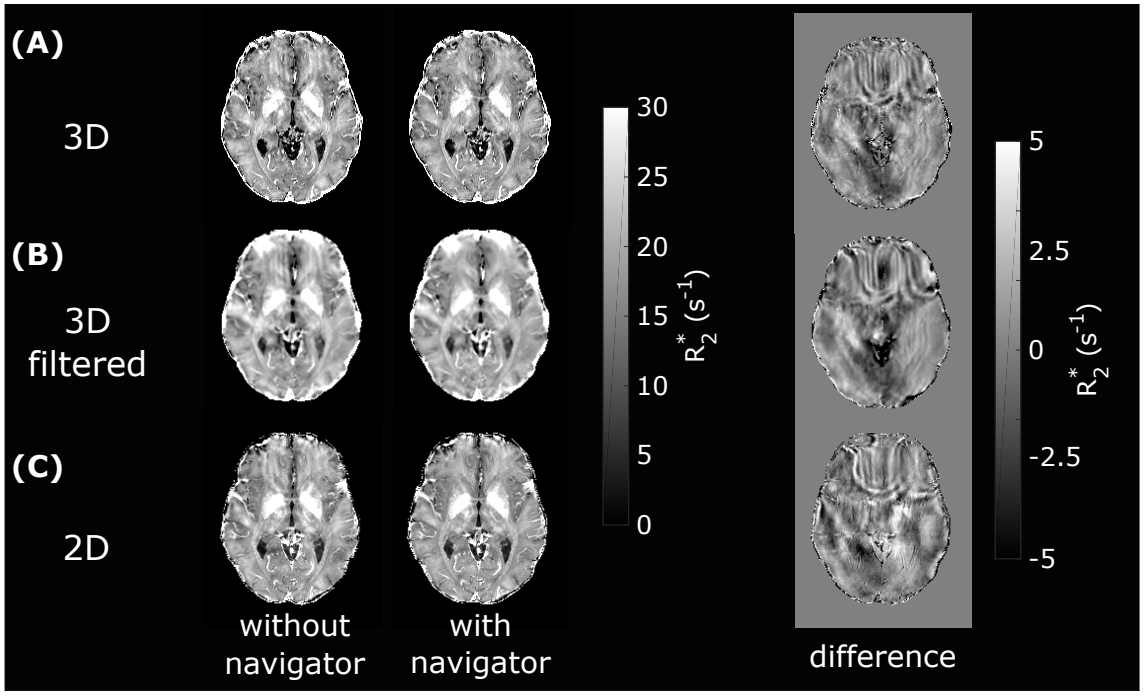

Figure 6.10: Comparison of R_2^* maps estimated without and with phase correction using the navigator echo for the non-filtered 3D data (A), the filtered 3D data (B), and the 2D data (C). For all three cases, the phase correction improves the quantification of the R_2^* maps.

6.4 Discussion

In this chapter, the difference in signal dephasing in the presence of macroscopic field variations between 2D and 3D spoiled *GRE* sequences was investigated. To model the signal dephasing of the 3D data, the *VSF* was used [250] and for 2D the signal model developed in this thesis was applied [202]. Compared with the 3D acquisitions, the results show that a regional similar *IQR* of R_2^* can be obtained with 2D acquisitions in all regions except in the brainstem, using a proper signal model in combination with an appropriate choice of TR and α. In addition, the results for the filtered 3D data show

slightly elevated R_2^* values compared with the 2D data and suggests a small bias in the modeling.
The similarity between the estimated R_2^* maps from 2D and 3D data can be explained by two essential things: first, the data-sets have a similar *SNR* and second, both approaches use an adequate signal model that include macroscopic field variations.

6.4.1 SNR

By increasing the TR_{2D} of 2D acquisitions and the flip angle, the *SNR* benefit of 3D acquisitions over 2D acquisitions can be decreased. For example, assuming *WM* tissue with a $T_1 = 800ms$ [231] and the given sequence parameters for the in vivo measurements, the ratio in Equation 6.3 becomes:

$$\begin{aligned} \frac{SNR_{3D}}{SNR_{2D}} &= \frac{S_{0,3D}}{S_{0,2D}}\sqrt{N_{phase,2}} \\ &= \frac{0.19}{0.96}\sqrt{48} = 1.46 \end{aligned} \tag{6.7}$$

Given these results, the *SNR* benefit for the 3D acquisition would be expected to be 1.46. For *GM* signal ($T_1 = 1300ms$ [231]), the benefit becomes even smaller with a ratio of 1.17. Thus, depending on the tissue type, 3D acquisitions is only slightly more efficient. In the 3D acquisitions the volume was excited with a slab-selective pulse, which results in flip angle variation through the excited volume. Hence, the comparison is only valid in the central part of the slab while for 2D acquisitions every slice is excited with the same flip angle (except B_1^+ field variations).
The difference between 2D and 3D *SNR* could be further decreased by using larger α for the 2D in vivo measurements because α is smaller than the Ernst angle α_{Ernst}. However, it would increase the sensitivity for potential errors in R_2^* caused by B_1^+ and T_1. Section 6.4.4 discusses this issue in detail.

6.4.2 Signal Dephasing and Modeling

Besides the *SNR* as a prerequirement, the next important aspect is the influence of macroscopic field gradients on the signal dephasing. In 2D acquisitions, the signal dephasing caused by a macroscopic field gradient g_z is given by integration of the phase dispersion due to the field gradient along complex transverse magnetization (neglecting in-plane dephasing) until the *TE*. Assuming $TR >> T_1$ and a small α, the shape of the signal decay is given by the shape of the *RF* excitation pulse for a constant g_z along the slice [178]. Thus, a sinc-Hanning-windowed pulse results in a sinc-Hanning-windowed shaped signal decay. In 3D acquisitions, the shape of the signal decay depends on the k-space trajectory, the number of sampling points, and potential k-space filters such as

the Hanning window, which was used in this chapter for the 3D filtered data. The *VSF* [250] includes all these effects and was validated in this chapter.
When comparing the non-filtered 3D data with the 2D data, two major observations can be seen that led to deviation from the simply monoexponential signal model S_{mono}. First, Gibb's ringing causes artifacts and leads to bias in R_2^*, which is most pronounced in the phantom measurements in the slice-direction (Figure 6.2). Gibb's ringing is a phenomena that can be explained by the effects of discrete sampling and truncation of the ideal continuous infinite k-space [25]. The amplitude of the ringing itself is independent of the number of k-space samples, but the oscillations increase their frequency for a fixed *FOV* [25]. The signal model of the *VSF* accounts for the ringing, which can be seen in the phantom (Figure 6.1). However, estimating R_2^* with the model S_{3D} results in a remaining bias associated with Gibb's ringing (Figure 6.3A). A possible explanation might be that the number of neighbors of a voxel N_{neigh}, used for estimating the *VSF*, were too small to properly represent the ringing. In the original publication eight neighbors were used for calculating the *VSF* [250]. Therefore, a larger number of N_{neigh} might improve the results of the non-filtered data. However, this comes at the cost of extremely large computation time. For example, for the in vivo data set the calculation for the *VSF* with $N_{neigh} = [5, 5, 5]$ took about $12h$ with 12 central processing unit (CPU) kernels. To reduce the Gibb's ringing and the required numbers of neighbors, a Hanning filter has been suggested by the authors [250]. This filter was incorporated into the calculations of the *VSF*. The results are in accordance with [250] and show that Gibb's ringing is reduced and that less numbers of neighbors N_{neigh} are required if a Hanning filter is used. The phantom and in vivo results suggest that $N_{neigh} = [2, 2, 2]$ are sufficient to estimate the *VSF*, whereas for the non-filtered data differences between $N_{neigh} = [2, 2, 2]$ and $N_{neigh} = [5, 5, 5]$ are clearly visible. Consequently, the computation time for calculating the *VSF* can be reduced because a smaller N_{neigh} is required. However, an obvious disadvantage of the Hanning filter is that it smooths the point spread function (PSF) leading to blurring in the image. Hence, fine structural details might be lost. Further, the filtering has a large impact on the signal decay of the *GRE* signal in the presence of macroscopic field variations. Because of the convolution of the broader *PSF* with the ideal image, the overall signal decay is increased, leading to a stronger sensitivity of the signal to field gradients. Therefore, when fitting R_2^* with S_{mono}, a much larger dependency on the field gradients can be observed. The results can be improved by accounting for the filtering directly in the *VSF*. However, a small bias in estimated R_2^* values appears compared with the non-filtered and 2D data (Table 6.1). Further investigations have to be performed to assess this difference.

6.4.3 Quantitative Interpretation of R_2^* Values

Besides the small bias in the filtered 3D data, a very good agreement between the in vivo estimated R_2^* values of the 3D non-filtered data and the 2D data was found (Table 6.1). In all evaluated gray matter regions (cudate nucleus, pallidum, putamen, and thalamus) the R_2^* values lie within the 95% interval a comparable large age study [197]. On the other hand, for the 3D filtered data all these regions lie above the confidence interval except for the pallidum. For example, in the thalamus Sedlacik et al. reported a R_2^* of 19.9 (18.8–21.0)s^{-1}. In contrast to that, a median value of 21.19s^{-1} was obtained with the non-filtered 3D data and of 19.85s^{-1} for the 2D data. In general, the non-filtered 3D data and the 2D data show a good agreement. Another interesting finding is that in the investigated regions only minor differences between R_2^* values with S_{mono} and S_{3D} were found for the 3D data. This can be explained by the sensitivity of S_{3D} to field gradients. Figure 6.4 shows that for S_{3D}, R_2^* is over a wide range of g_z values not affected (approximately $|g_z| < 80\mu/T$). After that, for larger g_z, R_2^* abruptly increases.

6.4.4 Limitations

The results further show that the signal modeling in the presence of macroscopic field gradients for 2D and 3D have common limitations. Both methods require accurate field gradient maps for estimating the *VSF* for 3D acquisitions or the signal dephasing along the slice profile for 2D acquisitions. Therefore, any error in the field gradient maps, for example caused by noise or missing field map values close to air/tissue interfaces, propagates into the F_{3D}, $F_{3D,filt}$, or F_{2D}. Another common problem of conventional *mGRE* sequences is that in areas with strong gradients the signal decays too fast to allow a reliable parameter estimation. This can be seen in in vivo R_2^* maps in Figure 6.9. Here, with none of the approaches an accurate R_2^* estimation close to the nasal cavities could be achieved. A possible solution in these areas would be to decrease the voxel size in the slice-direction to reduce signal dephasing. Apart from conventional *mGRE* sequences, z-shimming approaches, which compensate the effect of the field gradients by applying compensation moments in between the acquisitions could solve this issue. An overview of different approaches can be found in section 3.4.
In terms of modeling, the *VSF* is more complex to estimate because of the convolutions performed for a single voxel. In contrast to that, 2D aquisitions require only the complex transverse magnetization along the slice-direction. Another advantage of 2D acquisitions is that for small flip angles an analytic solution is given by the *RF* excitation pulse envelope [178]. A potential drawback in 2D acquisitions are B_1^+ effects and changes of transverse magnetization because of T_1 that might lead to bias in R_2^* [202]. If the performance in terms of *SNR* should be similar to 3D, $S_{0,2D}$ needs to be increased for a given T_1 (Equation 6.3). The optimal signal strength is given by the Ernst angle α_{Ernst}. However, this has the drawback that variations caused by B_1^+ become larger. Depending on the *RF* excitation pulse, B_1^+ leads to a bias in F_{2D} if not accounted for

[202]. Similarly, if the assumption $TR >> T1$ is not fulfilled the transverse magnetization along the slice-direction changes according to the steady-state equation [58] that might influence F_{2D} [202]. To decrease these effects, $\alpha = 60°$ and $TR = 2.45s$ have been used for the in vivo measurement, but with the downside of a smaller $S_{0,2D}$ because $\alpha < \alpha_{Ernst}$ for WM tissue ($T_1 = 800ms$, $\alpha_{Ernst} = 87°$).
In 3D acquisitions, the problems associated with B_1^+ and T_1 in terms signal dephasing are negligible. In 3D the volume is excited with a slab-selective RF excitation pulse or with a short hard-pulse and the whole volume is encoded with two phase encoding gradients and one readout gradient. The flip angle profile along the excited volume changes because of B_1^+ and thus only the signal intensity varies along the profile. Similarly, T_1 might lead to a change of the signal along the profile depending on TR/T_1 and α. However, the type of excitation pulse has an impact on the SNR and therefore on the quality of the estimated R_2^* maps. In these experiments the same FOV was used for 2D and 3D acquisitions to allow a reasonable comparison. The slab-selective excitation with a sinc-Hanning pulse leads to signal variations throughout the slab caused by the shape $B_1(t)$ of the RF pulse. The profile is given by the FT of $B_1(t)$ for small flip angles [98]. To reduced this variations and to achieve a homogeneous excitation, a phase oversampling of about 10% would be necessary. This would affect the acquisitions time and the SNR and was therefore not applied for the comparison here.
In addition to the signal dephasing associated with macroscopic field variations, the impact of phase variations resulting from physiologically induced fluctuations on 2D and 3D acquisitions were investigated. Independent of the acquisition type, similar artifacts were observed for 2D and 3D methods (Figure 6.10). By measuring the phase with a navigator echo [235], the image quality of R_2^* could be drastically improved. Therefore, before accounting for macroscopic field variations, it is recommended to use a navigator echo as well.

6.4.5 Applications 2D

An aspect where 2D acquisitions might be favorable over 3D acquisitions is quantitative multi-compartment imaging such as the estimation of the MWF. As reviewed in section 2.3.4, in the brain several signal compartments associated with the myelin water, the intracelluar, and extracelluar comparment exist. For the myelin water compartment, a longitudinal relaxation time $T_{1,my} < 400ms$ and for the intracellular and extracellular a $T_{1,intra/extra} = 800ms$ have been reported [131]. Therefore, the myelin compartment recovers at rates larger than the intracellular/extracellular compartment. If a short TR is used, which is common for 3D acquisitions, the steady-state solutions of the compartments differs. Consequently, depending on the choice of TR and α, a bias in the MWF can be introduced [198]. Shin et al. performed experiments using different TR and α for 2D and 3D acquisitions [198]. In 3D acquisitions, the authors used a short $TR = 70ms$ and

two flip angles, $\alpha = [20°, 40°]$ and in 2D acquisitions they used long $TR = 2000ms$ with $\alpha = [45°, 85°]$. Shin et al. found a significant difference in the MWF between the 3D acquisitions, whereas for the 2D acquisitions no significant difference were found. These results suggest that 2D acquisitions with long TR lead to a smaller T_1 bias in multi-compartment imaging.

7

Adaptive Slice-Specific z-Shimming for R_2^* mapping

This chapter is based on the publication:

M. Soellradl, J. Strasser, A. Lesch, R. Stollberger, S. Ropele, and C. Langkammer. Adaptive slice-specific z-shimming for 2D spoiled gradient-echo sequences. *Magnetic Resonance in Medicine*, (July):1–13, 2020, doi: 10.1002/mrm.28468

and on the ISMRM abstract:

M. Soellradl, J. Strasser, and C. Ropele, Stefan Langkammer. Adaptive and slice-specific z-shimming approach for signal rephasing in 2D multi gradient echo imaging. In *Proceedings of the 28th Annual Meeting of ISMRM*, 2020

Contents

7.1 Introduction

In the last two chapters advances in the modeling of the 2D *mGRE* signal in the presence of macroscopic field variations could be achieved. However, a major issue of any postprocessing approach that accounts for macroscopic field variations is the faster signal dephasing with increasing field gradients. As a consequence, a reliable estimation of quantitative parameters becomes challenging, or is even not possible if the signal dephases before the acquisition window. As mentioned in Section 3.4, one way to overcome this restriction are z-shimming approaches. These methods compensate the effect of macroscopic field gradients by applying additional compensation moments. Recently, Nam et al. proposed a single scan *mGRE* sequence with z-shimming gradients, combined with a

signal model [178] for R_2^* mapping [159]. A similar approach was proposed by Lee et al. for *MWF* mapping [130], but instead of applying z-shimming gradients starting from the first echo, they applied z-shimming gradients after the sixth echo to avoid signal crushing the myelin water signal.
A common limitation of the aforementioned approaches is that the compensation gradients are fixed for the entire *FOV* (global z-shim). Consequently, a misbalance with the actual field gradient leads to an incomplete rephasing or even spoiling of the signal.
To overcome this limitation, we propose an adaptive slice-specific z-shimming approach to address spatial variations of g_z in different slices. The corresponding slice-specific compensation gradients are estimated for each slice individually from a fast prescan. Additionally, a more effective z-shimming pattern is introduced, where six g_z values are successively compensated between echo acquisitions. By adapting a signal modeling approach for 2D spoiled *mGRE* sequences [202], we compare this novel approach, in terms of R_2^* mapping, with a global z-shim approach with linearly increasing moments [130, 159] and a conventional *mGRE* sequence without z-shim gradients. Furthermore, to highlight the importance of adequate signal modeling in the presence of g_z, R_2^* is also estimated from the conventional *mGRE* data with a more widespread utilized monoexponential signal model.

7.2 Methods

7.2.1 Signal Modeling

Signal dephasing caused by a field gradient g_z can be compensated at an TE by applying a short compensation gradient with duration t_c and amplitude G_c, which results in a compensation moment $m_c = G_c t_c = -g_z TE$. In the case of a train of k compensation gradients, each with the amplitude $G_c[k]$ and identical t_c, the accumulated moment $M_c[i]$ for the ith echo at TE_i is given by:

$$M_c[i] = \sum_{k=1}^{i} m_c[k] = \sum_{k=1}^{i} G_c[k] t_c = \bar{G}_c[i] TE_i. \tag{7.1}$$

The sum of all applied compensation moments $m_c[k]$ is equal to a single theoretical mean compensation gradient $\bar{G}_c[i]$ applied over the entire duration TE_i. This allows to superimpose g_z and $\bar{G}_c[i]$ for signal modeling independent of the shape and duration of the applied compensation gradients. Assuming a mono-exponential signal decay with R_2^*, the signal $S(TE_i)$ of the spoiled gradient-echo is given by integration of the complex transverse magnetization $\underline{M}_{xy}(z)$ weighted with the phase dispersion induced by both gradients along the z-direction:

$$\begin{aligned} S(TE_i) &= S_0 e^{-R_2^* TE_i} \int_{-\infty}^{\infty} \underline{M}_{xy}(z) e^{i\gamma(g_z + \bar{G}_c[i])zTE_i} dz \\ &= S_0 e^{-R_2^* TE_i} F_{z-shim}(TE_i), \end{aligned} \tag{7.2}$$

where S_0 describes the signal $S(TE = 0)$ and $F_{z-shim}(TE_i)$ summarizes the net effect of g_z and $\bar{G}_c[i]$. In the case of small flip angles, the resulting signal decay is described by the pulse envelope of the RF excitation pulse [178]. Otherwise, the integral in Equation 7.2 can be solved numerically, where $\underline{M}_{xy}(z)$ is obtained by numerical solution of the Bloch equations [94, 202].

7.2.2 Sequence

Figure 7.1 shows a 2D RF-spoiled $mGRE$ sequence (Figure 7.1A) and a combination of the global z-shimming patterns proposed by Nam et al. and Lee et al. [128, 159] (Figure 7.1B) along with the proposed slice-specific pattern presented in this work (Figure 7.1C). In addition, Table 1 lists the corresponding compensation gradients $\bar{G}_c[i]$ for the z-shimming approaches for each echo.
The compensation moments for the global z-shimming method (Figure 7.1B) are calculated for a single positive $\bar{G}_c^+$ and negative $\bar{G}_c^-$ value alternating. The first applied gradient moment after the fourth echo ($m_c[5] = \bar{G}_c^+ TE_5 = -g_z^- TE_5$) compensates effects of negative g_z^- followed by nulling the accumulative moment via inverting $m_c[5]$ ($m_c[6] = -m_c[5]$). This step is repeated for a positive g_z^+ by applying a negative compensation moment ($m_c[7] = \bar{G}_c^- TE_7 = -g_z^+ TE_7$). To avoid crushing of the signal in the first echoes, z-shim gradients are not applied for the first echoes as proposed by Lee et al. [128] .

Our work extends the compensation pattern in Figure 7.1B by two novel contributions. First, instead of using global $\bar{G}_c^{+/-}$ for all slices, slice-specific compensation gradients $\bar{G}_c^{+/-}[n]$ are applied for each slice n. These $\bar{G}_c^{+/-}[n]$ values are estimated from a field map measured with a fast prescan. Second, instead of a single $\bar{G}_c^+[n]$ and $\bar{G}_c^-[n]$, the coverage of compensated $g_z^{+/-}$ values is increased by a successive application of three positive and three negative compensation moments. Based on the estimated $\bar{G}_c^{+/-}[n]$, the moments between echoes are scaled such that $[\frac{1}{3}, \frac{2}{3}, \frac{3}{3}]\bar{G}_c^{+/-}[n]$ are compensated for three consecutive echoes, which is followed by a nulling of the total moment for the subsequent echo. To give an example, the moments $m_c[n, 5]$ to $m_c[n, 7]$ in the proposed pattern (Figure 7.1C) are calculated as follows, assuming equal echo spacing ΔTE:

$$\begin{aligned} m_c[n,5] &= \frac{1}{3}\bar{G}_c^+[n]TE_5 \\ m_c[n,6] &= \bar{G}_c^+[n](\frac{1}{3}TE_5 + \frac{2}{3}\Delta TE) \\ m_c[n,7] &= \bar{G}_c^+[n](\frac{1}{3}TE_5 + \frac{4}{3}\Delta TE) \end{aligned} \tag{7.3}$$

Moreover, to allow a more effective rephasing, the non-zero value is split up into

$[\frac{1}{5}, \frac{2}{5}, \frac{3}{5}, \frac{4}{5}, \frac{5}{5}]\bar{G}_c^+[n]$ or $[\frac{1}{5}, \frac{2}{5}, \frac{3}{5}, \frac{4}{5}, \frac{5}{5}]\bar{G}_c^-[n]$ if either $\bar{G}_c^+[n]$ or $\bar{G}_c^-[n]$ is zero. In addition to the inserted z-shim gradients, for all variants in Figure 7.1, a navigator echo is acquired after the last echo to compensate for physiologically induced field variations [100].

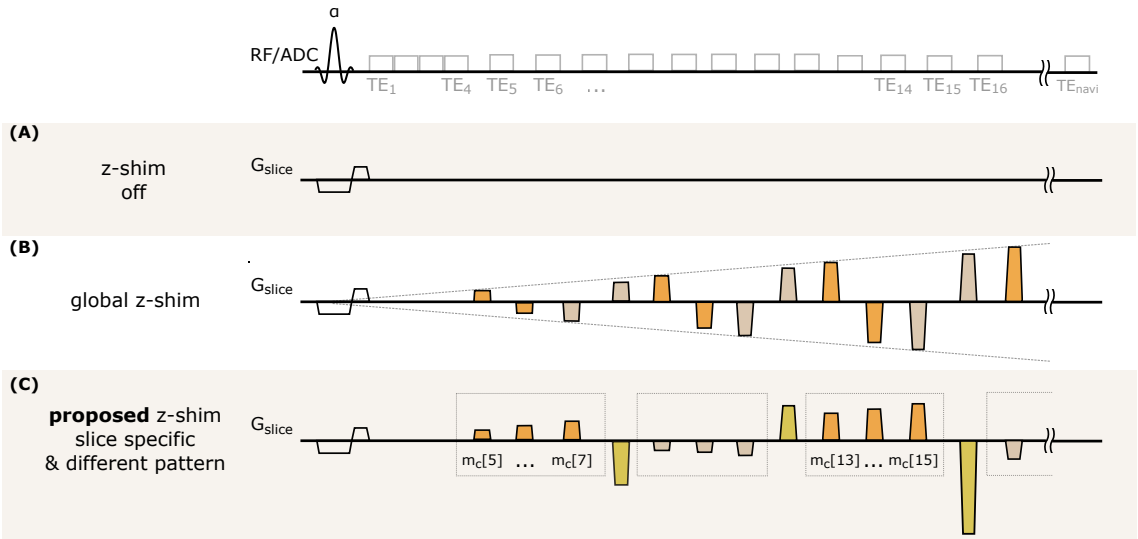

Figure 7.1: Schematic overview of the compared sequences. (A) shows a spoiled *mGRE* sequence without z-shimming. In the global z-shim approach (B), moments are applied through alternating pairs (same color) with a linear increase along TE. The first moment in each pair is calculated based on a single positive or negative $\bar{G}_c^{+/-}$ and the second moment balances the compensation moment to acquire a gradient-echo image with zero net-moment. The proposed slice-specific approach (C) applies slice-specific $\bar{G}_c^{+/-}[n]$, which are estimated from a prescan individually for each slice n. In addition, $\bar{G}_c^{+/-}[n]$ is split up with factors $[\frac{1}{3}, \frac{2}{3}, \frac{3}{3}]\bar{G}_c^{+/-}[n]$ (dashed boxes) followed by compensation of all moments. To correct for physiologically induced fluctuations, a navigator echo is acquired at TE_{navi}.

7.2.3 Simulations

7.2.3.1 Sensitivity for F_{z-shim}

To assess the sensitivity of F_{z-shim} in Equation 7.2 to variations caused by B_1^+ changes, λ, and incomplete T_1 relaxation, simulations were carried out for a standard *mGRE* sequence. Assuming $R_{2,sim}^* = 30s^{-1}$, the signal in Equation 7.2 was simulated with varying parameters (B_1^+, λ, and TR/T_1). The simulations have been performed using the same echo times and excitation pulse as used in the in vivo measurements. Next, $R_{2,est}^*$ was estimated from the simulated signal by nonlinear fitting without varying the parameters. The results were evaluated by calculating the error between the estimated $R_{2,est}^*$ and $R_{2,sim}^*$. To simulate B_1^+ variations, the flip angle was scaled with a factor $\xi = [0.6, 0.8, 1, 1.2, 1.4]$ ($\alpha_{sim} = \alpha\xi$). Variations in $\underline{M}_{xy}(z)$ due to λ were simulated by scaling the spatial coordinates along the slice direction with λ. To account for incomplete T_1 relaxation, the

steady-state equation for spoiled *GRE* sequences was included to calculate $\underline{M}_{xy}(z)$. Simulations were performed using $TR/T_1 = 2$ and $TR/T_1 = 5$.

7.2.4 R_2^* Estimation

For all measurements, the complex-valued raw data was first corrected with the phase of the navigator echo as described by Wen et al. [235] followed by a coil-combination using the method proposed by Luo et al. [145]. Then, $F_{z-shim}(TE_i)$ was calculated as described in [202] for the model $F_4(t)$ (Equation 5.5). In this model, $\underline{M}_{xy}(z)$ is estimated for a certain *RF* pulse shape and G_{slice} with a numerical Bloch solver [1]. Additionally, two potential factors that might affect $\underline{M}_{xy}(z)$ were included: First, nominal flip angle deviations due to the transmit *RF* field B_1^+ and second, g_z is superimposed with G_{slice}, which leads to a change of the spatial encoding from z to $z' = z\lambda$ with $\lambda = G_{slice}/(g_z + G_{slice})$ [183]. Thus, depending on the sign and amplitude of g_z, the nominal slice thickness Δz is changed to $\Delta z'$, which is given by $\Delta z' = \Delta z\lambda$.
After the estimation of $\underline{M}_{xy}(z)$, $F_{z-shim}(TE_i)$ was calculated for each echo by substituting $G_{z,input}[i]$ with $G_{z,input}[i] = g_z + \bar{G}_c[i]$ to include the z-shim gradients. Using $F_{z-shim}(TE_i)$, R_2^*, and S_0 were estimated by nonlinear fitting of the reconstructed magnitude data to Equation 7.2 using the *lsqnonlin()* function in MATLAB (MathWorks, Natick, MA).

7.2.5 Sequence and Model Evaluation

The differences between the investigated sequences and the proposed signal modeling were assessed by calculating four different R_2^* maps: From the measured data of all three sequences, R_2^* was estimated with the signal model described above. Additionally, R_2^* maps were calculated by fitting the standard spoiled *mGRE* data to a monoexponential signal decay ($S_{mono}(TE_i) = S_0 e^{-R_2^* TE_i}$).

7.2.6 Phantom Experiments

All experiments have been carried out on a whole body 3T *MRI* system (Magnetom Prisma, Siemens, Erlangen, Germany) using an 8-channel knee coil. To evaluate the proposed z-shim pattern, a homogenous phantom (5 g/L agar doped with $110\mu mol/L$ Magnevist® to shorten T_1) was built. Measurements with a spoiled 2D *mGRE* (Figure 7.1A), a global z-shim pattern (Figure 7.1B), and the proposed slice-specific z-shimming approach (Figure 7.1C) were performed. To allow a comparison between the acquisition methods for the estimation of R_2^*, all sequence parameters were set identically – except the amplitudes of the z-shim gradients. A sinc-Hanning-windowed *RF* excitation pulse (pulse duration $T_{pulse} = 2ms$, $TBP = 2.7$) with flip angle $\alpha = 60°$ was used. In total, 20 echoes with a monopolar readout and a $BW = 500Hz/Px$ were acquired. The ΔTE was $3.4ms$ for the first four echoes without z-shim gradients, starting with $TE_1 = 2.8ms$ up to $TE_4 = 12.9ms$. For the subsequent echoes with z-shim gradients ($t_c = 2ms$) ΔTE

was increased to $5.4ms$ ($TE_5 = 18.2ms$ to $TE_{20} = 98.8ms$). After the 20th echo, phase encoding was rewound to acquire a navigator echo at $TE_{navi} = 103.4ms$. A total of 26 slices with a spatial resolution of $1x1x4mm^3$ ($FOV = 128x128mm^2$) were acquired in an interleaved slice acquisition scheme with a TR of 3 seconds. For all z-shimming approaches, z-shim gradients were applied with $t_c = 2ms$ starting after the fourth echo. For the measurements with the global z-shim pattern (Figure 7.1B), $\bar{G}_c^{+/-}$ was set to $\pm 100\mu T/m$. This value was approximately half of the maximum magnitude of the observed field gradients g_z in the phantom. In addition to the $mGRE$ sequences, a B_1 map was acquired using a Bloch-Siegert approach [190].

7.2.6.1 Contributions of Fractioning $\bar{G}_c^{+/-}[n]$

In the proposed z-shim pattern (Figure 7.1C) two modifications of the global z-shim (Figure 7.1B) are introduced. The first one is that a slice-specific averaged compensation $\bar{G}_c^{+/-}[n]$ is estimated from the field gradient map g_z. The second one is that the gradients are split up in 3 factions of positive and negative $[\frac{1}{3}, \frac{2}{3}, \frac{3}{3}]\bar{G}_c^{+/-}[n]$ (or in five if one is zero). In order to assess the contribution of fractioning of $\bar{G}_c^{+/-}[n]$, measurements with an intermediate approach have been performed. The intermediate approach uses the same pattern as for the global z-shim (Figure 7.1B) but with slice-specific compensation gradients.

7.2.7 Prescan to Estimate $\bar{G}_c^{+/-}[n]$

For the proposed z-shim approach, a prescan was done to estimate $\bar{G}_c^{+/-}[n]$. The prescan acquisition was performed with the same slice thickness ($4mm$), an in-plane resolution of $2x2mm^2$ ($FOV = 64x64mm^2$), three echoes with $TE = [2.7ms, 4.8ms, 6.9ms]$ and generalized autocalibrating partial parallel acquisition (GRAPPA) acceleration of 2. The phase data of the prescan was then processed to estimate the positive $\bar{G}_c^{+}[n]$ and negative $\bar{G}_c^{-}[n]$ for each slice as follows: The phase data was unwrapped using PRELUDE [103] and the field map was estimated by dividing the phase difference by the echo time difference between the third and first echo. For evaluation, a mask was created by thresholding the magnitude image, which then was eroded with disk elements (radius of 5 pixels) to eliminate outliers close to the border. To estimate the field gradient map $G_{z,pre}$, the gradient in z-direction of the field map was calculated in regions within the mask and smoothed with a 3D Gaussian filter (standard deviation of 1). Then, the $G_{z,pre}$ map was quantized with an interval of $10\mu T/m$. For each slice, $\bar{G}_c^{+}[n]$ was set to the minimum of negative $G_{z,pre}[n]$ values ($\bar{G}_c^{+}[n] = \min(G_{z,pre}[n] < 0)$) and for $\bar{G}_c^{+}[n]$ to the maximum of $G_{z,pre}[n]$ ($\bar{G}_c^{-}[n] = \max(G_{z,pre}[n] > 0)$). Prior to scanning with the proposed z-shimming approach, the specific inter-echo compensation moments were calculated based on the pattern listed in Table 1.

Table 7.1: Mean compensation gradients $\bar{G}_c[i]$ (based on Equation 7.1) for the global and the proposed z-shim approaches as function of echo number i. In the global z-shim approach, compensation moments are calculated from a single positive $\bar{G}_c^+$ and negative $\bar{G}_c^-$ whereas with the proposed approach slice specific values for $\bar{G}_c^+[n]$ and $\bar{G}_c^-[n]$ are estimated for each slice n. To increase coverage of compensated field gradients, these values are divided into 3 fractions or 5 fractions in case that one compensation gradient ($\bar{G}_c^+$ or $\bar{G}_c^-$) is equal to zero.

Echo i		1	...	4	5	6	7	8	9	10	11	12	13	14
global z-shim	$\bar{G}_c^+$, $\bar{G}_c^-$,	0	...	0	$\bar{G}_c^+$	0	$\bar{G}_c^-$	0	$\bar{G}_c^+$	0	$\bar{G}_c^-$	0	$\bar{G}_c^+$	...
proposed z-shim	$\bar{G}_c^+[n] \neq 0$ $\bar{G}_c^-[n] \neq 0$	0	...	0	$\frac{1}{3}\bar{G}_c^+[n]$	$\frac{2}{3}\bar{G}_c^+[n]$	$\frac{3}{3}\bar{G}_c^+[n]$	0	$\frac{1}{3}\bar{G}_c^-[n]$	$\frac{2}{3}\bar{G}_c^-[n]$	$\frac{3}{3}\bar{G}_c^-[n]$	0	$\frac{1}{3}\bar{G}_c^+[n]$	... ...
	$\bar{G}_c^-[n] = 0$	0	...	0	$\frac{1}{5}\bar{G}_c^+[n]$	$\frac{2}{5}\bar{G}_c^+[n]$	$\frac{3}{5}\bar{G}_c^+[n]$	$\frac{4}{5}\bar{G}_c^+[n]$	$\frac{5}{5}\bar{G}_c^+[n]$	0	$\frac{1}{5}\bar{G}_c^+[n]$	$\frac{2}{5}\bar{G}_c^+[n]$	$\frac{3}{5}\bar{G}_c^+[n]$	...
	$\bar{G}_c^+[n] = 0$	0	...	0	$\frac{1}{5}\bar{G}_c^-[n]$	$\frac{2}{5}\bar{G}_c^-[n]$	$\frac{3}{5}\bar{G}_c^-[n]$	$\frac{4}{5}\bar{G}_c^-[n]$	$\frac{5}{5}\bar{G}_c^-[n]$	0	$\frac{1}{5}\bar{G}_c^-[n]$	$\frac{2}{5}\bar{G}_c^-[n]$	$\frac{3}{5}\bar{G}_c^-[n]$	...

7.2.8 In Vivo Experiments

The proposed slice-specific z-shimming approach (Figure 7.1C) was evaluated for in vivo R_2^* mapping by comparing the results with the global approach (Figure 7.1B) and the approach without z-shimming (Figure 7.1A). In total, 3 subjects were scanned on the same 3T *MRI* system using a 20-channel head coil. The study was approved by the local ethics committee and all subjects gave written informed consent. For all experiments the same *RF* excitation pulse as in the phantom measurements was used. 16 echoes and one navigator echo were acquired with $TE_1 = 3ms$ to $TE_4 = 9.7ms$ (without z-shim gradients, $\Delta TE = 2.2ms$), $TE_5 = 13.9ms$ to $TE_{16} = 60.6ms$ (with z-shim gradients $t_c = 2ms$, $\Delta TE = 4.2ms$) and $TE_{navi} = 64.8ms$. Further sequence parameters included a bipolar readout with $BW = 500Hz/Px$, $TR = 2.5s$, 35 slices with a voxel size of $1x1x3mm^3$ ($FOV = 256x176mm^2$). As proposed by Nam et al. [159], the value of $\bar{G}_c^{+/-}$ was set to $\pm 220\mu T/m$ for the global approach. The slice-specific compensation gradients $\bar{G}_c^{+/-}[n]$ were estimated from a prescan as described for the phantom measurements, except that the mask was generated with the brain extraction tool BET, part of *FSL* [200]. Sequence parameters of the prescan were: 35 slices with a voxel size of $2.3x2.3x3mm^3$ ($FOV = 96x78mm^2$), three echoes with $TE = [2.7ms, 4.8ms, 6.9ms]$ and a *GRAPPA* acceleration factor 3 with 20 reference lines, $TR = 344ms$, $\alpha = 20°$. The acquisition time was 15 seconds for the prescan and 7 minutes 20 seconds for each of the three *mGRE* sequences. In addition to the *mGRE* sequences, an *MPRAGE* sequence with $1mm^3$ isotropic resolution was acquired for anatomical segmentation. Further, B_1 mapping was performed with a highly accelerated approach based on the Bloch-Siegert shift [136].

The different methods were compared by calculating the median and *IQR* of R_2^* values in global *WM* and *GM* masks. The global *WM* masks were obtained from *MPRAGE* images using SIENAX [201], part of *FSL* [200] and subcortical *GM* masks using *FSL* FIRST [171]. Regional R_2^* evaluation (median; *IQR*) was performed after affine registration to *mGRE*-space with *FSL FLIRT* [102, 104].

7.3 Results

7.3.1 Simulations

7.3.1.1 Sensitivity for F_{z-shim}

Figure 7.2 shows the influence of B_1^+, λ, and TR/T_1 on F_{z-shim}. For $TR/T_1 = 5$ the relative error is negligible when including B_1^+ and λ for all simulated flip angles because of complete T_1 relaxation. Thus, the influence of T_1 can be neglected. Without B_1^+ and λ, for $\alpha = 30°$, the error is relatively small and mainly driven by λ. For larger α, the B_1^+ related error increases and becomes the dominant factor. In contrast, for $TR/T_1 = 2$, substantial errors due to incomplete T_1 relaxation can be observed in both models.

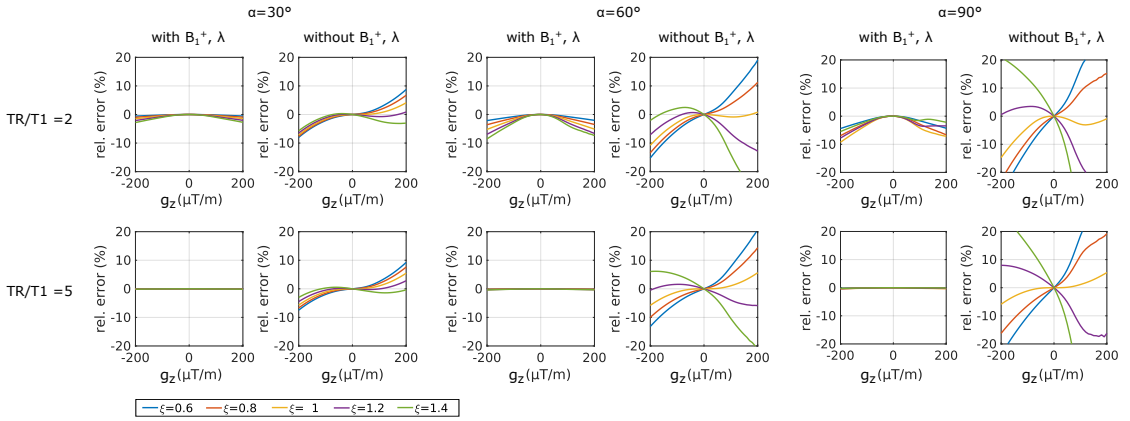

Figure 7.2: Simulation results for the sensitivity of B_1^+, λ, and TR/T_1 in Equation 7.2 for a spoiled *mGRE* sequence. The plots show the relative error (%) of the estimated R_2^* for three different flip angles α. For each α, simulations were carried out for $TR/T_1 = 2$ and $TR/T_1 = 5$ once by including B_1^+ and λ in the model and once without B_1^+ and λ. The curves show results for different ξ values accounting for B_1^+ variations $\alpha_{sim} = \alpha\xi$.

7.3.2 Phantom

Figure 7.3 shows the signal decay of the three investigated pulse sequences within one slice. To demonstrate effects of varying g_z, three *ROIs* (Figure 7.3B) with different g_z intervals were defined and their normalized averaged signal decay S_{norm} (Figure 7.3C) and averaged F_{z-shim} (Figure 7.3D) were plotted. The standard spoiled *mGRE* sequence reveals a faster decay of S_{norm} with increasing magnitude of g_z, whereas for the z-shim approaches S_{norm} is differently rephased or dephased. For the global z-shim, the best signal rephasing was achieved in *ROI* 2 where $\bar{G}_c^+ \approx -g_z = 100\mu T/m$ followed by *ROI* 3. In *ROI* 1 on the other hand, with a g_z interval of $g_z = [-70, -65]\mu T/m$, only a small portion of the signal was rephased. In contrast to the global z-shim, the prescan estimated compensation gradients for the proposed approach were $\bar{G}_c^+[n = 4] = 125\mu T/m$ and $\bar{G}_c^-[n = 4] = 0$. Thus, only positive compensation gradients were applied in 5 fractions ($[25, 50, 75, 100, 125]\mu T/m$). Depending on the g_z interval of each *ROI*, the best compensation varied with echo time for the proposed approach.

In Figure 7.4 S_{norm} and F_{z-shim} are plotted as function of the echo time for three different slices. In each slice, the values were averaged within *ROIs* of different g_z interval. Similar to Figure 7.3, with the global approach the best signal rephasing was achieved when $\bar{G}_c^- \approx -g_z = -100\mu T/m$ (Figure 7.4B). In contrast to that, with the proposed approach the signal was gradually rephased for all slices for each block of compensation gradients ($\bar{G}_c^+[n = 18, 21, 24] = 0$). Compared with the global approach, the estimated $\bar{G}_c^-$ for the depicted slices were $\bar{G}_c^-[18] = -55\mu T/m$, $\bar{G}_c^-[21] = -105\mu T/m$, and $\bar{G}_c^-[24] = -175\mu T/m$, which are close to the range of g_z values within the *ROIs*. Therefore, after each fifth compensation gradient, the signal is nearly ideally compensated in each block. This is indicated when comparing S_{norm} of the echoes $TE_9 = 39.7ms$ and $TE_{15} = 71.9ms$ with

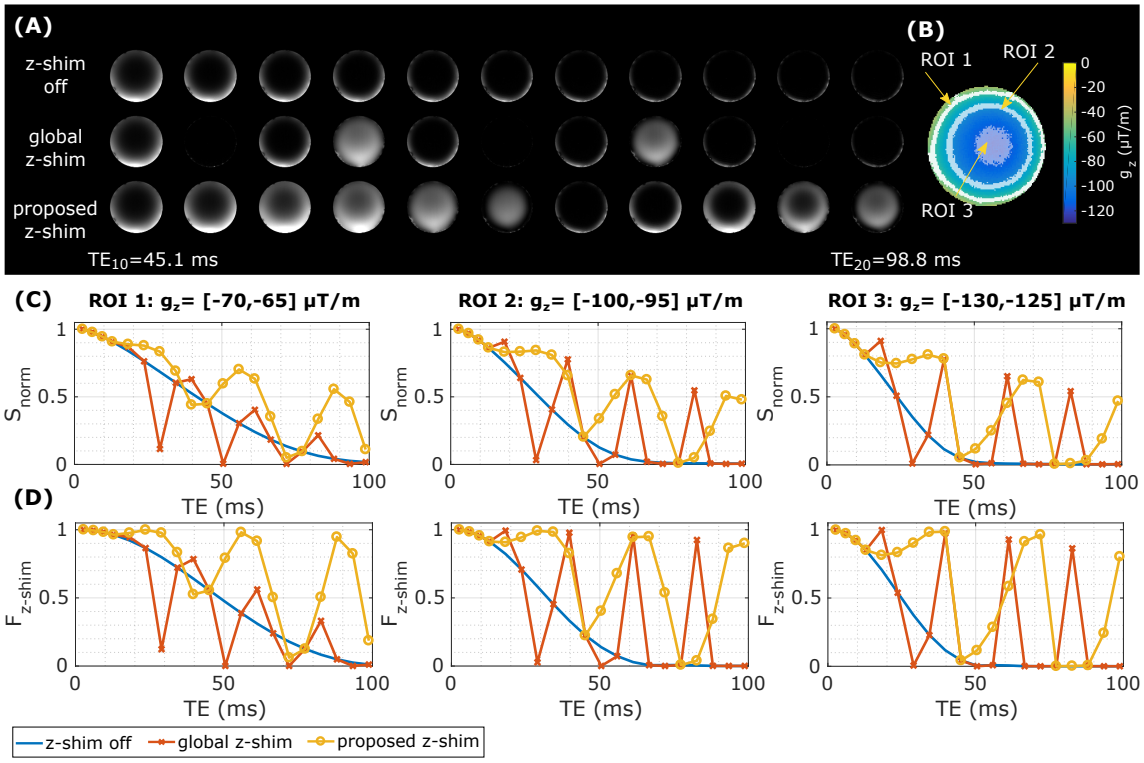

Figure 7.3: Comparison of the measured signal decay and the estimated dephasing functions $F_{z-shim}(TE)$ within one slice. (A) shows the magnitude images of TE_{10} to TE_{20} and in (B) *ROIs* were defined within different field gradients intervals g_z. In these *ROIs*, the measured averaged normalized $S_{norm}(TE_i) = S(TE_i)/S(TE_1)$ (C) and the averaged $F_{z-shim}(TE)$ (D) were estimated. The lines in (C) and (D) show the results from a spoiled *mGRE* sequence without z-shim gradients in blue, with the global z-shim approach ($|\bar{G}_c^{+/-}| = 100\mu T/m$) in red, and with the proposed slice-specific z-shimming in yellow. Note: The interpolation between echoes is solely for illustration purpose.

F_{z-shim}. Here, the dephasing functions $F_{z-shim} \approx 1$ suggesting an ideal compensation of g_z. Further, when comparing S_{norm} between the slices, S_{norm} is approximately equal for these echoes independent of g_z.

Figure 7.5 shows the estimated g_z map (Figure 7.5A) and the obtained R_2^* maps (Figure 7.5B-F). The R_2^* map from the monoexponential fit of the standard spoiled *mGRE* (Figure 7.5B) reveals a strong overestimation proportional to $|g_z|$, which can be drastically decreased by accounting for g_z in the signal model (Figure 7.5C). Nonetheless, compared with the R_2^* value of $6.4s^{-1}$ in the center of the phantom (g_z is close to zero), R_2^* becomes underestimated with increasing $|g_z|$. Applying a global z-shim ($|\bar{G}_c^{+/-}| = 100\mu T/m$) improved the results, especially in areas with $|g_z|$ around $100\mu T/m$ (Figure 7.5D, e.g. slice 5 and slice 20). Figure 7.5E demonstrates that the proposed slice-specific approach yielded more homogenous R_2^* maps over a wide range of g_z values (e.g. slice 2 and 23). Figure 7.6 shows the averaged R_2^* values of the phantom with a bin size of $g_z = 10\mu T/m$ as

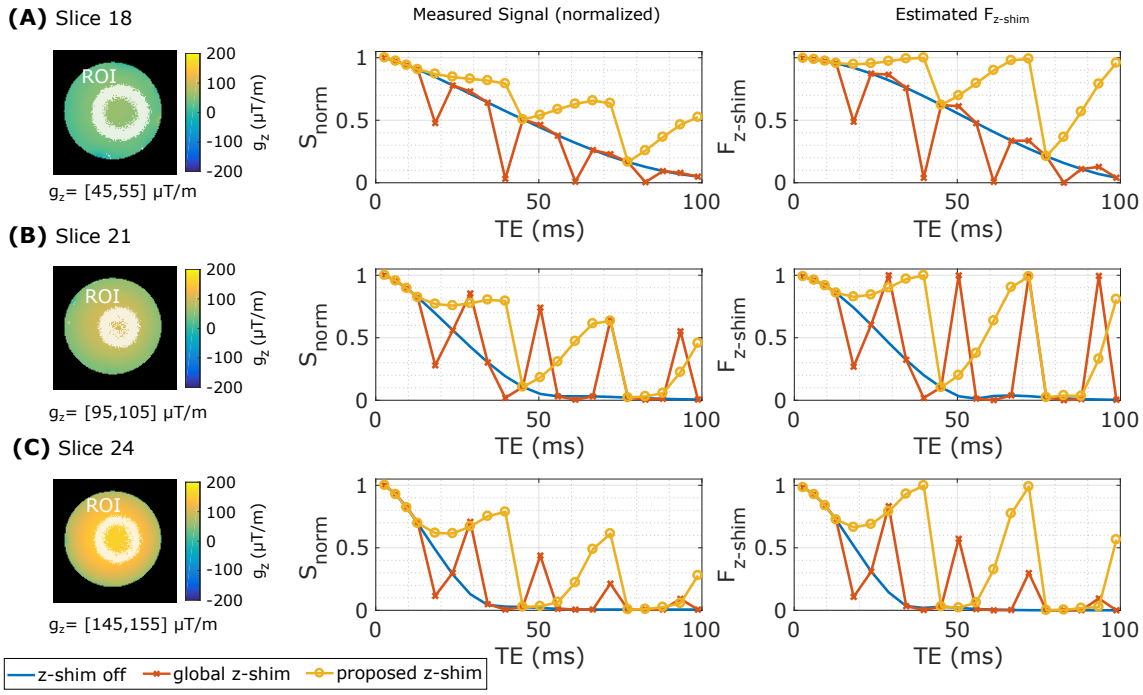

Figure 7.4: Comparison of the measured averaged normalized $S_{norm}(TE_i) = S(TE_i)/S(TE_1)$ (middle) and the averaged estimated dephasing functions $F_{z-shim}(TE)$ (right) in 3 slices (A, B, and C). In each slice, averaging was performed in a *ROI* defined by different intervals of field gradients g_z (left). The lines in the plots show the results from a spoiled *mGRE* sequence without z-shim gradients in blue, with the global z-shim approach ($|\bar{G}_c^{+/-}| = 100\mu T/m$) in red, and with the proposed slice-specific z-shimming in yellow. Note: The interpolation between echoes is solely for illustration purpose.

a function of g_z and demonstrates the difference between the proposed approach and the global z-shimming. While the global z-shim approach ($|\bar{G}_c^{+/-}| = 100\mu T/m$) corrected R_2^* values at around $|g_z| = 100\mu T/m$ to the expected value of $6.4s^{-1}$ (R_2^* value at $g_z \approx \mu T/m$), the proposed approach yielded constant R_2^* values over a broad range of g_z from $-150\mu T/m$ to $125\mu T/m$. Furthermore, the results from the monoexponetial fit of the standard spoiled *mGRE* data clearly showed the strong increase of R_2^* with $|g_z|$.

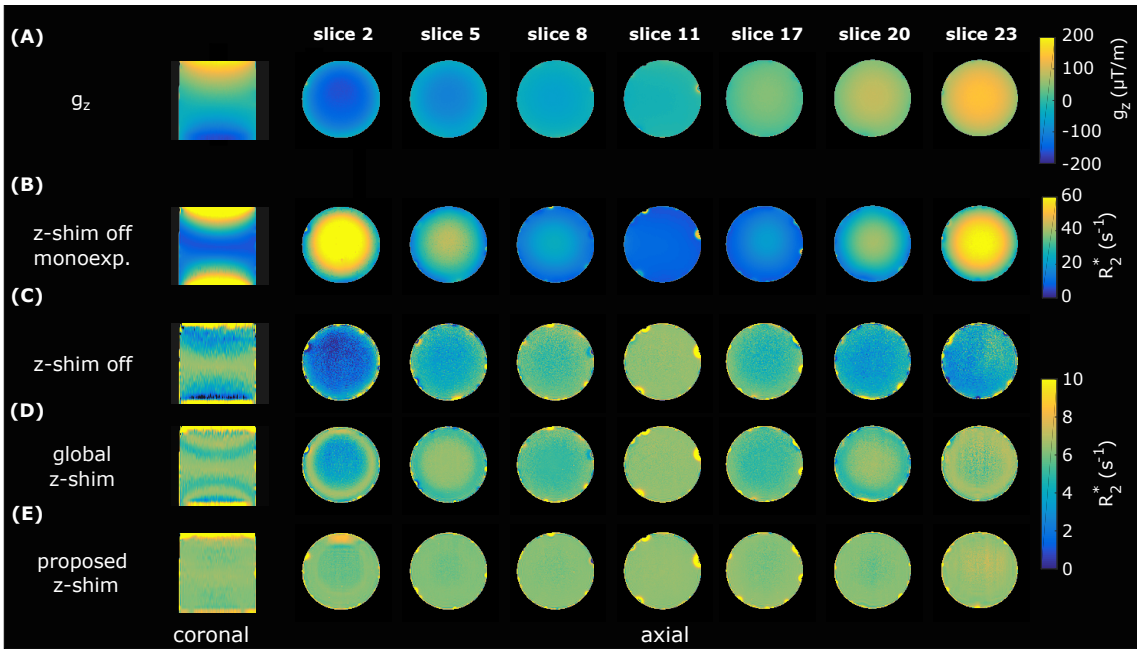

Figure 7.5: Comparison of estimated R_2^* maps of a homogenous phantom. (A) shows the field gradient map g_z. In (B), the R_2^* maps were calculated from the spoiled $mGRE$ data by assuming a monoexponential signal model neglecting g_z ($F_{z-shim} = 1$). The other R_2^* maps were calculated with the proposed signal model using the data of the spoiled $mGRE$ (C), from the global z-shim ($|\bar{G}_c^{+/-}| = 100\mu T/m$) (D), and from the proposed slice-specific approach (E).

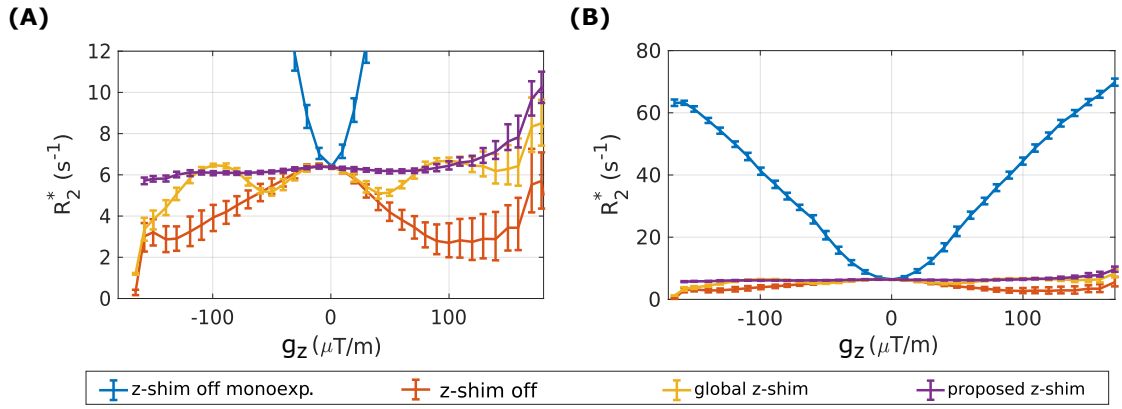

Figure 7.6: R_2^* values obtained from the phantom experiments as a function of the field gradient g_z (bin size $10\mu T/m$) with different scaling of the R_2^* axes (A, B). From the spoiled $mGRE$ data, R_2^* values were first estimated assuming a monoexponential signal model (blue line) neglecting g_z ($F_{z-shim} = 1$) and second, by using the proposed model (red line). Further, R_2^* values from the global z-shim approach ($|\bar{G}_c^{+/-}| = 100\mu T/m$) (yellow) and the proposed slice-specific method (purple) are plotted. R_2^* values are shown as median and 25th and 75th percentiles (whiskers).

7.3.2.1 Contributions of Fractioning $\bar{G}_c^{+/-}[n]$

Figure 7.7 shows the results obtained from a standard *mGRE* without z-shim, with a global z-shim, with the intermediate approach, and with the proposed z-shim approach for one slice. Figure 7.7A shows the magnitude echo images in this slice starting from the echo $TE_{10} = 45.1ms$ up to $TE_{20} = 98.8ms$ for the different approaches. Using the forward model for the signal decay $S(t)$ in Equation 7.2, the R_2^* maps (Figure 7.7B) were estimated. In general, all z-shim approaches perform superior compared with the standard *mGRE* sequence. However, when closely comparing the intermediate z-shim with the proposed slice-specific z-shim, differences can be observed close to the border of the phantom (blue arrows). Here, the R_2^* values were underestimated in all cases except for the proposed z-shim. This can be explained by comparing the signal decay in the individual *ROIs* (Figure 7.7D) with the field gradient map g_z (Figure 7.7C). In *ROI* 1 the median of $g_z = 104\mu T/m$ is close to the estimated $\bar{G}_c^- = -115\mu T/m$ ($\bar{G}_c^-[n] = 0$), which explains especially the good performance of the slice-selective z-shim, since a substantial amount of signal is rephased by the compensation gradients. In contrast, in *ROI* 2 the median $g_z = 69\mu T/m$ is smaller than $\bar{G}_c^-[n]$ and consequently the signal decay differs. The slice-specific approach with a single compensation gradient (intermediate z-shim) rephases a small portion of the signal. However, in the proposed z-shim, the signal is maximally rephased after the third moment in each block (out of 5), which corresponds to $\frac{3}{5}\bar{G}_c^-[n] = -\frac{3}{5}115\mu T/m = -69\mu T/m$. Thus, fractioning the compensation gradients $\bar{G}_c^{+/-}[n]$ is advantageous if a larger range of g_z values is present in a slice.

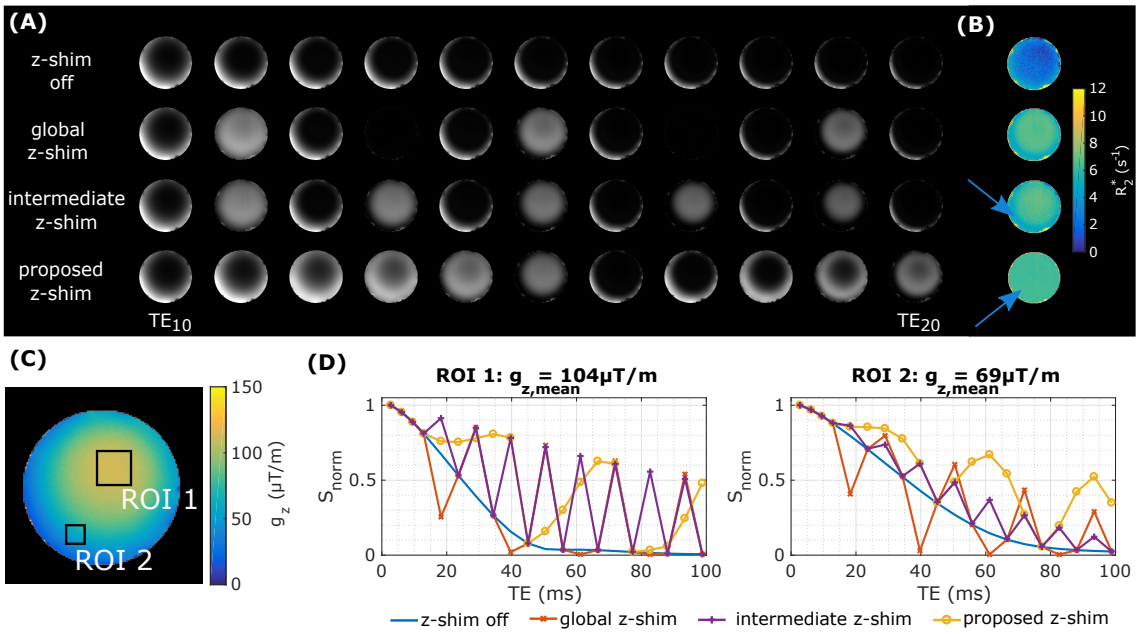

Figure 7.7: Phantom results obtained when extending the global z-shim pattern (Figure 7.1B) by a slice-specific (intermediate) pattern. (A) shows the magnitude images from TE_{10} to TE_{20} and (B), the R_2^* maps. The differences of the methods in two *ROIs* with different mean g_z (C) are assessed by comparing the measured signal decays (D). With the estimated single $\bar{G}_c^-[n] = -115\mu T/m$ a nearly ideal compensation can be achieved when $\bar{G}_c^-[n] \approx -g_z$ (*ROI* 1). In the case of heterogenous g_z values, a more robust compensation can be achieved when fractioning $\bar{G}_c^-[n]$ (ROI 2). Note: The interpolation between echoes is solely for illustration purpose.

7.3.3 In Vivo

Figure 7.8 shows representative *mGRE* images for the three investigated sequences (12th to 16th echo). For the spoiled *mGRE* sequence (Figure 7.8A), a faster signal decay in areas with strong g_z, e.g. close to the nasal cavities, can be observed. For all sequences, the 12th echo images as well as the 16th echo images were equal because of a zero net-moment ($M_{c,12} = 0$ and $M_{c,16} = 0$). Between these two echoes, the signal in various brain areas was differently rephased and dephased depending on the z-shim approach and g_z. The global z-shim pattern with $|\bar{G}_c^{+/-}| = 220\mu T/m$ shows that negative g_z values and positive g_z values were rephased at the 13th and 15th echo, respectively (Figure 7.8B). Instead of single positive and negative g_z, a larger range of g_z values can be covered by the proposed approach (Figure 7.8C) (red arrows). R_2^* maps in Figure 7.5 demonstrate improvements in areas with strong g_z from the global z-shim pattern using constant $|\bar{G}_c^{+/-}| = 220\mu T/m$ (Figure 7.5C) over the spoiled *mGRE* (Figure 7.5B and 7A), which are most pronounced in the temporal lobe and cerebellum (slice 3) or close to the sinuses (slice 9). Further improvements and additionally increased *SNR* are observed in the R_2^* maps obtained with the proposed adaptive z-shim (Figure 7.5D).

Table 7.2: Regional R_2^* (s^{-1}) presented as median (IQR) obtained with the 4 evaluated approaches in 3 subjects.

	z-shim method	Global White Matter		Caudate Nucleus		Globus Pallidus		Putamen		Thalamus		Brainstem	
subject 1 (m 33 years)	z-shim off monexp.	22.12	(4.26)	20.87	(3.97)	40.34	(8.33)	25.49	(5.11)	23.44	(3.47)	25.91	(6.88)
	z-shim off	19.25	(3.31)	19.77	(3.17)	36.03	(8.55)	22.74	(4.06)	19.96	(3.78)	16.99	(7.07)
	global z-shim	19.20	(3.19)	19.62	(2.96)	36.05	(8.09)	22.73	(4.16)	19.87	(3.71)	17.07	(5.93)
	proposed z-shim	19.20	(2.92)	19.74	(2.95)	35.98	(7.34)	22.77	(3.85)	19.89	(3.29)	17.80	(3.76)
subject 2 (m 30 years)	z-shim off monexp.	23.74	(4.89)	22.37	(3.93)	38.30	(6.55)	28.55	(5.99)	26.05	(3.66)	25.40	(5.65)
	z-shim off	18.75	(3.65)	19.85	(3.31)	31.50	(6.91)	22.33	(4.53)	18.87	(4.89)	17.01	(5.96)
	global z-shim	18.81	(3.47)	19.72	(3.09)	31.26	(6.30)	21.97	(4.32)	18.77	(4.30)	16.81	(5.67)
	proposed z-shim	18.84	(3.05)	19.78	(2.84)	31.78	(5.75)	22.34	(4.08)	18.93	(3.75)	17.41	(3.96)
subject 3 (m 51 years)	z-shim off monexp.	22.12	(4.87)	23.88	(5.17)	40.74	(14.08)	29.64	(7.31)	22.95	(4.15)	31.67	(12.46)
	z-shim off	19.56	(3.58)	22.35	(3.89)	37.87	(14.98)	27.10	(6.73)	20.60	(3.94)	18.22	(7.87)
	global z-shim	19.60	(3.44)	22.12	(3.32)	37.35	(14.27)	27.12	(6.26)	20.53	(3.79)	18.60	(5.81)
	proposed z-shim	19.73	(3.22)	22.14	(3.83)	37.38	(13.73)	27.12	(6.18)	20.86	(3.81)	18.69	(4.40)

Table 7.3: Regional R_2^* (s^{-1}) presented as median (IQR) obtained with the 4 evaluated methods in 3 subjects. Values were estimated without including variations of the nominal flip angle due to B_1^+ and spatial broadening or narrowing of $M_{xy}(z)$ with λ caused by the superposition of g_z and G_{slice} in the model for Equation 7.2.

	z-shim method	Global White Matter		Caudate Nucleus		Globus Pallidus		Putamen		Thalamus		Brainstem	
subject 1 (m 33 years)	z-shim off monexp.	22.12	(4.26)	20.87	(3.97)	40.34	(8.33)	25.49	(5.11)	23.44	(3.47)	25.91	(6.88)
	z-shim off	19.33	(3.31)	19.79	(3.14)	36.37	(8.47)	22.92	(4.12)	20.29	(3.68)	17.90	(6.74)
	global z-shim	19.27	(3.18)	19.61	(2.94)	36.32	(8.05)	22.88	(4.19)	20.14	(3.66)	17.75	(5.78)
	proposed z-shim	19.24	(2.92)	19.73	(2.94)	36.22	(7.33)	22.89	(3.93)	20.11	(3.29)	17.97	(3.81)
subject 2 (m 30 years)	z-shim off monexp.	23.74	(4.89)	22.37	(3.93)	38.30	(6.55)	28.55	(5.99)	26.05	(3.66)	25.40	(5.65)
	z-shim off	19.01	(3.63)	20.03	(3.36)	32.22	(6.76)	22.79	(4.50)	19.66	(4.67)	18.02	(5.68)
	global z-shim	19.02	(3.47)	19.88	(3.12)	31.77	(6.20)	22.37	(4.36)	19.40	(4.17)	17.62	(5.55)
	proposed z-shim	18.95	(3.07)	19.87	(2.85)	32.15	(5.70)	22.63	(4.14)	19.35	(3.75)	17.75	(4.05)
subject 3 (m 51 years)	z-shim off monexp.	22.12	(4.87)	23.88	(5.17)	40.74	(14.08)	29.64	(7.31)	22.95	(4.15)	31.67	(12.46)
	z-shim off	19.75	(3.57)	22.24	(3.87)	38.14	(14.98)	27.25	(6.84)	20.90	(3.93)	19.76	(7.57)
	global z-shim	19.75	(3.43)	22.03	(3.34)	37.70	(14.05)	27.28	(6.31)	20.80	(3.80)	19.44	(5.75)
	proposed z-shim	19.85	(3.22)	22.08	(3.83)	37.74	(13.71)	27.26	(6.33)	21.12	(3.81)	19.21	(4.46)

7.3.4 Results without Considering B_1^+

Table 7.4 summarizes the contributions of B_1^+ and λ variations on R_2^* obtained with the proposed signal model. The relative change of R_2^* was estimated from R_2^* values obtained without and with incorporating B_1^+ and λ variations in the signal modeling. In the brainstem, which corresponds to the region with largest g_z values of the evaluated regions, the biggest change of R_2^* was observed for the standard $mGRE$ data without z-shim, ranging from -5.35% to -8.44%. Both z-shimming techniques reduced the difference, but the proposed lead to the smallest relative change, ranging from -0.92% to -2.74%, in the brainstem.

Table 7.4: Relative change (%) of R_2^* (s^{-1}) values estimated with (Table 2) and without including B_1^+ and λ variations (Table 7.3) for modeling F_{z-shim}.

	z-shim method	Global White Matter	Caudate Nucleus	Globus Pallidus	Putamen	Thalamus	Brainstem
subject 1	z-shim off	-0.42	-0.08	-0.95	-0.81	-1.64	-5.35
(m 33 years)	global z-shim	-0.41	0.05	-0.76	-0.66	-1.34	-3.96
	proposed z-shim	-0.24	0.03	-0.66	-0.50	-1.12	-0.92
subject 2	z-shim off	-1.37	-0.92	-2.27	-2.10	-4.19	-5.93
(m 30 years)	global z-shim	-1.09	-0.84	-1.63	-1.83	-3.36	-4.87
	proposed z-shim	-0.59	-0.48	-1.15	-1.27	-2.26	-1.90
subject 3	z-shim off	-0.95	0.49	-0.73	-0.54	-1.45	-8.44
(m 51 years)	global z-shim	-0.77	0.41	-0.95	-0.60	-1.32	-4.51
	proposed z-shim	-0.61	0.27	-0.97	-0.50	-1.25	-2.74

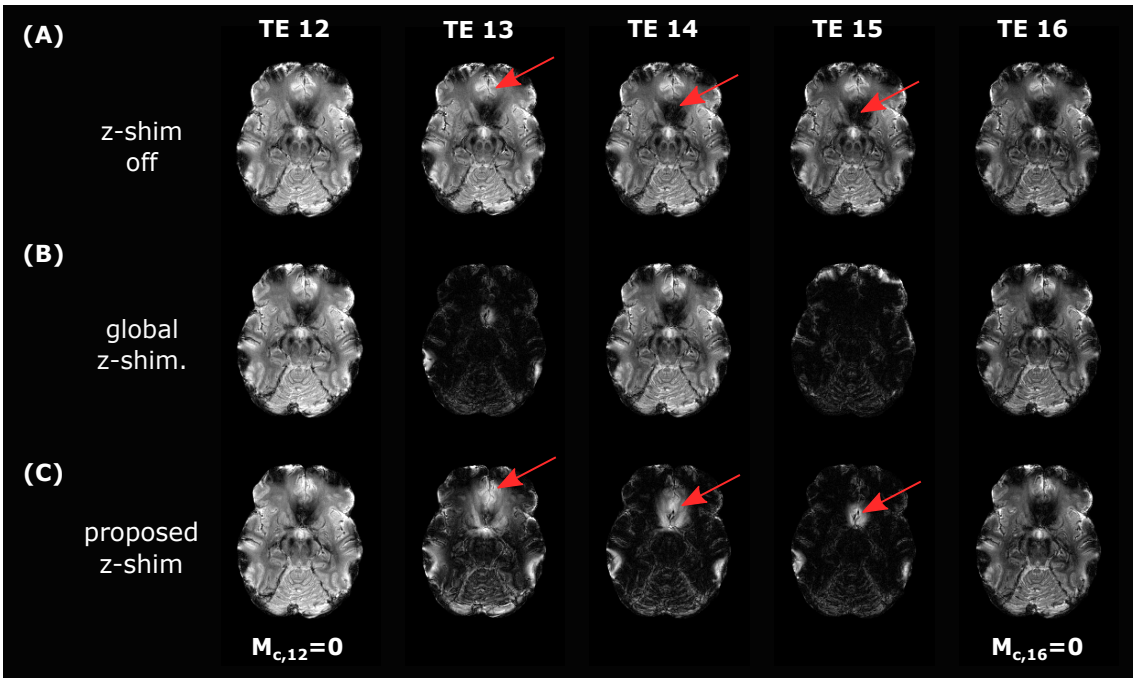

Figure 7.8: Last five gradient-echo images from TE_{12} to TE_{16} acquired with a spoiled $mGRE$ sequence without z-shimming (A), with the global z-shim (B), and with the proposed slice-specific z-shimming approach (C). At TE_{12} as well as at TE_{16} the sum of the compensation moments ($M_{c,12}$, $M_{c,16}$) is zero for all sequences. With the proposed approach, the signal can be rephased also in areas where it has already been completely dephased (arrows).

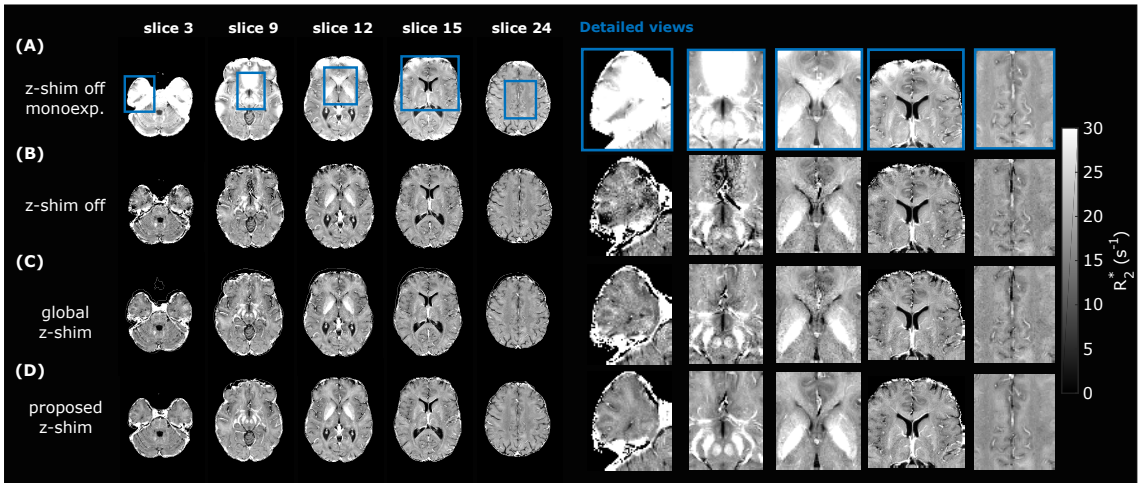

Figure 7.9: Axial views of estimated in vivo R_2^* maps (left) with detailed views of the blue rectangular regions (right). (A), the R_2^* maps were directly calculated from the spoiled $mGRE$ data by assuming a monoexponential signal model neglecting g_z (F_{z-shim}) = 1). The other R_2^* maps were calculated using the proposed signal model for the spoiled $mGRE$ (B), the global z-shim ($|\bar{G}_c^{+/-}| = 220\mu T/m$) (C), and the proposed slice-specific approach (D) data. An increase in SNR can be observed from (C) to (D) due to higher signal recovery.

7.4 Discussion

We have introduced an adaptive slice-specific z-shimming approach that allows minimizing effects of macroscopic field gradients in slice selection direction in 2D *mGRE* sequences. For each slice n, a maximum positive and negative compensation gradient $\bar{G}_c^{+/-}[n]$ is obtained from a fast prescan. In order to increase the coverage of compensated g_z values, $\bar{G}_c^{+/-}[n]$ is split into three fractions ($[\frac{1}{3}, \frac{2}{3}, \frac{3}{3}]\bar{G}_c^{+/-}[n]$). Based on these gradient values, a pattern of compensation moments between the echoes is calculated (Figure 7.1C).
Our novel adaptive slice-specific z-shimming was compared with a conventional spoiled *mGRE* sequence and a global z-shimming approach that applies a positive and negative $\bar{G}_c^{+/-}$ (Figure 7.1B) independent of the slice position [128, 159]. In contrast to modeling of the standard spoiled *mGRE*, the global z-shim enables to recover R_2^* values in areas with strong g_z, which is in line with the results of Nam et al. [159]. By performing slice-specific z-shimming with more compensated g_z values, the proposed approach results in *SNR* improvements (Figure 7.5). Quantitatively, the measured values are within the range of reported values in the literature at 3T. The z-shim approach by Nam et al. yielded a R_2^* of $20.77s^{-1}$ for the putamen and $34.22s^{-1}$ for the globus pallidus [159], which is close to the mean values of our 3 subjects with $24.08s^{-1}$ and $35.05s^{-1}$. When considering the age of the subjects, our R_2^* values are in good correspondence with a study reporting different age ranges [197]. Subjects' regional R_2^* values in the caudate nucleus, thalamus, and brainstem are within the 95% confidence interval of this study [197]. For subjects 1 and 3 the R_2^* values in the globus pallidus are slightly above the 95% confidence interval as well as in the putamen for subject 3. For example, in the putamen of subject 3 (51 years) R_2^* is $27.12s^{-1}$ compared with Sedlacik et al. who reported a R_2^* of $24.3(22.1 - 26.6)s^{-1}$ [197].
During the optimization process of selecting the optimal $\bar{G}_c^{+/-}[n]$ from the prescan field gradient map $G_{z,pre}[n]$, splitting of the compensation gradients into different magnitudes was performed. When using a single value (e.g. maximum and minimum of positive and negative $G_{z,pre}[n]$) improvements were only observed in areas with g_z values close to the specific compensation gradient. To demonstrate this relation, additional measurements with a slice-specific approach but with a single $\bar{G}_c^{+/-}[n]$ were performed. As shown in Figure 7.2, splitting $\bar{G}_c^{+/-}[n]$ led to a more robust compensation over a wide range of g_z values. A further refinement of our approach could be made by passing the desired compensation gradient for each echo $\bar{G}_c^{+/-}[n, TE_i]$ to the sequence. This comes with the advantage that the compensation gradients can be individually selected based on the distribution of g_z values in each slice.
Z-shim approaches mainly aim to avoid signal dephasing in areas with large g_z. In this context, a rather unexpected finding was that also areas with relatively low field gradients ($|g_z| < 50\mu T/m$) yielded higher *SNR* in R_2^* maps by applying small compensation gradients compared with postprocessing-only methods (e.g. Figure 7.5, slice 24). This *SNR* increase might be especially promising for combined applications with acceleration methods such

as parallel imaging [21, 72, 179].
The proposed approach has some limitations. First, a prescan with a duration of 15 seconds is necessary to the estimate $\bar{G}_c^{+/-}[n]$. However, this additional scan time is short compared with the fully sampled z-shim acquisition (7 minutes 20 seconds) itself and the increase in *SNR* compensates the prolonged scan time. Another issue, especially in vivo, is the estimation of a reliable field gradient g_z map from the prescan, which is used to define $\bar{G}_c^{+/-}[n]$. Here, we focused on a robust implementation and avoided potential gradient errors due to missing field map values in the skull by eroding the g_z map. Nevertheless, it might result in non-optimal compensation gradients in these areas. An alternative might be to match the slice position to a template g_z map instead of performing a prescan [224].
This work focuses on z-shimming because the signal dephasing is primarily along the slice-selective (z-)direction compared with the orthogonal directions. In addition, strong in-plane field gradients can be considered by calculating additional compensation moments in in-plane directions or, as proposed by Yablonskiy et al. [250], by modeling the signal dephasing with the *VSF*.
We have recently introduced a signal modeling approach for an arbitrary excitation pulse and g_z [202], which has been adapted in the current work to describe signal dephasing F_{z-shim} due to g_z and the compensation gradient $\bar{G}_c$. Because R_2^* is estimated from the measured data by nonlinear fitting of Equation 7.2, any modeling error in F_{z-shim} will propagate into the R_2^* estimate. Here, B_1^+ and λ have been considered for modeling, but additionally the ratio TR/T_1 can affect F_{z-shim}. If the assumption $TR \gg T_1$ is not fulfilled, $\underline{M}_{xy}(z)$ changes according to the steady-state equation for spoiled gradient-echo sequences [58] and might bias F_{z-shim}. To better assess the contributions of B_1^+, λ, and TR/T_1 to F_{z-shim}, additional simulations were carried out for different g_z values (Figure 7.2). For a ratio of $TR/T_1 = 5$, T_1 effects are negligibly small while errors due to B_1^+ increase with α. Compared with B_1^+, the estimated errors caused by λ are similar for each α. In contrast, for $TR/T_1 = 2$, a bias because of T_1 relaxation can be observed, which is small compared with the B_1^+ error. To investigate the influence of B_1^+ and λ in vivo, in Table 7.3 the results without considering B_1^+ and λ are shown. It reveals that the greatest relative change of R_2^* for the proposed approach was 2.7% for subject 3 in the brain stem (Table 7.4). These small changes in R_2^* suggest that B_1 mapping might not be necessary for the regions evaluated. However, when increasing α or when evaluation regions with stronger g_z, accounting for B_1^+ might be beneficial. Based on the simulation results, a potential small T_1 effect cannot be excluded with the $TR = 2.5s$ used in vivo.
Other sources for model deviations in F_{z-shim} are the input parameters g_z and $\bar{G}_c$. As for the prescan, g_z estimation is challenging if the field map values from adjacent slices are missing. For $\bar{G}_c$ it is assumed that it is ideally characterized by the actual applied gradient moment of the *MRI* system. Thus, errors might occur in the case of gradient imperfections or when a different *MRI* system is used. Here, a good correspondence between the signal dephasing F_{z-shim} and the measured signal S_{norm} (Figure 7.3 and Figure 7.4) was observed indicating a reasonable accurate $\bar{G}_c$ for the proposed approach.

7.5 Conclusion

A new adaptive slice-specific z-shim approach in combination with signal modeling for 2D *mGRE* data was introduced to minimize effects of macroscopic field gradients. The proposed approach allows a more robust correction of R_2^* maps over a broad range of field gradients and additionally provides a higher *SNR*.

8 Discussion and Outlook

The methods presented in this thesis lead to substantial advances in the modeling and compensation of macroscopic field variations in quantitative *GRE* imaging with a focus on 2D acquisitions. First, a numerical signal model to describe the signal decay in the presence of a macroscopic field gradient g_z was proposed [202]. The work revealed that for larger flip angles signal phase along the slice profile φ_{xy} becomes crucial for signal dephasing. By applying the model to R_2^* and *MWF* mapping, the influence of g_z on the parameters could be improved. Nonetheless, with increasing field gradients signal modeling becomes challenging because of the fast signal decay. To resolve this issue, an adaptive slice-specific z-shimming sequence was proposed and combined with the signal model [206]. The approach outperforms signal modeling of conventional *mGRE* data and leads to better results than a global z-shim with slice-independent compensation moments for each slice.

A detailed discussion about the developed methods can be found in the dedicated chapters. This section discusses open issues and suggests refinements for further work. It additionally gives an outlook about future directions and applications.

Navigator Echo

In the first experiments of this work, quantitative R_2^* analysis was carried out based on data obtained from the vendor's standard *mGRE* sequence. Although the proposed modeling approach in Chapter 3 worked well in the phantom measurements, a strong intrasubject variability in the estimated in vivo R_2^* maps was observed. These variations were later assigned to physiologically induced fluctuations of the phase signal during k-space acquisition [100]. As explained in Chapter 4, after implementation of a navigator echo [100], these artifacts could be substantially reduced. Based on literature and our findings, the use of navigator echoes is highly recommended when performing quantitative analyzes of *GRE* data. Further, the results of the 2D versus 3D comparison support that navigator echoes are also beneficial for 3D acquisitions.

Gradient and Field Maps

A critical parameter for the presented signal model and others [178, 250] are the macroscopic field gradients g_x, g_y, and g_z. The gradient maps were obtained by numerical differentiation of the field map ΔB_0. Thus, any error in ΔB_0 propagates into the field gradient maps.
In this work ΔB_0 was obtained from the spatially unwrapped phase data using PRELUDE [103]. However, ΔB_0 becomes larger in regions close to air/tissue interfaces such as the frontal sinuses or nasal cavities, leading to a faster signal decay that results in a noisy signal or in the worst case in a loss of signal. In these areas unwrapping might fail, and consequently ΔB_0 cannot be estimated in this region. To improve ΔB_0 in voxels with short T_2^* due to macroscopic fields, decreasing the echo time is an option, if possible, or by measuring ΔB_0 with an *ASE* acquisition [6, 240]. The *ASE* sequence has the advantage that a small shift Δ (Figure 2.5) between the *SE* and *GRE* readout gradient allows measuring signal decay in areas with strong inhomogeneities.
Besides the challenge of estimating ΔB_0 in areas with larger field variations, the border regions of the brain are an additional error source. For instance, estimating a reliable field gradient in the cortex is not a trivial task. When moving from cortex towards the meninges the signal becomes noisy or lost. Therefore, when calculating the through-slice or in-plane gradients, wrong ΔB_0 values lead to errors in the field maps.
A possible solution for the aforementioned problems might be to create a model for ΔB_0 that uses the measured data and to combine it with a forward model for ΔB_0, which is based on the subject's geometry and susceptibility [33, 115, 150]. Given that it is possible to describe ΔB_0 by a function, it would improve gradient estimation and the quality of the estimated parameters.

Model Validation

Apart from g_z, the influence of B_1^+, λ, and $TR/T1$ for 2D acquisitions was investigated. All these parameters can change $\underline{M}_{xy}(z)$, and thus they affect signal dephasing in the presence of g_z.
In the phantom experiments in Chapter 5, Figure 5.6 illustrates the dependency of the signal dephasing on TR/T_1 and g_z. Further, it shows that with increasing α the B_1^+ field has an impact on R_2^*. One unresolved issue is the challenge of separating changes of R_2^* caused by B_1^+ and TR/T_1 to quantify their individual contributions. When comparing results between 2D and 3D acquisitions in Chapter 6, a remarkable similarity between R_2^* values estimated in global *WM* and *GM* was found. In these experiments B_1^+ was neglected ($\alpha = 60°$), showing that B_1^+ and TR/T_1 have only minor contributions. However, to assess the individual influence, a better experimental setup is required to clarify the relation between B_1^+ and TR/T_1.
One possibility might be to perform phantom measurements in an area with a homogeneous field ($g_z \approx 0$). In this region a field gradient $g_{z,shim}$ could be superimposed using

the first order shim coil. This would lead to a relatively controlled environment for studying different dephasing effects. By varying the nominal flip angle, B_1^+ changes can be simulated, and by repeating the measurements with different TR, it allows studying the impact of TR/T_1.
The results from the adaptive slice-specific z-shimming approach in Chapter 7 provide further insights into the sensitivity of R_2^* estimates to these parameters. Apart from the signal rephasing caused by the additional compensation gradients, the sensitivity for parameters that change $\underline{M}_{xy}(z)$ decreases. In an ideal *GRE* imaging experiment, a homogeneous field without field gradients ($g_z \approx 0$) is desired. In this case, the signal decay rate in Equation 7.2 is independent of the $\underline{M}_{xy}(z)$. By applying proper z-shimming gradients, this condition can be partially fulfilled. Consequently, the sensitivity for parameters that affect $\underline{M}_{xy}(z)$ decreases. This relation can be seen in the regional comparison between estimated R_2^* with and without considering B_1^+ and λ in Table 7.4. Here, the greatest change was found in the conventional *mGRE* data, suggesting that the sensitivity for these parameters can be decreased by z-shimming.
A parameter that strongly influences the sensitivity for B_1^+ and TR/T_1 is the shape of *RF* excitation pulse. Here, non-optimized sinc-Hanning-windowed pulses were utilized that are based on the vendor's standard *GRE* pulses. Hence, one of the next steps is to design tailored *RF* pulses for specific applications. For example, the measurement of R_2^* in deep *GM* regions does not require necessarily a fast *RF* pulse, which enables designing pulses closely to an ideal rectangular shape with a constant phase. An ideal shape has the advantage that the sensitivity for B_1^+ and TR/T_1 would be decreased in the presence of field gradients. Although B_1^+ changes result in signal changes, the sinc-shaped signal decay is not affected, allowing signal modeling independent of α and B_1^+, respectively. Similar holds for the effect of TR/T_1. With an ideal slice profile, α is constant along the slice and depending on TR/T_1, the signal changes according to the steady-state equation [58], but independent of shape.

Future Directions and Applications

The focus in the present thesis was on quantitative *GRE* imaging in the brain, but the methods developed here can be extended to different tissue types. An interesting application is the measurement of the hepatic iron concentration with R_2^* [84, 244]. To allow R_2^* quantification outside the brain, the chemical shift of fat has to be accounted for in the signal model. Similar as proposed by Hernando et al. [94], additional compartments, including the amplitudes and frequency shifts of the fat components, need to be added in the signal model.
Another potential application could be the assessment of R_2^* in the heart for studying myocardial iron overload [4, 51, 61]. The typical protocols for cardiovascular *MRI* have a slice thickness of $10mm$ [90], which makes it extremely sensitive to macroscopic field variations. It would be interesting to investigate the impact of macroscopic field

variations on R_2^* estimation and to apply the proposed adaptive slice-specific z-shimming [206].
Another future project will be to extend the signal model for spoiled *GRE* to *ASE*-based sequences. As discussed in Chapter 2, the *ASE* allows studying R_2 and R_2^* with the same sequence. Depending on the shift Δ between *SE* and *GRE*, the *ASE* sequence is equally sensitive to macroscopic field variations. The proposed signal model can be adapted for the *ASE* by replacing the time t with Δ. Further, it would be possible to include z-shimming gradients in the sequence and in the modeling.
The developed adaptive slice-specific z-shimming approach was designed for 2D acquisitions. However, the sequence also works for 3D acquisition, which allows applying variable z-shim gradients for each k_z line proving a great flexibility for potential applications. In the future, the sequence might be extended to the 3D R_2^* mapping approach by Han et al. [81]. By applying alternating z-shim gradients between the echoes, the proposed sequence acquires z-shimming images and standard *mGRE* images (z-shim moment is zero). Similar as proposed in Chapter 7, an adaptive approach could be implemented based on the field gradient values from a prescan. With these gradients, echo images with different compensated field gradients could be acquired and by modeling the signal with the *VSF* [250] R_2^* can be estimated more accurately.
This work did not accelerate acquisition time with parallel imaging methods mainly to avoid potential changes of the *PSF* caused by the undersampled k-space. For future clinical applications, it would be of great interest to investigate the effect of macroscopic field variations for certain acceleration methods to allow a faster image acquisition. A promising direction might be to incorporate the proposed approaches in model-based image reconstruction [215, 216]. In these methods, quantitative *MRI* parameters are estimated by solving an inverse problem with iterative reconstruction techniques such as the non-linear conjugate gradient (CG) method [40]. This potentially speeds up image acquisition and the quality of estimated parameters such as R_2^* or the *MWF* for clinical applicability.

A

List of Acronyms

ASE	asymmetric spin-echo
AST	apparent susceptibility tensor
bmGESEPI	blipped multi gradient-echo slice excitation profile imaging
BOLD	blood oxygenation level dependent
bSSFP	balanced steady-state free precession
BW	bandwidth
CAIPIRINHA	controlled aliasing in volumetric parallel imaging
CG	conjugate gradient
CISS	constructive interference in steady-state
CNS	central nervous system
CPU	central processing unit
CSF	cerebrospinal fluid
CT	computed tomography
DAWM	diffusive-appearing white matter
DESPOT1	driven-equilibrium single-pulse observation of T1
DESPOT2	driven-equilibrium single-pulse observation of T2
DSU	dynamic shim updating
DSV	diameter of spherical volume
DTI	diffusion tensor imaging
EDSS	extended disability status scale
EPI	echo planar imaging
FDRI	field-dependent R_2 increase
FFT	fast Fourier transform
FID	free induction decay
FLIRT	FMRIB's linear image registration tool
fMRI	functional magnetic resonance imaging
FOV	field of view
FSL	FMRIB software library
FT	inverse Fourier transform
FWHM	full width half maximum

GESEPI	gradient-echo slice excitation profile imaging
GESFIDE	gradient-echo sampling of FID and echo
GLA	generalized Lorentzian approach
GLTA	generalized Lorentzian tensor approach
GM	gray matter
GRAPPA	generalized autocalibrating partial parallel acquisition
GRASE	gradient and spin-echo
GRE	gradient-echo
IFFT	inverse fast Fourier transform
IQR	interquartile range
MC	multi-coil
mcDESPOT	multi-comparment driven-equilibrium single-pulse
mGESEPI	multi gradient-echo slice excitation profile imaging
MGESIC	multi gradient-echo with magnetic susceptibility inhomogeneity compensation method
mGRE	multi-echo gradient-echo
MIP	maximum intensity projection
MPRAGE	magnetization-prepared rapid gradient-echo
MRI	magnetic resonance imaging
MRM	Magnetic Resonance in Medicine
MS	multiple sclerosis
MSE	multiple spin-echo
MWF	myelin water fraction
MWI	myelin water imaging
NAWM	normal appearing white matter
NMR	nuclear magnetic resonance
NNLS	non-negative least squares
OST	outer sphere theory
ppm	parts per million
PRIME	partially-refocused interleaved multiple echo
PSF	point spread function
qMRI	quantitative magnetic resonance imaging
QSM	quantitative susceptibility mapping
RF	radio frequency
RMSE	root mean squared error
ROI	region of interest
SAR	specific absorption rate
SE	spin-echo
SNR	signal-to-noise ratio
SSFP	steady-state free precession
SWI	susceptibility-weighted imaging

TBP	time bandwidth product
TE	echo time
TR	repetition time
UHF	ultra high field
VSF	voxel spread function
WM	white matter

B

Definitions and Derivations

B.1 Rectangular Function

$$\text{rect}\left(\frac{x}{x_0}\right) = \begin{cases} 1 & \text{if } |\frac{x}{x_0}| \leq \frac{1}{2} \\ 0 & \text{if} |\frac{x}{x_0}| > \frac{1}{2} \end{cases}. \tag{B.1}$$

B.2 VSF k-Space

The integral in Equation 3.8 can solved as follows:

$$\begin{aligned}
\tilde{S}(k_x, TE) &= \sum_{n=1}^{N_x} \int \text{rect}(\frac{\text{x} - \text{x}_\text{n}}{\text{a}_\text{x}}) \rho(x) \exp\left(-2\pi i k_x x + i\gamma b(x) TE + i\varphi_0(x)\right) dx \\
&= \sum_{n=1}^{N_x} \rho_n \int_{x_n - \frac{a_x}{2}}^{x_n + \frac{a_x}{2}} \exp\left(-2\pi i k_x x + i\gamma(b_n + g_{nx}(x - x_n))TE) + i(\varphi_{0,n} + \varphi_{nx}(x - x_n))\right) dx \\
&= \sum_{n=1}^{N_x} \rho_n \exp(i(\gamma b_n TE + \varphi_{0,n})) \int_{x_n - \frac{a_x}{2}}^{x_n + \frac{a_x}{2}} \exp\left(-2\pi i k_x x + (i\gamma g_{nx} TE + i\varphi_{nx})(x - x_n))\right) dx \\
&= \sum_{n=1}^{N_x} \rho_n \exp(i(\gamma b_n TE + \varphi_{0,n})) \frac{1}{i(-2\pi k_x + \gamma g_{nx} TE + \varphi_{nx})} \\
&\qquad \exp(-2\pi i k_x x + (i\gamma g_{nx} TE + i\varphi_{nx})(x - x_n)) \Big|_{x_n - \frac{a_x}{2}}^{x_n + \frac{a_x}{2}} \\
&= \sum_{n=1}^{N_x} \rho_n \exp(i(\gamma b_n TE + \varphi_{0,n})) \frac{1}{i(-2\pi k_x + \gamma g_{nx} TE + \varphi_{nx})} \\
&\qquad \left(\exp(-2\pi i k_x (x_n + \frac{a_x}{2}) + (i\gamma g_{nx} + i\varphi_{nx})\frac{a_x}{2}) - \exp(-2\pi k_x (x_n - \frac{a_x}{2}) + (i\gamma g_{nx} TE + i\varphi_{nx})\frac{-a_x}{2})\right) \\
&= \sum_{n=1}^{N_x} \rho_n \exp(i(\gamma b_n TE + \varphi_{0,n})) \exp(-2\pi i k_x x_n) \frac{1}{i(-2\pi k_x + \gamma g_{nx} TE + \varphi_{nx})} \\
&\qquad \left(\exp(-2\pi i k_x \frac{a_x}{2} + (i\gamma g_{nx} TE + i\varphi_{nx})\frac{a_x}{2}) - \exp(-2\pi i k_x (-\frac{a_x}{2}) + (i\gamma g_{nx} TE + i\varphi_{nx})\frac{-a_x}{2})\right).
\end{aligned} \tag{B.2}$$

The two exponential functions can be summarized to a sinc function ($\text{sinc}(u) = \frac{\sin(\pi u)}{(\pi u)}$) by:

$$\begin{aligned}\frac{1}{id}(\exp(i\frac{a_x}{2}d) - \exp(-i\frac{a_x}{2}d)) &= \frac{a_x}{i2\frac{a_x}{2}d}(\exp(i\frac{a_x}{2}d) - \exp(-i\frac{a_x}{2}d)) \\ &= a_x\frac{\sin(\frac{a_x}{2}d)}{\frac{a_xd}{2}} = a_x\text{sinc}(\frac{a_xd}{2\pi}) \\ &= a_x\text{sinc}(a_x(-k_x + \frac{\gamma g_{nx} + \varphi_{nx}}{2\pi})) = a_x\text{sinc}(a_x(-k_x + k_n)) \\ &= a_x\ \text{sinc}(a_x(k_x - k_n))\end{aligned} \tag{B.3}$$

with $d = -2\pi + \gamma g_{nx}TE + \varphi_{nx}$. Then, for Equation B.4 follows:

$$\tilde{S}(k_x, TE) = \sum_{n=1}^{N_x} \rho_n \exp(i(\gamma b_n TE + \varphi_{0,n})) \exp(-2\pi i k_x x_n) a_x \text{sinc}(a_x(k_x - k_n)). \tag{B.4}$$

C

List of Publications

Journal Publications

M. Soellradl, J. Strasser, A. Lesch, R. Stollberger, S. Ropele, and C. Langkammer. Adaptive slice-specific z-shimming for 2D spoiled gradient-echo sequences. *Magnetic Resonance in Medicine*, (July):1–13, 2020, doi: 10.1002/mrm.28468

A. Damulina, L. Pirpamer, M. Soellradl, M. Sackl, C. Tinauer, E. Hofer, C. Enzinger, B. Gesierich, M. Duering, S. Ropele, R. Schmidt, and C. Langkammer. Cross-sectional and longitudinal assessment of brain iron level in Alzheimer disease using 3-T MRI. *Radiology*, 296(3):619–626, 2020, doi: 10.1148/radiol.2020192541

M. Soellradl, A. Lesch, J. Strasser, L. Pirpamer, R. Stollberger, S. Ropele, and C. Langkammer. Assessment and correction of macroscopic field variations in 2D spoiled gradient-echo sequences. *Magnetic Resonance in Medicine*, 84(2):620–633, 2020, doi: 10.1002/mrm.28139

C. Birkl, M. Soellradl, A. M. Toeglhofer, S. Krassnig, M. Leoni, L. Pirpamer, T. Vorauer, H. Krenn, J. Haybaeck, F. Fazekas, S. Ropele, and C. Langkammer. Effects of concentration and vendor specific composition of formalin on postmortem MRI of the human brain. *Magnetic Resonance in Medicine*, 79(2):1111–1115, 2018, doi: 10.1002/mrm.26699

Conference Proceedings

M. Soellradl, J. Strasser, and C. Ropele, Stefan Langkammer. Adaptive and slice-specific z-shimming approach for signal rephasing in 2D multi gradient echo imaging. In *Proceedings of the 28th Annual Meeting of ISMRM*, 2020

C. Tinauer, S. Heber, L. Pirpamer, A. Damulina, M. Soellradl, M. Sackl, E. Hofer, M. Koini, R. Schmidt, S. Ropele, and C. Langkammer. Relevance-guided Deep Learning for Feature Identification in R2* Maps in Alzheimer's Disease Classificatio. In *Proceedings of the 28th Annual Meeting of ISMRM*, 2020

C. Langkammer, A. Damulina, L. Pirpamer, M. Soellradl, E. Hofer, C. Tinauer, M. Sackl, C. Enzinger, S. Ropele, and R. Schmidt. Longitudinal assessment of brain iron deposition in Alzheimer's disease. In *Proceedings of the 28th Annual Meeting of ISMRM*, 2020

J. Strasser, M. Soellradl, C. Enzinger, and S. Ropele. Accelerating DENSE MR elastography by including multi-axes motion encoding into the multiphase DENSE-MRE acquisition scheme. In *Proceedings of the 28th Annual Meeting of ISMRM*, 2020

M. Soellradl, S. Ropele, and C. Langkammer. Gradient echo modelling with macroscopic field variations and large flip angles. In *Proceedings of the 27th Annual Meeting of ISMRM*, Montreal, Canada, 2019

C. Langkammer, A. Damulina, L. Pirpamer, M. Sackl, M. Soellradl, E. Hofer, M. Koini, F. Fazekas, S. Ropele, and R. Schmidt. Quantitative Susceptibility Mapping in Alzheimer's Disease. In *Proceedings of the 27th Annual Meeting of ISMRM*, Montreal, Canada, 2019

M. Soellradl, L. Pirpamer, J. Sedlacik, F. Fazekas, S. Ropele, and C. Langkammer. R2* Correction for Gradient Echo with a Gaussian Excitation Pulse. In *Proceedings of the 26th Annual Meeting of ISMRM*, Paris, France, 2018

C. Birkl, M. Soellradl, A. Toeglhofer, J. Haybaeck, L. Pirpamer, F. Fazekas, S. Ropele, and C. Langkammer. Effect of Vendor Specific Formalin Composition and Concentration on Post-Mortem MRI of Human Brain Tissue. In *Proceedings of the 25th Annual Meeting of ISMRM*, Honolulu, USA, 2018

O. Katrin, T. Widek, S. Martin, T. PP, G. P, T. Schwark, and E. Scheurer. Age Determination of Traumatic Subcutaneous Hematomas Using 3.0T MRI: A Feasible Approach. In *Proceedings of the 70th AAFS Annual Scientific Meeting*, Seattle, USA, 2018

M. Soellradl, L. Pirpamer, C. Langkammer, and S. Ropele. Optimization of Imaging Parameters for Fast Bound Pool Fraction Estimation from a Single Off-Resonance Magnetization Transfer Measurement. In *Proceedings of the 34th Annual Scientific Meeting of ESMRMB*, Barcelona, Spain, 2018

Bibliography

[1] C. S. Aigner, C. Clason, A. Rund, and R. Stollberger. Efficient high-resolution RF pulse design applied to simultaneous multi-slice excitation. *Journal of Magnetic Resonance*, 263:33–44, feb 2016, doi: 10.1016/J.JMR.2015.11.013. (page 46, 57, 99)

[2] E. Alonso-Ortiz, I. R. Levesque, R. Paquin, and G. B. Pike. Field inhomogeneity correction for gradient echo myelin water fraction imaging. *Magnetic Resonance in Medicine*, 78(1):49–57, 2017, doi: 10.1002/mrm.26334. (page 25, 67, 72, 73)

[3] E. Alonso-Ortiz, I. R. Levesque, and G. B. Pike. MRI-based myelin water imaging: A technical review. *Magnetic Resonance in Medicine*, 73(1):70–81, 2015, doi: 10.1002/mrm.25198. (page 23)

[4] L. J. Anderson, S. Holden, B. Davis, E. Prescott, C. C. Charrier, N. H. Bunce, D. N. Firmin, B. Wonke, J. Porter, J. M. Walker, and D. J. Pennell. Cardiovascular T2-star (T2*) magnetic resonance for the early diagnosis of myocardial iron overload. *European Heart Journal*, 22(23):2171–2179, 2001, doi: 10.1053/euhj.2001.2822. (page 119)

[5] C. J. Bakker, R. Bhagwandien, M. A. Moerland, and M. Fuderer. Susceptibility artifacts in 2DFT spin-echo and gradient-echo imaging: The cylinder model revisited. *Magnetic Resonance Imaging*, 11(4):539–548, 1993, doi: 10.1016/0730-725X(93)90473-Q. (page 27)

[6] K. Bartusek, Z. Dokoupil, and E. Gescheidtova. Magnetic field mapping around metal implants using an asymmetric spin-echo MRI sequence. *Measurement Science and Technology*, 17(12):3293–3300, 2006, doi: 10.1088/0957-0233/17/12/015. (page 118)

[7] G. Bartzokis, M. Aravagiri, W. H. Oldendorf, J. Mintz, and S. R. Marder. Field dependent transverse relaxation rate increase may be a specific measure of tissue iron stores. *Magnetic Resonance in Medicine*, 29(4):459–464, apr 1993, doi: 10.1002/mrm.1910290406. (page 17)

[8] G. Bartzokis, M. Beckson, D. B. Hange, P. Marx, J. A. Foster, and S. R. Marder. MR evaluation of age-related increase of brain iron in young adult and older normal males. *Magnetic Resonance Imaging*, 1997, doi: 10.1016/S0730-725X(96)00234-2. (page 17)

[9] G. Bartzokis, D. Sultzer, J. Cummings, L. E. Holt, D. B. Hance, V. W. Henderson, and J. Mintz. In vivo evaluation of brain iron in Alzheimer disease using magnetic resonance imaging. *Archives of General Psychiatry*, 57(1):47–53, 2000, doi: 10.1001/archpsyc.57.1.47. (page)

[10] G. Bartzokis, D. Sultzer, J. Mintz, L. E. Holt, P. Marx, C. Kelly Phelan, and S. R. Marder. In vivo evaluation of brain iron in Alzheimer's disease and normal subjects using MRI. *Biological Psychiatry*, 35(7):480–487, apr 1994, doi: 10.1016/0006-3223(94)90047-7. (page 17)

[11] S. Baudrexel, S. Volz, C. Preibisch, J. C. Klein, H. Steinmetz, R. Hilker, and R. Deichmann. Rapid single-scan T2*-mapping using exponential excitation pulses and image-based correction for linear background gradients. *Magnetic Resonance in Medicine*, 62(1):263–268, 2009, doi: 10.1002/mrm.21971. (page 72, 73)

[12] N. Ben-Eliezer, D. K. Sodickson, and K. T. Block. Rapid and accurate T2 mapping from multi-spin-echo data using bloch-simulation-based reconstruction. *Magnetic Resonance in Medicine*, 73(2):809–817, 2015, doi: 10.1002/mrm.25156. (page 18)

[13] B. Bender and U. Klose. The in vivo influence of white matter fiber orientation towards B0 on T2* in the human brain. *NMR in Biomedicine*, 23(9):1071–1076, nov 2010, doi: 10.1002/nbm.1534. (page 19)

[14] M. A. Bernstein, K. F. King, and X. J. Zhou. *Handbook of MRI Pulse Sequences*. Elsevier Inc., sep 2004, doi: 10.1016/B978-0-12-092861-3.X5000-6. (page 45, 76)

[15] B. Bilgic, A. Pfefferbaum, T. Rohlfing, E. V. Sullivan, and E. Adalsteinsson. MRI estimates of brain iron concentration in normal aging using quantitative susceptibility mapping. *NeuroImage*, 59(3):2625–2635, 2012, doi: 10.1016/j.neuroimage.2011.08.077. (page 17)

[16] C. Birkl, M. Soellradl, A. Toeglhofer, J. Haybaeck, L. Pirpamer, F. Fazekas, S. Ropele, and C. Langkammer. Effect of Vendor Specific Formalin Composition and Concentration on Post-Mortem MRI of Human Brain Tissue. In *Proceedings of the 25th Annual Meeting of ISMRM*, Honolulu, USA, 2018. (page)

[17] C. Birkl, M. Soellradl, A. M. Toeglhofer, S. Krassnig, M. Leoni, L. Pirpamer, T. Vorauer, H. Krenn, J. Haybaeck, F. Fazekas, S. Ropele, and C. Langkammer. Effects of concentration and vendor specific composition of formalin on postmortem MRI of the human brain. *Magnetic Resonance in Medicine*, 79(2):1111–1115, 2018, doi: 10.1002/mrm.26699. (page)

[18] A. M. Blamire, D. L. Rothman, and T. Nixon. Dynamic shim updating: A new approach towards optimized whole brain shimming. *Magnetic Resonance in Medicine*, 36(1):159–165, jul 1996, doi: 10.1002/mrm.1910360125. (page 28)

[19] F. Bloch. Nuclear induction. *Physical Review*, 70(7-8):460–474, 1946, doi: 10.1103/PhysRev.70.460. (page 7)

[20] N. Bloembergen, E. M. Purcell, and R. V. Pound. Relaxation effects in nuclear magnetic resonance absorption. *Physical Review*, 73(7):679–712, 1948, doi: 10.1103/PhysRev.73.679. (page 7, 8)

[21] F. A. Breuer, M. Blaimer, M. F. Mueller, N. Seiberlich, R. M. Heidemann, M. A. Griswold, and P. M. Jakob. Controlled aliasing in volumetric parallel imaging (2D CAIPIRINHA). *Magnetic Resonance in Medicine*, 55(3):549–556, mar 2006, doi: 10.1002/mrm.20787. (page 74, 114)

[22] R. A. Brooks. T2-shortening by strongly magnetized spheres: A chemical exchange model. *Magnetic Resonance in Medicine*, 47(2):388–391, 2002, doi: 10.1002/mrm.10064. (page 9, 10)

[23] R. A. Brooks, F. Moiny, and P. Gillis. On T2-shortening by weakly magnetized particles: The chemical exchange model. *Magnetic Resonance in Medicine*, 45(6):1014–1020, 2001, doi: 10.1002/mrm.1135. (page 10)

[24] R. J. Brown. Distribution of fields from randomly placed dipoles: Free-precession signal decay as result of magnetic grains. *Physical Review*, 121(5):1379–1382, 1961, doi: 10.1103/PhysRev.121.1379. (page 7, 9, 10)

[25] R. W. Brown, Y. C. N. Cheng, E. M. Haacke, M. R. Thompson, and R. Venkatesan. *Magnetic Resonance Imaging: Physical Principles and Sequence Design: Second Edition*, volume 9780471720. Wiley Blackwell, Chichester, UK, jun 2014, doi: 10.1002/9781118633953. (page 28, 76, 90)

[26] H. Y. Carr. Steady-state free precession in nuclear magnetic resonance. *Physical Review*, 112(5):1693–1701, dec 1958, doi: 10.1103/PhysRev.112.1693. (page 11)

[27] K. E. Chappell, M. D. Robson, A. Stonebridge-Foster, A. Glover, J. M. Allsop, A. D. Williams, A. H. Herlihy, J. Moss, P. Gishen, and G. M. Bydder. Magic Angle Effects in MR Neurography. *American Journal of Neuroradiology*, 25(3):431–440, 2004, doi: 10.1016/s0513-5117(08)70339-9. (page 18)

[28] N. K. Chen and A. M. Wyrwicz. Removal of intravoxel dephasing artifact in gradient-echo images using a field-map based RF refocusing technique. *Magnetic Resonance in Medicine*, 42(4):807–812, oct 1999, doi: 10.1002/(SICI)1522-2594(199910)42:4⟨807::AID-MRM25⟩3.0.CO;2-8. (page 38)

[29] W. C. Chen, S. Foxley, and K. L. Miller. Detecting microstructural properties of white matter based on compartmentalization of magnetic susceptibility. *NeuroImage*, 70:1–9, 2013, doi: 10.1016/j.neuroimage.2012.12.032. (page 21)

[30] A. Cherubini, P. Péran, G. E. Hagberg, A. E. Varsi, G. Luccichenti, C. Caltagirone, U. Sabatini, and G. Spalletta. Characterization of white matter fiber bundles with

T2* relaxometry and diffusion tensor imaging. *Magnetic Resonance in Medicine*, 61(5):1066–1072, 2009, doi: 10.1002/mrm.21978. (page 18)

[31] Z. H. Cho and Y. M. Ro. Reduction of susceptibility artifact in gradient-echo imaging. *Magnetic resonance in medicine*, 23(1):193–200, jan 1992. (page 38)

[32] K. A. Christensen, D. M. Grant, E. M. Schulman, and C. Walling. Optimal determination of relaxation times of Fourier transform nuclear magnetic resonance. Determination of spin-lattice relaxation times in chemically polarized species. *Journal of Physical Chemistry*, 78(19):1971–1976, 1974, doi: 10.1021/j100612a022. (page 24)

[33] C. M. Collins, B. Yang, Q. X. Yang, and M. B. Smith. Numerical calculations of the static magnetic field in three-dimensional multi-tissue models of the human head. *Magnetic Resonance Imaging*, 20(5):413–424, 2002, doi: 10.1016/S0730-725X(02)00507-6. (page 118)

[34] J. R. Connor, B. S. Snyder, J. L. Beard, R. E. Fine, and E. J. Mufson. Regional distribution of iron and iron-regulatory proteins in the brain in aging and Alzheimer's disease. *Journal of Neuroscience Research*, 31(2):327–335, 1992, doi: 10.1002/jnr.490310214. (page 16)

[35] R. T. Constable and D. D. Spencer. Composite image formation in z-shimmed functional MR imaging. *Magnetic Resonance in Medicine*, 42(1):110–117, 1999, doi: 10.1002/(SICI)1522-2594(199907)42:1⟨110::AID-MRM15⟩3.0.CO;2-3. (page 38)

[36] A. P. Crawley, M. L. Wood, and R. M. Henkelman. Elimination of transverse coherences in FLASH MRI. *Magnetic Resonance in Medicine*, 8(3):248–260, 1988, doi: 10.1002/mrm.1910080303. (page 13)

[37] R. Crichton. *Iron Metabolism: From Molecular Mechanisms to Clinical Consequences: Fourth Edition*. 2016, doi: 10.1002/9781118925645. (page 15)

[38] R. Cusack, B. Russell, S. M. Cox, C. De Panfilis, C. Schwarzbauer, and R. Ansorge. An evaluation of the use of passive shimming to improve frontal sensitivity in fMRI. *NeuroImage*, 24(1):82–91, 2005, doi: 10.1016/j.neuroimage.2004.08.029. (page 29)

[39] H. Dahnke and T. Schaeffter. Limits of detection of SPIO at 3.0 T using T2* relaxometry. *Magnetic Resonance in Medicine*, 53(5):1202–1206, may 2005, doi: 10.1002/mrm.20435. (page 31, 72, 73, 76)

[40] Y. H. Dai and Y. Yuan. A nonlinear conjugate gradient method with a strong global convergence property. *SIAM Journal on Optimization*, 10(1):177–182, jul 1999, doi: 10.1137/S1052623497318992. (page 120)

[41] R. Damadian. Tumor detection by nuclear magnetic resonance. *Science*, 171(3976):1151–1153, 1971, doi: 10.1126/science.171.3976.1151. (page 1)

[42] A. Damulina, L. Pirpamer, M. Soellradl, M. Sackl, C. Tinauer, E. Hofer, C. Enzinger, B. Gesierich, M. Duering, S. Ropele, R. Schmidt, and C. Langkammer. Cross-sectional and longitudinal assessment of brain iron level in Alzheimer disease using 3-T MRI. *Radiology*, 296(3):619–626, 2020, doi: 10.1148/radiol.2020192541. (page)

[43] R. A. de Graaf. Magnetic Field Shimming. In *Proceedings of the 27th Annual Meeting of ISMRM, Montreal, Canada*, 2019. (page 28)

[44] R. A. De Graaf, P. B. Brown, S. McIntyre, T. W. Nixon, K. L. Behar, and D. L. Rothman. High magnetic field water and metabolite proton T1 and T 2 relaxation in rat brain in vivo. *Magnetic Resonance in Medicine*, 56(2):386–394, 2006, doi: 10.1002/mrm.20946. (page 6, 7)

[45] R. A. De Graaf, P. B. Brown, S. McIntyre, D. L. Rothman, and T. W. Nixon. Dynamic shim updating (DSU) for multislice signal acquisition. *Magnetic Resonance in Medicine*, 49(3):409–416, 2003, doi: 10.1002/mrm.10404. (page 28)

[46] H. W. De Haan. Mechanisms of proton spin dephasing in a system of magnetic particles. *Magnetic Resonance in Medicine*, 66(6):1748–1758, 2011, doi: 10.1002/mrm.22966. (page 9, 10)

[47] C. Denk, E. H. Torres, A. Mackay, and A. Rauscher. The influence of white matter fibre orientation on MR signal phase and decay. *NMR in Biomedicine*, 24(3):246–252, 2011, doi: 10.1002/nbm.1581. (page 18)

[48] S. C. L. Deoni, B. K. Rutt, and T. M. Peters. Rapid combined T1 and T2 mapping using gradient recalled acquisition in the steady state. *Magnetic Resonance in Medicine*, 49(3):515–526, 2003, doi: 10.1002/mrm.10407. (page 24)

[49] S. C. Deoni, B. K. Rutt, T. Arun, C. Pierpaoli, and D. K. Jones. Gleaning multicomponent T1 and T2 information from steady-state imaging data. *Magnetic Resonance in Medicine*, 60(6):1372–1387, 2008, doi: 10.1002/mrm.21704. (page 24)

[50] D. T. Dexter, F. R. Wells, F. Agid, Y. Agid, A. J. Lees, P. Jenner, and C. D. Marsden. Increased nigral iron content in postmortem parkinsonian brain, nov 1987, doi: 10.1016/S0140-6736(87)91361-4. (page 16)

[51] A. A. Di Tucci, G. Matta, S. Deplano, A. Gabbas, C. Depau, D. Derudas, G. Caocci, A. Agus, and E. Angelucci. Myocardial iron overload assessment by T2* magnetic resonance imaging in adult transfusion dependent patients with acquired anemias. *Haematologica*, 93(9):1385–1388, 2008, doi: 10.3324/haematol.12759. (page 119)

[52] W. T. Dixon. Simple proton spectroscopic imaging. *Radiology*, 153(1):189–94, oct 1984, doi: 10.1148/radiology.153.1.6089263. (page 14)

[53] M. D. Does. Multi Exponential Relaxation Analysis toolbox for MATLAB. (page 61)

[54] P. Douek, R. Turner, J. Pekar, N. Patronas, and D. Le Bihan. Mr color mapping of myelin fiber orientation. *Journal of Computer Assisted Tomography*, 15(6):923–929, 1991, doi: 10.1097/00004728-199111000-00003. (page 18)

[55] Y. P. Du, R. Chu, D. Hwang, M. S. Brown, B. K. Kleinschmidt-DeMasters, D. Singel, and J. H. Simon. Fast multislice mapping of the myelin water fraction using multicompartment analysis of T2* decay at 3T: A preliminary postmortem study. *Magnetic Resonance in Medicine*, 58(5):865–870, nov 2007, doi: 10.1002/mrm.21409. (page 24, 30)

[56] A. N. Dula, D. F. Gochberg, H. L. Valentine, W. M. Valentine, and M. D. Does. Multiexponential T2, magnetization transfer, and Quantitative histology in white matter tracts of rat spinal cord. *Magnetic Resonance in Medicine*, 63(4):902–909, 2010, doi: 10.1002/mrm.22267. (page 23)

[57] J. H. Duyn and T. M. Barbara. Sphere of lorentz and demagnetization factors in white matter. *Magnetic Resonance in Medicine*, 72(1):1–3, 2014, doi: 10.1002/mrm.25021. (page 20)

[58] R. R. Ernst and W. A. Anderson. Application of Fourier Transform Spectroscopy to Magnetic Resonance. *Review of Scientific Instruments*, 37(1):93–102, jan 1966, doi: 10.1063/1.1719961. (page 13, 56, 92, 114, 119)

[59] M. A. Fernndez-Seara and F. W. Wehrli. Postprocessing technique to correct for background gradients in image-based R2/(*) measurements. *Magnetic Resonance in Medicine*, 44(3):358–366, 2000, doi: 10.1002/1522-2594(200009)44:3⟨358::AID-MRM3⟩3.0.CO;2-I. (page 31, 72, 73, 76)

[60] G. C. Ford, P. M. Harrison, D. W. Rice, J. M. Smith, A. Treffry, J. L. White, and J. Yariv. Ferritin: design and formation of an iron-storage molecule. *Philosophical transactions of the Royal Society of London. Series B, Biological sciences*, 304(1121):551–565, 1984, doi: 10.1098/rstb.1984.0046. (page 16)

[61] A. Fragasso, A. Ciancio, C. Mannarella, C. Gaudiano, O. Scarciolla, C. Ottonello, M. Francone, M. Nardella, A. Peluso, A. Melpignano, M. R. Veglio, G. Quarta, and C. Turchetti. Myocardial iron overload assessed by magnetic resonance imaging (MRI)T2* in multi-transfused patients with thalassemia and acquired anemias. *European Journal of Internal Medicine*, 22(1):62–65, 2011, doi: 10.1016/j.ejim.2010.10.005. (page 119)

[62] J. Frahm, K. D. Merboldt, and W. Hänicke. Direct FLASH MR imaging of magnetic field inhomogeneities by gradient compensation, apr 1988, doi: 10.1002/mrm.1910060412. (page 38, 39)

[63] R. Freeman and H. D. Hill. Phase and intensity anomalies in fourier transform NMR. *Journal of Magnetic Resonance (1969)*, 4(3):366–383, 1971, doi: 10.1016/0022-2364(71)90047-3. (page 12)

[64] G. D. Fullerton, I. L. Cameron, and V. A. Ord. Orientation of tendons in the magnetic field and its effect on T2 relaxation times. *Radiology*, 155(2):433–435, 1985, doi: 10.1148/radiology.155.2.3983395. (page 18)

[65] N. Gelman, J. M. Gorell, P. B. Barker, R. M. Savage, E. M. Spickler, J. P. Windham, and R. A. Knight. MR imaging of human brain at 3.0 T: Preliminary report on transverse relaxation rates and relation to estimated iron content. *Radiology*, 210(3):759–767, mar 1999, doi: 10.1148/radiology.210.3.r99fe41759. (page 17)

[66] P. Gillis and S. H. Koenig. Transverse Relaxation of Solvent Protons Induced by Magnetized Spheres. *Magnetic Resonance in Medicine*, 345(5):323–345, 1987. (page 9, 16)

[67] G. H. Glover. 3D z-shim method for reduction of susceptibility effects in BOLD fMRI. *Magnetic Resonance in Medicine*, 42(2):290–299, aug 1999, doi: 10.1002/(SICI)1522-2594(199908)42:2⟨290::AID-MRM11⟩3.0.CO;2-N. (page 41)

[68] J. M. Gorell, R. J. Ordidge, G. G. Brown, J. C. Deniau, N. M. Buderer, and J. A. Helpern. Increased iron-related mri contrast in the substantia nigra in parkinson's disease. *Neurology*, 45(6):1138–1143, 1995, doi: 10.1212/WNL.45.6.1138. (page 17)

[69] Y. Gossuin, P. Gillis, A. Hocq, Q. L. Vuong, and A. Roch. Magnetic resonance relaxation properties of superparamagnetic particles. *Wiley Interdisciplinary Reviews: Nanomedicine and Nanobiotechnology*, 1(3):299–310, 2009, doi: 10.1002/wnan.36. (page 17)

[70] Y. Gossuin, A. Roch, R. N. Muller, P. Gillis, and F. Lo Bue. Anomalous nuclear magnetic relaxation of aqueous solutions of ferritin: An unprecedented first-order mechanism. *Magnetic Resonance in Medicine*, 48(6):959–964, 2002, doi: 10.1002/mrm.10316. (page 16, 17)

[71] J. M. Graham. Brain iron deposition in Parkinson's disease imaged using the PRIME magnetic resonance sequence. *Brain*, 123(12):2423–2431, 2000, doi: 10.1093/brain/123.12.2423. (page 17)

[72] M. A. Griswold, P. M. Jakob, R. M. Heidemann, M. Nittka, V. Jellus, J. Wang, B. Kiefer, and A. Haase. Generalized Autocalibrating Partially Parallel Acquisitions (GRAPPA). *Magnetic Resonance in Medicine*, 47(6):1202–1210, 2002, doi: 10.1002/mrm.10171. (page 114)

[73] E. M. Haacke, M. Ayaz, A. Khan, E. S. Manova, B. Krishnamurthy, L. Gollapalli, C. Ciulla, I. Kim, F. Petersen, and W. Kirsch. Establishing a baseline phase behavior in magnetic resonance imaging to determine normal vs. abnormal iron content in the brain. *Journal of Magnetic Resonance Imaging*, 26(2):256–264, 2007, doi: 10.1002/jmri.22987. (page 16)

[74] E. M. Haacke, R. W. Brown, M. R. Thompson, and R. Venkatesan. *Magnetic Resonance Imaging: Physical Principles and Sequence Design*. 1999. (page 6, 7, 21)

[75] E. M. Haacke, N. Y. Cheng, M. J. House, Q. Liu, J. Neelavalli, R. J. Ogg, A. Khan, M. Ayaz, W. Kirsch, and A. Obenaus. Imaging iron stores in the brain using magnetic resonance imaging. *Magnetic Resonance Imaging*, 23(1):1–25, jan 2005, doi: 10.1016/j.mri.2004.10.001. (page 16)

[76] E. L. Hahn. Nuclear induction due to free larmor precession, jan 1950, doi: 10.1103/PhysRev.77.297.2. (page 5)

[77] E. L. Hahn. Spin echoes. *Physical Review*, 80(4):580–594, 1950, doi: 10.1103/PhysRev.80.580. (page 6, 14)

[78] L. Haider, C. Simeonidou, G. Steinberger, S. Hametner, N. Grigoriadis, G. Deretzi, G. G. Kovacs, A. Kutzelnigg, H. Lassmann, and J. M. Frischer. Multiple sclerosis deep grey matter: The relation between demyelination, neurodegeneration, inflammation and iron. *Journal of Neurology, Neurosurgery and Psychiatry*, 85(12):1386–1395, 2014, doi: 10.1136/jnnp-2014-307712. (page 16)

[79] B. Hallgrven and P. Sourander. The effect of age on the non-haemin iron in the human brain. *Journal of Neurochemistry*, 3(1):41–51, oct 1958, doi: 10.1111/j.1471-4159.1958.tb12607.x. (page 15, 17)

[80] S. Hametner, I. Wimmer, L. Haider, S. Pfeifenbring, W. Brück, and H. Lassmann. Iron and neurodegeneration in the multiple sclerosis brain. *Annals of Neurology*, 74(6):848–861, 2013, doi: 10.1002/ana.23974. (page 16)

[81] D. Han, Y. Nam, S. M. Gho, and D. H. Kim. Volumetric R2* mapping using z-shim multi-echo gradient echo imaging. *Magnetic Resonance in Medicine*, 73(3):1164–1170, 2015, doi: 10.1002/mrm.25206. (page 42, 74, 120)

[82] H. Han, A. W. Song, and T. K. Truong. Integrated parallel reception, excitation, and shimming (iPRES). *Magnetic Resonance in Medicine*, 70(1):241–247, 2013, doi: 10.1002/mrm.24766. (page 29)

[83] K. D. H. Han D, Nam Y, Gho SM. Macroscopic B0 inhomogeneity corrected QSM based on a field mapping algorithm using a singlescan 3D z-shim multi-echo GRE. In *Proceedings of the 21th Annual Meeting of ISMRM, Salt Lake City, USA*, page 3852, Salt Lake City, 2013. (page 42)

[84] J. S. Hankins, M. B. McCarville, R. B. Loeffler, M. P. Smeltzer, M. Onciu, F. A. Hoffer, C. S. Li, W. C. Wang, R. E. Ware, and C. M. Hillenbrand. R2* magnetic resonance imaging of the liver in patients with iron overload. *Blood*, 113(20):4853–4855, 2009, doi: 10.1182/blood-2008-12-191643. (page 119)

[85] S. Hao, J. A. Fessler, D. C. Noll, and J. F. Nielsen. Joint design of excitation k-space trajectory and RF pulse for small-tip 3D tailored excitation in MRI. *IEEE Transactions on Medical Imaging*, 35(2):468–479, 2016, doi: 10.1109/TMI.2015.2478880. (page 38)

[86] K. D. Harkins, A. N. Dula, and M. D. Does. Effect of intercompartmental water exchange on the apparent myelin water fraction in multiexponential T2 measurements of rat spinal cord. *Magnetic Resonance in Medicine*, 67(3):793–800, 2012, doi: 10.1002/mrm.23053. (page 23)

[87] C. T. Harris, W. B. Handler, and B. A. Chronik. A new approach to shimming: The dynamically controlled adaptive current network. *Magnetic Resonance in Medicine*, 71(2):859–869, 2014, doi: 10.1002/mrm.24724. (page 29)

[88] P. M. Harrison and P. Arosio. The ferritins: Molecular properties, iron storage function and cellular regulation. *Biochimica et Biophysica Acta - Bioenergetics*, 1275(3):161–203, 1996, doi: 10.1016/0005-2728(96)00022-9. (page 16)

[89] K. M. Hasan, I. S. Walimuni, L. A. Kramer, and P. A. Narayana. Human brain iron mapping using atlas-based T 2 relaxometry. *Magnetic Resonance in Medicine*, 67(3):731–739, 2012, doi: 10.1002/mrm.23054. (page 17)

[90] T. He. Cardiovascular magnetic resonance T2* for tissue iron assessment in the heart. *Quantitative imaging in medicine and surgery*, 4(5):407–40712, 2014, doi: 10.3978/j.issn.2223-4292.2014.10.05. (page 119)

[91] X. He and D. A. Yablonskiy. Biophysical mechanisms of phase contrast in gradient echo MRI. *Proceedings of the National Academy of Sciences of the United States of America*, 106(32):13558–13563, aug 2009, doi: 10.1073/pnas.0904899106. (page 20, 21)

[92] K. A. Heberlein and X. Hu. Simultaneous Acquisition of Gradient-Echo and Asymmetric Spin-Echo for Single-Shot Z-Shim: Z-SAGA. *Magnetic Resonance in Medicine*, 51(1):212–216, 2004, doi: 10.1002/mrm.10680. (page 38)

[93] R. M. Henkelman, G. J. Stanisz, J. K. Kim, and M. J. Bronskill. Anisotropy of NMR properties of tissues. *Magnetic Resonance in Medicine*, 32(5):592–601, 1994, doi: 10.1002/mrm.1910320508. (page 18)

[94] D. Hernando, K. K. Vigen, A. Shimakawa, and S. B. Reeder. R2* mapping in the presence of macroscopic B0 field variations. *Magnetic Resonance in Medicine*, 68(3):830–840, 2012, doi: 10.1002/mrm.23306. (page 56, 73, 76, 97, 119)

[95] T. Hikita, K. Abe, S. Sakoda, H. Tanaka, K. Murase, and N. Fujita. Determination of transverse relaxation rate for estimating iron deposits in central nervous system. *Neuroscience Research*, 51(1):67–71, 2005, doi: 10.1016/j.neures.2004.09.006. (page 17)

[96] E. C. Hirsch, J. P. Brandel, P. Galle, F. Javoy-Agid, and Y. Agid. Iron and Aluminum Increase in the Substantia Nigra of Patients with Parkinson's Disease: An X-Ray Microanalysis. *Journal of Neurochemistry*, 56(2):446–451, feb 1991, doi: 10.1111/j.1471-4159.1991.tb08170.x. (page 16)

[97] N. M. Hirsch and C. Preibisch. T2* mapping with background gradient correction using different excitation pulse shapes. *AJNR. American journal of neuroradiology*, 34(6):E65–8, jun 2013, doi: 10.3174/ajnr.A3021. (page 72, 73)

[98] D. I. Hoult. The solution of the bloch equations in the presence of a varying B1 field-An approach to selective pulse analysis. *Journal of Magnetic Resonance (1969)*, 35(1):69–86, jul 1979, doi: 10.1016/0022-2364(79)90078-7. (page 32, 45, 57, 92)

[99] D. I. Hoult and D. Lee. Shimming a superconducting nuclear-magnetic-resonance imaging magnet with steel. *Review of Scientific Instruments*, 56(1):131–135, 1985, doi: 10.1063/1.1138480. (page 28)

[100] X. Hu and S. G. Kim. Reduction of signal fluctuation in functional MRI using navigator echoes. *Magnetic Resonance in Medicine*, 31(5):495–503, 1994, doi: 10.1002/mrm.1910310505. (page 25, 48, 60, 98, 117)

[101] D. Hwang, D. H. Kim, and Y. P. Du. In vivo multi-slice mapping of myelin water content using T2* decay. *NeuroImage*, 52(1):198–204, aug 2010, doi: 10.1016/j.neuroimage.2010.04.023. (page 20, 24, 25)

[102] M. Jenkinson and S. Smith. A global optimisation method for robust affine registration of brain images. *Medical image analysis*, 5(2):143–56, jun 2001. (page 60, 61, 102)

[103] M. Jenkinson. Fast, automated, N-dimensional phase-unwrapping algorithm. *Magnetic Resonance in Medicine*, 49(1):193–197, 2003, doi: 10.1002/mrm.10354. (page 59, 78, 100, 118)

[104] M. Jenkinson, P. Bannister, M. Brady, and S. Smith. Improved Optimization for the Robust and Accurate Linear Registration and Motion Correction of Brain Images. *NeuroImage*, 17(2):825–841, oct 2002, doi: 10.1006/NIMG.2002.1132. (page 60, 61, 102)

[105] P. Jezzard. Shim Coil Design, Limitations and Implications. *Abstracts from the International Society of Magnetic Resonance in Medicine (ISMRM) Annual Meeting*, pages 0–5, 2006. (page 27)

[106] G. Johnson, Y. Z. Wadghiri, and D. H. Turnbull. 2D multislice and 3D MRI sequences are often equally sensitive. *Magnetic Resonance in Medicine*, 41(4):824–828, 1999, doi: 10.1002/(SICI)1522-2594(199904)41:4⟨824::AID-MRM23⟩3.0.CO;2-1. (page 76)

[107] C. Juchem, P. B. Brown, T. W. Nixon, S. McIntyre, D. L. Rothman, and R. A. De Graaf. Multicoil shimming of the mouse brain. *Magnetic Resonance in Medicine*, 66(3):893–900, 2011, doi: 10.1002/mrm.22850. (page 29)

[108] C. Juchem, T. W. Nixon, S. McIntyre, V. O. Boer, D. L. Rothman, and R. A. De Graaf. Dynamic multi-coil shimming of the human brain at 7 T. *Journal of Magnetic Resonance*, 212(2):280–288, 2011, doi: 10.1016/j.jmr.2011.07.005. (page 28, 29)

[109] E. Kandel, E. R. Kandel, e. al], J. H. Jessell, J. Schwartz, and T. Jessell. *Principles of Neural Science, Fourth Edition*. McGraw-Hill Companies,Incorporated, 2000. (page 15)

[110] O. Katrin, T. Widek, S. Martin, T. PP, G. P, T. Schwark, and E. Scheurer. Age Determination of Traumatic Subcutaneous Hematomas Using 3.0T MRI: A Feasible Approach. In *Proceedings of the 70th AAFS Annual Scientific Meeting*, Seattle, USA, 2018. (page)

[111] H. H. Kitzler, J. Su, M. Zeineh, C. Harper-Little, A. Leung, M. Kremenchutzky, S. C. Deoni, and B. K. Rutt. Deficient MWF mapping in multiple sclerosis using 3D whole-brain multi-component relaxation MRI. *NeuroImage*, 59(3):2670–2677, 2012, doi: 10.1016/j.neuroimage.2011.08.052. (page 23)

[112] K. M. Koch, P. B. Brown, D. L. Rothman, and R. A. de Graaf. Sample-specific diamagnetic and paramagnetic passive shimming. *Journal of Magnetic Resonance*, 182(1):66–74, 2006, doi: 10.1016/j.jmr.2006.06.013. (page 28)

[113] K. M. Koch, S. McIntyre, T. W. Nixon, D. L. Rothman, and R. A. de Graaf. Dynamic shim updating on the human brain. *Journal of Magnetic Resonance*, 180(2):286–296, 2006, doi: 10.1016/j.jmr.2006.03.007. (page 28)

[114] K. M. Koch, D. L. Rothman, and R. A. de Graaf. Optimization of static magnetic field homogeneity in the human and animal brain in vivo. *Progress in Nuclear Magnetic Resonance Spectroscopy*, 54(2):69–96, 2009, doi: 10.1016/j.pnmrs.2008.04.001. (page 28)

[115] M. Kochan, P. Daga, N. Burgos, M. White, M. J. Cardoso, L. Mancini, G. P. Winston, A. W. McEvoy, J. Thornton, T. Yousry, J. S. Duncan, D. Stoyanov, and S. Ourselin. Simulated field maps: Toward improved susceptibility artefact correction in interventional MRI. *Lecture Notes in Computer Science (including subseries Lecture Notes in Artificial Intelligence and Lecture Notes in Bioinformatics)*, 8498 LNCS:226–235, 2014, doi: 10.1007/978-3-319-07521-1_24. (page 118)

[116] P. Kozlowski, J. Liu, A. C. Yung, and W. Tetzlaff. High-resolution myelin water measurements in rat spinal cord. *Magnetic Resonance in Medicine*, 59(4):796–802, 2008, doi: 10.1002/mrm.21527. (page 22)

[117] M. Kruszewski. Labile iron pool: The main determinant of cellular response to oxidative stress. *Mutation Research - Fundamental and Molecular Mechanisms of Mutagenesis*, 531(1-2):81–92, 2003, doi: 10.1016/j.mrfmmm.2003.08.004. (page 15)

[118] C. Langkammer, A. Damulina, L. Pirpamer, M. Sackl, M. Soellradl, E. Hofer, M. Koini, F. Fazekas, S. Ropele, and R. Schmidt. Quantitative Susceptibility Mapping in Alzheimer's Disease. In *Proceedings of the 27th Annual Meeting of ISMRM*, Montreal, Canada, 2019. (page)

[119] C. Langkammer, A. Damulina, L. Pirpamer, M. Soellradl, E. Hofer, C. Tinauer, M. Sackl, C. Enzinger, S. Ropele, and R. Schmidt. Longitudinal assessment of brain iron deposition in Alzheimer's disease. In *Proceedings of the 28th Annual Meeting of ISMRM*, 2020. (page)

[120] C. Langkammer, N. Krebs, W. Goessler, E. Scheurer, F. Ebner, K. Yen, F. Fazekas, and S. Ropele. Quantitative MR imaging of brain iron: A postmortem validation study. *Radiology*, 257(2):455–462, 2010, doi: 10.1148/radiol.10100495. (page 17, 18)

[121] C. Langkammer, F. Schweser, N. Krebs, A. Deistung, W. Goessler, E. Scheurer, K. Sommer, G. Reishofer, K. Yen, F. Fazekas, S. Ropele, and J. R. Reichenbach. Quantitative susceptibility mapping (QSM) as a means to measure brain iron? A post mortem validation study. *NeuroImage*, 62(3):1593–1599, 2012, doi: 10.1016/j.neuroimage.2012.05.049. (page 16)

[122] C. Laule, E. Leung, D. K. B. Lis, A. L. Traboulsee, D. W. Paty, A. L. MacKay, and G. R. W. Moore. Myelin water imaging in multiple sclerosis: quantitative correlations with histopathology. *Multiple sclerosis (Houndmills, Basingstoke, England)*, 12(6):747–53, dec 2006, doi: 10.1177/1352458506070928. (page 22)

[123] C. Laule, I. M. Vavasour, G. R. Moore, J. Oger, D. K. Li, D. W. Paty, and A. L. MacKay. Water content and myelin water fraction in multiple sclerosis: A T 2 relaxation study. *Journal of Neurology*, 251(3):284–293, 2004, doi: 10.1007/s00415-004-0306-6. (page 23)

[124] C. Laule, P. Kozlowski, E. Leung, D. K. Li, A. L. MacKay, and G. R. Moore. Myelin water imaging of multiple sclerosis at 7 T: Correlations with histopathology. *NeuroImage*, 40(4):1575–1580, 2008, doi: 10.1016/j.neuroimage.2007.12.008. (page 22)

[125] C. Laule, I. M. Vavasour, E. Leung, D. K. Li, P. Kozlowski, A. L. Traboulsee, J. Oger, A. L. MacKay, and G. R. Wayne Moore. Pathological basis of diffusely abnormal white matter: Insights from magnetic resonance imaging and histology. *Multiple Sclerosis Journal*, 17(2):144–150, 2011, doi: 10.1177/1352458510384008. (page 23)

[126] P. C. Lauterbur. Image formation by induced local interactions: Examples employing nuclear magnetic resonance. *Nature*, 242(5394):190–191, 1973, doi: 10.1038/242190a0. (page 1)

[127] T. H. Le and X. Hu. Retrospective estimation and correction of physiological artifacts in fMRI by direct extraction of physiological activity from MR data. *Magnetic Resonance in Medicine*, 35(3):290–298, 1996, doi: 10.1002/mrm.1910350305. (page 48)

[128] D. Lee, J. Lee, J. Lee, and Y. Nam. Single-scan z-shim method for reducing susceptibility artifacts in gradient echo myelin water imaging. *Magnetic Resonance in Medicine*, 80(3):1101–1109, sep 2018, doi: 10.1002/mrm.27127. (page 25, 41, 74, 97, 113)

[129] H. Lee, Y. Nam, and D. H. Kim. Echo time-range effects on gradient-echo based myelin water fraction mapping at 3T. *Magnetic Resonance in Medicine*, 81(4):2799–2807, oct 2019, doi: 10.1002/mrm.27564. (page 72)

[130] H. Lee, Y. Nam, H. J. Lee, J. J. Hsu, R. G. Henry, and D. H. Kim. Improved three-dimensional multi-echo gradient echo based myelin water fraction mapping with phase related artifact correction. *NeuroImage*, 169:1–10, 2018, doi: 10.1016/j.neuroimage.2017.11.058. (page 25, 96)

[131] J. Lee, J. W. Hyun, J. Lee, E. J. Choi, H. G. Shin, K. Min, Y. Nam, H. J. Kim, and S. H. Oh. So You Want to Image Myelin Using MRI: An Overview and Practical Guide for Myelin Water Imaging, 2020, doi: 10.1002/jmri.27059. (page 23, 92)

[132] J. Lee, K. Shmueli, M. Fukunaga, P. Van Gelderen, H. Merkle, A. C. Silva, and J. H. Duyn. Sensitivity of MRI resonance frequency to the orientation of brain tissue microstructure. *Proceedings of the National Academy of Sciences of the United States of America*, 107(11):5130–5135, mar 2010, doi: 10.1073/pnas.0910222107. (page 19, 21)

[133] J. Lee, K. Shmueli, B.-T. Kang, B. Yao, M. Fukunaga, P. van Gelderen, S. Palumbo, F. Bosetti, A. C. Silva, and J. H. Duyn. The contribution of myelin to mag-

netic susceptibility-weighted contrasts in high-field MRI of the brain. *NeuroImage*, 59(4):3967–3975, feb 2012, doi: 10.1016/J.NEUROIMAGE.2011.10.076. (page 67)

[134] J. Lee, P. van Gelderen, L. W. Kuo, H. Merkle, A. C. Silva, and J. H. Duyn. T2*-based fiber orientation mapping. *NeuroImage*, 57(1):225–234, jul 2011, doi: 10.1016/j.neuroimage.2011.04.026. (page 19, 20, 21)

[135] C. Lenz, M. Klarhöfer, and K. Scheffler. Feasibility of in vivo myelin water imaging using 3D multigradient-echo pulse sequences. *Magnetic Resonance in Medicine*, 68(2):523–528, aug 2012, doi: 10.1002/mrm.23241. (page 24, 61)

[136] A. Lesch, M. Schloegl, M. Holler, K. Bredies, and R. Stollberger. Ultrafast 3D Bloch–Siegert B1+-mapping using variational modeling. *Magnetic Resonance in Medicine*, 81(2):881–892, feb 2019, doi: 10.1002/mrm.27434. (page 60, 61, 102)

[137] L. Li and J. S. Leigh. Quantifying Arbitrary Magnetic Susceptibility Distributions with MR. *Magnetic Resonance in Medicine*, 51(5):1077–1082, may 2004, doi: 10.1002/mrm.20054. (page 16)

[138] T. Q. Li, P. van Gelderen, H. Merkle, L. Talagala, A. P. Koretsky, and J. Duyn. Extensive heterogeneity in white matter intensity in high-resolution T2*-weighted MRI of the human brain at 7.0 T. *NeuroImage*, 32(3):1032–1040, 2006, doi: 10.1016/j.neuroimage.2006.05.053. (page 18)

[139] X. Li, P. Van Gelderen, P. Sati, J. A. De Zwart, D. S. Reich, and J. H. Duyn. Detection of demyelination in multiple sclerosis by analysis of T2* relaxation at 7 T. *NeuroImage: Clinical*, 7:709–714, 2015, doi: 10.1016/j.nicl.2015.02.021. (page 23)

[140] Z. Li, G. Wu, X. Zhao, F. Luo, and S. J. Li. Multiecho segmented EPI with z-shimmed background gradient compensation (MESBAC) pulse sequence for fMRI. *Magnetic Resonance in Medicine*, 48(2):312–321, 2002, doi: 10.1002/mrm.10219. (page 38)

[141] C. Liu. Susceptibility tensor imaging. *Magnetic Resonance in Medicine*, 63(6):1471–1477, 2010, doi: 10.1002/mrm.22482. (page 19)

[142] M. A. Lovell, J. D. Robertson, W. J. Teesdale, J. L. Campbell, and W. R. Markesbery. Copper, iron and zinc in Alzheimer's disease senile plaques. *Journal of the Neurological Sciences*, 158(1):47–52, 1998, doi: 10.1016/S0022-510X(98)00092-6. (page 16)

[143] K. M. Lüdeke, P. Röschmann, and R. Tischler. Susceptibility artefacts in NMR imaging. *Magnetic Resonance Imaging*, 3(4):329–343, 1985, doi: 10.1016/0730-725X(85)90397-2. (page 27)

[144] J. Luo, X. He, and D. A. Yablonskiy. Magnetic susceptibility induced white matter MR signal frequency shifts - Experimental comparison between Lorentzian sphere and generalized Lorentzian approaches. *Magnetic Resonance in Medicine*, 71(3):1251–1263, 2014, doi: 10.1002/mrm.24762. (page 20)

[145] J. Luo, B. D. Jagadeesan, A. H. Cross, and D. A. Yablonskiy. Gradient Echo Plural Contrast Imaging – signal model and derived contrasts: T2*, T1, Phase, SWI, T1f, FST2*and T2*-SWI. *NeuroImage*, 60(2):1073–1082, 2012, doi: 10.1016/j.neuroimage.2012.01.108. (page 51, 52, 60, 74, 99)

[146] Y. Lvovsky and P. Jarvis. Superconducting systems for MRI-present solutions and new trends. *IEEE Transactions on Applied Superconductivity*, 15(2 PART II):1317–1325, 2005, doi: 10.1109/TASC.2005.849580. (page 28)

[147] J. Ma and F. W. Wehrli. Method for image-based measurement of the reversible and irreversible contribution to the transverse-relaxation rate. *Journal of Magnetic Resonance - Series B*, 111(1):61–69, 1996, doi: 10.1006/jmrb.1996.0060. (page 17)

[148] A. Mackay, K. Whittall, J. Adler, D. Li, D. Paty, and D. Graeb. In vivo visualization of myelin water in brain by magnetic resonance. *Magnetic Resonance in Medicine*, 31(6):673–677, 1994, doi: 10.1002/mrm.1910310614. (page 20, 21, 23, 30)

[149] P. Mansfield and A. A. Maudsley. Medical imaging by NMR. *British Journal of Radiology*, 50(591):188–194, 1977, doi: 10.1259/0007-1285-50-591-188. (page 1)

[150] J. P. Marques and R. Bowtell. Application of a fourier-based method for rapid calculation of field inhomogeneity due to spatial variation of magnetic susceptibility. *Concepts in Magnetic Resonance Part B: Magnetic Resonance Engineering*, 25(1):65–78, 2005, doi: 10.1002/cmr.b.20034. (page 118)

[151] H. Marshall, J. V. Hajnal, J. E. Warren, R. J. Wise, and D. J. Larkman. An efficient automated z-shim based method to correct through-slice signal loss in EPI at 3T. *Magnetic Resonance Materials in Physics, Biology and Medicine*, 22(3):187–200, 2009, doi: 10.1007/s10334-009-0164-4. (page 38)

[152] Y. Meng and H. Lei. A single-scan T2* mapping method based on two gradient-echo images with compensation for macroscopic field inhomogeneity. *Magnetic Resonance in Medicine*, 60(6):1388–1395, dec 2008, doi: 10.1002/mrm.21731. (page 40, 42)

[153] K. A. Miszkiel, M. N. Paley, I. D. Wilkinson, M. A. Hall-Craggs, R. Ordidge, B. E. Kendall, R. F. Miller, and M. J. Harrison. The measurement of R2, R2 and R2' in HIV-infected patients using the prime sequence as a measure of brain iron deposition. *Magnetic Resonance Imaging*, 15(10):1113–1119, 1997, doi: 10.1016/S0730-725X(97)00089-1. (page 17)

[154] G. R. Moore, C. Laule, A. MacKay, E. Leung, D. K. Li, G. Zhao, A. L. Traboulsee, and D. W. Paty. Dirty-appearing white matter in multiple sclerosis: Preliminary observations of myelin phospholipid and axonal loss. *Journal of Neurology*, 255(11):1802–1811, 2008, doi: 10.1007/s00415-008-0002-z. (page 23)

[155] S. S. Mori and B. J. Crain. *MRI atlas of human white matter*. Elsevier, 2005. (page 61)

[156] S. Mori, B. J. Crain, V. P. Chacko, and P. C. Van Zijl. Three-dimensional tracking of axonal projections in the brain by magnetic resonance imaging. *Annals of Neurology*, 45(2):265–269, 1999, doi: 10.1002/1531-8249(199902)45:2⟨265::AID-ANA21⟩3.0.CO;2-3. (page 18)

[157] S. Mori, B. J. Crain, V. P. Chacko, and P. C. Van Zijl. Three-dimensional tracking of axonal projections in the brain by magnetic resonance imaging. *Annals of Neurology*, 45(2):265–269, feb 1999, doi: 10.1002/1531-8249(199902)45:2⟨265::AID-ANA21⟩3.0.CO;2-3. (page 18)

[158] G. Morrell and D. Spielman. Dynamic shimming for multi-slice magnetic resonance imaging. *Magnetic Resonance in Medicine*, 38(3):477–483, 1997, doi: 10.1002/mrm.1910380316. (page 28)

[159] Y. Nam, D. Han, and D. H. Kim. Single-scan R2* measurement with macroscopic field inhomogeneity correction. *NeuroImage*, 63(4):1790–1799, dec 2012, doi: 10.1016/j.neuroimage.2012.08.062. (page 40, 41, 42, 96, 97, 102, 113)

[160] Y. Nam, D. H. Kim, and J. Lee. Physiological noise compensation in gradient-echo myelin water imaging. *NeuroImage*, 120:345–349, oct 2015, doi: 10.1016/j.neuroimage.2015.07.014. (page 25)

[161] Y. Nam, J. Lee, D. Hwang, and D. H. Kim. Improved estimation of myelin water fraction using complex model fitting. *NeuroImage*, 116:214–221, 2015, doi: 10.1016/j.neuroimage.2015.03.081. (page 24, 74)

[162] S. Ogawa, T. M. Lee, A. R. Kay, and D. W. Tank. Brain magnetic resonance imaging with contrast dependent on blood oxygenation. *Proceedings of the National Academy of Sciences of the United States of America*, 87(24):9868–9872, 1990, doi: 10.1073/pnas.87.24.9868. (page 2)

[163] S. Ogawa, D. W. Tank, R. Menon, J. M. Ellermann, S. G. Kim, H. Merkle, and K. Ugurbil. Intrinsic signal changes accompanying sensory stimulation: functional brain mapping with magnetic resonance imaging. *Proceedings of the National Academy of Sciences of the United States of America*, 89(13):5951–5, jul 1992, doi: 10.1073/pnas.89.13.5951. (page 2)

[164] R. J. Ogg, J. W. Langston, E. M. Haacke, R. G. Steen, and J. S. Taylor. The correlation between phase shifts in gradient-echo MR images and regional brain iron concentration. *Magnetic Resonance Imaging*, 17(8):1141–1148, oct 1999, doi: 10.1016/S0730-725X(99)00017-X. (page 16)

[165] J. Oh, E. T. Han, M. C. Lee, S. J. Nelson, and D. Pelletier. Multislice brain myelin water fractions at 3T in multiple sclerosis. *Journal of Neuroimaging*, 17(2):156–163, 2007, doi: 10.1111/j.1552-6569.2007.00098.x. (page 24)

[166] J. Oh, E. T. Han, D. Pelletier, and S. J. Nelson. Measurement of in vivo multi-component T2 relaxation times for brain tissue using multi-slice T2 prep at 1.5 and 3 T. *Magnetic Resonance Imaging*, 24(1):33–43, 2006, doi: 10.1016/j.mri.2005.10.016. (page 24)

[167] S. S. Oh, S. H. Oh, Y. Nam, D. Han, R. B. Stafford, J. Hwang, D. H. Kim, H. Park, and J. Lee. Improved susceptibility weighted imaging method using multi-echo acquisition. *Magnetic Resonance in Medicine*, 72(2):452–458, 2014, doi: 10.1002/mrm.24940. (page 43)

[168] A. Oppelt, R. Graumann, H. Barfuss, H. Fischer, W. Hartl, and W. Schajor. FISP, a novel, fast pulse sequence for nuclear magnetic resonance imaging. *Electromedica*, 54(1):15–18, 1986. (page 11)

[169] R. J. Ordidge, J. M. Gorell, J. C. Deniau, R. A. Knight, and J. A. Helpern. Assessment of relative brain iron concentrations using T2-weighted and T2*-weighted MRI at 3 Tesla. *Magnetic Resonance in Medicine*, 32(3):335–341, 1994, doi: 10.1002/mrm.1910320309. (page 17)

[170] K. Oshio and D. A. Feinberg. GRASE (Gradient-and Spin-Echo) imaging: A novel fast MRI technique. *Magnetic Resonance in Medicine*, 20(2):344–349, 1991, doi: 10.1002/mrm.1910200219. (page 23)

[171] B. Patenaude, S. M. Smith, D. N. Kennedy, and M. Jenkinson. A Bayesian model of shape and appearance for subcortical brain segmentation. *NeuroImage*, 56(3):907–922, jun 2011, doi: 10.1016/j.neuroimage.2011.02.046. (page 60, 79, 102)

[172] A. Pfefferbaum, E. Adalsteinsson, T. Rohlfing, and E. V. Sullivan. MRI estimates of brain iron concentration in normal aging: Comparison of field-dependent (FDRI) and phase (SWI) methods. *NeuroImage*, 47(2):493–500, 2009, doi: 10.1016/j.neuroimage.2009.05.006. (page 17)

[173] S. K. Piechnik, J. Evans, L. H. Bary, R. G. Wise, and P. Jezzard. Functional changes in CSF volume estimated using measurement of water T2 relaxation. *Magnetic Resonance in Medicine*, 61(3):579–586, 2009, doi: 10.1002/mrm.21897. (page 6, 8)

[174] B. P. Poncelet, V. J. Wedeen, R. M. Weisskoff, and M. S. Cohen. Brain parenchyma motion: Measurement with cine echo-planar MR imaging. *Radiology*, 185(3):645–651, 1992, doi: 10.1148/radiology.185.3.1438740. (page 47)

[175] C. S. Poon and R. M. Henkelman. Practical T2 quantitation for clinical applications. *Journal of Magnetic Resonance Imaging*, 2(5):541–553, 1992, doi: 10.1002/jmri.1880020512. (page 18, 22)

[176] S. Posse and W. P. Aue. Susceptibility artifacts in spin-echo and gradient-echo imaging. *Journal of Magnetic Resonance (1969)*, 88(3):473–492, 1990, doi: 10.1016/0022-2364(90)90282-E. (page 27)

[177] T. Prasloski, A. Rauscher, A. L. MacKay, M. Hodgson, I. M. Vavasour, C. Laule, and B. Mädler. Rapid whole cerebrum myelin water imaging using a 3D GRASE sequence. *NeuroImage*, 63(1):533–539, 2012, doi: 10.1016/j.neuroimage.2012.06.064. (page 23)

[178] C. Preibisch, S. Volz, S. Anti, and R. Deichmann. Exponential excitation pulses for improved water content mapping in the presence of background gradients. *Magnetic Resonance in Medicine*, 60(4):908–916, 2008, doi: 10.1002/mrm.21730. (page 31, 32, 40, 55, 72, 73, 76, 89, 91, 96, 97, 118)

[179] K. P. Pruessmann, M. Weiger, M. B. Scheidegger, and P. Boesiger. SENSE: sensitivity encoding for fast MRI. *Magnetic resonance in medicine*, 42(5):952–62, nov 1999. (page 74, 114)

[180] I. I. Rabi, J. R. Zacharias, S. Millman, and P. Kusch. A new method of measuring nuclear magnetic moment, feb 1938, doi: 10.1103/PhysRev.53.318. (page 1)

[181] D. Raj, D. P. Paey, A. W. Anderson, R. P. Kennan, and J. C. Gore. A model for susceptibility artefacts from respiration in functional echo-planar magnetic resonance imaging. *Physics in Medicine and Biology*, 45(12):3809–3820, 2000, doi: 10.1088/0031-9155/45/12/321. (page 48)

[182] J. R. Reichenbach, R. Venkatesan, D. J. Schillinger, D. K. Kido, and E. M. Haacke. Small vessels in the human brain: MR venography with deoxyhemoglobin as an intrinsic contrast agent. *Radiology*, 204(1):272–277, 1997, doi: 10.1148/radiology.204.1.9205259. (page 16)

[183] J. R. Reichenbach, R. Venkatesan, D. A. Yablonskiy, M. R. Thompson, S. Lai, and E. M. Haacke. Theory and application of static field inhomogeneity effects in gradient-echo imaging, mar 1997, doi: 10.1002/jmri.1880070203. (page 27, 57, 99)

[184] P. Riederer, E. Sofic, W. D. Rausch, B. Schmidt, G. P. Reynolds, K. Jellinger, and M. B. Youdim. Transition Metals, Ferritin, Glutathione, and Ascorbic Acid

in Parkinsonian Brains. *Journal of Neurochemistry*, 52(2):515–520, feb 1989, doi: 10.1111/j.1471-4159.1989.tb09150.x. (page 16)

[185] B. R. Roberts, T. M. Ryan, A. I. Bush, C. L. Masters, and J. A. Duce. The role of metallobiology and amyloid-β peptides in Alzheimer's disease. *Journal of Neurochemistry*, 120(SUPPL. 1):149–166, 2012, doi: 10.1111/j.1471-4159.2011.07500.x. (page 16)

[186] S. D. Robinson, K. Bredies, D. Khabipova, B. Dymerska, J. P. Marques, and F. Schweser. An illustrated comparison of processing methods for MR phase imaging and QSM: combining array coil signals and phase unwrapping. *NMR in Biomedicine*, 30(4), 2017, doi: 10.1002/nbm.3601. (page 51, 74)

[187] P. B. Roemer, W. A. Edelstein, C. E. Hayes, S. P. Souza, and O. M. Mueller. The NMR phased array. *Magnetic Resonance in Medicine*, 16(2):192–225, nov 1990, doi: 10.1002/mrm.1910160203. (page 74)

[188] F. Roméo and D. I. Hoult. Magnet field profiling: Analysis and correcting coil design. *Magnetic Resonance in Medicine*, 1(1):44–65, 1984, doi: 10.1002/mrm.1910010107. (page 28)

[189] S. Ropele, I. D. Kilsdonk, M. P. Wattjes, C. Langkammer, W. L. De Graaf, J. L. Frederiksen, H. B. Larsson, M. Yiannakas, C. A. Wheeler-Kingshott, C. Enzinger, M. Khalil, M. A. Rocca, T. Sprenger, M. Amann, L. Kappos, M. Filippi, A. Rovira, O. Ciccarelli, F. Barkhof, and F. Fazekas. Determinants of iron accumulation in deep grey matter of multiple sclerosis patients. *Multiple Sclerosis Journal*, 20(13):1692–1698, 2014, doi: 10.1177/1352458514531085. (page 16)

[190] L. I. Sacolick, F. Wiesinger, I. Hancu, and M. W. Vogel. B1 mapping by Bloch-Siegert shift. *Magnetic Resonance in Medicine*, 63(5):1315–1322, 2010, doi: 10.1002/mrm.22357. (page 59, 60, 100)

[191] P. Sati, P. van Gelderen, A. C. Silva, D. S. Reich, H. Merkle, J. A. De Zwart, and J. H. Duyn. Micro-compartment specific T2* relaxation in the brain. *NeuroImage*, 77:268–278, 2013, doi: 10.1016/j.neuroimage.2013.03.005. (page 20, 21)

[192] L. M. Sayre, G. Perry, P. L. Harris, Y. Liu, K. A. Schubert, and M. A. Smith. In situ oxidative catalysis by neurofibrillary tangles and senile plaques in Alzheimer's disease: A central role for bound transition metals. *Journal of Neurochemistry*, 74(1):270–279, 2000, doi: 10.1046/j.1471-4159.2000.0740270.x. (page 16)

[193] K. Scheffler and S. Lehnhardt. Principles and applications of balanced SSFP techniques. *European Radiology*, 13(11):2409–2418, 2003, doi: 10.1007/s00330-003-1957-x. (page 11, 12)

[194] J. F. Schenck. The role of magnetic susceptibility in magnetic resonance imaging: MRI magnetic compatibility of the first and second kinds. *Medical Physics*, 23(6):815–850, 1996, doi: 10.1118/1.597854. (page 7, 48)

[195] J. F. Schenck. Magnetic resonance imaging of brain iron. *Journal of the Neurological Sciences*, 207(1-2):99–102, 2003, doi: 10.1016/S0022-510X(02)00431-8. (page 16)

[196] C. Schenker, D. Meier, W. Wichmann, P. Boesiger, and A. Valavanis. Age distribution and iron dependency of the T2 relaxation time in the globus pallidus and putamen. *Neuroradiology*, 35(2):119–124, 1993, doi: 10.1007/BF00593967. (page 17)

[197] J. Sedlacik, K. Boelmans, U. Löbel, B. Holst, S. Siemonsen, and J. Fiehler. Reversible, irreversible and effective transverse relaxation rates in normal aging brain at 3T. *NeuroImage*, 84:1032–1041, jan 2014, doi: 10.1016/j.neuroimage.2013.08.051. (page 91, 113)

[198] H. G. Shin, S. H. Oh, M. Fukunaga, Y. Nam, D. Lee, W. Jung, M. Jo, S. Ji, J. Y. Choi, and J. Lee. Advances in gradient echo myelin water imaging at 3T and 7T. *NeuroImage*, 188:835–844, 2019, doi: 10.1016/j.neuroimage.2018.11.040. (page 2, 25, 92)

[199] K. Shmueli, S. J. Dodd, T.-Q. Li, and J. H. Duyn. The contribution of chemical exchange to MRI frequency shifts in brain tissue. *Magnetic Resonance in Medicine*, 65(1):35–43, 2011, doi: 10.1002/mrm.22604. (page 20)

[200] S. M. Smith, M. Jenkinson, M. W. Woolrich, C. F. Beckmann, T. E. J. Behrens, H. Johansen-Berg, P. R. Bannister, M. De Luca, I. Drobnjak, D. E. Flitney, R. K. Niazy, J. Saunders, J. Vickers, Y. Zhang, N. De Stefano, J. M. Brady, and P. M. Matthews. Advances in functional and structural MR image analysis and implementation as FSL. *NeuroImage*, 23 Suppl 1:S208–19, jan 2004, doi: 10.1016/j.neuroimage.2004.07.051. (page 60, 79, 102)

[201] S. M. Smith, Y. Zhang, M. Jenkinson, J. Chen, P. Matthews, A. Federico, and N. De Stefano. Accurate, Robust, and Automated Longitudinal and Cross-Sectional Brain Change Analysis. *NeuroImage*, 17(1):479–489, sep 2002, doi: 10.1006/nimg.2002.1040. (page 60, 79, 102)

[202] M. Soellradl, A. Lesch, J. Strasser, L. Pirpamer, R. Stollberger, S. Ropele, and C. Langkammer. Assessment and correction of macroscopic field variations in 2D spoiled gradient-echo sequences. *Magnetic Resonance in Medicine*, 84(2):620–633, 2020, doi: 10.1002/mrm.28139. (page 3, 32, 76, 77, 78, 88, 91, 92, 96, 97, 99, 114, 117)

[203] M. Soellradl, L. Pirpamer, C. Langkammer, and S. Ropele. Optimization of Imaging Parameters for Fast Bound Pool Fraction Estimation from a Single Off-Resonance

Magnetization Transfer Measurement. In *Proceedings of the 34th Annual Scientific Meeting of ESMRMB*, Barcelona, Spain, 2018. (page)

[204] M. Soellradl, L. Pirpamer, J. Sedlacik, F. Fazekas, S. Ropele, and C. Langkammer. R2* Correction for Gradient Echo with a Gaussian Excitation Pulse. In *Proceedings of the 26th Annual Meeting of ISMRM*, Paris, France, 2018. (page)

[205] M. Soellradl, S. Ropele, and C. Langkammer. Gradient echo modelling with macroscopic field variations and large flip angles. In *Proceedings of the 27th Annual Meeting of ISMRM*, Montreal, Canada, 2019. (page)

[206] M. Soellradl, J. Strasser, A. Lesch, R. Stollberger, S. Ropele, and C. Langkammer. Adaptive slice-specific z-shimming for 2D spoiled gradient-echo sequences. *Magnetic Resonance in Medicine*, (July):1–13, 2020, doi: 10.1002/mrm.28468. (page 3, 117, 120)

[207] M. Soellradl, J. Strasser, and C. Ropele, Stefan Langkammer. Adaptive and slice-specific z-shimming approach for signal rephasing in 2D multi gradient echo imaging. In *Proceedings of the 28th Annual Meeting of ISMRM*, 2020. (page)

[208] A. W. Song. Single-shot EPI with signal recovery from the susceptibility-induced losses. *Magnetic Resonance in Medicine*, 46(2):407–411, 2001, doi: 10.1002/mrm.1205. (page 38)

[209] L. Squire, D. Berg, F. E. Bloom, S. du Lac, A. Ghosh, and N. C. Spitzer. *Fundamental Neuroscience*. Elsevier Science, 2012. (page 15)

[210] G. J. Stanisz, E. E. Odrobina, J. Pun, M. Escaravage, S. J. Graham, M. J. Bronskill, and R. M. Henkelman. T1, T2 relaxation and magnetization transfer in tissue at 3T. *Magnetic Resonance in Medicine*, 54(3):507–512, 2005, doi: 10.1002/mrm.20605. (page 6, 8)

[211] D. D. Stark, N. M. Bass, A. A. Moss, B. R. Bacon, J. H. McKerrow, C. E. Cann, A. Brito, and H. I. Goldberg. Nuclear magnetic resonance imaging of experimentally induced liver disease. *Radiology*, 148(3):743–751, sep 1983, doi: 10.1148/radiology.148.3.6192464. (page 16)

[212] V. A. Stenger, F. E. Boada, and D. C. Noll. Three-Dimensional Tailored RF Pulses for the Reduction of Susceptibility Artifacts in T2* Weighted Functional MRI. *Magnetic Resonance in Medicine*, 44(4):525–531, 2000, doi: 10.1002/1522-2594(200010)44:4⟨525::AID-MRM5⟩3.0.CO;2-L. (page 38)

[213] J. P. Stockmann, T. Witzel, B. Keil, J. R. Polimeni, A. Mareyam, C. Lapierre, K. Setsompop, and L. L. Wald. A 32-channel combined RF and B0 shim array for 3T brain imaging. *Magnetic Resonance in Medicine*, 75(1):441–451, 2016, doi: 10.1002/mrm.25587. (page 29)

[214] J. Strasser, M. Soellradl, C. Enzinger, and S. Ropele. Accelerating DENSE MR elastography by including multi-axes motion encoding into the multiphase DENSE-MRE acquisition scheme. In *Proceedings of the 28th Annual Meeting of ISMRM*, 2020. (page)

[215] T. J. Sumpf, A. Petrovic, M. Uecker, F. Knoll, and J. Frahm. Fast T2 mapping with improved accuracy using undersampled spin-echo MRI and model-based reconstructions with a generating function. *IEEE Transactions on Medical Imaging*, 33(12):2213–2222, dec 2014, doi: 10.1109/TMI.2014.2333370. (page 120)

[216] T. J. Sumpf, M. Uecker, S. Boretius, and J. Frahm. Model-based nonlinear inverse reconstruction for T2 mapping using highly undersampled spin-echo MRI. *Journal of Magnetic Resonance Imaging*, 34(2):420–428, aug 2011, doi: 10.1002/jmri.22634. (page 120)

[217] C. Tinauer, S. Heber, L. Pirpamer, A. Damulina, M. Soellradl, M. Sackl, E. Hofer, M. Koini, R. Schmidt, S. Ropele, and C. Langkammer. Relevance-guided Deep Learning for Feature Identification in R2* Maps in Alzheimer's Disease Classificatio. In *Proceedings of the 28th Annual Meeting of ISMRM*, 2020. (page)

[218] T. K. Truong, D. W. Chakeres, D. W. Scharre, D. Q. Beversdorf, and P. Schmalbrock. Blipped multi gradient-echo slice excitation profile imaging (bmGESEPI) for fast T2* measurements with macroscopic B0 inhomogeneity compensation. *Magnetic Resonance in Medicine*, 55(6):1390–1395, jun 2006, doi: 10.1002/mrm.20916. (page 39, 40)

[219] T. K. Truong, D. Darnell, and A. W. Song. Integrated RF/shim coil array for parallel reception and localized B0 shimming in the human brain. *NeuroImage*, 103:235–240, 2014, doi: 10.1016/j.neuroimage.2014.09.052. (page 29)

[220] P. F. Van de Moortele, J. Pfeuffer, G. H. Glover, K. Ugurbil, and X. Hu. Respiration-induced Bo fluctuations and their spatial distribution in the human brain at 7 Tesla. *Magnetic Resonance in Medicine*, 47(5):888–895, 2002, doi: 10.1002/mrm.10145. (page 25, 47, 48)

[221] P. Van Gelderen, J. A. De Zwart, J. Lee, P. Sati, D. S. Reich, and J. H. Duyn. Non-exponential T2* decay in white matter. *Magnetic Resonance in Medicine*, 67(1):110–117, 2012, doi: 10.1002/mrm.22990. (page 24, 25)

[222] V. Vasilescu, E. Katona, V. Simplâceanu, and D. Demco. Water compartments in the myelinated nerve. III. Pulsed NMR result. *Experientia*, 34(11):1443–1444, nov 1978, doi: 10.1007/BF01932339. (page 21)

[223] M. J. Versluis, J. M. Peeters, S. van Rooden, J. van der Grond, M. A. van Buchem, A. G. Webb, and M. J. van Osch. Origin and reduction of motion and

f0 artifacts in high resolution T2*-weighted magnetic resonance imaging: Application in Alzheimer's disease patients. *NeuroImage*, 51(3):1082–1088, 2010, doi: 10.1016/j.neuroimage.2010.03.048. (page 47, 48)

[224] S. Volz, M. F. Callaghan, O. Josephs, and N. Weiskopf. Maximising BOLD sensitivity through automated EPI protocol optimisation. *NeuroImage*, 189:159–170, apr 2019, doi: 10.1016/j.neuroimage.2018.12.052. (page 114)

[225] J. Vymazal, M. Hajek, N. Patronas, J. N. Giedd, J. W. Bulte, C. Baumgarner, V. Tran, and R. A. Brooks. The quantitative Relation Between T1-Weighted and T2-Weighted MRI of Normal gray Matter and iron concentration. *Journal of Magnetic Resonance Imaging*, 5(5):554–560, 1995, doi: 10.1002/jmri.1880050514. (page 17)

[226] J. Vymazal, R. A. Brooks, O. Zak, C. Mcrill, C. Shen, and G. D. Chiro. T1 and t2 of ferritin at different field strengths: effect on mri. *Magnetic Resonance in Medicine*, 27(2):368–374, 1992, doi: 10.1002/mrm.1910270218. (page 16)

[227] J. Vymazal, A. Righini, R. A. Brooks, M. Canesi, C. Mariani, M. Leonardi, and G. Pezzoli. T1 and T2 in the brain of healthy subjects, patients with Parkinson disease, and patients with multiple system atrophy: Relation to iron content. *Radiology*, 211(2):489–495, 1999, doi: 10.1148/radiology.211.2.r99ma53489. (page 17)

[228] J. Vymazal, O. Zak, J. W. Bulte, P. Aisen, and R. A. Brooks. T1 and T2 of ferritin solutions: Effect of loading factor. *Magnetic Resonance in Medicine*, 36(1):61–65, jul 1996, doi: 10.1002/mrm.1910360111. (page 16)

[229] K. Wachowicz. Evaluation of active and passive shimming in magnetic resonance imaging. *Research and Reports in Nuclear Medicine*, page 1, 2014, doi: 10.2147/rrnm.s46526. (page 27, 28)

[230] A. J. Walsh, R. M. Lebel, A. Eissa, G. Blevins, I. Catz, J. Q. Lu, L. Resch, E. S. Johnson, D. J. Emery, K. G. Warren, and A. H. Wilman. Multiple sclerosis: Validation of MR imaging for quantification and detection of iron. *Radiology*, 267(2):531–542, 2013, doi: 10.1148/radiol.12120863. (page 17, 18)

[231] J. P. Wansapura, S. K. Holland, R. S. Dunn, and W. S. Ball. NMR relaxation times in the human brain at 3.0 Tesla. *Journal of Magnetic Resonance Imaging*, 9(4):531–538, 1999, doi: 10.1002/(SICI)1522-2586(199904)9:4⟨531::AID-JMRI4⟩3.0.CO;2-L. (page 89)

[232] S. Webb, C. A. Munro, R. Midha, and G. J. Stanisz. Is multicomponent T2 a good measure of myelin content in peripheral nerve? *Magnetic Resonance in Medicine*, 49(4):638–645, 2003, doi: 10.1002/mrm.10411. (page 22)

[233] N. Weiskopf, C. Hutton, O. Josephs, R. Turner, and R. Deichmann. Optimized EPI for fMRI studies of the orbitofrontal cortex: Compensation of susceptibility-induced gradients in the readout direction. *Magnetic Resonance Materials in Physics, Biology and Medicine*, 20(1):39–49, 2007, doi: 10.1007/s10334-006-0067-6. (page 58)

[234] R. Weisskoff, C. S. Zuo, J. L. Boxerman, and B. R. Rosen. Microscopic susceptibility variation and transverse relaxation: Theory and experiment. *Magnetic Resonance in Medicine*, 31(6):601–610, 1994, doi: 10.1002/mrm.1910310605. (page 9)

[235] J. Wen, A. H. Cross, and D. A. Yablonskiy. On the role of physiological fluctuations in quantitative gradient echo MRI: implications for GEPCI, QSM, and SWI. *Magnetic Resonance in Medicine*, 73(1):195–203, jan 2015, doi: 10.1002/mrm.25114. (page 48, 51, 60, 92, 99)

[236] S. Wharton and R. Bowtell. Fiber orientation-dependent white matter contrast in gradient echo MRI. *Proceedings of the National Academy of Sciences of the United States of America*, 109(45):18559–18564, 2012, doi: 10.1073/pnas.1211075109. (page 20)

[237] K. P. Whittall and A. L. MacKay. Quantitative interpretation of NMR relaxation data. *Journal of Magnetic Resonance (1969)*, 84(1):134–152, aug 1989, doi: 10.1016/0022-2364(89)90011-5. (page 61)

[238] C. Wiggins, V. Gudmundsdottir, D. Le Bihan, V. Lebon, and M. Chaumeil. Orientation Dependence of White Matter T2* Contrast at 7 T : A Direct Demonstration. *Proceedings 16th Scientific Meeting, International Society for Magnetic Resonance in Medicine, Toronto*, (January):237, 2008. (page 19)

[239] J. M. Wild, W. R. Wayne Martin, and P. S. Allen. Multiple gradient echo sequence optimized for rapid, single-scan mapping of R2* at high B0. *Magnetic Resonance in Medicine*, 48(5):867–876, nov 2002, doi: 10.1002/mrm.10291. (page 39, 42)

[240] J. L. Wilson, M. Jenkinson, and P. Jezzard. Optimization of static field homogeneity in human brain using diamagnetic passive shims. *Magnetic Resonance in Medicine*, 48(5):906–914, 2002, doi: 10.1002/mrm.10298. (page 29, 118)

[241] J. L. Wilson, M. Jenkinson, and P. Jezzard. Protocol to determine the optimal intraoral passive shim for minimisation of susceptibility artifact in human inferior frontal cortex. *NeuroImage*, 19(4):1802–1811, 2003, doi: 10.1016/S1053-8119(03)00225-8. (page 29)

[242] G. L. Wismer, R. B. Buxton, B. R. Rosen, C. R. Fisel, R. F. Oot, T. J. Brady, and K. R. Davis. Susceptibility induced MR line broadening: Applications to brain iron mapping. *Journal of Computer Assisted Tomography*, 12(2):259–265, 1988, doi: 10.1097/00004728-198803000-00014. (page 14)

[243] R. L. Wixom, L. Prutkin, and H. N. Munro. Hemosiderin: nature, formation, and significance. *International Review of Experimental Pathology*, Vol.22:193–225, 1980. (page 16)

[244] J. C. Wood, C. Enriquez, N. Ghugre, J. M. Tyzka, S. Carson, M. D. Nelson, and T. D. Coates. MRI R2 and R2* mapping accurately estimates hepatic iron concentration in transfusion-dependent thalassemia and sickle cell disease patients. *Blood*, 106(4):1460–1465, aug 2005, doi: 10.1182/blood-2004-10-3982. (page 119)

[245] B. Wowk, M. C. McIntyre, and J. K. Saunders. k-Space detection and correction of physiological artifacts in fMRI. *Magnetic Resonance in Medicine*, 38(6):1029–1034, 1997, doi: 10.1002/mrm.1910380625. (page 47)

[246] D. A. Yablonskiy. Quantitation of intrinsic magnetic susceptibility-related effects in a tissue matrix. Phantom study. *Magnetic Resonance in Medicine*, 39(3):417–428, 1998, doi: 10.1002/mrm.1910390312. (page 2, 8, 31, 56)

[247] D. A. Yablonskiy and E. M. Haacke. Theory of NMR Signal Behavior in Magnetically Inhomogeneous Tissues: The Static Dephasing Regime. *Magnetic Resonance in Medicine*, 32(4):749–763, 1994. (page 9, 10, 17, 19)

[248] D. A. Yablonskiy, X. He, J. Luo, and A. L. Sukstanskii. Lorentz sphere versus generalized Lorentzian approach: What would lorentz say about it? *Magnetic Resonance in Medicine*, 72(1):4–7, 2014, doi: 10.1002/mrm.25230. (page 20)

[249] D. A. Yablonskiy and A. L. Sukstanskii. Generalized Lorentzian Tensor Approach (GLTA) as a biophysical background for quantitative susceptibility mapping. *Magnetic Resonance in Medicine*, 73(2):757–764, 2015, doi: 10.1002/mrm.25538. (page 21)

[250] D. A. Yablonskiy, A. L. Sukstanskii, J. Luo, and X. Wang. Voxel spread function method for correction of magnetic field inhomogeneity effects in quantitative gradient-echo-based MRI. *Magnetic Resonance in Medicine*, 70(5):1283–1292, 2013, doi: 10.1002/mrm.24585. (page 3, 30, 32, 34, 35, 36, 42, 74, 76, 77, 78, 88, 90, 114, 118, 120)

[251] Q. X. Yang, B. J. Dardzinski, S. Li, P. J. Eslinger, and M. B. Smith. Multi-gradient echo with susceptibility inhomogeneity compensation (MGESIC): Demonstration of fMRI in the olfactory cortex at 3.0 T. *Magnetic Resonance in Medicine*, 37(3):331–335, 1997, doi: 10.1002/mrm.1910370304. (page 39, 40)

[252] Q. X. Yang, G. D. Williams, R. J. Demeure, T. J. Mosher, and M. B. Smith. Removal of local field gradient artifacts in T2*-weighted images at high fields by gradient-echo slice excitation profile imaging. *Magnetic Resonance in Medicine*, 39(3):402–409, 1998, doi: 10.1002/mrm.1910390310. (page 39, 40, 41)

[253] S. Yang, H. Kim, M.-O. Ghim, B.-U. Lee, and D.-H. Kim. Local in vivo shimming using adaptive passive shim positioning. *Magnetic Resonance Imaging*, 29(3):401–407, apr 2011, doi: 10.1016/J.MRI.2010.10.004. (page 29)

[254] X. Yang, S. Sammet, P. Schmalbrock, and M. V. Knopp. Postprocessing correction for distortions in T2* decay caused by quadratic cross-slice B0 inhomogeneity. *Magnetic Resonance in Medicine*, 63(5):1258–1268, 2010, doi: 10.1002/mrm.22316. (page 31, 73, 76)

[255] S. M. Yang QX, Dardzinski BJ, Demeure RJ, Briggs RW. Removal of local field gradient artifacts in T2* measurement and T2* contrast at high field. In *Proceedings of the 6th Annual Meeting of ISMRM, Sydney, Australia*, page 578. Proceedings of the 6th Annual Meeting of ISMRM, Sydney, Australia, 1998. (page 39, 40)

[256] C. Y. Yip, J. A. Fessler, and D. C. Noll. Advanced three-dimensional tailored RF pulse for signal recovery in T 2*-weighted functional magnetic resonance imaging. *Magnetic Resonance in Medicine*, 56(5):1050–1059, 2006, doi: 10.1002/mrm.21048. (page 38)

[257] P. A. Yushkevich, J. Piven, H. C. Hazlett, R. G. Smith, S. Ho, J. C. Gee, and G. Gerig. User-guided 3D active contour segmentation of anatomical structures: Significantly improved efficiency and reliability. *NeuroImage*, 31(3):1116–1128, jul 2006, doi: 10.1016/j.neuroimage.2006.01.015. (page 61)

[258] K. Zhong, J. Leupold, D. von Elverfeldt, and O. Speck. The molecular basis for gray and white matter contrast in phase imaging. *NeuroImage*, 40(4):1561–1566, 2008, doi: 10.1016/j.neuroimage.2008.01.061. (page 20)

[259] Y. Zur, M. L. Wood, and L. J. Neuringer. Motion-insensitive, steady-state free precession imaging. *Magnetic Resonance in Medicine*, 16(3):444–459, 1990, doi: 10.1002/mrm.1910160311. (page 13)

[260] Y. Zur, M. L. Wood, and L. J. Neuringer. Spoiling of transverse magnetization in steady-state sequences. *Magnetic Resonance in Medicine*, 21(2):251–263, 1991, doi: 10.1002/mrm.1910210210. (page 13)